Magneto-Rayleigh-Taylor Instability: theory and simulation in planar and cylindrical pulsed power targets

by

Matthew R. Weis

A dissertation submitted in partial fulfillment
of the requirements for the degree of
Doctor of Philosophy
(Nuclear Science)
in The University of Michigan
2015

Doctoral Committee:

Professor Yue Ying Lau, Chair
Professor John E. Foster
Professor Ronald M. Gilgenbach
Kyle J. Peterson, Sandia National Laboratories
Assistant Professor Louise Willingale

For the many important people in my life.

ACKNOWLEDGEMENTS

Completing this thesis would be impossible without the help of many others. I would first like to thank Professors Y. Y. Lau and Ronald Gilgenbach for inviting me into their group at the University of Michigan and supporting me throughout my time here since September of 2010 as well as serving on my dissertation committee. Professor Lau's knack for theoretical problem solving is something to behold and I hope to carry on that tradition. I would also like to thank Prof. Lau for serving as chair and mentor. I have learned a great deal of the world from Professors Lau and Gilgenbach, particularly when it comes to the financial side of science. This is certainly knowledge one does not typically find in plasma physics courses. Professor Lau was also kind enough to invite me along to the first MagLIF meeting in Albuquerque, which has been one of the largest influencing events of my graduate career. Of course, Professor Gilgenbach was also kind enough to introduce me to Dr. Mike Cuneo who helped bring me out to Sandia for a summer. Additionally, I would like to thank my current and future manager at Sandia National Laboratories, Dr. Kyle J. Peterson for joining my dissertation committee. I am more than happy and very grateful to continue to work in his group after graduation. I would also like to thank Professors John E. Foster and Louise Willingale for being a part of my doctoral committee. I am also thankful for the opportunities I had to learn from them in my plasma physics coursework. Between the two of them my knowledge spanned from first learning about what a plasma is to being initiated to the complexities of laser-plasma interactions.

A number of unique opportunities have also contributed to where I am today. I am thankful to Lawrence Livermore National Laboratory's High Energy Density Physics summer scholar program that I participated in for three summers: 2009, 2010, and 2011. There I was exposed to high energy density physics (HEDP) for the first time through activities at the National Ignition Facility. Because of my time there I not only met many great friends but set my academic course for HEDP research. I am thankful for my mentors at Livermore, Peter Anninos, Rob Hoffman, and in particular, Jay Salmonson, who first introduced me to the HYDRA code which I have used throughout graduate school. Joe Koning, the designer of the HYDRA MHD package, has also been an invaluable resource throughout the years.

Following my summers in Livermore, I also spent time at Sandia National Laboratories in Albuquerque. I am thankful to Mike Cuneo and Charlie Nahkleh who were kind enough to invite me out to the lab for the summer in 2012 and then for a six month period the following year. When Charlie went to Los Alamos, Kyle Peterson stood in as my manager and has supported me ever since and I am thankful to join his group this fall. Throughout my entire time affiliated with Sandia, Mark Hess has been my mentor and I am thankful for his guidance. Being located outside of the cleared areas, I had few HEDP neighbors, but Dr. Chris Jennings more than made up for that. Chris was always willing to talk with me, and I learned a great deal about the physics of Z-pinches on the Z-machine.

I was lucky enough to spend a few months in the Michigan Plasma, Pulsed Power, and Microwave lab while Drs. David French, Jacob Zier, and Matt Gomez were still finishing their dissertations and learn from them about being a graduate student in the short time we overlapped. David, Matt and Dr. Brad Hoff (another graduate of Professor Gilgenbach) also introduced me to Albuquerque and made a six-month stay much more enjoyable. Over the years I've also enjoyed our theory meetings and happy hours with Professor Lau, Dr. Peng Zhang, Dr. Ian Rittersdorf and David

Simon where I often learned more about high power microwave devices than I ever thought I would. Overall, the comradery of our lab including everyone else I haven't mentioned, David Yager-Elorriaga, Steven Exelby, Sonal Patel, and Adam Steiner, made for an incredible grad school experience. I was also happy to hear that Geoff Greening decided to join our lab shortly after myself, after many good years as Geoff's roommate for nearly all of undergrad.

Overall, I could not have asked for a more enjoyable graduate school experience and I am thankful for all my friends and family who helped to make it possible. On a personal level, my family and friends were instrumental in helping me to complete my dissertation. My contemporaries David Simon and Matt Franzi have been great friends as well as co-workers. Having lived in Ann Arbor for more than eight years now, I'll always have a soft spot for Ashley's and the bar at 327 Braun Court and the memories there. One personal triumph was shared with Matt Franzi and Matt Gomez running the 11 mile Tough Mudder obstacle course in the cold and rain and then sharing a miserable four hour car ride home (thanks for driving Matt G.!). The gym and tennis were my stress alleviators throughout graduate school. Somehow Ian and I managed to ride our bikes to the gym at 7 AM and then bike up to North Campus to do plasma theory. Through tennis I met many wonderful people including my partner Liz Copeland. She has supported me unwaveringly through a great deal of difficult decisions for which I am eternally grateful. That, and allowing a pair of crazy cats, Gracie and Shadow to join us.

Last but not least, this research was supported by the U.S. DOE awards DE-SC0002590 and DE-SC0012328. Additional support for the author was provided by Sandia National Laboratories and the SEERI program there. Sandia National Laboratories is a multi-program laboratory operated by Sandia Corporation, a Lockheed Martin Company, for the United States Department of Energys National Nuclear Security Administration under Contract DEAC04- 94AL85000.

TABLE OF CONTENTS

LIST OF FIGURES

Figure

LIST OF APPENDICES

Appendix

ABSTRACT

Magneto-Rayleigh-Taylor Instability: theory and simulation in planar and cylindrical pulsed power targets

by

Matthew R. Weis

Chair: Professor Yue Ying Lau

Cylindrical liner implosions in the Magnetized Liner Inertial Fusion (MagLIF) concept are susceptible to the magneto-Rayleigh-Taylor instability (MRT). The danger of MRT enters in two phases, (1) during the main implosion, the outer surface of the liner is MRT unstable, and (2) during the short time period when the liner decelerates onto the hot fuel, the inner surface becomes unstable. Growth of MRT on the outer surface may also feedthrough, which may seed the inner surface leading to high MRT growth in the second phase. If MRT growth becomes large enough, confinement of the fuel is lost.

To characterize MRT, we solve the linearized, ideal MHD equations in both planar and cylindrical geometries, including an axial magnetic field and the effects of sausage and kink modes. To evaluate our analytic growth rates, 1D HYDRA MHD simulations are used to generate realistic, evolving profiles (in density, pressure, and magnetic field) during the implosion. In general, the total instability growth rates in cylindrical geometry are larger than those in planar geometry. MRT and feedthrough are suppressed by strong magnetic field line bending (tension). We apply our analytic

MRT growth rates to experiments on the Z-machine at Sandia National Laboratories. Analytic MRT growth rates for a typical magnetized MagLIF-like implosion show the kink mode to be the fastest growing early and very late in the liner implosion (during deceleration).

Sophisticated 2D HYDRA simulations show that highly compressed axial magnetic fields can reduce the growth of perturbations at the fuel/liner interface during the implosion phase, enhancing the stability of the implosion. HYDRA 2D simulations also show that a non-uniform shock, driven from the liner exterior, can seed the liner interior, leading to substantial growth of instability far in excess of feedthrough. Large-scale perturbations on the liner interior may also feedout to the liner exterior when a shock wave interacts with the surface, which further destabilizes the liner. These effects are reduced when shock compression is minimized or significant perturbations are not present during shock compression. The feedthrough effects then dominate.

CHAPTER I

Introduction

1.1 Introduction

Fluid instabilities are found everywhere in nature. The Rayleigh-Taylor instability (RT) is one of these fluid instabilities [1][2]. Interchange of light and heavy fluid in an effective gravity is the source of RT. A slightly more general condition for RT is the presence of opposing density and pressure gradients, stated mathematically as $\nabla\rho \cdot \nabla p < 0$. This relatively simple configuration is found both terrestrially and throughout the universe. For example, this simple relation explains the instability of water supported by air in Earth's gravity. It also explains the stable form of RT in deep-water waves. RT is also found in astrophysical systems such as supernovae and their remnants [3]. Often times significant electrical currents are present, generating strong magnetic fields. These magnetic fields can affect RT and thus the term magnetic or magneto-Rayleigh-Taylor instability (MRT) is coined [4][5][6]. In this case, $\nabla\rho \cdot \nabla p < 0$ still holds, where p is now interpreted as the total pressure including the magnetic pressure. The natural analog of water supported by air is then plasma supported by magnetic pressure. Figure 1.1 presents a simple scenario of MRT where a heavy fluid is supported by a 'light fluid' which is the magnetic field. The growth rate of MRT for $\vec{k} \cdot \vec{B} > 0$ (LHS of Fig. 1.1) is less than $\gamma_{MRT} = \sqrt{kg}$ due to the magnetic tension of the bent field lines. The growth rate for the case where $\vec{k} \cdot \vec{B} = 0$

(RHS of Fig. 1.1) is the well-known $\gamma_{MRT} = \sqrt{kg}$. The result is that MRT evolves anisotropically which differentiates it from classic RT. While natural sources of MRT

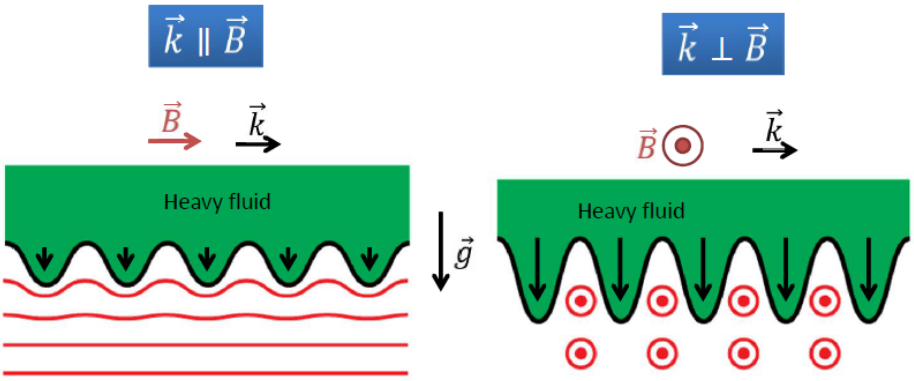

Figure 1.1: A simple scenario of MRT where a heavy fluid is supported by a 'light fluid', the magnetic field. The growth rate of MRT for $\vec{k} \cdot \vec{B} > 0$ (LHS) is less than $\gamma_{MRT} = \sqrt{kg}$ due to the magnetic tension of the bent field lines. The growth rate for the case where $\vec{k} \cdot \vec{B} = 0$ (RHS) is the well-known $\gamma_{MRT} = \sqrt{kg}$.

on Earth are somewhat more limited, advances in pulsed power technology have made MRT important to a wide range of laboratory experiments. These include but are not limited to imploding Z-pinches[7][8][9], magnetically launched flyer plates [10][11], inertial confinement fusion (ICF) [12][13], and even railguns [14]. In most planar targets, MRT is likely the dominant instability which may be seeded by the electrothermal instability (discussed in later paragraphs) [15][16][17][18][19][20]. Cylindrical targets introduce additional instabilities when there is sufficient current flowing in the target. Prime examples of this are the sausage and kink modes in Z-pinches.

Much of this thesis is devoted to the Z-pinch, one of the first attempts at controlled nuclear fusion. In a Z-pinch, a strong axial electric current flows along the z-axis of a cylindrical column of plasma (hence 'Z-pinch'). The axial current generates an azimuthal magnetic field. The combination of the axial current and azimuthal magnetic field implodes the plasma column via the $\vec{J} \times \vec{B}$ force. As originally designed, the pinch would achieve equilibrium between the hot fusing plasma and its confining magnetic pressure (known as $\beta = 1$ plasma, where the magnetic and kinetic pressures

are equal). One model is the Bennett pinch [21]. In practice, the instability modes known as the sausage and kink modes destroy confinement of the current carrying plasma. The sausage mode is the familiar axisymmetric mode that breaks a plasma column into what can be described as 'sausage links'. With the tendency to increase its inductance, a current carrying plasma column could coil up, which is the physical basis of the kink mode [22]. The kink mode is no longer axisymmetric and is a fully 3D mode. In a Z-pinch there is also very little confinement along the z-axis leading to end losses. To solve this problem, the Z-pinch ends were closed by looping them into, what is now, the tokamak to achieve long timescale confinement. This field of fusion research is called magnetic confinement fusion, where the plasma tends to be overall stationary and the plasma is confined by a strong magnetic field on the order of seconds (with the goal of steady-state operation).

1.1.1 History and background of ICF and Z-pinches

The Rayleigh-Taylor instability was first studied by Lord Rayleigh in 1882 [1] and then Sir G. I. Taylor in 1950 [2]. This laid the groundwork for 60 + years of additional theoretical, numerical, and experimental research into RT. Lord Rayleigh's original interest, in what is now known as the Rayleigh-Taylor instability (RT), was in explaining cirrous cloud formations (long before considering RT in laser or magnetically accelerated ICF targets). Taylor introduced the idea that strong acceleration in the lab could also generate RT [2] (still before ICF but probably related to uncontrolled fusion). Even before the advent of the laser, inertial confinement fusion was conceived by John Nuckolls [23]. The idea was further tested in computer simulations. The vast majority of the remainder of the century focused on these laser driven ICF concepts [24]. To this day, RT remains one of the greatest challenges of a successful ICF campaign.

Early work by Kruskal and Schwarzchild [4], Tayler [25] and Chandrasekhar [5]

began the study of Z-pinch instabilities in the 50s and early 60s. Linhart [26] and Harris [6] later studied the magneto-Rayleigh-Taylor instability including Z-pinch instabilities. The motivation for the work, stated by Harris, who also cites Linhart, is, "The use of a collapsing conducting shell in a magnetic field has been proposed as a method of producing thermonuclear power and as a method of producing high magnetic fields". Sixty years later the overall idea remains the same for magnetically driven ICF at Sandia National Laboratories, the preeminent pulsed power laboratory in world. Though the shells are thicker and a laser preheats the fusion fuel, the **Mag**netized **L**iner **I**nertial **F**usion (MagLIF [12]) program at Sandia (to be described in the following section) could still be described by what Harris wrote. However, Harris somewhat understates the importance of MRT. As with laser driven ICF, RT or MRT is the major design consideration in any ICF target.

In its current form, laser driven ICF is very much distinct from magnetically driven ICF. To begin, laser driven ICF almost always uses a spherical capsule, which requires 3D compression, whereas the Z-pinch geometry is only in 2D. Though this theoretically requires higher compression to achieve the same volumetric compression as a spherical capsule, there are many techniques to relax this requirement [12][27]. Additionally, the Z-pinch is a part of the driver circuit itself whereas the laser is its own element. This means the target itself must be considered with respect to the entire driver (a simple example is that increasing the length of a cylindrical target, increases its inductance, which reduces the total current) [28][21]. With the current state of technology, magnetically driven ICF is more efficient in coupling the driver energy to the target, particularly when comparing indirect radiation drive methods. In indirect drive laser ICF there are numerous inefficiencies: laser energy is first converted to X-rays which then must be coupled to the spherical capsule. These inefficiencies can be very detrimental to relatively low yield targets if not enough of the driver energy is coupled to the target. There is also indirectly driven magnetic

ICF, where a wire array generates X-rays which then implode a target [29], however current interest lies in directly driven magnetic ICF.

Common to both spherical and cylindrical implosions is the susceptibility to feedthrough of RT or MRT. ICF typically includes a fairly dense material confining a lower density fuel during an implosion. As the shell implodes the exterior is unstable to RT or MRT, the interior fuel/shell interface remains stable. However, the ripples generated from the unstable outer shell surface might feedthrough to the inner shell surface, so that the latter is not guaranteed to remain smooth [30]. The amplitude of the ripple that feeds-through is exponentially reduced when the shell thickness becomes appreciable.

Z-pinches today are used in a wide variety of experimental platforms including radiation generation (X-rays, neutrons) [31][32][33], materials effects [10][11][34], equation of state measurements [35][36][37], and still inertial confinement fusion[12][38][39]. The X-rays produced can be used for a wide variety of additional measurements including radiation effects on materials, indirect drive fusion [29][20][21], and opacity measurements as related to astrophysical atmospheres [40][41]. The two Z-pinch drivers that will be considered in this thesis are the Z-accelerator at Sandia National Laboratories in Albuquerque, NM [42][29] and the Michigan Accelerator for Inductive Z-pinch Experiments (MAIZE) [43][44][45][46][47][48]. The Z-machine stores 22 MJ of energy in its capacitor banks and can deliver a peak current of 27 MA in 100 ns for a well matched load [38]. MAIZE can drive perfectly matched loads with 1 MA on the order of 150 ns. More typical currents for ICF targets are 20 MA for Z (cylindrical liners) and 0.6 MA for MAIZE (aluminum foils). Nevertheless, both these current levels are sufficient to generate significant acceleration that drives MRT growth in cylindrical and planar Z-pinch loads. Much of the work on MAIZE has focused on fundamental issues related to MRT, while work on Z has investigated both fundamental problems as well as fully integrated magneto-inertial fusion experiments.

1.1.2 Motivation

The magneto-Rayleigh-Taylor instability has received renewed interest as technology has improved and driver and design capabilities bring the world closer to controlled thermonuclear fusion via ICF. The early work on MRT occurred before the advent of multi-physics codes, sophisticated mathematical analysis software, and versatile numerical solvers of non-linear differential equations. Advances in experimental facilities and diagnostics have also occurred, certainly no more so than at the Z-accelerator. These advances have paved the way for the current magneto-inertial fusion program at Sandia, MagLIF [12]. The concept is depicted in Fig. 1.2 as originally presented by Gomez et al. [38] with the first experimental results.

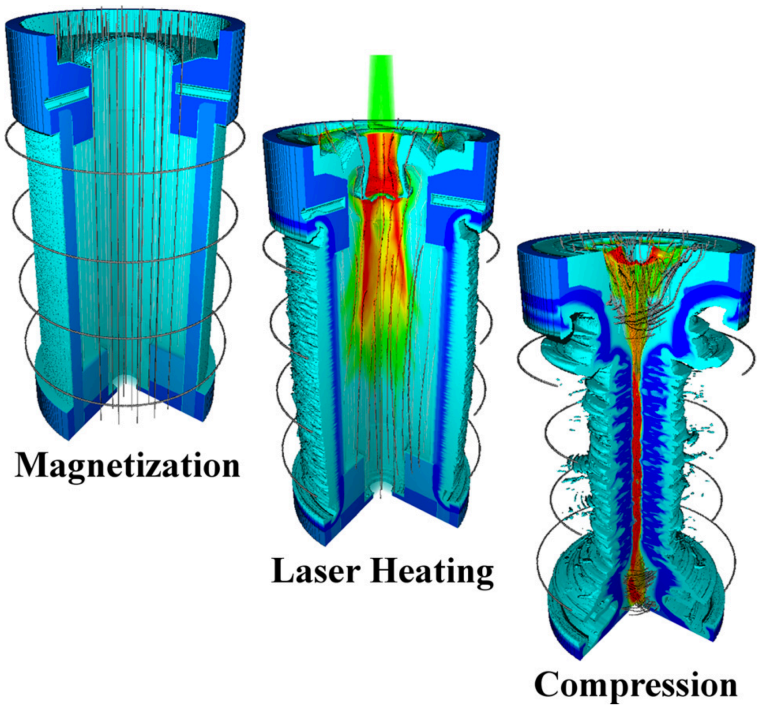

Figure 1.2: Simulation images showing the three main phases of a MagLIF implosion: magnetization with a > 10 T axial magnetic field, pre-heating of the fuel via a kiloJoule class laser, and finally compression via the pinch force. The magneto-Rayleigh-Taylor instability is featured prominently on the liner exterior as the liner compresses[38].

Lindemuth and Kirkpatrick studied magnetized capsule regimes where initial fuel densities and implosion velocities were low, known now as magnetized target fusion (MTF) [49][50]. MagLIF, like MTF, is a hybrid between traditional ICF and magnetic confinement fusion. Laser driven ICF typically is on the order of nanoseconds, while magnetic confinement fusion occurs on the order of seconds with the ultimate goal of steady state operation. As MagLIF is designed for the Z-machine, implosions on the order of 100 ns are typical with an approximately 10 ns window of time during which the fusion occurs. This is known as a fast Z-pinch [21][20]. A MagLIF target is a cylindrical metallic tube, called a liner, with a fusion fuel in the center of the tube. There are two key features of MagLIF: the initial pre-heat of the fusion fuel and applied axial magnetic field. The preheat of the fuel reduces the compression required to achieve fusion relevant conditions. This is particularly important since implosion velocities are slower than at facilities such as the NIF. Since less compression is required, this has the potential to reduce the danger of MRT as well. The pre-magnetization helps keep the fusion fuel hot by reducing thermal conduction in the radial direction. A strong axial magnetic field can also help to confine the burning ions as well. This thesis will show the potential of the axial magnetic field to reduce feedthrough and improve the stability of the implosion.

These liners are designed to be relatively thick (100s of microns) to be robust to MRT. As with nearly any other ICF concept, the basic goal is to mitigate the impact of MRT/RT growth but retain sufficient implosion velocity to deliver enough energy to the fuel. The MagLIF liner straddles both of these goals as the liner is thick enough to tolerate any MRT, yet energetic enough to achieve fusion relevant conditions [38]. Since the liner provides the inertial confinement of the fuel, it must remain intact and increasing the thickness of the liner is one of the most straightforward ways to improve its survivability. The ρr of the liner and fuel, respectively, at peak compression is ~ 1 g/cm^2 and 0.01 g/cm^2. The ρr of the liner is the more important of the two for

inertial confinement unlike the capsules at the NIF which require high ρr of the fuel [12]. The combination of the preheat, premagnetization, and implosion of a MagLIF target have generated exciting experimental results. In the four short years after the original design paper by Slutz et al. [12], the first integrated MagLIF experiments by Gomez et al. [38][39] obtained yields in excess of 10^{12} neutrons and inferred ion temperatures of > 2 keV. Many important experiments preceded the fully integrated experiments, a short history of which is discussed next.

In Slutz's paper introducing MagLIF [12], MRT was already a primary concern. One year later, Sinars et al. [51] published the first controlled measurements of MRT evolution for a fast Z-pinch. The experiments utilized aluminum liners with machined sinusoidal perturbations on the exterior. This fixed the axial wavelength of MRT. The liners were then imploded on the Z-machine with a peak current of nearly 20 MA but without any preheat or axial magnetic field. To measure the MRT growth two-frame 6.151 keV X-ray radiography was used [52]. A photograph of the seeded aluminum liner and an example cropped radiograph is shown in Fig. 1.3. The temporal evolution

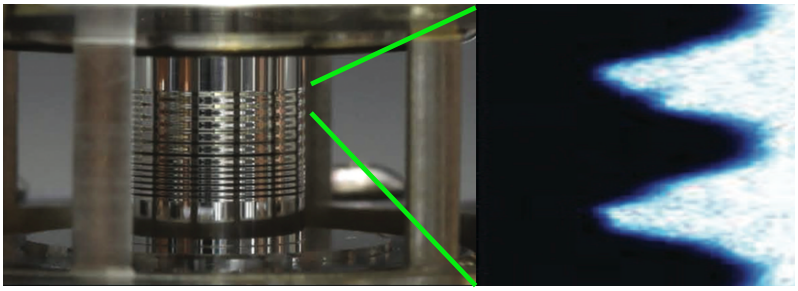

Figure 1.3: Experiments by Sinars et al. [51] imploded a seeded aluminum liner on the Z-machine. To the right is a blown up radiograph of the 400 μm axial wavelength region.

of the perturbations was then determined from a collection of shots (a shot in this instance refers to a liner experiment on the Z-machine), observed at different points in the current pulse. Single mode perturbations were observed to grow according to linear theory for much of the evolution. Additional experiments were performed with

liners with only the perturbations intrinsic to liner production process. These liners showed that early-on, the growth of MRT was not azimuthally correlated (was non-axisymmetric). Later experiments by McBride et al. examined these sort of liners in more depth [53].

McBride et al. [53] performed experiments using unseeded beryllium liners (leaving only the natural surface roughness), the liner material for the MagLIF point-design, again, without an axial magnetic field. Beyond different material properties, beryllium surfaces are typically characterized by overall rougher surfaces following the liner production. The initially smaller perturbations, both in wavelength and amplitude, allow higher compression to be achieved. These experiments provided strong evidence for a large amplitude 3D growth though azimuthally correlated structure remained. Such features could not be obtained by 2D simulations. Because beryllium is less opaque to 6.151 keV X-rays, information on the liner inner surface could also be obtained (see Fig. 1.4 below where the inner surface is apparent). A total of 8 radiographs were obtained and from them the evolution of the dominant MRT wavelength and amplitude, liner ρr, and trajectories of the liner inner and outer surface could be determined. Based on the observed axial variation in ρr it was postulated that the yield could be reduced by 16 % due to the growth of the MRT [53].

The next step for MagLIF was to include an axial magnetic field (still without any preheat), as was done by Awe et al. [54][55]. These experiments produced some of the most visually stunning liner implosion data to date. An example radiograph of such is shown in Fig. 1.4. Beryllium liners were used again but now with 7 and 10 T axial magnetic fields made possible by the new Applied B_z (known as ABZ [56]) capability on Z. The radiographs from Awe et al. [54][55], clearly showed the MRT taking on a helical pattern wrapping around the liner; a feature not present without the axial magnetic field. Another striking feature of the radiographs was the lack of time integrated self-emission (TISE) from the implosion. This emission is often found

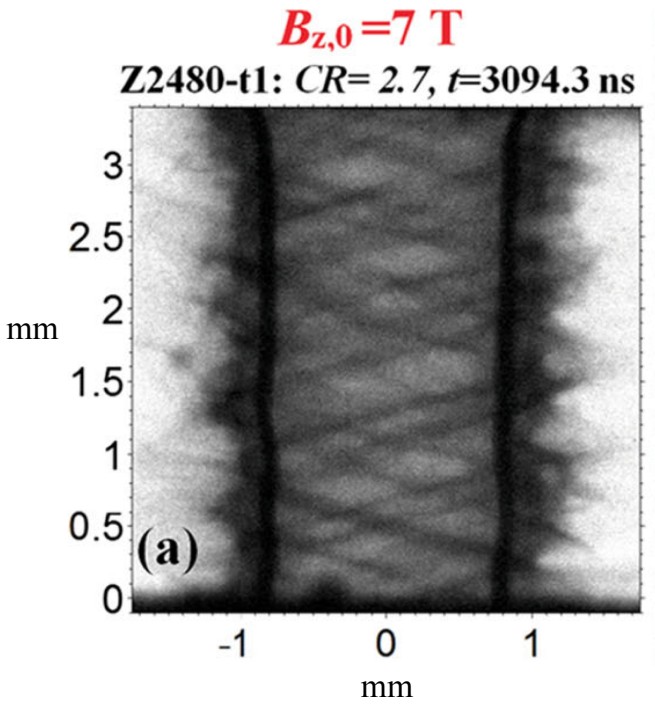

Figure 1.4: Experiments by Awe et al. [55] imploded a pre-magnetized (10 T) beryllium liner on the Z-machine and imaged by the radiography system.

at pinch points of an implosion and indicates non-uniform compression. Thus the lack TISE may also indicate improved stability of the liner implosion. One possible source of this enhanced stability is due to reduction of feedthrough of MRT due to successful compression of the axial magnetic field. This is a result anticipated by Lau et al. in 2011 [57]. The major requirement for enhanced stability to MRT feedthrough is that $B_z \approx B_\theta$ which is achievable only with successful axial magnetic field compression. Recently [9], we have also provided an explanation of the persistence of the observed helical structures in [54][55] as reproduced in Fig. 1.4 here.

The most recent MagLIF shots at Sandia utilized both a 10 T axial magnetic field and the laser preheat. These shots were found to successfully create thermonuclear neutrons, with D-D neutron yields on the order of 10^{12}, with additional secondary D-T reactions present [38][39]. Strong axial magnetic field compression was also inferred via a number of neutron diagnostics [58][59]. Spectroscopy was used to determine

the ion fuel temperature to be on the order of 2-3 keV [60]. Overall, these results were considered a great success but also suggested some avenues for improvement. For example, based on integrated 2D HYDRA simulations, the measured yields were lower than anticipated. Experimental yields were consistent with HYDRA simulations that only deposited on the order of 100 J of laser energy into the deuterium fuel [27]. The Z-beamlet total laser energy for these shots was 2 kJ, thus only a small fraction of the energy seems to have been coupled to the fuel. Studies of the preheat phase are currently underway at Sandia and at the Laboratory of Laser Energetics (LLE) at Rochester using the Omega and Omega-EP laser. Laser filamentation is a major suspect for low coupling of laser energy [27]. These experiments seek to determine if there is significant mix of liner material into the fuel from the preheat phase as well as characterize the preheat itself. Mix was postulated as another mechanism for degraded yield [27].

To reduce MRT growth in these experiments, a novel technique has been used to reduce a seed to MRT growth, by reducing growth of the electrothermal instability (ETI). The current theory is that the electrothermal instability provides the initial seed for MRT and reducing the ETI growth can subsequently slow the development of MRT. ETI is unique to current driven pulsed power loads as the instability is driven by the temperature dependence of electrical resistivity, η [17][20]. A simple form of the growth rate, γ, for the striation form (defined below) is $\gamma = (J_z^2 \partial\eta/\partial T - k_z^2\kappa)/\rho_0 c_v$, where κ is the thermal conductivity, c_v is the metal heat capacity, ρ_0 the metal density, J_z the axial current density, and k_z the axial wavenumber. In solid metals, the resistivity increases with increasing temperature ($\partial\eta/\partial T > 0$). As the current heats the metal, nonuniformities can lead to nonuniform heating. Because $\partial\eta/\partial T > 0$, this leads to runaway of nonuniform heating (instability). Thermal conductivity is stabilizing since transport of heat from the hot spots limits the runaway heating of the hot spot. This instability can also occur in plasma despite the opposite scaling,

$\partial\eta/\partial T < 0$ (using Spitzer scaling), but the perturbations become azimuthally oriented ("filamentation" form), as opposed to axially oriented ("striation" form).

ETI grows from the initial non-uniformities present on the liner surface. For aluminum or beryllium, these initial perturbations are very small (on the order of 100s of nm to 1 μm [51]) but nonetheless can become quite important for the overall stability of the liner. Experiments by Peterson et al. [17][18] have made great progress towards solving the ETI problem by coating the exterior liner surface with a thin dielectric coating [19]. The dielectric is theoretically stable to ETI and also provides hydrodynamic tamping of any mass redistribution in the metal due to the current flowing there. The exact mechanism for enhanced stability has not yet been determined between these mechanisms. These stand-alone experiments (no axial magnetic field or preheat) have successfully shown dramatic reduction in instability growth [19].

Though there have been many successes with MagLIF, many interesting problems still remain with regard to liner stability. While the dielectric coating seems capable of significantly improving resilience to MRT, the current in the liner drives the sausage-like and kink-like modes. Since this is not inhibited by the coating, perturbations could penetrate into the bulk and potentially become more important at high compression [9]. Most of the early design of MagLIF targets was done using 2D (r, z) simulation codes which certainly cannot account for 3D modes such as the kink mode which has been shown to be the dominant modes in integrated experiments [54][55][38][39]. As mentioned above, experiments by Awe et al. [54][55] show the kink and perhaps higher azimuthal mode number modes to be very important to the instability structure. Currently, these helical modes can only be generated with an ad-hoc seed on the liner in 3D simulations [55]. Since the helical modes are present in experiment, analytic models ([6][7][9]) can also calculate their evolution. Helical modes may also feedthrough the most strongly, however they are not captured in 2D simulations. The laser preheat is also largely not well understood, particularly

with regard to filamentation and energy deposition at the liner surface which could lead to ETI or other non-uniformities. Since ETI requires the presence of electrical current, some sources are magnetic diffusion of the azimuthal field, or currents generated by axial magnetic field gradients near the liner inner surface. Even without the sausage and kink modes there is intrinsic anisotropy to MRT due to the very large driving field [57]. Understanding this anisotropy is the basis a large number of experiments on MAIZE performed by previous graduate students and continue today at the University of Michigan [48][46][61][62][63][64][65].

While there has been a great deal of experimental progress for magnetized liner implosions, such as MagLIF, the stability theory has been slow to follow. Works by Harris [6] (1962) and Bud'ko [7] (1990) are the most relevant for MRT in magnetized liner implosions but of course were developed without the capabilities of modern facilities, such as Z, in mind. One of the limitations of the work by Harris [6] is that he did not de-couple the kinetic and magnetic pressures driving acceleration. This also clouds the effect of field line bending $(\vec{k} \cdot \vec{B})^2$ on MRT growth rates and feedthrough. Harris [6] also introduced the idea that MRT and sausage and kink modes could coexist using analytic theory. However, his models did not show how. As just mentioned, his definition of g was also too intertwined with the azimuthal magnetic pressure to be versatile (e.g. he could not account for the deceleration phase, since there was no kinetic pressure in his formulation). Bud'ko et al. [7] significantly extended Harris' work using a thick shell and adiabatic gas law, though their governing equation was presented without any details or derivation. Analytic insight for this work was also limited, as the solutions they provided required numerical integration of analytic liner implosion models for the evolution of a pinch. We have improved on the assumptions in these works in our recent publications by introducing a more general approach [57][66][8][9]. This thesis places significant emphasis on the new analytic formulation for MRT and feedthrough.

1.1.3 Thesis organization

Chapter 2 builds on the work by Lau et al. [57], by fully developing the analytic linear theory of MRT and feedthrough in the framework of ideal MHD in planar geometry [8], including experimentally relevant boundaries, as well as comparing the model to experiments at Sandia National Laboratories. We have also illustrated the integration of 1D HYDRA simulations to provide realistic equilibrium models for our analytic theory. The theory allows for an arbitrary amount of field line bending as well as acceleration due to an arbitrary combination of kinetic and magnetic pressures. The growth rate and feedthrough of MRT are analyzed analytically. Applications to U-M experiments are featured. Chapter 2 also introduces the utilization of the HYDRA MHD code [67] for implosion histories that can be used to numerically compute our growth rates and feedthrough. The last third of Chapter 2 is devoted to application of the growth rates and feedthrough factors to liner experiments.

Chapter 3 introduces the coupling of MRT, sausage, and kink instabilities as well as feedthrough in cylindrical liners [9]. The sausage and kink modes are not present in planar geometry. An exact analytic theory is presented, again in the framework of ideal MHD. These exact solutions of instability growth rates and feedthrough are analyzed for MRT, sausage and kink modes for a liner of arbitrary thickness (from very thin to almost solid column). The growth rates are also applied to MagLIF relevant liner implosions, again using the HYDRA MHD code. Several stages of evolution in kink-MRT and sausage-MRT are identified in MagLIF. The cylindrical model is also extended further by modeling magnetic diffusion effects in liner implosions.

Chapter 4 relies heavily on 2D HYDRA MHD simulations of liner implosions. Many non-ideal effects not found in ideal MHD theory, such as shock compression and non-linear MRT growth and feedthrough are examined using HYDRA. In these cases, our linear theory of MRT growth and feedthrough is best suited to qualitative understanding of these simulation results. Whereas in Chapters 2 and 3, many of the

test problems for 2D HYDRA simulations were fairly linear in design, non-linear MRT growth is the dominant process in MagLIF liner implosions on Z. We also examine the effect of large scale perturbations at the fuel/liner interface on the stability of a liner implosion. Additionally, Richtmyer-Meshkov-like [68][69] instabilities are also addressed. These could be a significant issue during the preheat phase of MagLIF.

Chapter 5 summarizes the conclusions of this thesis and potential future work. Appendix A presents a bound on MRT/RT growth in terms of wavenumber and accelerated distance. Appendix B presents additional details on the derivation on cylindrical MRT. Appendix C shows some preliminary 3D HYDRA simulations.

CHAPTER II

MRT Growth Rates of a Planar Slab

2.1 Introduction

Chapter 2 introduces the magneto-Rayleigh-Taylor instability (MRT) and its feedthrough in a Cartesian coordinate system. A theoretical model is presented and coupled with 1D magneto-hydrodynamics (MHD) simulations. These 1D MHD simulations give realistic estimates for the physical quantities needed for the model at any required time. The model is tested against small-scale experiments and 2D magneto-hydrodynamic (MHD) simulations which are also benchmarked to higher current experiments on the Z-accelerator.

The development of the planar model that follows, lays much of the theoretical groundwork that permeates the remainder of this thesis. Overall, the equations developed in planar geometry are easier to work with and analyze and yet remain applicable to a large number of physical scenarios. In particular, application to exploding foils[47], flyer plates[10][11], and cylindrical liners [51][8][9] will be presented. At the appropriate level of generality, many of the classic Rayleigh-Taylor solutions can also be recovered, as the underlying equations are nearly the same. This formulation of MRT also introduces many key concepts related to the effect of magnetic fields on MRT and feedthrough. Early work focused a great deal on MRT [4][5][6] with little discussion of feedthrough. This chapter and the model discussed herein

will provide detailed discussion of feedthrough of MRT.

2.2 Development of an Ideal MHD model of the Magneto-Rayleigh-Taylor Instability

The linearized ideal MHD equations, that will be the focus of this chapter, will be used to describe the magneto-Rayleigh-Taylor instability and its feedthrough in planar geometry. We will show the equations to be highly versatile for a number of different experimental geometries. To begin, any MRT calculation, an appropriate equilibrium state for the magneto-fluid is required. Once this is determined, the ideal MHD equations are perturbed and subsequently linearized. The equilibrium quantities themselves can be determined any number of ways, whether from theory, simulation or experiment. They need only satisfy the MHD force balance discussed in the next subsection. It is important to note that the physical picture of MRT growth is that of an accelerated slab, which can be moving at some finite speed. This is unlike an equilibrium Z-pinch where the plasma is motionless due to the balance of magnetic and kinetic pressures. Thus, the equilibrium discussed next will be an instantaneous equilibrium valid at some instant in time during the implosion, launch, explosion, etc.

2.2.1 Equilibrium

A fairly general statement of force balance describes MHD equilibrium. In the rest frame of the fluid, it reads

$$-\nabla p + \vec{J} \times \vec{B} + \rho \vec{g} = 0. \tag{2.1}$$

When $g = 0$, there is no motion in the lab frame, and the various expressions describing an equilibrium pinch can be recovered (Z, θ, screw). While this is a general

expression, we shall consider variations in equilibrium quantities in only one dimension. For the foils and imploding liners that will be discussed, the dominant motion is generally found in one direction. In Cartesian coordinates this is taken to be in the $\hat{x}$ direction, and in cylindrical geometry (see Chapter 3) this will be the $\hat{r}$ direction. For variation only in the $\hat{x}$ direction, Eq. 2.1 becomes a simple statement relating the balance of kinetic and magnetic pressure in an effective gravity. For accelerated flyers and foils or Z-pinches the overall dynamics are essentially 1D so these assumptions are quite valid. Thus, we begin by simplifying Eq. 2.1 for one dimensional motion in Cartesian coordinates, arriving at the well known equation [22][70]

$$\frac{\partial p}{\partial x} = \frac{\partial}{\partial x}\left(\frac{|B|^2}{2\mu_0}\right) + \rho g, \tag{2.2}$$

where $|B|^2 = B_x^2 + B_y^2 + B_z^2$. For the purposes of this work, the assumption that $B_x = 0$ will be made, leaving the field components of interest as $\vec{B} = \langle 0, B_y, B_z \rangle$. Equation 2.2 implies that $g > 0$ corresponds to acceleration in the lab frame in the $-\hat{x}$ direction, while $g < 0$ corresponds to acceleration in the $+\hat{x}$ direction. Note that thus far, no assumptions have been made about the plasma resistivity or equation of state, only the assumption of the validity of the MHD equations is assumed (i.e. no displacement current, plasma as a single fluid, etc.). These features cannot be retained for the linearized ideal MHD equations, but this allows for the equilibrium to be constructed from simulations or experiments where non-ideal MHD effects are important.

The utility of this property is most easily presented via example. Let us consider planar foil magnetically accelerated by the force produced by an axially directed current ($\hat{z}$) and the corresponding induced magnetic field in the $\hat{y}$ direction (also know as the pinch force in planar geometry). This is also the basis for magnetically accelerated flyer plates [10][11], except the magnetic pressure is located on only one

side of the plate. Flyer plates are common loads on the Z-machine and are much thicker than the foils considered on the Linear Transformer Driver (LTD) at the University of Michigan. The foil, in addition to being accelerated, can be compressed, ohmically heated, ablated, among many other physical processes. Many of these effects require incorporating an equation of state, as well as thermal and electrical conductivities. A suitably advanced resistive MHD code incorporates all of these effects to the best abilities of the models used. For the purposes of Eq. 2.2, this means that there is likely some density distribution (Gaussian for example) and pressure distribution, as well as a distribution of currents and magnetic fields as described by magnetic diffusion. However, given the x or radial dependence of p, ρ, and $\vec{B}$ as determined by the MHD code, an effective gravity, g, is readily determined from integration of Eq. 2.2, and thus accounts for all of the dynamical 1D motion introduced by more complicated pieces of physics. Before introducing the linearized equations, some special cases of the equilibrium will be considered.

We employ a three-region sharp boundary model for analytically determining the instantaneous MRT growth rate for a given set of equilibrium quantities. We will use a three region sharp boundary model (Fig. 2.1). The regions typically correspond to a plasma region surrounded either by vacuum or a fill gas. The various magnetic field components and densities in each region are allowed to take on arbitrary values. In a vacuum region, there is no kinetic pressure, p, though there may be some finite magnetic pressure. This of course is the essence of the classic MRT problem where a magneto-fluid is supported by magnetic pressure in the vacuum that was discussed in the introduction. For the three-region model that will be described, a finite slab of plasma may be supported an arbitrary combination of kinetic and magnetic pressure. To model a flyer plate, region I would be vacuum with B_{01} being the drive magnetic field, region II would be the flyer plate with ρ_{02} and region III would be vacuum. In the planar limit of a liner implosion, the problem would remain the same, but region

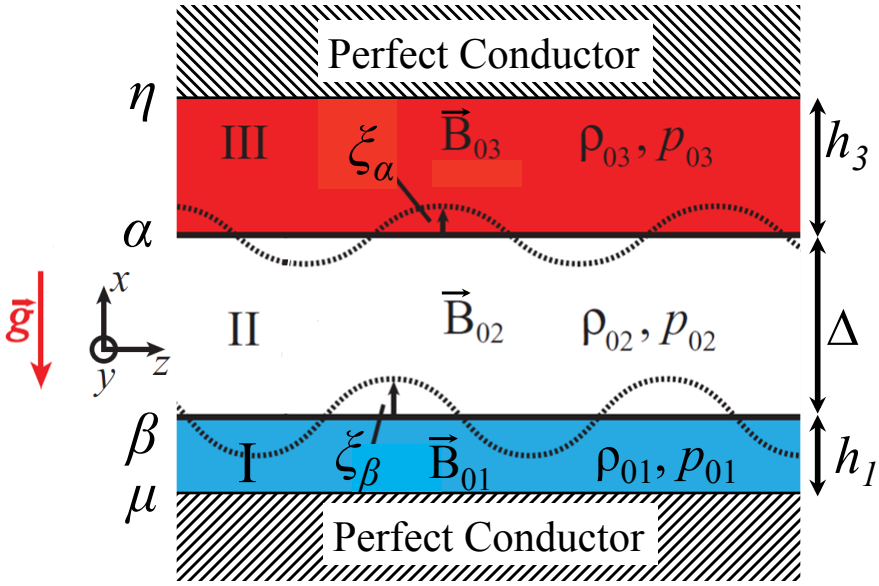

Figure 2.1: Three region sharp boundary model surrounded by perfectly conducting surfaces.

III could be a fuel region with finite density, ρ_{03}. In this model, h_1 and h_3 may take on arbitrary values as well, allowing for both a finite and infinite domain problem. This model has been discussed in great depth in Lau et al. [57] and Weis et al. [8]. An additional assumption that is required for ready analytic evaluation of the linearized ideal MHD equations is that while the equilibrium may take on arbitrary values in each region, those values must be constant in the region. Work by Zhang et al. [66] considered a three region sharp boundary model where the plasma region (region II) was allowed to contain an arbitrary current distribution in order to study magnetic shear. While the current distribution selected was analytic, numerical calculation was required to determine the MRT growth rate by this simple change.

For the three region model shown in Fig. 2.1, with uniform equilibrium values in each region, the equilibrium condition can be integrated across region II (for Eq. 2.2), from $x = \beta^-$ (at the top of region I) to $x = \alpha^+$ (at the bottom of region III), to obtain

a relation that describes g based on a statement of continuity of total pressure,

$$\rho g \Delta = \left(\frac{\left|\vec{B_{01}}\right|^2}{2\mu_0} + p_{01} \right) - \left(\frac{\left|\vec{B_{03}}\right|^2}{2\mu_0} + p_{03} \right), \tag{2.3}$$

where Δ is the thickness of the plasma slab. The effective gravity is then determined by an arbitrary combination of kinetic and magnetic pressure but does rely on the thickness of the slab for consistency. This feature is particularly important for many of the MRT experiments performed at the University of Michigan, the reason for which will be discussed later. Generally, a three region model will be used, but a similar two region model equilibrium could be obtained by taking $\Delta \to 0$

$$0 = \left(\frac{\left|\vec{B_{01}}\right|^2}{2\mu_0} + p_{01} \right) - \left(\frac{\left|\vec{B_{03}}\right|^2}{2\mu_0} + p_{03} \right). \tag{2.4}$$

Taking $p_{01} = 0, |\vec{B_{03}}| = \vec{0}$ gives the simple equilibrium,

$$\frac{|\vec{B}_{01}|^2}{2\mu_0} = p_{03}. \tag{2.5}$$

which describes the classic Kruskal and Schwarzschild [4] case of a plasma supported by magnetic pressure in a vacuum. Appendix A of Ref. [8] considers various limiting cases of the 3-region model shown in Fig. 2.1.

These equilibria provide the necessary starting point for the MRT calculations that follow and will be referenced often. Chapter 3 will again look at MHD equilibria except in cylindrical geometry, which introduces additional complexities. This may be anticipated considering the substantial work that has gone into understanding equilibrium in tokamaks and Z-pinches.

2.2.2 Linearization and perturbation

Before introducing the solutions to the sharp boundary model, the process of linearization will first be discussed. The linearized MHD equations can be formulated quite generally and then the appropriate approximations for our sharp boundary model can be applied. Before the coordinate system is fixed, many of the early results are also directly applicable to cylindrical geometry. To begin, the familiar equations of ideal MHD are

$$\frac{\partial \rho}{\partial t} = -\nabla \cdot (\rho \vec{v}) \,, \tag{2.6}$$

$$\rho \frac{\partial \vec{v}}{\partial t} + (\vec{v} \cdot \nabla) \, \vec{v} = -\nabla p + \vec{J} \times \vec{B} + \rho g, \tag{2.7}$$

$$\vec{E} + \vec{v} \times \vec{B} = 0, \tag{2.8}$$

$$-\frac{\partial \vec{B}}{\partial t} = \nabla \times \vec{E}, \tag{2.9}$$

$$\nabla \times \vec{B} = \mu_0 \vec{J}. \tag{2.10}$$

For the fluid equations, only the continuity and momentum equation have been included, leaving out the energy equation due to the additional complexity introduced. Faraday's law (Eq. 2.9) and Ohm's law with infinite electrical conductivity (Eq. 2.8) can be combined to give

$$\frac{\partial \vec{B}}{\partial t} = \nabla \times \left(\vec{v} \times \vec{B} \right), \tag{2.11}$$

which is also known as the "Frozen-in" law. The interpretation of Eq. 2.11 is that the magnetic field lines are tied to the motion of the plasma and vice-versa. The addition of a finite resistivity, by including the term $\eta \vec{J}$ in the right-hand-side of Eq. 2.8, allows for field lines to essentially slip out of the plasma it would otherwise be attached to. Finite resistivity can lead to many other physical processes, such as magnetic reconnection [22]. The assumption of ideal MHD is indeed restrictive,

however the results that can be obtained from this model will be shown to be highly insightful, in part because the limitations are known and the exact solutions are possible.

The next step is to linearize the ideal MHD equations with the given equilibrium presented in Eq. 2.2. The equilibrium quantities are denoted with a subscript, '0'. To be explicit, the equilibrium quantities are the mass density, $\rho_0(x)$, kinetic pressure, $p_0(x)$, magnetic field, $\vec{B}_0(x) = \langle 0, B_{0y}(x), B_{0z}(x) \rangle$. Once more, the formulation is in the moving frame of the plasma so that $\vec{v}_0 = 0$. To linearize, the equilibrium quantities are modified by a small signal perturbation, $f(x, y, z, t) = f_0(x) + f_1(x, y, z, t)$ where $f_1 << f_0$. Hereafter, quantities with subscript, '1', are the perturbation quantities. The last important definition is that $\vec{v}_1 = \frac{\partial \vec{\xi}}{\partial t}$, where $\vec{\xi}_1$ is the perturbed displacement of the plasma parcel. As $\vec{\xi}_1$ is assumed to be a small quantity, for clarity the subscript '1' will be dropped. An eigenmode (normal mode) analysis will be used in this work so that the time dependence of the perturbation quantities takes the form $f_1(x, y, z)e^{i\omega t}$. To accomplish this, a Fourier transform from $t \to \omega$ is applied to the MHD equations, which has the useful effect that $\partial/\partial t \to i\omega$ and $\partial^2/\partial t^2 \to -\omega^2$.

The linearized normal mode form for each of the perturbed equilibrium quantities is then inserted into the ideal MHD equations. Products of first order quantities are ignored in linear theory (e.g. p_1^2, $\vec{B}_1^2$, ξ^2, ξB_1). Following this procedure the MHD equations can be distilled into a single linearized vector equation for the displacement, $\vec{\xi}$:

$$\rho_0 \frac{\partial^2 \vec{\xi}}{\partial t^2} = -\nabla p_1 + \vec{J}_0 \times \vec{B}_1 + \vec{J}_1 \times \vec{B}_0 + \rho_1 \vec{g}, \tag{2.12}$$

$$\begin{aligned} -\rho_0 \omega^2 \vec{\xi} = &-\nabla p_1 + (\nabla \times \vec{B}_0) \times [\nabla \times (\vec{\xi} \times \vec{B}_0)]/\mu_0 \\ &+ \{\nabla \times [\nabla \times (\vec{\xi} \times \vec{B}_0)] \times \vec{B}_0\}/\mu_0 + \rho_1 \vec{g}, \end{aligned} \tag{2.13}$$

where we have combined the 'frozen-in' law, Faraday's law, and Ampère's law, re-

spectively, in linearized form:

$$\vec{E_1} = -\vec{v}_1 \times \vec{B}_0 = -i\omega\vec{\xi} \times \vec{B}_0, \tag{2.14}$$

$$\vec{B_1} = \nabla \times \vec{E_1}/(-i\omega) = \nabla \times (\vec{\xi} \times \vec{B}_0), \tag{2.15}$$

$$\nabla \times \vec{B_1} = \mu_0 \vec{J_1}. \tag{2.16}$$

Also required, is the linearized continuity equation, which relates the perturbation density to the perturbed motion

$$\frac{d}{dt}\rho_1 = -\nabla \cdot (\rho_0 \vec{v}_1), \tag{2.17}$$

$$\rho_1 = -\nabla \cdot (\rho_0 \vec{\xi}) = -\left(\vec{\xi} \cdot \nabla\rho_0 + \rho_0 \nabla \cdot \vec{\xi}\right). \tag{2.18}$$

Lastly, an equation of state (EOS) is required to relate the perturbation kinetic pressure to the perturbed density and motion. To this end, the perturbations in the plasma are assumed to be incompressible, requiring that $\nabla \cdot \vec{v}_1 = 0 = \nabla \cdot \vec{\xi}$. For a more complicated EOS, the energy equation is needed, increasing the difficulty of determining analytic solutions.

Note that incompressibility significantly simplifies the continuity equation by directly zeroing the second RHS term in Eq. 2.18. Note also, that if $\nabla\rho_0 = 0$ then $\rho_1 = 0$. This will be the case for the sharp boundary model with constant density within each region. The above equations are applicable to the plasma regions. For the case of a vacuum, $\nabla \times \vec{B_1} = 0$ (no current in vacuum), the magnetic field perturbations take the general form:

$$\vec{B_1} = \nabla\phi, \tag{2.19}$$

$$\nabla^2\phi = 0. \tag{2.20}$$

Up until this point, the force law, Eq. 2.13, and continuity equation, Eq. 2.18, are

valid in a general coordinate system and will be needed in Chapter 3.

For the Cartesian coordinate system, a spatial Fourier transform is applied in $\hat{y}, \hat{z}$ directions defining k_y and k_z to be the wavenumber in the corresponding direction in an eigenfunction formulation. Combining the spatial Fourier transform with the temporal Fourier transform, perturbations quantities then have the complete Fourier form, $f_1(x,y,z,t) = f_1(x)e^{i\omega t - i(k_y y + k_z z)}$. The spatial Fourier transform then allows further simplification of the gradient operators on all perturbation quantities in the linearized ideal MHD equations, $\left\langle 0, \frac{\partial}{\partial y}, \frac{\partial}{\partial z} \right\rangle \rightarrow \langle 0, -ik_y, -ik_z \rangle$. At this point, the only remaining derivatives are in the $\hat{x}$ direction involving the equilibrium quantities and $\vec{\xi}(x)$.

The remainder of the work to get to the analytic growth rate is a good deal of algebra to reduce the linearized ideal MHD equations to a single second order ordinary differential equation (ODE) for $\xi_x(x)$, as ξ_y and ξ_z and their derivatives (with respect to x) can be eliminated. The fully simplified ODE is (see Bellan [22] or Chandrasekhar [5] for details)

$$\frac{\partial}{\partial x}\left\{\left[-\rho_0\omega^2 + \frac{\left(\vec{k}\cdot\vec{B}_0\right)^2}{\mu_0}\right]\frac{\partial \xi_x(x)}{\partial x}\right\} - k^2\left(-\rho_0\omega^2 + g\frac{\partial \rho_0}{\partial x} + \frac{\left(\vec{k}\cdot\vec{B}_0\right)^2}{\mu_0}\right)\xi_x(x) = 0, \tag{2.21}$$

where the simplified expressions for the wavenumbers is given by $\vec{k} = \langle 0, k_y, k_z \rangle$ and $k^2 = k_y^2 + k_z^2$. Equation 2.21 is valid for general $\rho_0(x)$ and $\vec{B}_0(x) = \hat{y}B_{0y}(x) + \hat{z}B_{0z}(x)$. Note further that $p_0(x)$ does not enter Eq. 2.21 explicitly. The equilibrium condition, Eq. 2.2, is satisfied.

A key requirement for determining the analytic expressions describing the MRT growth rate is the ability to determine the exact solution to Eq. 2.21. For a sharp boundary model, assuming no x-dependence in each region, the planar ODE, Eq. 2.21 is substantially simplified. The term $\partial\rho_0/\partial x$ drops out and the remaining coefficients

of ξ_x and its derivatives drop out except for k^2. The ODE then is $\xi_x'' = k^2\xi_x$ whose solutions are a linear combination of exponential functions. These solutions are discussed extensively in [8]. The unknowns to be determined are the eigenfunction $\xi_x(x)$ and eigenvalue, $\omega(\vec{k})$. A very useful property of the linearized ideal MHD equations is that ω^2 is guaranteed to be real valued (by the MHD energy principle, see [22], Chandrasekhar [5]). Thus, unstable solutions exist if and only if $\omega^2 < 0$. The unstable MRT modes are then those modes where $\mathrm{Im}[\omega(k_y, k_z)] < 0$. A simple example solution is $\omega = -i\sqrt{kg}$ which then grows like $e^{\sqrt{kg}t}$. Before introducing the sharp boundary model and required boundary conditions, techniques for solving Eq. 2.21 will be briefly discussed.

A well known example for RT is that the growth of short wavelengths are stabilized by a finite density gradient of scale length, L and the RT growth rate takes the form $\gamma = \sqrt{kg/(1+kL)}$ [30]. This scaling was obtained using an exponential form for ρ_0 and determined exactly for a single interface. The situation becomes far more complicated when a second interface is introduced as in [66]. Solution of Eq. 2.21 requires experimental, theoretical or numerical density and magnetic field profiles. The basic requirement is that the profiles and derivatives be sufficiently well behaved. Work by Zhang et al. [66] showed that even if the density and magnetic field in the z-direction is assumed constant (i.e. the remaining nonuniformity is only in $B_{0y}(x)$), numerical integration of Eq. 2.21 is required to determine $\xi_x(x)$ between two boundaries. Despite using a perfectly well defined functional form for $B_{0y}(x)$, only for very special cases can $\xi_x(x)$ be analytically determined without some manner of approximation. Nonetheless numerical solutions of Eq. 2.21 can incorporate more properties of the equilibrium that can stabilize or destabilize MRT such as the magnetic shear discussed by Zhang et al. [66]. This work essentially still used a sharp boundary model but made use of analytic solutions to determine the boundary conditions. Again, it is reiterated that such a method requires the knowledge of the exact eigenfunctions

outside the boundaries. This is a standard technique (see Melcher [71], Bud'ko [7]).

The most general solution of the planar ODE would be to solve a geometry like that shown in Fig. 2.1 but containing one region with smooth profiles in density and magnetic field between two conducting walls. The problem remains a boundary value problem (BVP) for an undetermined eigenfunction $\xi_x(x)$ and eigenvalue, $\omega(\vec{k})$. On the surface, the solution of this BVP may sound quite easy and the solution very enticing. The true challenge lies in determining sufficiently smooth equilibrium profiles and expediency in determining the solution of the BVP. Many techniques exist for tackling this kind of problem, such as a shooting method or finite difference (matrix) method or even finite element methods. The shooting method requires solving the ODE as an initial value problem (IVP) with a known initial value at one of the boundaries ($\xi_x(0) = \xi_0$, one of the known boundary conditions from the BVP) along with a guess of $\xi_x'(0)$ and ω. One can easily imagine the challenges of such a technique as a particular guess for the initial slope may not yield a solution of $\xi_x(x)$ for any value of ω. Since the equations are linear, a finite difference method can be very advantageous as no iterative solutions of the matrix are required and the boundary conditions are directly encoded in the matrix (depending on the form of the boundary conditions, without approximation). Depending on the boundary conditions, in order to determine $\xi_x(x)$ for a particular ω the matrix must be invertible (for non-homogeneous boundary conditions) or singular (for homogeneous boundary conditions). Tests for invertibility or singular-ness are theoretically very simple. Numerical tests however, are more complicated due to finite precision computing. The author has tried both methods and found the finite difference (matrix) method to be the most robust. This method was implemented in Chapter 3.

2.2.3 Boundary Conditions

Across each interface in Fig. 2.1 the underlying boundary conditions are continuity of total pressure, continuity of the normal component of magnetic field (= 0), and continuity of the fluid velocity which physically means there are no voids. Integration of Eq. 2.21 across an interface effectively determines the continuity of total pressure condition and is the most straightforward way to determine the boundary conditions. An example of this is given for the β interface as shown in Weis et al. [8]. First, an integral over the β interface is applied to Eq. 2.21

$$\int_{\beta^-}^{\beta^+} \frac{\partial}{\partial x} \left\{ \left[-\rho_0\omega^2 + \frac{\left(\vec{k}\cdot\vec{B}_0\right)^2}{\mu_0} \right] \frac{\partial \xi_x(x)}{\partial x} \right\} \mathrm{d}x$$

$$= \int_{\beta^-}^{\beta^+} k^2 \left(-\rho_0\omega^2 + g\frac{\partial \rho_0}{\partial x} + \frac{\left(\vec{k}\cdot\vec{B}_0\right)^2}{\mu_0} \right) \xi_x(x)\mathrm{d}x, \tag{2.22}$$

$$\rightarrow \left[-\rho_0\omega^2 + \frac{\left(\vec{k}\cdot\vec{B}_0\right)^2}{\mu_0} \right] \frac{\partial \xi_x(x)}{\partial x}\bigg|_{\beta^-}^{\beta^+} = k^2 g \rho_0 \xi_x\Big|_{\beta^-}^{\beta^+}. \tag{2.23}$$

The boundary condition at $x = \beta$ is then given by Eq. 2.23, where the $\pm$ means $x = \beta \pm \epsilon$ and ϵ is small. Alternatively, '$-$' corresponds to equilibrium quantities in region I, and '$+$' corresponding to those in region II. A similar procedure determines the boundary condition at $x = \alpha$. These two boundary conditions essentially determine the BVP for region II. The last two boundary conditions are for the perfect conductor walls. The wall boundary requires that $\xi_x(x_w) = 0$. Alternatively, the wall can be moved to $-\infty$ which merely requires $\xi_x(-\infty)$ remains bounded (in fact, zero, as we do not expect perturbations on a surface can affect the solution infinitely far away). The other wall must behave similarly for $x \rightarrow \infty$. The other requirement is that the normal component of the magnetic field to the perfect conducting wall be 0, $\vec{B}_1 \cdot \hat{x} = 0$.

The boundary conditions for a three-region sharp boundary model are summarized

as

$$\xi_x(x_{\text{wall}}) = 0 \qquad \text{or} \qquad \xi_x(\pm\infty) < \infty, \tag{2.24}$$

$$\vec{B}_1(x) \cdot \hat{x}\Big|_{x_{\text{wall}}} = 0 \qquad \text{or} \qquad \vec{B}_x(\pm\infty) < \infty, \tag{2.25}$$

$$\left[-\rho_0\omega^2 + \frac{\left(\vec{k}\cdot\vec{B}_0\right)^2}{\mu_0}\right] \frac{\partial\xi_x(x)}{\partial x}\Bigg|_{x_s^-}^{x_s^+} = k^2 g\rho_0\xi_x\Big|_{x_s^-}^{x_s^+} \qquad x_s = \alpha, \beta. \tag{2.26}$$

Equations 2.24 and 2.25 provide the perfect conducting wall boundary conditions for regions I and III and Eq. 2.26 provides the boundary conditions needed for region II and then matching regions I and III to region II. Note that the pressure matching condition, Eq. 2.26, requires knowledge of the eigenfunction in all regions. For the case of uniform equilibrium profiles in all three-regions, these solutions are known. The solution methodology is discussed briefly in the next section as it has been published elsewhere [8]. Additionally, the derivation in cylindrical coordinates proceeds similarly and requires more attention.

2.2.4 Solution of the planar BVP for MRT and feedthrough

The previous sections have presented nearly all that is required to solve the three region sharp boundary model for MRT and feedthrough. As stated earlier, the governing ODE (Eq. 2.21, assuming equilibrium quantities are constant in each region), is simplified to, for each region,

$$\frac{\partial^2\xi_x}{\partial x^2} = k^2\xi_x, \tag{2.27}$$

$$\Rightarrow \xi_x(x) = Ae^{-kx} + Be^{kx}. \tag{2.28}$$

The general solution is straightforward, with the coefficients, A and B determined by the boundary conditions for the region. For example, if the conducting walls

are moved to $\pm\infty$ respectively, the corresponding solutions in regions I and III are $\xi_\alpha e^{-k(x-\alpha)}$ and $\xi_\beta e^{k(x-\beta)}$. The solutions for ξ_x in all regions, including the conductors, reads [71][8]

$$\xi_x(x) = \xi_\beta \frac{\sinh[k(x-\mu)]}{\sinh[k(\beta-\mu)]}, \qquad \mu < x < \beta \qquad \text{(region I)} \tag{2.29}$$

$$\xi_x(x) = \xi_\alpha \frac{\sinh[k(x-\beta)]}{\sinh[k\Delta]} - \xi_\beta \frac{\sinh[k(x-\alpha)]}{\sinh[k\Delta]}, \qquad \alpha < x < \beta \qquad \text{(region II)} \tag{2.30}$$

$$\xi_x(x) = \xi_\alpha \frac{\sinh[k(x-\eta)]}{\sinh[k(\alpha-\eta)]}, \qquad \alpha < x < \eta \qquad \text{(region III)} \tag{2.31}$$

where $\Delta = \beta - \alpha$ and we have defined $\xi_\alpha = \xi_x(\alpha)$ and the same for the β interface so that the solutions are continuous. These three solutions allow direct evaluation of the boundary conditions which will allow exact determination of $\omega(\vec{k})$ for nontrivial solutions of ξ_α and ξ_β. This leaves evaluating Eq. 2.26 at the α and β surfaces. At the α surface, this results in the expression

$$\left[-\rho_0\omega^2 + \frac{\left(\vec{k}\cdot\vec{B}_0\right)^2}{\mu_0}\right]\frac{\partial\xi_x(x=\alpha)}{\partial x}\bigg|_{\text{II}} - \left[-\rho_0\omega^2 + \frac{\left(\vec{k}\cdot\vec{B}_0\right)^2}{\mu_0}\right]\frac{\partial\xi_x(x=\alpha)}{\partial x}\bigg|_{\text{I}} = k^2 g\rho_0\xi_x(x=\alpha)|_{\text{II}} - k^2 g\rho_0\xi_x(x=\alpha)|_{\text{I}}. \tag{2.32}$$

Recall again, the only functions having an x dependence in each region is the eigenfunction ξ_x and that ξ_x is continuous across the interface. Thus, if $\rho_2 = \rho_1$ (the densities are the same in regions I and II) then the right-hand-side of Eq. 2.32 is identically zero. The last step is to compute the derivatives of Eqs. 2.29-2.31 and evaluate at $x = \alpha$. A similar procedure follows at $x = \beta$. The result of these two

evaluations is two equations containing the various equilibrium quantities, $\vec{k}$ and the unknowns: $\xi_\alpha, \xi_\beta, \omega$. In Weis et al. [8] they are known as F_a and F_b and can be written in the very convenient form of Eq. 2.33.

$$\frac{\xi_\alpha}{\xi_\beta} = F(\omega), \tag{2.33}$$

$$F_a = \left\{ \cosh k\Delta + \frac{\left[(\vec{k}\cdot\vec{B_{03}})^2/\mu_0 - \omega^2\rho_{03}\right]\coth kh_3 + kg(\rho_{02}-\rho_{03})}{(\vec{k}\cdot\vec{B_{02}})^2/\mu_0 - \omega^2\rho_{02}} \sinh k\Delta \right\}^{-1}, \tag{2.34}$$

$$F_b = \cosh k\Delta + \frac{\left[(\vec{k}\cdot\vec{B_{01}})^2/\mu_0 - \omega^2\rho_{01}\right]\coth kh_1 + kg(\rho_{01}-\rho_{02})}{(\vec{k}\cdot\vec{B_{02}})^2/\mu_0 - \omega^2\rho_{02}} \sinh k\Delta \tag{2.35}$$

The ratio, ξ_α/ξ_β is defined as the feedthrough factor. It is given by Eq. 21 or 22 of [8] and we have reproduced them here. The dispersion relation, $\omega = \omega(\vec{k})$, is obtained by setting $F_a = F_b$. F is the ratio of the amplitude of the eigenfunction (in region II) at one interface to the other. The physical interpretation is that if the β surface contains a ripple of ξ_β units in amplitude, the feedthrough factor, F_a or F_b, describes the corresponding amplitude of the α surface [57][8][66]. It is a measure of the relative effect of one surface on the other. Generally, it is most important to consider the effect the MRT unstable surface has on the stable surface. $F(\omega)$ is dependent on ω which in turn is dependent upon the equilibrium quantities and the wavelengths under consideration. If we consider Fig. 2.1 as the purely hydro RT case (all magnetic fields are 0 and density only in region II and regions I and III are semi-infinite) $F(\omega) = F(-i\sqrt{kg}) = e^{-k\Delta}$ which does not at all depend on the acceleration, only the wavelength and thickness of the slab of fluid [57]. Most importantly, this simple expression shows that feedthrough decreases exponentially with increasing thickness and wavenumber (or decreasing wavelength). The message is clear in that thick slabs are robust to feedthrough and *any feedthrough is dominated by long wavelengths*. To better quantify this, the most dangerous MRT modes are

those where $\lambda \sim \Delta$ for which the feedthrough factor is also appreciable. This is well known in the laser fusion community [30] for RT.

In order to determine the feedthrough factor exactly, $\omega(\vec{k})$ must first be found. Recall, the two boundary condition evaluations resulted two expressions for $F(\omega)$. The only way these two expressions can be consistent is if ω satisfies the dispersion relation, $\omega(\vec{k})$, found by the equality $F_a(\omega) = F_b(\omega)$ (Eqs. 2.35,2.34). The solution of this equality yields the dispersion relation and takes the form

$$A\omega^4 + B\omega^2 + C = 0, \tag{2.36}$$

$$= A\sigma^2 + B\sigma + C = 0, \tag{2.37}$$

where $\omega^2 = \sigma$ (as a reminder, in ideal MHD σ is always real). The coefficients A, B and C in Eqs. 2.36,2.37 are given by Eqs. 25-27 in Weis et al. [8]. The four eigenvalue solutions, ω always come in $\pm$ pairs, denoted in the form: $+\omega_1, -\omega_1, +\omega_3, -\omega_3$. So ω is either purely real or purely imaginary and marginal stability always occurs at $\omega = 0$. Given the Fourier form $e^{i\omega t}$, real ω represents the purely oscillatory solution, while imaginary ω represents the exponentially decaying and growing solutions. Using the pure hydro RT case as an example again, the exact solutions are succinctly written as $\sigma = \pm kg$. At this point, $F(\omega)$ can also be evaluated exactly for each value of ω. The classic RT case is again $F(-i\sqrt{kg}) = e^{-k\Delta}$. Some simplifications can be made. First, ω appears in F only as ω^2, thus F can be written as $F(\sigma)$. Often we are only concerned with the most dangerous mode (fastest growing negative imaginary solution) whose temporal growth rate we will refer to as γ. So we mainly consider F evaluated for the value of ω with the largest negative imaginary part. As a final point, as stated in Weis et al. [8], if $g = 0$ then $\gamma = 0$ and there is no unstable MRT mode.

This chapter has outlined the derivation of the feedthrough factor and dispersion

relation for MRT in Cartesian coordinates. Solutions in planar geometry are fairly easy to write down (c.f. Eqs. 2.29-2.31). The same equations in cylindrical geometry are substantially more complicated (see Chapter 3). Many of the techniques described in this chapter nonetheless translate to cylindrical geometry with the result being exact, but long and cumbersome expressions. Thus the author hopes to strike a balance between this chapter and the next by providing enough detail to replicate the calculations and describe the features of the equations that result without showing lines and lines of algebra. As such, this chapter and the work found in Weis et al. [8] will be heavily referenced in the next chapter and the more subtle details in the derivation of MRT and feedthrough in cylindrical coordinates will be emphasized.

2.2.5 Features and scaling of MRT growth rates and feedthrough

This section will focus on reaping the benefits of obtaining the analytic expressions for MRT growth and feedthrough in planar geometry. The original motivation [57] for deriving these expressions was to understand the MRT experiments occurring at the University of Michigan [47][48]. The first experiments utilized a 400 nm ($= \Delta$) aluminum foil ($\rho_2 = 2.7$ g/cc) placed between the anode/cathode gap of a 1 mega-ampere linear transformer driver (LTD). The dimensions of the foil in $\hat{y}, \hat{z}$ were on the order of 1 cm, thus fitting the idea of a planar slab. The driving current of the LTD was then intended to magnetically accelerate the foil, initiating MRT growth on one of the surfaces and hopefully observing feedthrough on the other surface. Some problems and interpretations of these experiments from a theoretical standpoint will be addressed later. They are given in great detail in Zier's thesis [48][47]. The analytic MRT growth rates and feedthrough factors will be examined quantitatively.

To understand the quantitative results, it is convenient to first quote some results for simple limits for which the behavior of ω and $F(\sigma)$ is easily interpretable. First, consider a two region (I and II) case ($\Delta \to \infty$, $h_1 \to \infty$ in Fig. 2.1) with perturbations

only in k_y and magnetic field $\vec{B} = \langle 0, 0, B_z \rangle$. Examining, Eq. 2.21, the current scenario eliminates the $\vec{k} \cdot \vec{B}_0$ terms, leaving only the classic RT problem. The growth rate, γ is given by

$$\gamma^2 = \frac{\rho_2 - \rho_1}{\rho_2 + \rho_1} kg = A_t kg, \tag{2.38}$$

where $A_t = \frac{\rho_2 - \rho_1}{\rho_2 + \rho_1}$ is known as the Atwood number. While this looks like the classic RT result, it is important to remember that g may arise not only from kinetic pressure, but also magnetic pressure (c.f. Eq. 2.2). Thus, the familiar condition for RT, $\nabla\rho \cdot \nabla p < 0$ must be modified to read,

$$\nabla\rho \cdot \nabla(p_{\text{kin.}} + p_{\text{mag.}}) = \nabla\rho \cdot \nabla p_{\text{tot}} < 0. \tag{2.39}$$

For this case ($\vec{k} \cdot \vec{B}_0 = 0$), this is the only manner in which the magnetic field affects the growth rate. Now consider perturbations in z, $k_y = 0, k_z > 0$ with the same magnetic field configuration and the result is much different from classic RT,

$$\gamma^2 = A_t kg - \frac{k_z^2 (B_{z,2}^2 + B_{z,1}^2)}{\mu_0(\rho_2 + \rho_1)}. \tag{2.40}$$

This result clearly shows a direct reduction of the MRT growth rate by the magnetic field depending on the degree of bending of the magnetic field line as measured by $(\vec{k} \cdot \vec{B}_0)^2$. The reason for this is well-known and is made even clearer in taking the limit of a vacuum region I ($\rho_1 \to 0$), with $B_{z,1} = B_{z,2}$ yielding

$$\gamma^2 = kg - \frac{2(\vec{k} \cdot \vec{B})^2}{\mu_0 \rho_{02}} = kg - 2(\vec{k} \cdot \vec{v}_A)^2, \tag{2.41}$$

where $\vec{v}_A = \vec{B}_0 / \sqrt{\mu_0 \rho_{02}}$ is the Alfvén velocity for the particular magnetic field orientation. The physical interpretation of this result is that the MRT growth rate is

reduced due to the generation of Alfvén waves which occur due to the bending of the magnetic field line. The origin of the term, $(\vec{k}\cdot\vec{v}_A)^2$, derives from the magnetic tension contribution of the $\vec{J}\times\vec{B}$ term in the MHD force law [22]. This term is prominent in ideal MHD as the magnetic field is assumed to be frozen-in to the plasma. As MRT ripples grow, the field lines trapped in the plasma are rippled and bent as well. Magnetic field lines have tension and attempt to relax. As the field lines attempt to relax, the plasma is pulled along as well with the overall result being that the magnetic field lines resist being bent. In essence, in order to continue to ripple the plasma, additional energy is required to bend magnetic field lines.

Equation 2.41 also directly shows the anisotropy introduced by MRT. Often times in planar geometry the magnetic field is very strong in one direction and the ripples aligned with this magnetic field are suitably stabilized. Meanwhile, in the orthogonal direction, no field line bending is occurring, so the MRT growth looks exactly like pure RT. Thus, in the two directions the MRT can look very different. The ability of the magnetic field to stabilize perturbations is dependent upon the ideal MHD condition. In a highly resistive medium, magnetic diffusion can occur very quickly. If the plasma becomes rippled, the magnetic field lines need not be bent along with the plasma, they can simply diffuse instead. This will be an important consideration later. Nonetheless, the very important concept of stabilization of MRT by magnetic field line bending has been introduced. Regardless of magnetic diffusion or magnetic tension, it appears that the MRT (or RT) growth rate is bounded by $\gamma = \sqrt{kg}$. The bound on the instability amplitude is $\exp\sqrt{2ks}$, which depends only on the wavenumber and the distance, s, over which the slab is accelerated or decelerated and is independent of g itself (see Appendix A).

The feedthrough factor, $F = F_a = F_b$, depends upon the MRT growth rate squared, γ^2, so it is anticipated similar magnetic field stabilization effects appear in F. Introduction of the feedthrough factor requires a return to the three region model

incorporating a second interface [8][57][66] (the two region model assumes $\Delta \to \infty$ which would have eliminated the feedthrough factor). The question to be answered now, is how MRT growth at one interface can affect the other interface. To begin to answer this question, a simpler case will again be examined first. Referring to Fig. 2.1, the following simplifying assumptions are made: $\rho_1 = \rho_3 = B_{y2} = B_{z1,2,3} = 0$, $\rho_2 = \rho_0$, $h_1 = h_3 = \infty$, $B_{y1} = -B_{y3}$. This physically corresponds to a plasma region surrounded by two vacuum regions with a magnetic field oriented in the $\hat{y}$ direction. Now, taking $g > 0$, the MRT unstable interface is at $x = \beta$ and the concern is how MRT growth there can feedthrough to the $x = \alpha$ interface. It will be sufficient to quote the feedthrough factor for this case

$$F(\omega^2) = \cosh(k\Delta) + \left[\frac{kg}{\omega^2} - \frac{(k_y B_y)^2}{\mu_0 \rho_0 \omega^2}\right] \sinh(k\Delta). \tag{2.42}$$

From the form of Eq. 2.42, the stabilizing influence of field line bending is again observed. Similar to ω, the idea is to minimize F and this is accomplished by increasing the quantity $(k_y B_y)^2$. The two interface form of ω^2 shows this familiar behavior as well, though the feedthrough factor exhibits more favorable scaling with $\vec{k} \cdot \vec{B}$,

$$\omega^2 = \frac{(k_y B_y)^2}{\mu_0 \rho_0} \coth(k\Delta) - \sqrt{(kg)^2 + \left[\frac{(k_y B_y)^2}{\mu_0 \rho_0}\right]^2 \operatorname{csch}^2(k\Delta)}. \tag{2.43}$$

One very important feature of this result (plasma surround by vacuum), is that the finite thickness only affects the MRT growth rate if the magnetic field contributions are non-zero. If $B_y = 0$ then the growth rate reverts to kg. The finite thickness only affects the pure RT growth rate if the Atwood number $A_t \neq 1$, meaning that there is at least one interface that is not next to a vacuum. It is not difficult to recover these pure RT results from our dispersion relation but for a more thorough discussion see Goncharov et al. [72]. For example, consider the pure RT case ($\vec{B_0} = 0$) where

$\rho_{03} = 0$ and $\rho_{01} > 0$. The dispersion relation is then simplified to

$$\gamma^2 = \frac{kg(\rho_{02} - \rho_{01}) \sinh k\Delta}{\rho_{02} \sinh k\Delta + \rho_{01} \cosh k\Delta}, \tag{2.44}$$

where it is clear that if $\rho_{01} \to 0$, then $\gamma^2 \to kg$ as found in Goncharov et al. [72]. The scaling is such that at large $k\Delta$ (liner looks thick to the perturbation), the traditional $\gamma^2 = A_t kg$ is also recovered. Additionally, for fixed thickness Δ, the growth rate is reduced for longer wavelengths, but only for $A_t < 1$. This is a scenario encountered when there is low-density material ablated from the RT unstable surface. However, if instead $\rho_{03} > 0$ (e.g. as a gas is compressed), the growth rate reverts closer to $\sqrt{kg}$.

For $|B_{y1}| \neq |B_{y3}|$, it is convenient to introduce a few normalized parameters for the magnetic field contributions in these two regions. These will be the same as found in Lau et al. [57] and are reproduced as follows

$$b_l^2 = b_1^2 = \frac{(\vec{k} \cdot \vec{B}_1)^2}{\mu_0 \rho_2 kg}, \tag{2.45}$$

$$b_2^2 = \frac{(\vec{k} \cdot \vec{B}_2)^2}{\mu_0 \rho_2 kg} = 0, \tag{2.46}$$

$$b_u^2 = b_3^2 = \frac{(\vec{k} \cdot \vec{B}_3)^2}{\mu_0 \rho_2 kg}. \tag{2.47}$$

The b_n then take on values between 0 and 1; 0 corresponding to no magnetic field line bending, 1 corresponding to maximum magnetic field line bending. If $b_l > 1$ there is no unstable root for MRT. It is also important to note that g is not equal to zero, as there is no unstable MRT solution for the case $g = 0$. This ensures the good behavior of the normalizations. A final assumption is that $\rho_1 = \rho_3 = 0$ (vacuum) and that the plasma region is magnetic field free, $\vec{B}_2 = \vec{0}$. Typically there are very few circumstances where $\rho_1/\rho_2 << 1$ and $\rho_3/\rho_2 << 1$ do not hold. Such cases will mostly be discussed in Chapters 3 and 4.

Three cases will be considered where $b_u = b_3$ is fixed and $b_l = b_1$ is varied. g is

assumed positive such that the unstable surface is $x = \beta$ and feedthrough occurs at $x = \alpha$ (Fig. 2.1). First, $b_u = 0$ corresponds to zero magnetic field line bending in region III and b_l is subsequently varied, localizing any field line bending in region I. The calculation of Eq. 2.37 and Eq. 2.34 are shown in Fig. 2.2. When b_l= 0, there is abso-

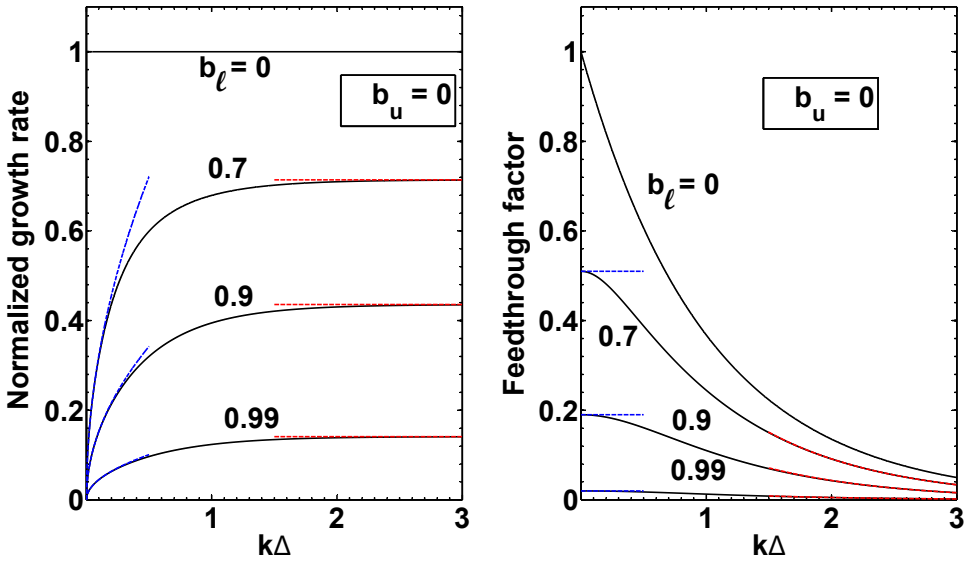

Figure 2.2: Normalized MRT growth rate, $\gamma/\sqrt{kg}$ and feedthrough factor, ξ_α/ξ_β, for fixed $b_u = b_3 = 0$. The analytic asymptotic formulae for $k\Delta << 1$ and $k\Delta >> 1$ are shown as the blue lines and red lines, respectively [57].

lutely no magnetic field line bending present and the problem reverts to the solution for RT. Hence the normalized growth rate, $\gamma/\sqrt{kg} = 1$ and the feedthrough factor is exactly $e^{-k\Delta}$. The physical picture describing Fig. 2.2 is a plasma slab being accelerated from bottom (right) to top (left) (Fig. 2.1), so that the MRT unstable surface (β) is next to a strong magnetic field with significant field line bending (b_l Fig. 2.2). The traditionally MRT stable surface (α) is next to vacuum with no magnetic field in the region. As the magnetic field is raised at the MRT unstable surface (increasing b_l) the growth rate is continually reduced. Inspecting the feedthrough factor for this scenario shows that while there is not magnetic field next to the feedthrough surface, stabilization of MRT also stabilizes feedthrough. If the MRT does not grow as much

because of the magnetic field, the feedthrough most certainly is reduced as well. The strength of the feedthrough is directly related to the strength of the MRT. However, this is not the only way to affect the feedthrough factor as will be presented next. The analytic asymptotic formulae for $k\Delta << 1$ and $k\Delta >> 1$ shown in Figs. 2.2-2.4 are given explicitly in Eqs. 11-12 of Ref. [57].

We now set $b_u = b_3$ to 0.5 so that significant field line bending is now present at the feedthrough surface (α, Fig. 2.1). The first feature of the results observed in Fig. 2.3 is that magnetic field line bending present in the vacuum region next to the feedthrough surface can only marginally reduce the MRT growth rate. In essence, resistance of the feedthrough surface to grow feeds back to the MRT surface and this effect disappears for large Δ. However, the most pronounced effect of the newly included field is on the feedthrough factor. A reasonably strong magnetic field next to the feedthrough surface can reduce the feedthrough factor independent of any magnetic field bending present at the MRT unstable interface. This is perhaps one of the most powerful results that will be presented. The physical picture for this case is an accelerating plasma slab moving from bottom to top (Fig. 2.1) with b_l units of magnetic field line bending at the MRT surface and significant field line bending at the feedthrough surface. Such a scenario is directly applicable to magnetic flux compression experiments where an initially uniform axial magnetic field is swept up and compressed by an imploding slab or liner. In such a scenario, the amount of axial magnetic field in the compressed region can significantly exceed the initial magnetic field strength. Such a scenario would then strongly resist feedthrough, a point emphasized in Awe et al.'s experiments [54][55]. Clearly, increasing b_l continues to decrease the MRT growth rate and feedthrough as was observed in Fig. 2.2, now with the additional contribution from nonzero b_u.

In Fig. 2.4, b_u is dramatically increased to 0.9 and shows that despite a large amount of magnetic field line bending at both interfaces, MRT growth and feedthrough

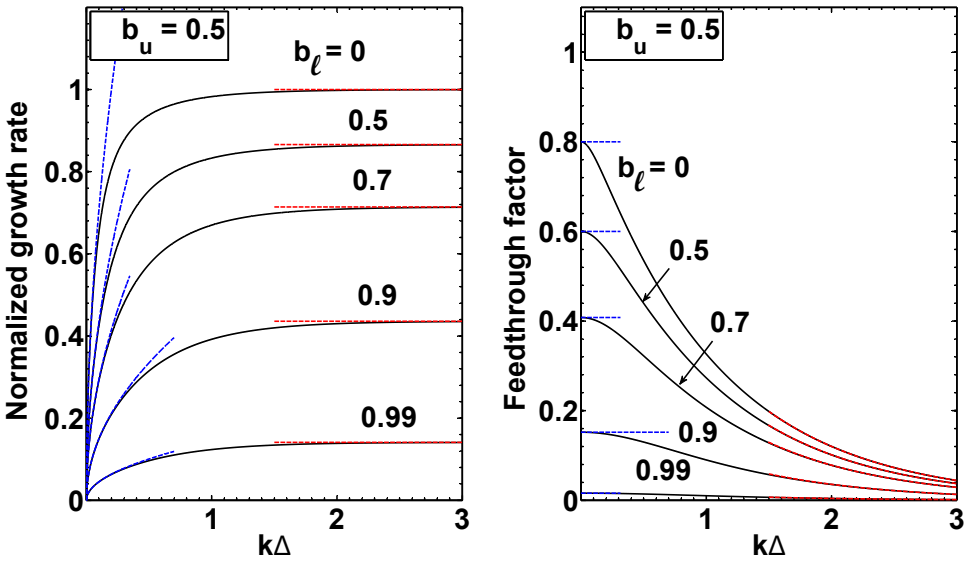

Figure 2.3: Normalized MRT growth rate, $\gamma/\sqrt{kg}$, and feedthrough factor, ξ_α/ξ_β, for fixed $b_u = b_3 = 0.5$. The analytic asymptotic formulae for $k\Delta << 1$ and $k\Delta >> 1$ are shown as the blue lines and red lines, respectively [57].

cannot be completely suppressed (though the feedthrough becomes quite small). For $b_l = 0$ the feedthrough factor is reduced further, from $0.8 \rightarrow 0.55$ for $b_u = 0.5 \rightarrow 0.9$ but not completely suppressed. The MRT growth rate remains relatively unchanged. Once again, as b_l is increased, careful consideration shows that the MRT growth rates remain very similar, except for at the knee around $k\Delta = 0.7$. For $b_u = 0.9$, the knee is slightly depressed as compared to $b_u = 0.5$ but the change is certainly far from dramatic. The feedthrough factor continues to exhibit stronger dependence with increasing magnetic field line bending, but only for the very largest b_l is feedthrough nearly suppressed. Such strong field line bending is difficult to realize in experiments due to magnetic diffusion effects. Nonetheless, this section has introduced the key result of the ideal MHD model of MRT growth and feedthrough derived in the preceding section. That being, that there exists the possibility of substantial reduction of feedthrough due to the presence of significant magnetic field line bending. More

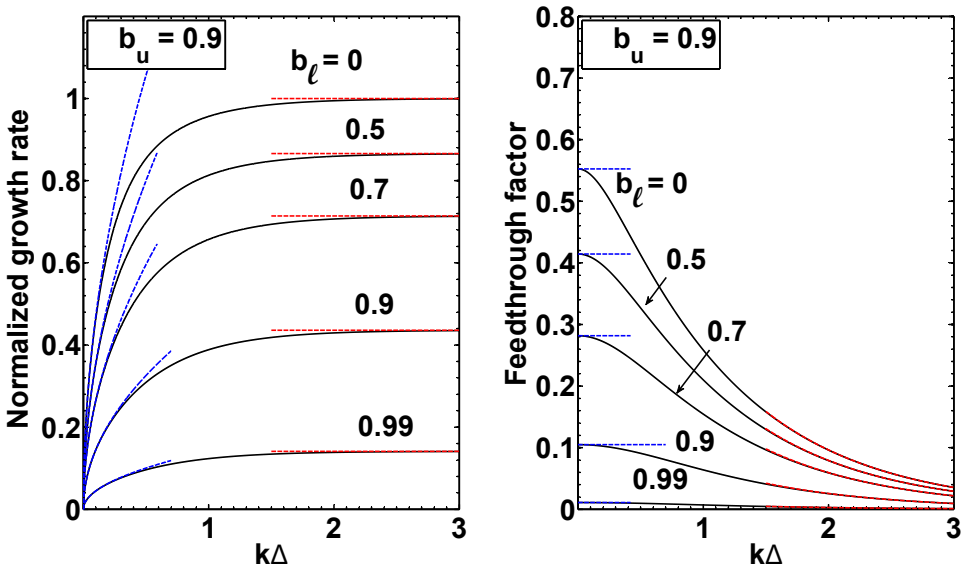

Figure 2.4: Normalized MRT growth rate, $\gamma/\sqrt{kg}$, and feedthrough factor, ξ_α/ξ_β, for fixed $b_u = b_3 = 0.9$. The analytic asymptotic formulae for $k\Delta << 1$ and $k\Delta >> 1$ are shown as the blue lines and red lines respectively, [57].

quantitatively, such a scenario requires that

$$\frac{(\vec{k}\cdot\vec{B})^2}{\mu_0\rho_0} \sim kg \tag{2.48}$$

and in many cases this is nearly equivalent to requiring that the strength of the compressed magnetic field is on the order of the driving magnetic field since $g \sim B^2$. This derives from the fact that the major force accelerating the plasma is typically the $\vec{J}\times\vec{B}$ force in pulsed power experiments. Now that some features of the MRT and feedthrough model have been presented, the next section will be devoted to applying the analytic growth rates directly to experimental scenarios.

2.3 Methods for analyzing MRT growth in Experiments

This section applies MRT growth rates and feedthrough factors to scenarios common to pulsed power experiments. The first question that could be asked is how to determine ρ, B_z, etc.? What is a reasonable acceleration, g or slab thickness, Δ? Ideally, these values would come directly from experiment and many times some of these parameters can be extracted but typically, not all of them. This section will discuss the use of 1D MHD simulations to deduce these values for input into the analytic theory. This illustrates a general technique to obtain MRT growth rates and feedthrough factors in a pulsed power experiment.

Often the simplest parameter to infer from experiment is the acceleration, which from our equilibrium expression, Eq. 2.3, takes the form

$$g \approx \frac{|B_0|^2}{2\mu_0 \rho_0 \Delta}, \tag{2.49}$$

where the magnetic field is deduced from the current driven through the load via Ampere's law in integral form

$$\int_C \vec{B} \cdot \mathrm{d}\vec{l} = \mu_0 I_{\mathrm{tot}}. \tag{2.50}$$

The major limitation of these expressions is that they implicitly assume that kinetic pressure of the plasma is negligible as compared to the driving magnetic field. In such cases g can be more difficult to determine. One of the first applications of the MRT calculations was to such a case so this will be discussed first. Following that discussion, for the remainder of this chapter, Eq. 2.49 will be quite sufficient. In chapter 3, a kinetic pressure dominated g will again be discussed, as related to the stagnation phase of an inertial confinement fusion Z-pinch concept. Lastly, in the case where stabilization effects are absent, a simple scaling for MRT growth is described

in Appendix A, where g is eliminated and the MRT amplitude gain dependent only upon the distance the slab has moved.

2.3.1 MRT growth rates applied to pulsed power driven thin foils

The original application of our analytically derived MRT growth rates and feedthrough factor was to thin foil plasma load experiments driven by the linear transformer driver (LTD) at the University of Michigan. The LTD is a pulsed power driver capable of delivering $\sim$ 650 kA to a 400 nm thick aluminum foil. A typical experimental geometry is shown in Fig. 2.5, used by Jacob Zier [47] and the subject of his thesis [48]. In Fig. 2.5, the foil is fitted between the anode-cathode gap and surrounded by

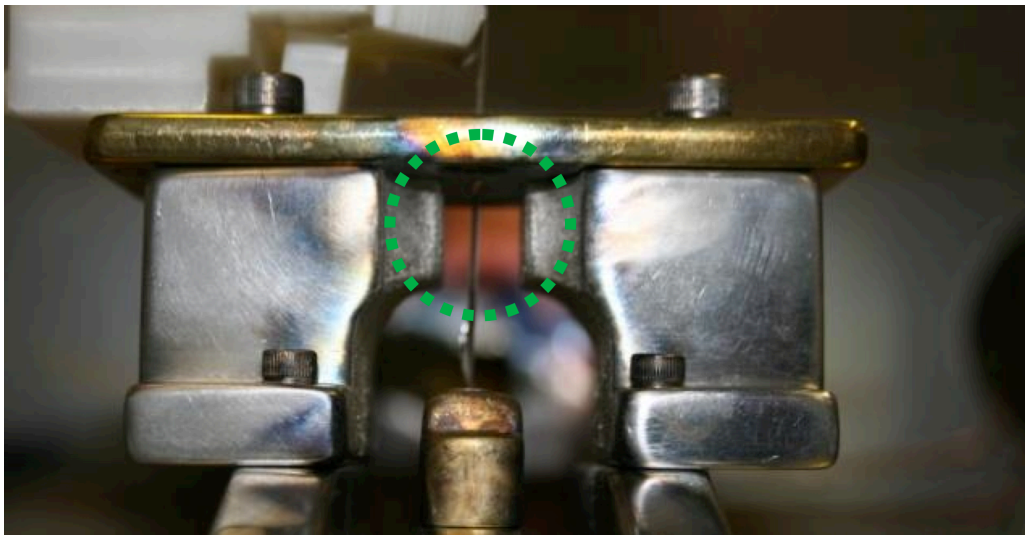

Figure 2.5: Experimental geometry for a typical aluminum foil experiment on the LTD as setup by Jacob Zier. The green dashed circle highlights the 400 nm thick foil. The current flows in the vertical direction and returns along the plates to the left and right of the foil in the circled region[48][47].

the return current plates on the left and right side, highlighted in the green dashed region. Thus, the rectangular region in the green dashed circle is the region of interest and can be modeled by our theory. The three region model in this context is then simply two vacuum regions (regions I and III) surrounding a plasma region of finite thickness (region II). It is most natural to consider Fig. 2.1 rotated by 90°

so that the foil moves either left or right as in the experiment. The return current plates are aligned vertically with the foil and located at $x = \mu, \eta$ (to the far left and right of the green highlighted region of Fig. 2.5).The current flows axially ($\hat{z}$) so that the corresponding induced magnetic field is in the $\hat{y}$ direction (into the page at the β-surface or out of the page at the α-surface). If the foil is positioned symmetrically at $x = 0$ (midway between the perfect conductors in Fig. 2.1), $B_{y,3} = -B_{y,1}$ and the magnetic pressure on either side of the foil is exactly the same. In this case, the foil does not move as the equilibrium condition is exactly satisfied, although the ablation plasma expands from both sides. This case is also the same as if the return plates were at $x = \pm\infty$. The result of this experimental setup should then be that there is limited MRT growth, as the foil should not be significantly accelerated.

If the foil is offset from $x = 0$ then the foil should be accelerated due to the imbalance of magnetic pressure caused by $B_{y,1} > B_{y,3}$ or vice-versa depending upon the offset. This imbalance of course derives from the conducting walls containing magnetic field (Fig. 2.1). The offset scenario should then produce MRT at one interface with corresponding feedthrough at the other interface. The results of both centered and offset cases are presented in detail in [48][47]. The surprising observation was that in both cases, large amounts of perturbation growth were observed on both surfaces, clearly visible in Fig. 2.6. The dominant wavelengths, as determined by Zier [47] were ~ 700 μm. In retrospect these results were in fact far from surprising. The first clue was that while the initial foil thickness was 400 nm, laser shadowgraph images showed that very quickly the foil ablation plasma expands out to a thickness ~ 1.5 mm (Fig. 2.6). The first implication of this is for feedthrough. At $\lambda = 700$ μm, the RT feedthrough factor, $F = e^{-k\Delta}$, is $F(\Delta = 400 \text{ nm}) = 0.99$ as compared to $F(\Delta = 1.5 \text{ mm}) = 10^{-6}$ which is practically 0. Hence, at $\Delta = 1.5$ mm the interfaces are effectively decoupled for the largest observed wavelength. Also important to keep in mind is that the shadowgraphs obtained by Zier were imaged along the magnetic

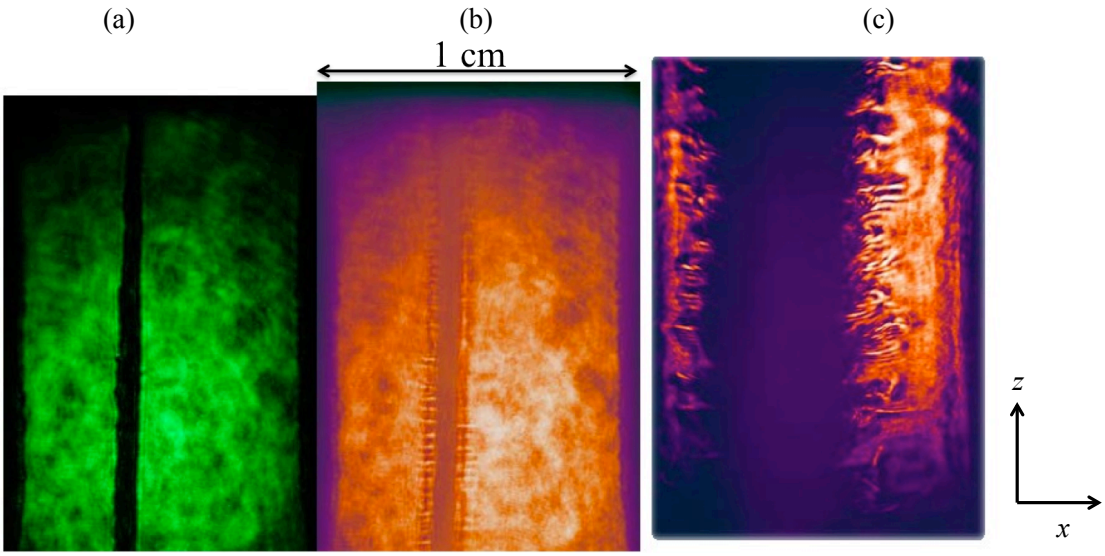

Figure 2.6: Experimental laser shadowgraphs obtained by Jacob Zier of 400 nm aluminum foil plasma from [48]. Laser probes perpendicular to foil current (i.e., in the z-direction): a) pre-shot foil, b) 38 ns, 0.215 MA, c) 199 ns, 0.6 MA.

field lines, thus observing perturbations without any field line bending present. The images, obtained in the (x, z) plane thus integrate out any perturbations in the $\hat{y}$ direction where field line bending may be important.

The explanation for the MRT observed in these experiments (Fig. 2.6) came from physical intuition and confirmed by 1D resistive MHD simulations utilizing the HYDRA code [67]. The code used for these simulations will be more adequately discussed later, so only some key features of the code and the subsequent results are presented here. HYDRA is able to utilize advanced equations of state and models for thermal and electrical conductivities so that a load can be simulated from the solid to the plasma phase as best as possible given the MHD functionality of the code. The physical picture of these foils at early times is that they are rapidly ohmically heated volumetrically as the magnetic diffusion length, $L_m >> \Delta$.The current is initially confined to the outer surface of the foil, but the finite resistivity of the foil allows for ohmic heating of the surface, which further increases the resistivity and allows more magnetic field to diffuse into the foil. Since the foil is thin, it does not take

long for current to diffuse into the entire foil thickness. The ohmic heating of the plasma leads to rapid increase in the kinetic pressure of the foil resulting in the observed physical expansion of the foil plasma dimensions. Figure 2.7 shows a snapshot from a 1D HYDRA simulation of a foil offset to the left in the geometry of Fig. 2.5. At this point the foil has exploded to a thickness of 250 μm but the magnetic pressure has not yet begun to accelerate the foil. Initially, as the foil plasma expands,

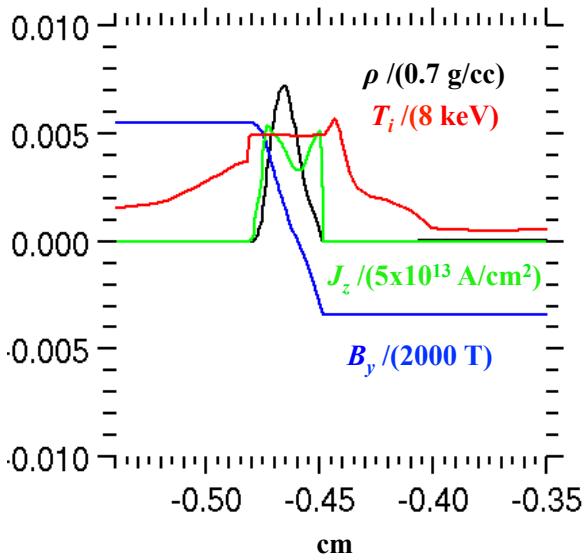

Figure 2.7: Snapshot of 1D HYDRA simulation at 50 ns of initially 400 nm thick aluminum foil. The foil plasma is accelerated from left to right. Note that the current thickness of the foil plasma is roughly 250 μm at this point, a factor of 625 times thicker but the peak density is much smaller than solid density.

the conditions required for MRT are not met as the pressure and density gradients are in the same direction. As the plasma expands, the load current continues to rise as the typical LTD current pulse $I(t) \sim \sin^2(t/t_{rise})$. This corresponds to an increasing magnetic field in the vacuum region. This leads to the source of MRT, when $\nabla\rho \cdot \nabla(p_{\text{kin.}} + p_{\text{mag.}}) < 0$ is finally satisfied. The physical picture of the MRT growth is that it is caused by deceleration of the expansion of the foil plasma on a strong magnetic pressure on both sides of the exploded foil. Any offset of the foil should still show asymmetry as the MRT condition will be satisfied at different times,

but feedthrough should not enter as the two interfaces are effectively independent (Fig. 2.6). This was indeed observed, and certainly not the intended mechanism for studying MRT growth, though it was certainly sufficient for showing the evolution of MRT growth, $\gamma \sim \sqrt{kg}$. It should be noted that the growth was slightly faster on the right side of the foil plasma, which was closer to the return electrode. Again a more detailed presentation of the experimental results is given in [48][47] for the interested reader.

2.3.2 Using the HYDRA code for MRT and feedthrough calculations

In many cases, the experiments on pulsed power machines involve highly dynamic changes in pressures, densities, and magnetic fields. One way to understand how these parameters vary in time is to consider simple 0D models such as the snowplow model [21] or 1D self-similar solutions for implosions [7][21]. These models tend to require fairly strict assumptions such as a perfectly conducting plasma or an ideal equation of state for the material. To escape these restrictions, 1D HYDRA [67] simulations can be distilled into evolving, quasi-equilibrium models needed for the planar model, shown in Fig. 2.1. HYDRA is capable of integrating an MHD load into a circuit described by the pulsed power machine being used. In this way a self-consistent drive current can be determined from a voltage pulse. The work that follows relies on experiments already performed where the experimental load current was measured and can be used to drive the simulation. Certainly there are some uncertainties in the load current, however, any uncertainties will be consistent between the simulations and analytic calculations, so any differences would appear in comparisons with the experiments themselves. Any differences between 2D MHD simulations and analytic calculations will have to be described by other means.

The basic procedure in one of these integrated calculations is to first determine the experimental configuration and use that to set the initial conditions for HYDRA.

This requires defining the foil thickness and position relative to the boundaries, material and equation of state and conductivity models for each material and lastly the current source (as determined by the experiment in this case) and required boundary conditions for a 1D problem. The specified current defines the driving magnetic field. The simulation is then run for a desired time and results are then post-processed to determine the required parameters for the analytic MRT model. Each simulation data dump then gives the equilibrium parameters at the simulation time and the dispersion relation $\omega(k_y, k_z)$ and $F(\omega)$ can be exactly computed for that simulation time. Thus, the instantaneous MRT growth rate (and feedthrough factor) can be determined at any time, for any sign of the acceleration. Of course, the problem solved in this case is a linear one, but the perturbations themselves are nonetheless 3D. The time investment in the calculation comes mostly from the 1D simulation, which most likely will never exceed 1 hour. Once the simulation is complete, the post-processing and calculation of the dispersion relation and feedthrough factor takes no more than 10 minutes (even less if all of the simulation results are on the same computer). Hence, the MRT growth of 3D modes is computed on the order of an hour or less. This is certainly not possible for a 3D MHD simulation. Despite the many assumptions inherent in planar (and cylindrical model), this work will show that the insight gained by this technique is very powerful and applicable to a wide variety of circumstances and may shed light on a number of unanticipated features observed in experiments.

With the motivation in mind, an example calculation is presented next. To best illustrate the general situations allowed by the planar model, consider the compression of a gas and axial magnetic field (B_z by an accelerated planar plasma slab (foil, flyer plate, etc - Fig. 2.1). The slab is accelerated in the lab frame from $x < 0$ towards $x = 0$ due to the magnetic field generated, $B_y(t)$, by an axially directed current. The gas is located in region III and the axial magnetic field is initially uniform across the whole problem. As the slab is accelerated, the axial field is compressed as it is confined

by a perfectly conducting boundary. B_y and g increase in time in region I due to the increasing load current. At each timestep, quantities such as $\rho(x)$, $\vec{B}(x)$, $p(x)$ must be transformed into ρ_1, ρ_2, ρ_3 and $\vec{B}_1, \vec{B}_2, \vec{B}_3$, etc.. The plasma slab thickness must also be determined, and may possibly change in time as $\rho_2(t)$ changes. A particular challenge of the sharp boundary model is defining Δ and what the actual extents of the plasma are.

A 1D HYDRA simulation can easily be run in Lagrangian mode, thus the nodes defining the liner boundary remain the liner boundary. However, ablation or expansion/compression can introduce significant density gradients, making the concept of a 'boundary' much more nebulous. Large ablation can easily add millimeters to the estimated thickness based on this simple definition. The result is that the Lagrangian boundaries determine the maximum thickness of the plasma slab but most likely overestimate it, particularly for cases like the thin foils on the LTD [47][48]. Overestimating the thickness, may have limited impact on the MRT growth rate calculation, but the feedthrough factor strongly depends on the thickness. Thus, quantifying feedthrough exactly is significantly challenging but the qualitative insights are very useful. After thorough investigation, two plausible methods emerged for determining an effective thickness of region II. (1) Take the average density between the Lagrangian boundaries as ρ_2 and then assume the total liner mass is uniformly distributed around the peak. (2) Take the peak density as ρ_2 and assume the total liner mass is distributed uniformly. Method 2 will give the smallest thickness, as an effectively higher density will be used, while method (1) is somewhere in between. With $\alpha(t)$ and $\beta(t)$ determined, all other parameters in each region can be calculated

as well according to the formulae:

$$\langle f_1(t)\rangle = \frac{\int_\mu^\beta f(x,t)\mathrm{d}x}{\int_\mu^\beta \mathrm{d}x} = \frac{1}{h_1}\int_\mu^\beta f(x,t)\mathrm{d}x, \tag{2.51}$$

$$\langle f_2(t)\rangle = \frac{\int_\beta^\alpha f(x,t)\mathrm{d}x}{\int_\beta^\alpha \mathrm{d}x} = \frac{1}{\Delta}\int_\beta^\alpha f(x,t)\mathrm{d}x \tag{2.52}$$

$$\langle f_3(t)\rangle = \frac{\int_\alpha^\eta f(x,t)\mathrm{d}x}{\int_\alpha^\eta \mathrm{d}x} = \frac{1}{h_3}\int_\alpha^\eta f(x,t)\mathrm{d}x, \tag{2.53}$$

$$\langle f_2(t)\rangle = \frac{\int_\alpha^\beta rf(r,t)\mathrm{d}r}{\int_\alpha^\beta r\mathrm{d}r} = \frac{2}{\beta^2-\alpha^2}\int_\alpha^\beta rf(r,t)\mathrm{d}r, \tag{2.54}$$

Equation 2.54 shows a sample calculation for 1D cylindrically symmetric problem which is necessary for this section and will be important in Chapter 3. In either case, $f(x,t)$ is the 1D profile from HYDRA. The last variable to be determined is g. The acceleration can be computed a number of ways. The acceleration of each zone can be computed and subsequently averaged to determine the bulk motion of the foil, however this tends to be quite noisy. A better way is to use Eq. 2.2 with all the other equilibrium parameters determined. Oftentimes, Eq. 2.49 is sufficient, but it is just a limit of the equilibrium condition. With these formulae, any 1D HYDRA simulation can be reduced to an effective three regions at any time of interest to give the instantaneous MRT growth rate $\omega(\vec{k},t)$ and feedthrough factor, $F(\omega)$.

2.3.3 Temporal growth of MRT

The next question is how to use the information obtained from HYDRA to understand an experiment with MRT. For the most part, WKBJ solutions are very

adequate, where the amplitude gain, G of a particular mode is given by

$$G = \exp\left(\int_0^{t_0} \gamma(\vec{k}, t)\mathrm{d}t\right). \tag{2.55}$$

As pointed out by Sinars et al. [51], substituting exp $\rightarrow$ cosh leads to a slightly more accurate solution. The most accurate method proves to be, for a single interface, solving the more general ODE with initial conditions

$$\frac{d^2}{dt^2}\xi_{\mathrm{MRT}} = \gamma^2\xi_{\mathrm{MRT}}, \tag{2.56}$$

$$\xi_{\mathrm{MRT}}(t=0) = \xi_0, \tag{2.57}$$

$$\frac{d}{dt}\xi_{\mathrm{MRT}}(t=0) = 0, \tag{2.58}$$

where ξ_0 is the initial amplitude of the perturbation with wavenumber $\vec{k}$. With two interfaces the ripples, ξ_β and ξ_α are represented as a superposition of four modes given by [8]

$$\xi_\beta(t) = a_1 e^{i\omega_1 t} + a_2 e^{i\omega_2 t} + a_3 e^{i\omega_3 t} + a_4 e^{i\omega_4 t}, \tag{2.59}$$

$$\xi_\alpha(t) = F(\omega_1)a_1 e^{i\omega_1 t} + F(\omega_2)a_2 e^{i\omega_2 t} + F(\omega_3)a_3 e^{i\omega_3 t} + F(\omega_4)a_4 e^{i\omega_4 t}, \tag{2.60}$$

where $F(\omega_j)$, $j = 1, 2, 3, 4$ are the feedthrough factor of the j^{th} mode [57][8][2]. The coefficients, a_j are determined by the initial conditions on ξ_α and ξ_β. Often times the initial conditions are just

$$\xi_\beta(0) = \xi_{\beta 0}, \qquad \dot{\xi}_\beta(0) = 0, \tag{2.61}$$

$$\xi_\alpha(0) = \xi_{\alpha 0}, \qquad \dot{\xi}_\alpha(0) = 0, \tag{2.62}$$

stating that the ripples on each surface have some initial amplitude but zero initial velocity. The amplitudes may also be negative, introducing a phase to the ripples.

For example, $\xi_{\alpha 0} \rightarrow \xi_{\alpha 0} e^{i\phi}$, where ϕ is the phase. If $\phi = \pi$ for α and $\phi = 0$ for β, then the α ripple amplitude is now "negative" or 180° out of phase with respect to the β ripple. These ripple amplitudes could also depend on the perturbation wavenumber, $\vec{k}$. Thus, a linear combination of surface ripples could be applied, again with arbitrary phase. Given an initial spectrum, $f(k_y, k_z)$, the solution of $\xi(y, z, t)$ is easily obtained via Fourier transform. Since this analysis is linear, the modes grow independently according to Eq. 2.59 and Eq. 2.60. Such a method can only be taken so far as the shorter wavelengths tend to grow very quickly. These modes reach saturation and can possibly couple with other modes to generate longer wavelengths, which is not accounted for in linear theory. Something like Steve Haan's saturation model could then be used [73][72]. Early on, natural perturbations on the surface of aluminum targets can have wavelengths as low as 1 μm and physical processes such as melting as well as material strength can play a larger role in the development of perturbations so long as electrical current is also present [17][18]. Because of these factors, the planar model that has been described is best suited to longer wavelengths, in particular, pre-seeded longer wavelengths. The Sandia experiments by Sinars et al. [51] are an excellent example of this scenario and will be referred to frequently.

2.3.4 A brief discussion of the HYDRA code for 2D problems

1D HYDRA simulations are invaluable for our analytic MRT calculations. Moving into 2D allows for direct comparison of HYDRA estimates of MRT growth and the result of the analytic calculations. 2D HYDRA simulations can also be directly compared to experiments following some post-processing under the right circumstances. This provides a direct link between experiment, simulation, and theory and lays not only the groundwork for benchmarking simulations, but also allows for understanding of experimental results. Some further details of HYDRA are discussed to illustrate its capabilities.

HYDRA is a massively parallel 3D arbitrary-Lagrangian-Eulerian (ALE) code developed at Lawrence Livermore National Laboratory [67]. ALE grid motion implies that at any time during the calculation any portion of the mesh may move with the fluid, may be locked in place, or somewhere in between. Oftentimes the mesh moves with the fluid and then is relaxed to some extent, depending upon the level of mesh distortion. Along with this feature are developed packages for radiation transport, laser propagation, and resistive MHD, amongst many others. The ion and electron temperatures can be tracked independently with the appropriate equation of state selected. As mentioned earlier, HYDRA can utilize tabular equations of state and transport models (electrical and thermal conductivity, radiation opacities) which are invaluable for modeling experiments. The major features used in this work are the resistive MHD package and tabular EOS (equation of state) and electrical/thermal conductivities. While HYDRA is capable of 3D calculations, 1D and 2D calculations will be the workhorse for this thesis due to their far less demanding computational cost. The 3D simulations also contain an extreme amount of information, significantly more challenging to digest than the 2D results. There are certainly intrinsic limitations as to the applicability of 2D simulations. Often a direction of symmetry is not present. For example, consider the LTD foils discussed earlier and the often anisotropic nature of MRT. If 2D simulation of the foil is in the $(x - z)$ plane, with axial current, then the 2D simulations neglect all affects of $(k_y B_y)^2$.

The major requirements to study MRT in the lab are to be able to: (1) identify the wavelengths present with their corresponding amplitudes, and (2) follow their evolution in time. Unless perturbations are seeded, the nonlinear behavior of MRT makes reproducibility between experiments challenging, but not impossible [53]. Of course, knowledge of the density of the material and how diffuse it is, is also very useful. Measurements of densities, acceleration histories, and magnetic fields, in particular, are often very challenging [53]. The main tool for identifying (1) and (2) is the use of

high-resolution imaging. At the University of Michigan, laser shadowgraphy is used, which is able to view plasmas reaching densities 10^{21} /cc (= cm^3). The laser is capable of taking four images during a single experimental shot so that MRT growth at four different times can be compared. At Sandia National Laboratories, the pulsed power targets are imaged with two-frame 6.151 keV radiography [52], allowing for much higher densities to be imaged. One of the best ways then to compare 2D simulations and experiment, is to take a HYDRA simulation at the appropriate radiograph time and post-process the data to generate a synthetic radiograph (or shadowgraph).

This process is relatively straightforward with the appropriate software available. SPECT3D [74] can be used to create the experimental imaging geometry based on an imported simulation. An example of radiography is discussed. To set up a post-processing simulation, the X-ray source position as well as spectral intensity is specified and aligned appropriately with the imaging detector. For the Z-beamlet backlighter (ZBL) at Sandia, this requires that the source be 3° above or below horizontal [51] and the image taken in the (x,z) plane or (r,z) in cylindrical coordinates. A 2D MHD simulation can then be imported and appropriately extended to 3D via rotation or extrusion. The opacity, κ, of the material to the X-rays must be specified as κ typically depends on the density and temperature of the fluid element (and X-ray energy itself). Opacities are usually specified in units of cm^2/g, such that the transmission through a material scales, in the simplest sense, as $e^{-\kappa\rho L}$, where L is the path length. The detector resolution in space and time can also be set according to the capabilities of the experiment. For ZBL, this is 20 μm and $\sim$ 2 ns (temporal "blur" will be neglected for the calculations in this thesis). SPECT3D then takes care of the rest. It performs the x-ray transport calculation and generates the synthetic image on a transmission scale. The image can then be directly compared to experimental images. Such comparisons can be done a number of ways and two will be discussed next.

Due to the high opacity of aluminum to the ZBL produced X-rays (102 cm^2/g as compared to 2.24 cm^2/g for beryllium [51]), the experimental radiographs are observed to have very rapid drop off from 0 % transmission to 100 % transmission. This produces a very distinctive boundary, amenable to simple methods of analysis. The easiest place to start is to identify a transmission contour level to track. For the aluminum simulations discussed below 50 % was selected, however, there was not a great deal of variation between that and 20 % or 80 %. With the contour level selected, a radial line-out can be taken at each axial position and the radius recorded of the chosen transmission level. The result of this calculation is a trace detailing the axial variation of the surface, $r_0(z)$, for a particular transmission level. For well-defined perturbations (e.g., single mode, k_z), the minimum and maximum of $r_0(z)$ give the peak to valley amplitude of the mode and this is often sufficient, in these cases, for determining the MRT growth. For more complicated mode structure, $r_0(z)$ is best analyzed by examining its Fourier components using a Fast Fourier Transform (FFT) algorithm. Comparing planar target experiments with 2D simulations presents additional challenges, if both k_y and k_z are present. Experimental images obtained in the (x, z) integrate through any dimension in the $\hat{y}$ direction, appearing as additional opaqueness in the (x, z) image. This is less of an issue for cylindrical imaging in (r, z) as observed MRT growth occurs at the periphery of the target. The curvature reduces the amount of material directly imaged in the (r, z), however a similar problem would crop up in efforts to image the (r, θ) plane. Thus, the easiest to interpret images are those containing only preferentially seeded wavelengths or where symmetry is high. Also important to note, is that SPECT3D can certainly account for these effects given a proper 3D simulation, as opposed to a 2D simulation spun around an axis.

Of course, HYDRA simulations do not necessarily need to be post-processed to such an extent in order to determine MRT growth rates, feedthrough, etc. The previous methods can provide a nice benchmark case, but the density contours from the

simulation can easily stand in for transmission and thus eliminates any line integration effects introduced by the SPECT3D method. Often this is the simplest method to use in (r, θ) simulations. In simulations, rippling at the inner surface is usually much easier to characterize. This is because this interface usually sees very little ablation, keeping the density gradient high across the interface. Thus, the interface and feedthrough is fairly straightforward to track. While this is not always the case, feedthrough has proven to be easier to characterize. The 3D perturbations of course add another degree of complexity in analysis, but the interface surface, $r_0(\theta, z)$ is still straightforward to determine. Appendix C presents some preliminary 3D HYDRA simulations of a cylindrical liner with pre-seeded wavelengths.

2.4 Comparison of analytic MRT growth rates with simulation and experiments at Sandia National Laboratories

To test the analytic growth rates of the planar model, as well as the HYDRA code's MHD modeling capabilities, a series of experiments by Dan Sinars et al. at Sandia National Labs is examined [13][51]. Note that Ref. [51] is an extended version of Ref. [13], for the remainder of this Chapter we shall reference the more in-depth work of Ref. [51]. The purpose of the experiments was to directly measure the growth of MRT in cylindrical liner implosions on the Z-accelerator. Z implodes these liners with a peak current, directed axially, of nearly 20 MA on the order of 100 ns risetime. Such a pulse is shown in Fig. 2.8. The liners used in these experiments were aluminum with sinusoidal perturbations machined on the outer surface of the liner aligned with the axial direction (Fig. 2.9). The machined perturbations were, most importantly, azimuthally symmetric which eliminates a great deal of uncertainty in measuring MRT from a 2D image. Sinars et al. [51] also shows radiographs of unseeded aluminum liners which show substantial asymmetry between the two sides of the liner indicating

$k_y = k_\theta > 0$ (lack of azimuthal symmetry). McBride et al. [53] also showed that 2D simulations of liners with only machining level imperfections ($\lambda \sim 5$ μm) dramatically overestimated MRT growth. Seeded liners of the type discussed above, thus are the best for comparing 2D simulation with experiment and will be the focus for much of the discussion in this section.

The other important consideration is cylindrical nature of the targets. The $1/(k_z r)$ terms common to cylindrical geometry are minimized when $k_z r$ is large. This condition holds true for all but the longest wavelengths. Thus, the majority of the simulations were performed in 2D (r, z) with perturbations where $k_z r >> 1$. A comparison with a planar geometry simulation will show this to be true. The other reason for this is that the current HYDRA boundary conditions on the electromagnetics does not allow for both a B_y and B_z in a planar problem, as has been considered in the MRT model derived earlier. In cylindrical coordinates, such boundary conditions have been developed (where $B_y \sim B_\theta$) which allows for more thorough comparisons of the analytic model. Development of the 2D simulations is discussed next.

The major example that will be used throughout, are the liners containing 400 and 200 μm wavelengths which were studied in the most detail in Sinars et al. [51]. Shown in Fig. 2.9 is an axial section of such a liner from the first timestep of the 2D HYDRA simulation performed in (r, z) coordinates. The red corresponds to the liner material (aluminum). The liner itself has the exact same dimensions as in the experiment where $r_\alpha = 2.876$ mm and $r_\beta = 3.168$ mm giving a thickness, $\Delta = 292$ μm. The perturbation peak to valley amplitudes are set, as in experiment, to be 5 % the perturbation wavelength. The 400 μm and 200 μm peak-to valley amplitudes are then, respectively, 20 μm and 10 μm. This fixes the initial value of $k\xi_0 =$ const. for any wavelength.

Both the 1D and 2D simulations were driven by the current pulse used in the experiment, reproduced in Fig. 2.8. Both simulations also used the SESAME EOS

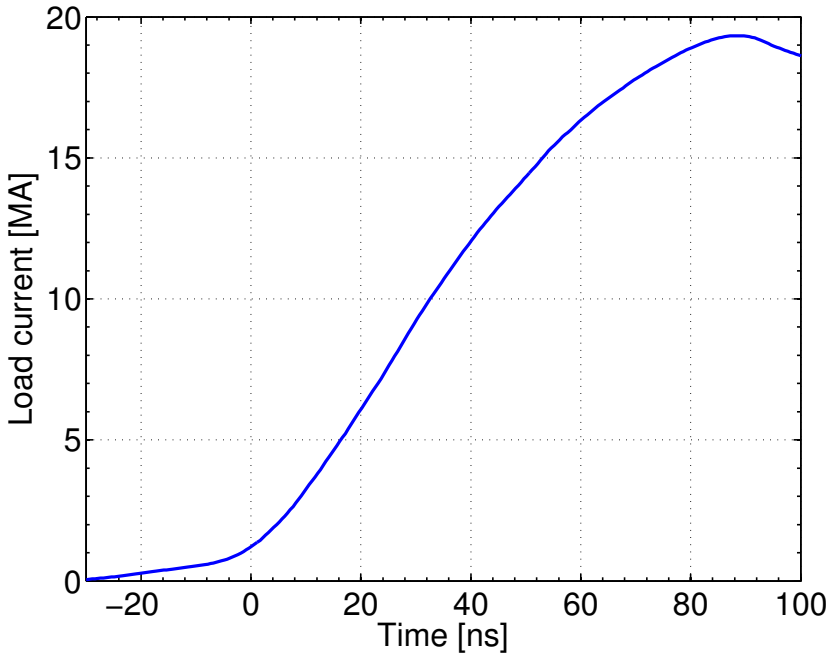

Figure 2.8: Current pulse used to drive 2D HYDRA simulations. In Sinars et al.[51] this corresponds to shot z1965.

3719 [75] and 29373 [76] for the conductivities which were the most accurate models available. The Livermore EOS (LEOS) 130 was also used, but no substantial differences were observed in the MRT growth. HYDRA affords the ability to conform the grid around the perturbations so that the sinusoidal perturbations are smooth. Purely Eulerian codes generally require some sharp corners when there is curvature. The 1D radial grid can be gridded as finely as desired, major requirement being that the skin depth (of order 20 μm for aluminum) is resolved in the material. In 2D, the radial grid is non-uniform with the majority of the zones devoted to the liner material with a radial resolution near the outer surface of under a micron. The interior of the liner has slightly larger radial resolution. The requirement on the axial zoning is that there are at least 20 axial zones per wavelength, which is not too intensive for only a section of the liner. 128 axial zones is the lowest number that can be used in the simulation geometry shown in Fig. 2.9. The corresponding resolution is 9.3 μm giving 22 zones/200 μm wavelength. Simulations were run at this resolution as well

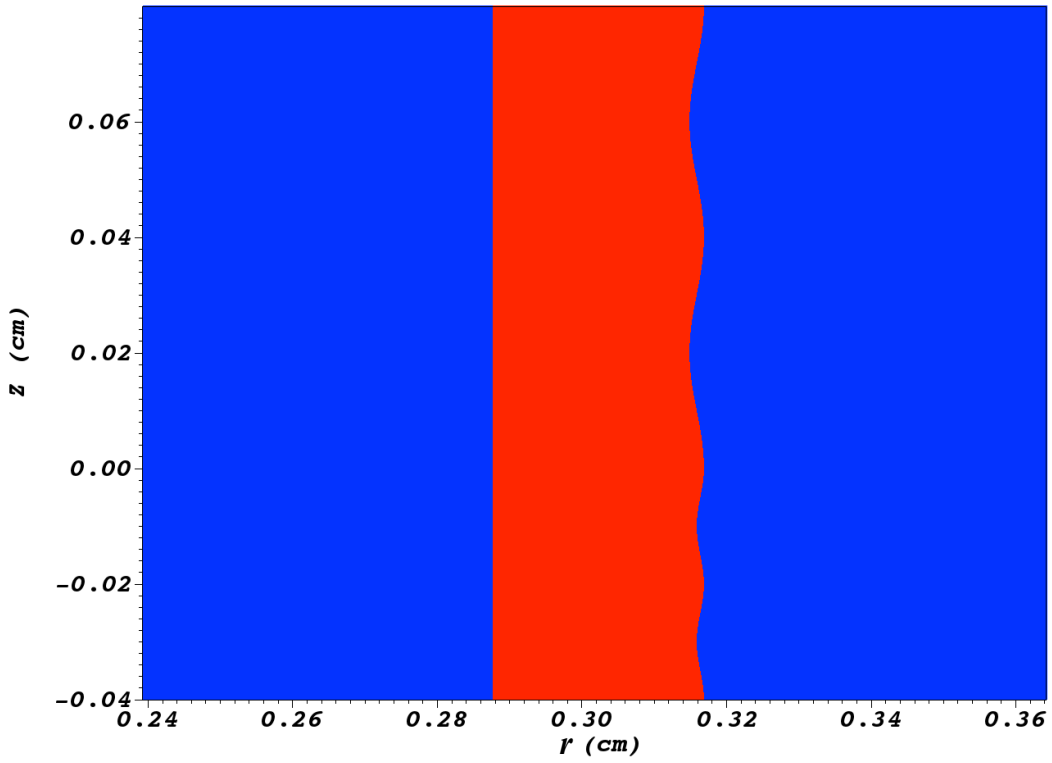

Figure 2.9: Simulated geometry for seeded liner implosion, with the liner in red at $t = 0$. The top portion contains 400 μm perturbations and the bottom contains the 200 μm perturbations. The peak-to-valley amplitudes are 20 μm and 10 μm respectively, with an unperturbed liner thickness, $\Delta = 292$ μm.

as double the axial resolution ($\sim$ 4.5 μm/zone). Both simulations were more than sufficient for capturing the growth of both perturbations.

2.4.1 Results of the ideal MHD model and 2D HYDRA simulations for seeded liner experiments

As shown in Sinars et al.[51], the 400 μm perturbation was the primary wavelength under quantitative study. It was found that the shorter the seeded wavelength used, the more complicated the behavior became. Thus, analysis of the 400 μm perturbation will be the starting point. Both 1D and 2D HYDRA simulations were run according to the experimental geometry and drive conditions described by Sinars et al. [51]. An additional 2D simulation was run in planar geometry (x, z) to show the validity of applying the planar model to cylindrical implosions. In order to directly compare the 2D simulations to the experiment results, synthetic radiographs (6.151 keV) were generated with SPECT3D following the discussion at the end of the previous section. The images were also post-processed, isolating the 50 % transmission contour to identify the aluminum/vacuum boundary, which subsequently determines the ripple amplitude. The planar geometry simulation required setting a roughly equivalent path length for the x-rays to travel through the plasma. Lastly, the 1D simulations were distilled into the required data for the ideal MHD MRT model.

Since the only strong magnetic field present is the azimuthal magnetic field contributing to the pinch force, no appreciable magnetic field line bending is present in these experiments/simulations. Additionally, except for during the very early current rise, $p_{\text{mag}} >> p_{\text{kinetic}}$ which makes g straightforward to determine from Eq. 2.49, where $|B_0| = B_\theta(t)$. Hence, the implosion is completely driven by the magnetic pressure. The dispersion relation for this case is also very simple since all $\vec{k} \cdot \vec{B}$ terms are zero and any magnetic field enters only in g. This would not be the case for finite $k_y \approx m/R$ where $k_y B_y$ terms will appear. For these simulations, $k_z \Delta \sim 5 \rightarrow 10$ for

the 400 and 200 μm wavelengths, which means feedthrough should be quite limited until the MRT growth is very large. The growth rate and feedthrough factor are then no more than the RT growth rate, $\sqrt{kg}$ and RT feedthrough factor, $e^{-k\Delta}$ [2][57][6]. With the feedthrough factor being very small, this case can essentially be considered as a single interface. Nonetheless, the full dispersion relation, Eq. 2.36, was evaluated according to the 1D data at each time step in the simulation. To compare with 400 μm data, Eq. 2.56 was solved using $\omega(k_z, t)$, with $k_z = 2\pi/400$ μm and the initial condition $\xi_0 = 20$ μm.

The comparison of the growth of the 400 μm ripple determined by the analytic model, 2D simulations and experiment is depicted in Fig. 2.10, where excellent agreement is observed between all methods. The dip in amplitude just past 20 ns corresponds to the time just before the magnetic pressure exceeds the kinetic pressure. Physically, the rippled surface is heated and material effectively explodes off of the surface due to high pressure, generating significant ablation. It is possible that this is a form of ablative stabilization, but it occurs on a very short timescale. This has the effect of seemingly reducing the ripple amplitude in the radiograph. This effect is less observable in the planar radiograph as the line integration in the $\hat{y}$ direction is not the same as in the (r, θ) simulation. So, although the dip corresponds to a time when a physical phenomenon is occurring, it is also a small artifact of the imaging system. Overall this effect is also not important to the later time MRT evolution. Discrepancies between the experimental data and calculations are easily explainable in terms of uncertainty in g. Any uncertainty in the current measurement propagates into the simulations and calculations. So in this case, it may be anticipated the current was slightly underestimated. Finite density gradients would be expected to reduce growth rates further.

The time history of acceleration of the liner, the singularly most important parameter in the planar model, is provided in Fig. 2.11. The acceleration, $a(t)$ is equal

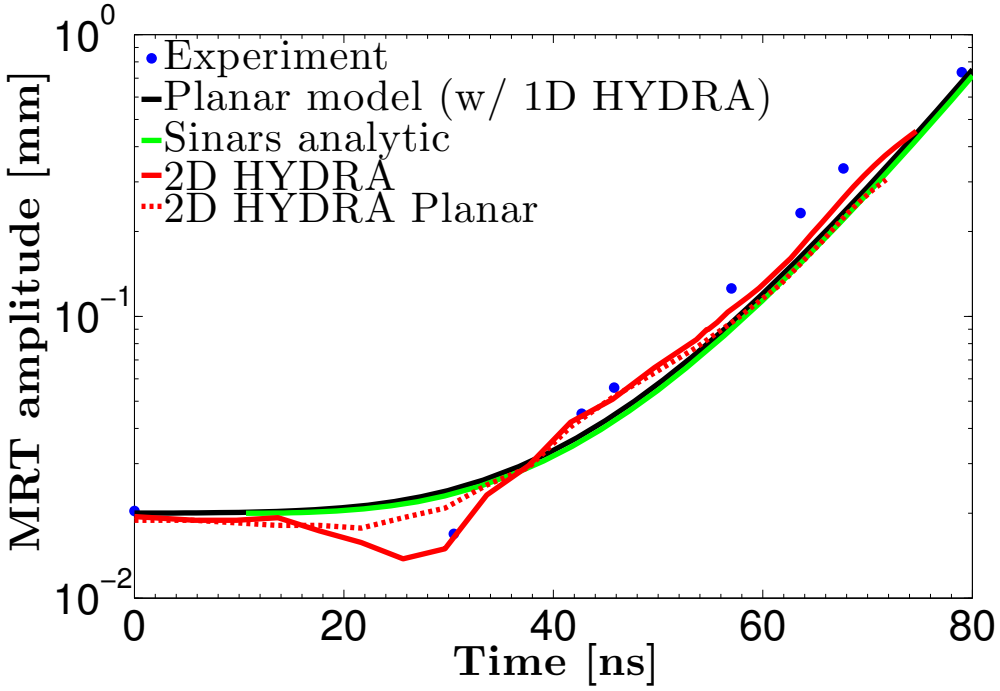

Figure 2.10: Growth of the 400 μm perturbation as determined by the analytic planar model, 2D simulations and experiment by Sinars et al. [51]. The resolution of the radiography system at Sandia is 20 μm, otherwise no uncertainties are given in the amplitude measurement.

to $-g(t)$ by definition in the derivation of the MRT growth rate. From Fig. 2.11(a) it clear that the thickness, Δ (= 292 μm when unperturbed) remains roughly constant, with only slight compression and expansion present. Between 20 ns and 40 ns, the outer radius position can be seen to expand slightly, while the inner surface remains immobile for over 40 ns. The expansion corresponds to the explosive ablation discussed with regard to the dip in MRT growth in Fig. 2.10. Additionally,

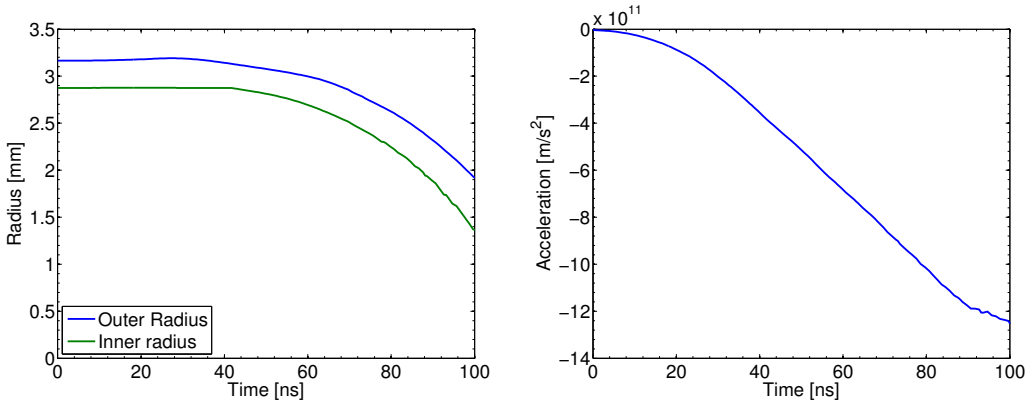

(a) Trajectories of inner and outer radii of Sinars et al. [51] liner implosion.

(b) Average acceleration history of Sinars et al. [51] liner implosion.

Figure 2.11: HYDRA simulated 1D liner dynamics of an imploding aluminum liner using the current in Fig. 2.8.

the liner does not implode much on the time scale of interest, up until 80 ns or so. The convergence ratio, $CR = r_i(t = 0)/r_i(t)$ does not exceed 2, where r_i is the liner inner radius ($r_i(t = 0) = 2.876$ mm). This justifies the planar approximation for MRT since $k_z r = 45.18 >> 1$. Beyond 80 ns, the 400 μm mode begins to saturate and no longer grows exponentially. From the radiographs in Sinars et al. [51], it is interesting to note just how well the linear theory does despite the highly elongated bubbles and spikes. This is not the case for many of the shorter wavelengths presented, particularly those below 200 μm. These modes exhibit plasma jetting as well as some coupling between the axial modes.

The 200 μm mode is somewhat more irregular in appearance, and the jetting makes determining the spike radius highly uncertain (see Fig. 2.18 below). The

imaging angle may also introduce some uncertainty in the trough region as the line of sight may be somewhat obstructed for larger amplitudes. However, it is clear from the experimental radiographs that the amplitude is increasing. Using the scale provided in the experimental radiographs, the amplitude of the 200 μm mode was calculated manually. The result of this calculation is shown in Fig. 2.12 as the blue connected dots. Before 40 ns, the amplitudes were imperceptible to the eye (likely clouded by 20 μm resolution of the instrument), so the amplitude was set to the initial amplitude of 10 μm. Results of the analytic calculation are plotted in black

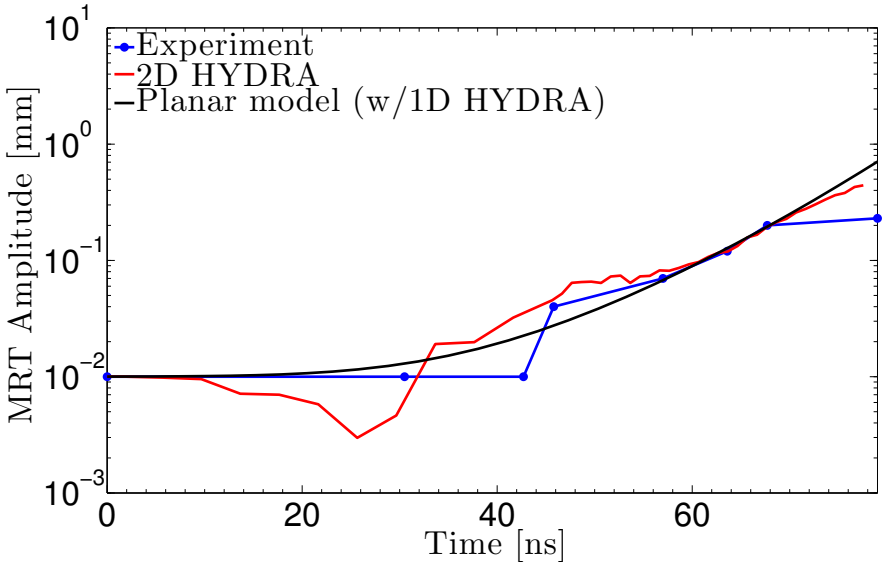

Figure 2.12: Growth of the 200 μm perturbation as determined by the analytic planar model, 2D simulations and experiment by Sinars et al. [51].

and agree fairly well over the time range available for comparison. The 2D HYDRA simulation results came from directly analyzing the HYDRA output data to illustrate that the 200 μm amplitude continues to grow past 70 ns. The dip in amplitude at late times in experiment, appears to be shadowing of the bubble/spike for the 3° line of sight. A comparison of the radiographs with and without the offset from horizontal in Figs. 7 and 9 of Sinars et al. [51] shows this difference for 200 μm as the trough is considerably better defined in the 0° case. The shadowing effect becomes important

only for larger amplitudes as an example shows in Fig. 2.13. Figure 2.13 shows the

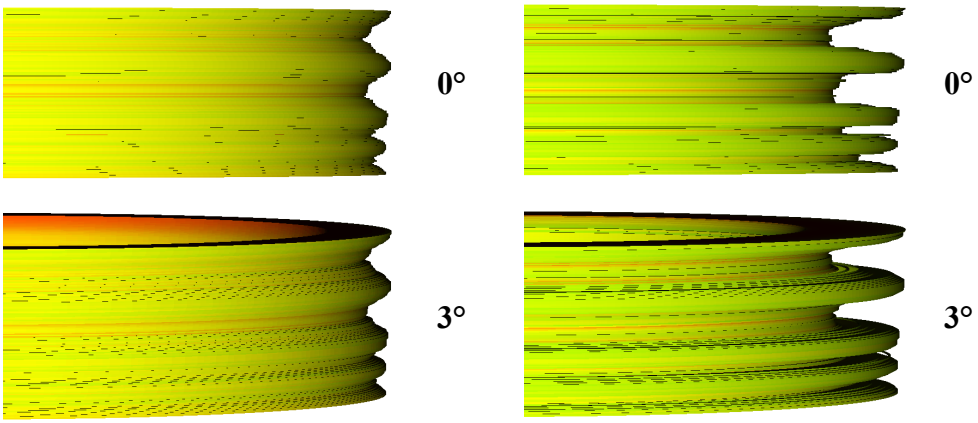

(a) Comparison of viewing angle effect, displaying liner density surface at time, $t = 63$ ns.

(b) Comparison of viewing angle effect, displaying liner density surface at time, $t = 74$ ns.

Figure 2.13: HYDRA simulation showing the effect of viewing angle to be the most important at later times for large amplitude, short wavelength (200 μm) perturbations.

output of a 2D HYDRA simulation at a density cutoff of 0.1 g/cc. The 2D simulations were spun around the axis using VisIt to generate the 3D effect. The view was then adjusted from 0° to 3° for the times 63 ns and 74 ns. From Fig. 2.12, the 63 ns image should show very little shadowing, as all calculation methods were in agreement. The time, $t = 74$ ns should show shadowing to be more important, which is indeed observed. Assuming this effect explains the discrepancy in amplitude at later times, it then appears that the experimental data is in agreement with the analytic linear growth rate as they were with the 400 μm wavelength. Nonlinear effects at 200 μm could also contribute to the slowed growth.

As wavelengths longer than 400 μm are often observed in experiments, an 800 μm wavelength simulation was run on a 1.6 mm axial extent (two wavelengths). The initial amplitude for the perturbation was the same as for the 400 μm case. The results were again in excellent agreement with the analytic prediction, as shown in Fig. 2.14, despite the amplitude dip and rebound.

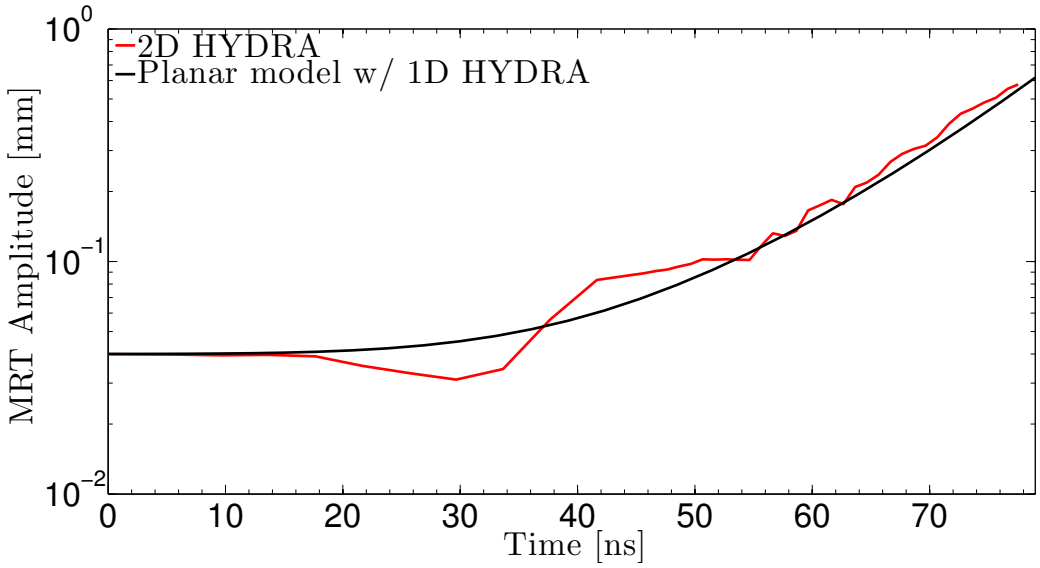

Figure 2.14: Growth of the 800 μm perturbation as determined by the analytic planar model and 2D HYDRA simulation (no experimental data for this mode).

It is remarkable that despite the ablative dip near 30 ns for both the 400 and 800 μm cases (Figs. 2.10, 2.14), 2D HYDRA simulations retain the memory of the linear growth rate for $t > 50$ ns. A possible explanation, in the scope of linear theory, is to decompose the problem into three time periods. The first, $t < 15$ ns, is the very early time before much acceleration or growth occurs at all. The second, between roughly $15 < t < 45$ ns, where the ablative dip and then rebound occurs. Lastly, the very linear growth phase of MRT, for $t > 45$ ns. In general, we can write the ripple amplitude, $\xi(t)$ as a linear combination of the linear MRT growth, ξ_{linear} and additional effects, $\xi_{a.e.}$ (denoted a.e. for legibility),

$$\xi(t) = \xi_{linear}(t) + \xi_{a.e.}(t). \tag{2.63}$$

The solution for the linear MRT component is

$$\ddot{\xi}_{linear} = \gamma_{MRT}^2 \xi_{linear}, \tag{2.64}$$

$$\Rightarrow \xi_{linear}(t) = \xi_0 \cosh \int \gamma_{MRT} dt. \tag{2.65}$$

The modification of the linear MRT growth is then accounted for by $\xi_{a.e.}$, which is non-zero only for $15 < t < 45$ ns where the ablative dip and rebound occurs. Outside of this time interval, $\xi_{a.e.} \cong 0$ and the growth returns to the linear MRT solution. The additional effects can incorporate effects such as ablation. However, it is clear that while the linear theory for MRT does not capture this somewhat transient effect, the late time evolution remains extremely well modeled.

Overall, the agreement between analytic theory and the 2D simulations and experiments is surprisingly excellent considering all of the approximations inherent in the planar ideal MHD model. However, the effect of magnetic field line bending has, so far, been neglected. There are two simple ways to introduce this effect: (1) to consider perturbations aligned with the driving field (k_y), and (2) consider perturbations perpendicular to the driving field but including an arbitrary strength magnetic field aligned with these perturbations (like the MagLIF pre-magnetization). The latter will be considered next for a number of reasons. If k_y were used, the value of $(k_y B_y)^2$ would not remain constant in time and thus the overall effect more difficult to assess. Of course, in this case there is always field line bending – there is no way to turn it off. Using k_z in conjunction with an applied $B_z > 0$, allows for direct comparisons with results from this section where no bending is present.

2.4.2 Effect of an applied axial magnetic field on MRT growth rates

Application of an axial magnetic field in (r, z) geometry with a seeded k_z introduces magnetic field line bending. This axial field has the potential to significantly

modify the dominant MRT growth rate [57][8]. Once again, the same sort of seeded aluminum liner will be used. Unfortunately such experiments have not been carried out, therefore comparisons will be made only between analytic theory and 2D HYDRA simulations.

To design a useful simulation, Eq. 2.41 can be utilized. Since the feedthrough factor is small, only the MRT unstable interface is of major interest. As of this writing, $B_z = 10 \rightarrow 30$ T is state of the art for liner experiments at Sandia, with the upper end requiring reducing diagnostic access for experiments. While an axial field of 10 T is sufficient to modify very short wavelengths (~ 10 μm), longer wavelengths are much less affected. Considering the 200 or 400 μm perturbation and the typical value of g from Fig. 2.11(b), it is not hard to see that the $(\vec{k} \cdot \vec{B})^2$ term is small in Eq. 2.41 when using even up to 30 T. We evaluate Eq. 2.56 in conjunction with the MRT mode given by Eq. 2.41, to illustrate the importance of the axial magnetic field to the MRT growth rate (Fig. 2.15).

Early on, for large enough axial magnetic fields, the surface is oscillatory. The phase of the velocity, $\xi'(t)$, when g becomes large enough such that the particular k_z becomes unstable, determines whether the amplitude is out of phase, in comparison to the initial seed. For any value of B_z there is some critical value of g such that the mode becomes unstable (exponentially growing as opposed to oscillatory). Larger values of g are of course, required for larger values of B_z. For a fixed wavenumber, B_z essentially increases the time for onset of MRT, t_{MRT}. This can have some interesting implications. For example, if $\xi(t < t_{\mathrm{MRT}}) > 0$, yet the amplitude was decreasing $(\dot{\xi}(t) < 0)$ due to oscillation, then when g becomes large enough the growth must first overcome the oscillation reducing the amplitude leading to much slower growth. On the other hand, if $\xi(t < t_{\mathrm{MRT}})) > 0$ and $\dot{\xi}(t) > 0$, the MRT effectively has a 'head-start' on growth. The result being that the MRT growth can become larger in the same time, than if $\dot{\xi}(t) \leq 0$. This effect becomes more apparent as the wavelength

decreases and can introduce some perplexing behavior as shown in Fig. 2.15. The curves were generated using the combination of Eq. 2.56 and Eq. 2.41.

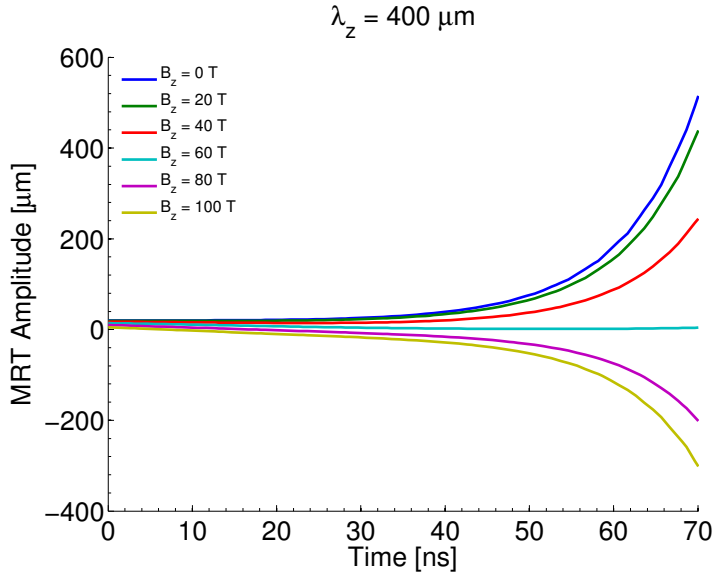

(a) Effect of increasing axial magnetic field on overall MRT gain for $\lambda_z = 400$ μm.

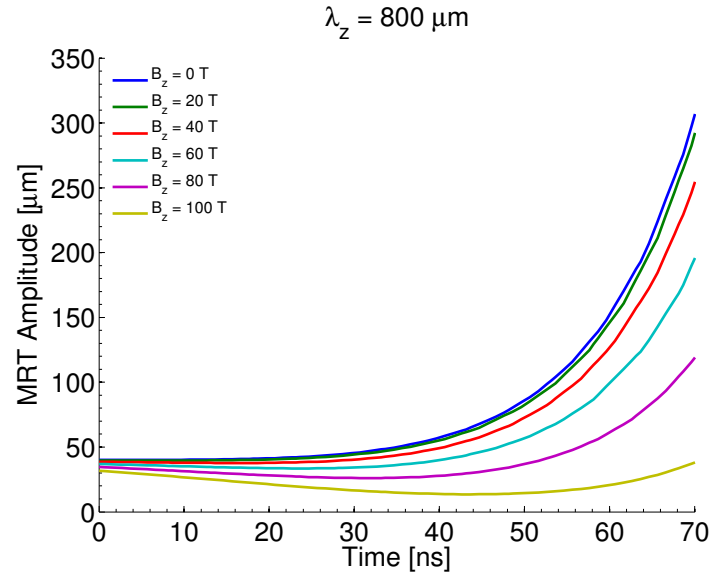

(b) Effect of increasing axial magnetic field on overall MRT gain for $\lambda_z = 800$ μm.

Figure 2.15: Comparison of MRT growth on with increasing applied B_z for two different wavelengths. The shorter wavelength exhibits amplitude inversion.

Figure 2.15(a) shows that very strong axial fields can actually allow larger amplitude MRT growth than for moderate fields. This is because of the phase effect

discussed. Before kg exceeded the stabilizing term, the amplitude oscillated and became negative. As kg exceeded the stabilizing term, the amplitude was still increasing (with the inverted amplitude) and thus the inverted amplitude was locked in and started to grow due to instability. Fig. 2.15(b) shows the same calculation but for 800 μm. Here the amplitude never inverted and the expected behavior is observed, where increasing B_z decreases the overall MRT growth. In resistive MHD simulations of liner implosions the effect observed for the 400 μm case is not observed (no inversion), results are more in line with the behavior of the 800 μm case. This will be discussed further, but a small amount of dissipation, afforded by finite resistivity, is all that is needed to limit the phase effect from the oscillations. Since, Eq. 2.56 is essentially the ODE describing an oscillator when $\omega^2 < 0$, an additional dissipation term can be added, phenomenologically, by incorporating a finite resistivity, η, and corresponding diffusion length, δ. Since the axial magnetic field is initially uniform, perturbations growing on the liner exterior would be affected by the diffusion only if $\delta \approx \xi_0$, where ξ_0 is the perturbation amplitude (i.e. the significant magnetic field line bending occurs near the interface).

$$\frac{d^2}{dt^2}\xi(t) = \gamma^2\xi(t) - \frac{\eta}{\mu_0\delta^2}\frac{d}{dt}\xi(t) \tag{2.66}$$

$$\frac{\eta}{\mu_0\delta^2} \approx 10^7 \text{ 1/s} \tag{2.67}$$

The amplitude of both perturbations begin at 20 μm. Important to note, is that the bulk resistivity of the aluminum tends to only increase as it is ohmically heated. The majority of the liner does not enter the plasma state, so the resistivity increases with temperature. Hence, dissipation tends to increase in time. Initially, with $\eta = 28$ nΩ, $\eta/\mu_0\delta^2 = 5 \times 10^7$ 1/s. Keep in mind that the dissipation-like term is completely phenomenological as it is simply the inverse of the diffusion time. In the limit that $\eta \to 0$ ideal MHD conditions are recovered. For non time-dependent coefficients, the

solution of Eq. 2.66 takes the form, $\xi \sim e^{-\zeta t/2} \sin(\gamma t + \phi)$, where $\zeta = \eta/(\mu_0 \delta^2)$.

Whatever the source of the dissipation, such a term is necessary to eliminate the oscillation seen at 100 T. Performing the same calculation as for Fig. 2.15, now with the dissipation included produces much more realistic results. Adding the dissipation

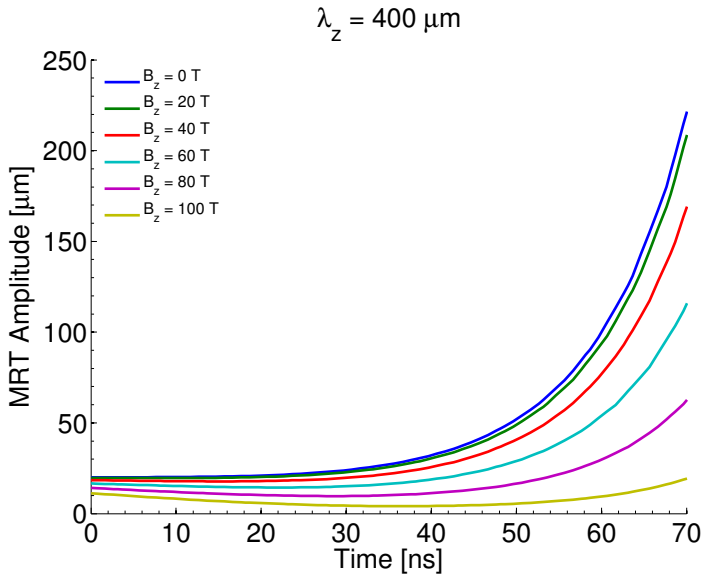

(a) Effect of increasing axial magnetic field on overall MRT gain for $\lambda_z = 400$ μm.

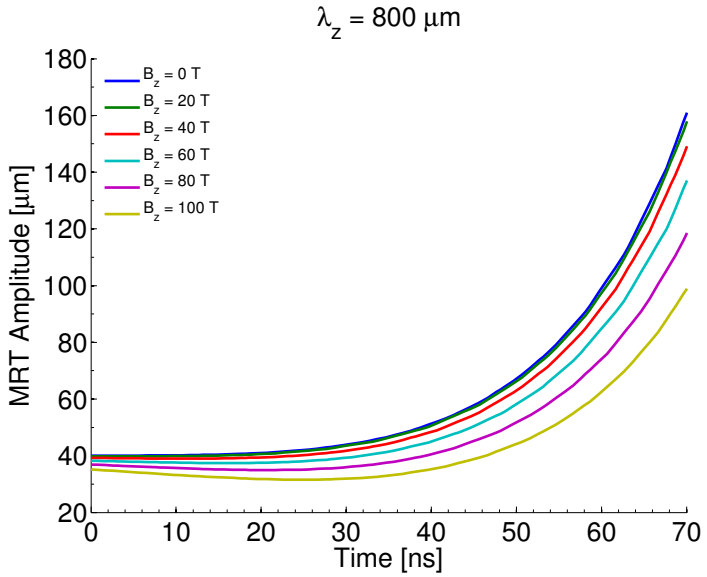

(b) Effect of increasing axial magnetic field on overall MRT gain for $\lambda_z = 400$ μm.

Figure 2.16: Comparison of MRT growth with increasing applied B_z and slight dissipation due to finite resistivity.

removes the amplitude inversion for the 400 μm case, this is in agreement with 2D HYDRA simulations that will be presented later on. However, Eq. 2.66 is only a qualitative solution which can address how additional dissipation affects the solution. For shorter wavelengths, some amplitude inversion remains and determining the exact cutoff for inversion is not possible (nor physically illuminating). Ablation and density gradients more strongly affect shorter wavelengths, which compound the difficulty in correctly modeling them. With the above considerations in mind, results of 2D HYDRA simulations with the addition of an axial magnetic field will be presented next.

Whether or not dissipation is considered, from the above figures, it is clear that a 10 T axial magnetic field is quite insufficient to affect MRT for long wavelengths, such as 400 μm and even 200 μm based purely on the linear growth rate. To proceed, a much higher field of 100 T is used to more strongly affect the MRT growth (such magnetic fields, or even higher values, are achieved after the seeded axial magnetic field is greatly compressed in MagLIF experiments [54][55][38][39]). These 2D HYDRA simulations were run with the exact same setup as that which produced Figs. 2.9, 2.10, 2.12 except with an additional (initially) uniform axial magnetic field of 100 T. The MRT growth for the 400 μm perturbation is shown in Fig. 2.17 and directly compared to the case without an axial magnetic field as the solid curves. Figure 2.17(a) also shows the corresponding analytic solution as the dashed curves. It is clear from Fig. 2.17(a) that the MRT stabilization is strongly overestimated when a finite resistivity is included and there is certainly no amplitude inversion. As a reminder, these 2D simulations were run using tabular values for the electrical resistivity, which are the best available. In order to isolate the source of the discrepancy, a second HYDRA simulation was run enforcing a constant resistivity ($\sim$ 10x room temperature aluminum conductivity). This essentially turns the calculation into an almost ideal MHD calculation. The result of this simulation is shown in Fig. 2.17(b)

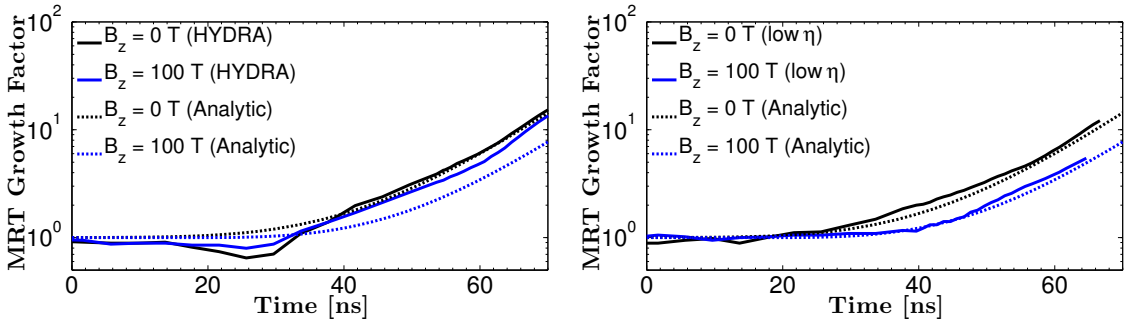

(a) Comparison of the planar model and 2D resistive MHD simulations with $B_z = 0, 100$ T for the growth of 400 μm perturbations.

(b) Comparison of the planar model and 2D ∼ideal MHD simulations with $B_z = 0, 100$ T for the growth of 400 μm perturbations.

Figure 2.17: Growth comparison of MRT in the presence of a strong axial magnetic field using resistive and ideal MHD.

and the agreement is observed to be excellent between the simulation and analytic calculation. When significant resistivity is present the magnetic field lines are no longer frozen into the aluminum, hence bent field lines need not relax the aluminum when the field lines themselves relax. Thus the magnetic tension can be reduced simply by magnetic diffusion, which reduces the efficacy of stabilization of MRT by field line bending. The magnetic diffusion time scale was estimated to be 5×10^7 s^{-1}. Over 70 ns, the magnetic field decays to $\exp\left[-(1/2) \times (5 \times 10^7) \times (70 \times 10^{-9})\right] = 0.174$ of the original value. The magnetic tension is reduced by a factor of $(0.174)^2 = 0.0303$, i.e., as if $B_z \approx 0$, explaining the HYDRA results shown in Fig. 2.17 for both 0 T and 100 T applied axial magnetic field.

While overall, not a particularly surprising result, the extent of the reduction of MRT stabilization is somewhat surprising. Of course, there are very few ways to combat these resistive effects to achieve better MRT stabilization other than completely turning most of the liner to conductive plasma or slowing the azimuthal magnetic field diffusion wave heating the liner. As mentioned though, 100 T is somewhat beyond any current technological capabilities for MagLIF-like implosions, so this problem merely serves as a benchmarking one. It may also be possible to flux compress an initially uniform axial magnetic field by a thin shell or foam located at a larger radius

to achieve larger fields at the liner surface [66]. The implications of a finite resistivity for feedthrough stabilization will be discussed later in this chapter.

As the last additional proof that the axial magnetic field has very little impact on the evolution of MRT for the wavelengths considered, synthetic radiographs for $B_z = 0, 10, 100$ T are shown in Fig. 2.18 at 65 ns. The obvious feature for increasing axial

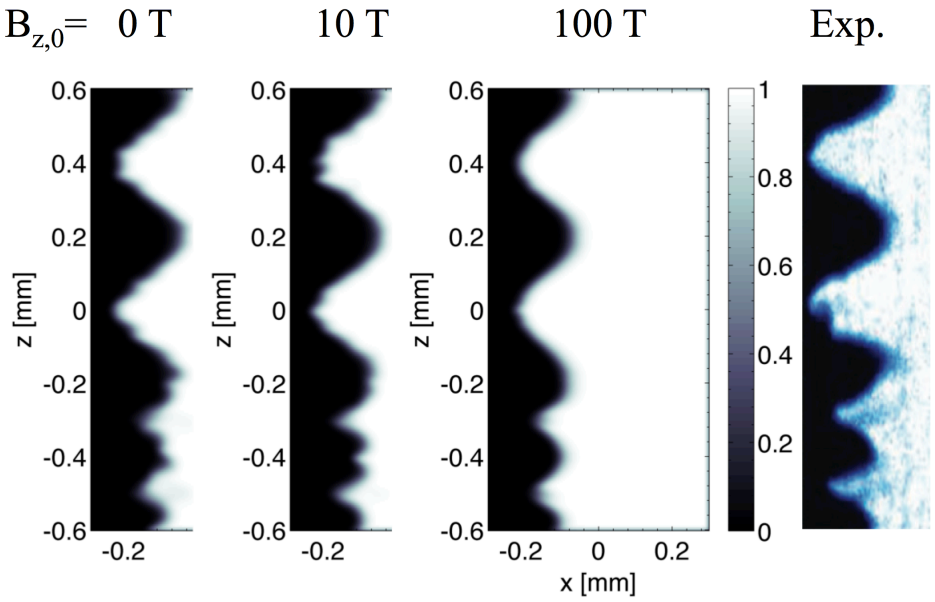

Figure 2.18: Synthetic radiographs compared to Sandia experiments by Sinars et al. [51] ($B_z = 0$) for increasing axial magnetic field strength in the simulations at 65 ns.

magnetic field strength is that short wavelength modulation of the larger wavelength structure is reduced and nearly vanishes at 100 T. This makes sense from what the analytic model predicts. Despite the finite resistivity, an axial magnetic field certainly seems to affect very short wavelengths. The 400 μm and 200 μm modes of course, look very much the same and have nearly unnoticeable differences in amplitude. Chapter 3 will investigate the effect of an axial magnetic field on shorter wavelengths in high convergence cylindrical targets that use only surface roughness. With some idea of how the planar model performs with regard to MRT growth, the focus is next turned to feedthrough of MRT.

2.4.3 Feedthrough in seeded liner experiments

The previous sections have focused on the growth of MRT on the exterior surface of a seeded liner. This section now focuses on the inner surface of the liner, where feedthrough is expected to be observed. Of course, as can be seen in the experimental radiographs by Sinars et al. [51], the opacity of aluminum is too high for 6.151 keV x-rays to image the inner surface. While this is less of an issue for beryllium (until high convergence), the focus will remain on aluminum, since all previous simulations have been based on this material. The implicit assumption will be that since HYDRA models MRT well, the feedthrough should also be well modeled. There will be no experimental evidence to back up this claim.

The seeded liners used in the previous section will also be used here. Thus, the feedthrough factor for the 200 and 400 μm perturbations is quite small. $F(400\ \mu\text{m}) = 0.01$ which has the implication that rippling on the inner surface will only become appreciable after significant time or MRT growth. However, an interesting result is obtained when the amplitude of the ripple on the inner surface is plotted as a function of time using the exact configuration of Sinars et al. [51]. Measuring the ripple amplitude in this case is straightforward as the interface nodes are Lagrangian. There is slight expansion of the interface zones due to the shock transmission at the interface, but nonetheless, the Lagrangian position of the nodes, well defines the surface. The amplitude of the ripple for a particular wavelength is just the maximum radius minus the minimum over the appropriate axial extent. Figure 2.19 shows a comparison of the 2D HYDRA data along with the analytic result using the planar model using Eqs. 2.59-2.60. The agreement is far from favorable. The reason for the large discrepancy is due to the shock compression of the liner, by the current drive. While the incompressibility condition holds well for the perturbation growth on the exterior of the liner, the presence of a shock in the interior of the liner invalidates that assumption. The shock carries the initial perturbation on the exterior liner surface

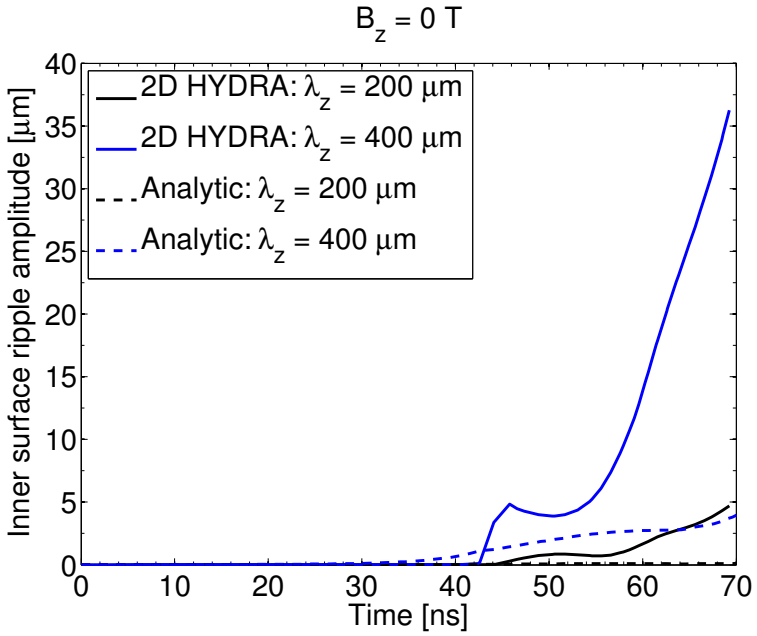

Figure 2.19: Growth of the 200 and 400 μm perturbations on the inner surface of a 292 μm thick liner driven by the Z-machine current pulse of Fig. 2.8.

to the inner surface in a finite time ($\sim$ 40 ns). While the ripple on the shock decays as it moves through the liner, qualitatively similar to feedthrough becoming smaller for larger thickness, the ripple does not decay as fast as feedthrough predicts. This leads to a substantial ripple on the inner liner surface. This effect will be discussed in greater detail in Chapter 4 (which will concentrate on the inner liner surface), but suffice to say, the shock ripples the liner inner surface more strongly than feedthrough predicts. Additionally, the subsequent growth of the ripples on the inner liner surface does not continue exponentially in time, as would be observed if feedthrough were the source of the amplitude increase. This is more apparent for 400 μm, but the scaling in time is roughly linear, a signature of what is known as the post-shock Richtmyer-Meshkov instability [68][69]. This will also be explored further in Chapter 4. In order to better compare 2D simulation and analytic theory, it is easiest to reduce the strength of the shock by modifying the load current.

A well known technique to do this, is to isentropically compress the liner [37].

By definition no shock is produced and such a pulse also reduces the shock heating of the liner inner surface. The method to determine an appropriate drive current to produce isentropic compression is not so simple but has nonetheless been done in experiments by Martin et al. [37] at Sandia. Perfect isentropic compression is not needed for feedthrough comparisons as will be shown, only significant reduction in shock strength such that the exponential evolution in time of feedthrough can dominate the evolution. The general feature for such a current pulse, as compared the shock compression pulse, is a lengthening of the rise-time of the current pulse. This serves to keep the compression waves launched in the liner from overlapping, as opposed over taking of the earlier launched waves by the later launched waves. Hence, the characteristics of the waves must not intersect in order to achieve isentropic compression. If the current rises too quickly, these characteristics intersect and a shock is generated.

A sample empirically determined current pulse that achieves this is shown in Fig. 2.20; note the increased pulse length but could still be used on Z. The peak current is of less importance since the most interesting feedthrough effects occur before this. As shown in the previous section, linear theory also begins to breakdown near peak current as the MRT amplitude becomes large. To test analytic theory, four 2D simulations were run each with a different wavelength seeded on the liner exterior: 200, 400, 800, and 1500 μm (all included two wavelengths per simulation except the 1500 μm case which used just one). This covers a wide range of feedthrough factors, from $10^{-4} \rightarrow 0.3$. The result of the four simulations using the new current drive is shown in Fig. 2.21. Plotted is the normalized amplitude of the corresponding ripple wavelength on the liner inner surface. The dashed lines correspond to the analytic solution for feedthrough and the solid curves are the 2D HYDRA results. The results are overall excellent, though for the agreement here, the thickness used in the feedthrough calculation had to be reduced by 15 % indicating an effectively, thin-

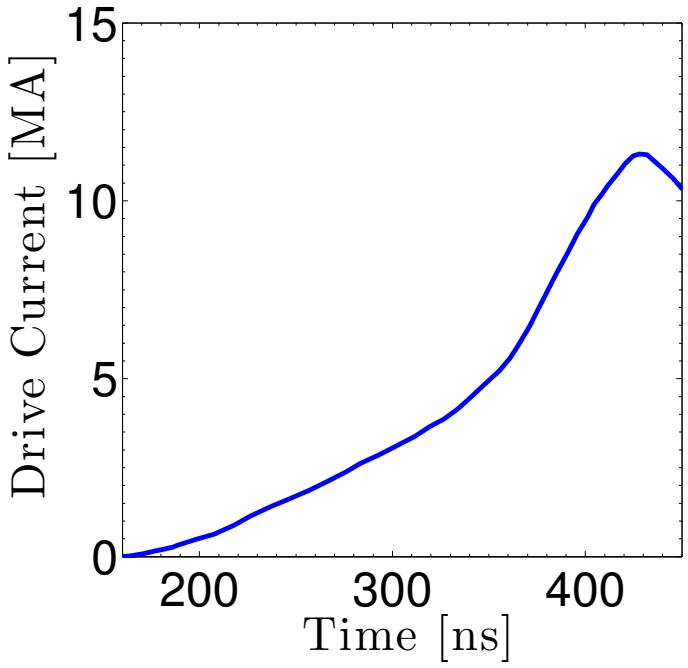

Figure 2.20: Empirically determined current pulse achieving low shock strength.

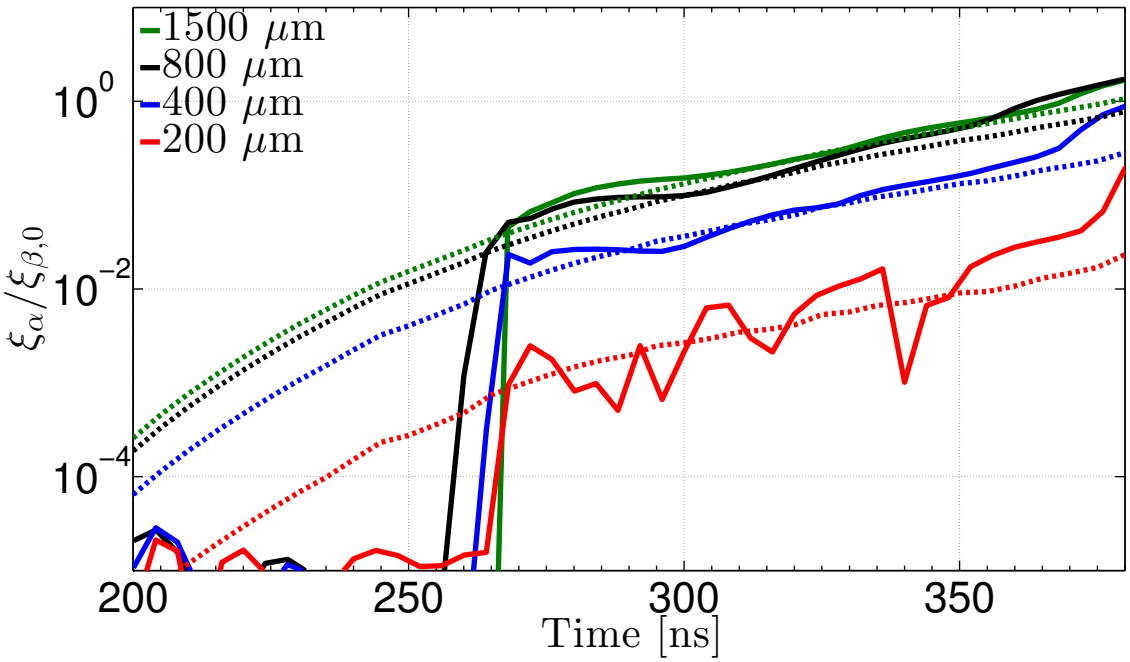

Figure 2.21: Evolution of inner liner surface for four different seeds on the liner exterior. The analytic calculation is shown as the dashed line, while the HYDRA simulations are the solid curves.

ner liner. Nevertheless, exponential-in-time scaling is observed which corresponds exactly to the scaling predicted by the feedthrough model. While most of the wavelengths show very smooth behavior after the 'shock', the 200 μm case has the smallest feedthrough, and is considerably more noisy due to the radial resolution required to measure it. Note that a weak shock may still exist, but the propagation speed (and corresponding breakout time) is only slightly greater than the ambient sound speed in aluminum. A perfectly isentropically compressed liner would still exhibit some finite delay time until feedthrough begins, limited by the sound speed of the material. In the incompressible theory used, the sound speed is effectively ∞. Despite the delay time, the feedthrough theory still shows excellent agreement. In essence, we have found that feedthrough, propagating at or near the sound speed of the material, is very well approximated by our incompressible feedthrough factor. This platform instills a good deal of confidence in studying feedthrough based on these results, so once again, the next most interesting addition to the problem is an axial magnetic field.

As shown in the previous section, as well as in the earlier figures (Fig. 2.2-2.4), looking at the scaling of feedthrough with an axial magnetic field, an axial magnetic field on the order of the drive magnetic field (field providing the acceleration) is needed to provide a noticeable effect (see Figs. 2.3,2.4). In a real experiment, this is accomplished by compressing the axial magnetic field via the imploding liner [54][55][38][39]. The seeded liners, however, do not survive long enough to compress the field sufficiently, due to the initial seed of the large amplitude perturbations. Thus, once again, an unreasonably large initial axial magnetic field is used for the following study with initial seeds. For the current pulse described by Fig. 2.20, the drive field is on the order of a couple hundred Tesla, thus a suitable axial field is also a couple hundred Tesla. Important to note though, is that achieving $B_z \approx B_\theta$, in unseeded liners, is not unreasonable at high convergence [54][55][38][39]. Additionally,

at higher convergence MRT typically develops to characteristic wavelengths varying between 500 μm and 1 mm. So the results presented next, while principally a sample problem, are still intended to simulate reality, to a degree. We also know that the 100 T field does not strongly affect the long-wavelength growth of MRT. Though it does reduce growth of shorter modes (Fig. 2.18), these modes do not feedthrough anyway because their feedthrough factor is so small. Meanwhile, Fig. 2.3 showed feedthrough reduction even for very little field bending at the exterior (note: $k\Delta \sim 3$).

A set of 2D HYDRA simulations were run for both 400 and 800 μm seeded wavelengths with $B_z = 0,\ 100,\ 200$ T. The 800 μm mode is the most dangerous to feedthrough but also the least affected by the axial field. For the following cases, the inner surface ripple amplitude is normalized by the null case where $B_z = 0$ T, $\xi_{\alpha,0}$. Thus, $\xi_{\alpha,B_z}/\xi_{\alpha,0}$ is the ratio of the ripple amplitude with an axial magnetic field to without. This directly shows the magnitude of the reduction in ripple amplitude by the axial magnetic field. The normalized amplitude of the ripple on the inner liner surface is plotted as a function of time, first for the 800 μm perturbation (Fig. 2.22). On average, the 100 T field reduces the amplitude by 25 % and the 200 T field reduces the amplitude by roughly 60 %. Included in Fig. 2.22 is also a 2D simulation using artificially low resistivity, as was done in the MRT study with an axial magnetic field. While ideal MHD again over-predicts the reduction in amplitude of the ripple, in this case, the magnetic field has a much larger effect on the inner surface. This qualitatively agrees with what was seen early on in Fig. 2.3. More importantly, for larger axial magnetic field, even considering real resistivity values, substantial reduction in the ripple amplitude is observed even at 800 μm. This is a highly encouraging result as the more pristine the inner liner surface in a liner implosion, usually the better. The 400 μm case shows even better results, shown in Fig. 2.23. This is also expected since magnetic field line bending (tension) better stabilizes shorter wavelengths. The 200 T case actually exhibits oscillation in this scenario, which is the source of the

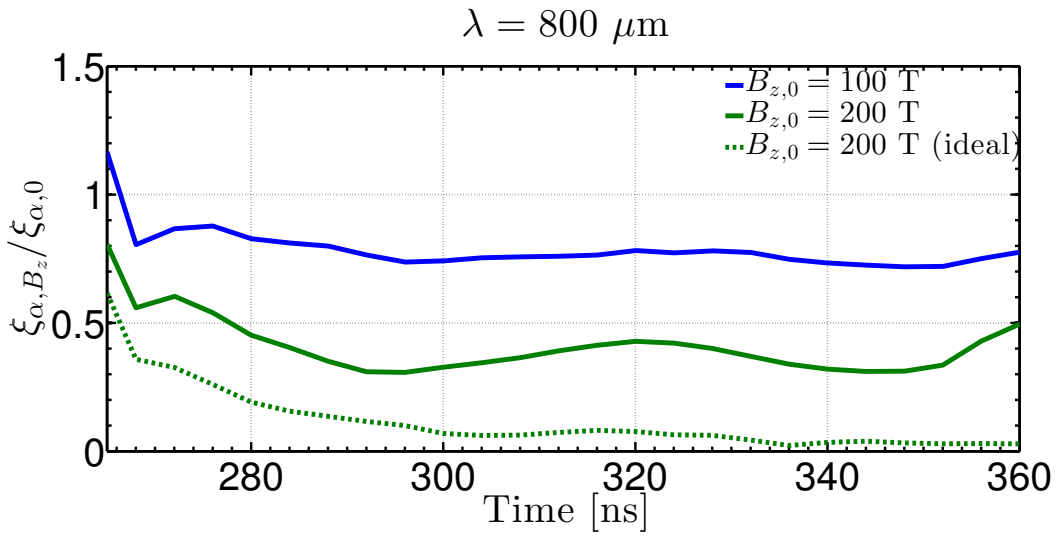

Figure 2.22: Evolution of inner liner surface for an 800 μm axial wavelength perturbation including two different axial magnetic field strengths. The ideal calculation again uses an artificially large and constant resistivity in the simulation.

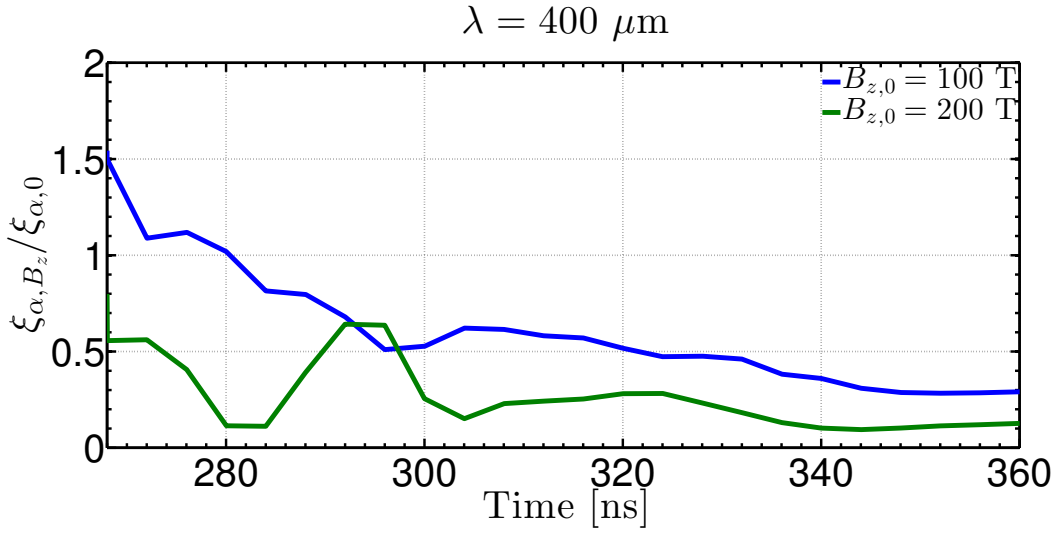

Figure 2.23: Evolution of inner liner surface for a 400 μm axial wavelength perturbation including two different axial magnetic field strengths.

ripple between 280 and 300 ns. This oscillation damps quite quickly and the ripple on the inner surface becomes quite small. The liners in these simulations also showed marginally lower overall resistivity, which may help contribute to these key results.

In the final section of this chapter, the planar model will be applied to scenarios where an axial magnetic field is highly compressed to illustrate further the importance of the above results.

2.4.4 Temporal evolution of surface ripples and application to magnetic flux compression platforms

This section will feature extensive use of Eqs. 2.59-2.60 to accomplish three things: (1) examine the evolution of MRT from various initial surface spectra, (2) evaluate the evolution of the feedthrough surface when ripples are already present, and (3) determine the extent of feedthrough reduction via flux compression.

2.4.4.1 Growth of MRT from arbitrary surface perturbations

In almost any real target, there are a large number of very short wavelength perturbations on the target surface due to the production of the target itself. These perturbations vary by material, but wavelengths are typically on the order of 10s of micron with amplitudes ranging from 100s of nanometers to a few micron [51] (aluminum is typically smoother than beryllium). According to RT scaling these short wavelengths grow the fastest. Two examples are shown next to illustrate this effect using $k_y = 0$ and $k_z > 0$. Figure 2.24 shows the result of two calculations using two different initial surface spectra, $f_0(k_z)$. Figure 2.24(a) uses a Gaussian shape for f_0, centered about 100 μm, while Fig. 2.24(b) uses an initially flat profile (500 nm). Figure 2.24 uses $g(t)$ from the usual 1D HYDRA simulation (Fig. 2.11(b)) to calculate the evolution of the these spectra according to Eqs. 2.59-2.60 over 85 ns. Each color is separated by 5 ns in time. In both cases it is clear, that the shorter wavelengths can

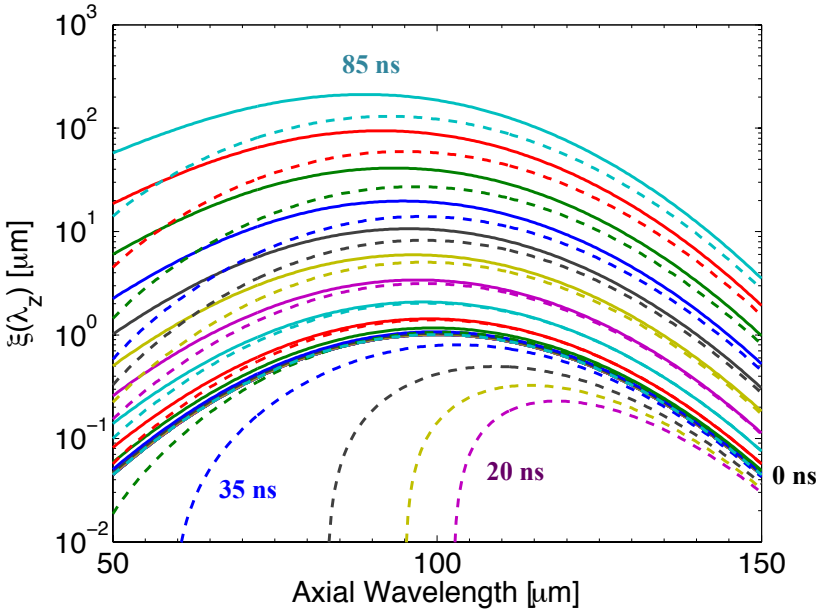

(a) RT evolution of an initially Gaussian axial wavelength spectrum in wavenumber space over 85 ns beginning at $t = 0$. Each color is separated by 5 ns in time. **The dashed curves were calculated using $B_z = 10$ T**, which show reduced growth. Note that the initial spectral distribution is defined by the lowest solid curves. The dashed curves that fall below the lowest solid curves are initially stabilized by the axial magnetic field.

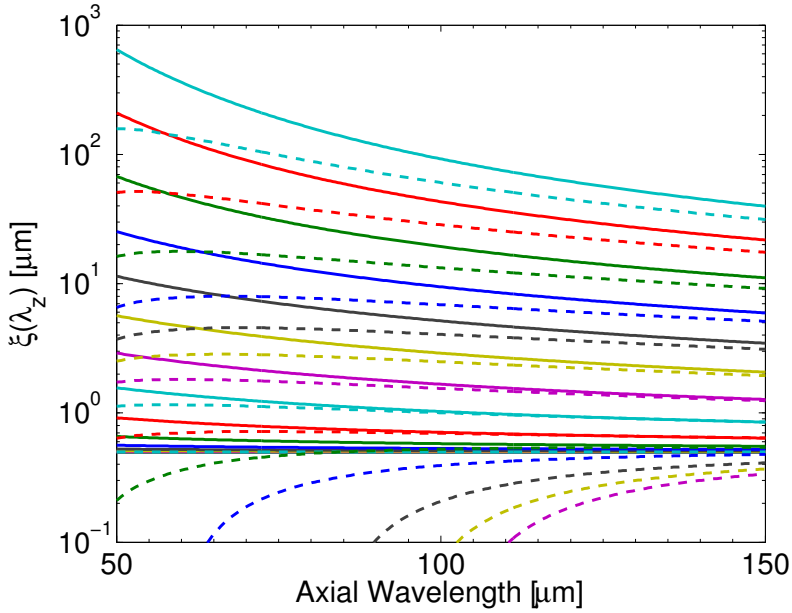

(b) RT evolution of an initially flat axial wavelength spectrum in wavenumber space over 85 ns beginning at $t = 0$. Each color is separated by 5 ns in time. **The dashed curves were calculated using $\mathbf{B_z = 10}$ T**, which show reduced growth. The dashed curves that fall below the lowest solid curves are initially stabilized by the axial magnetic field.

Figure 2.24: Comparison of RT growth from different initial surfaces (different axial wavelength spectra). Dashed curves were calculated with $B_z = 10$ T. Time is increasing as the MRT grows.

quickly overtake any longer wavelengths initially present. The dashed curves show the same calculation with a constant $B_z = 10$ T that slows the development of short wavelength modes. Additionally, at early times ($t < 50$ ns), the mode amplitudes are reduced from their original amplitude (as in Fig. 2.16) for both spectra. By 85 ns, the shorter wavelengths dominate the growth unless the axial field is present. However, the amplitudes remain quite large whether there is an axial field or not. A well-known limitation of such a calculation is the assumption of linearity. The gain shown in Fig. 2.24 is certainly much too large for the shorter wavelengths. Without accounting for saturation and mode coupling, the shorter wavelengths grow without bound which is not physical. A simple solution to this problem is to simply turn off the growth of short wavelengths once their amplitude has reached the traditional $\sim \lambda_z/10$ or use the Haan saturation model [73]. Nonlinear processes, however described, may turn short wavelengths to longer wavelengths that grow slower.

In the next set of simulations, to give the long wavelengths an advantage, a Gaussian, peaked at 3 mm with a large tail to short wavelengths, was used as the initial spectrum. The initial spectrum is the bottom (lowest amplitude) curve in Fig. 2.25. To understand the impact of the axial field, this spectrum is evolved according to the 1D HYDRA profile deduced growth rates for two cases, with and without a 10 T axial magnetic field. In these cases, the axial magnetic field is fixed at this value. Figure 2.25 shows the unnormalized evolution of the spectrum for the both the unmagnetized (solid) and magnetized case (dashed). At $t = 0$ the two curves ($B_{z,0} = 0$ T, $B_{z,0} = 10$) begin with the exact same spectrum . As time increases the MRT grows, with the shorter wavelength's growth being reduced the most by the 10 T magnetic field, then each color curve steps by 10 ns. The differences between the solid ($B_z = 0$ T) and dashed ($B_z = 10$ T) curves for the shortest wavelengths show the unmagnetized to grow faster while the long wavelengths are minimally different. The sloped nearly horizontal line in Fig. 2.25 at short wavelengths, shows when the

short wavelengths reach $\lambda_z/10$ and are artificially stopped from growth. Since the short wavelengths initially present on targets are most affected by the axial magnetic field, it seems possible that the axial field can affect the later time MRT structure by interfering at early times. The physical picture may then be that the axial magnetic field is able to slow the nonlinear generation of longer wavelengths since the short wavelengths do not grow quite as quickly. Though the degree to which this can occur is difficult to estimate based on the results of the 2D HYDRA simulations including an axial magnetic field, showing finite resistivity playing a role in reducing this stabilization mechanism. Also important to note is that the perturbations are stabilized to different degrees in the $y \sim \theta$ direction. This can be investigated more thoroughly in 2D simulations and eventually, 3D simulations.

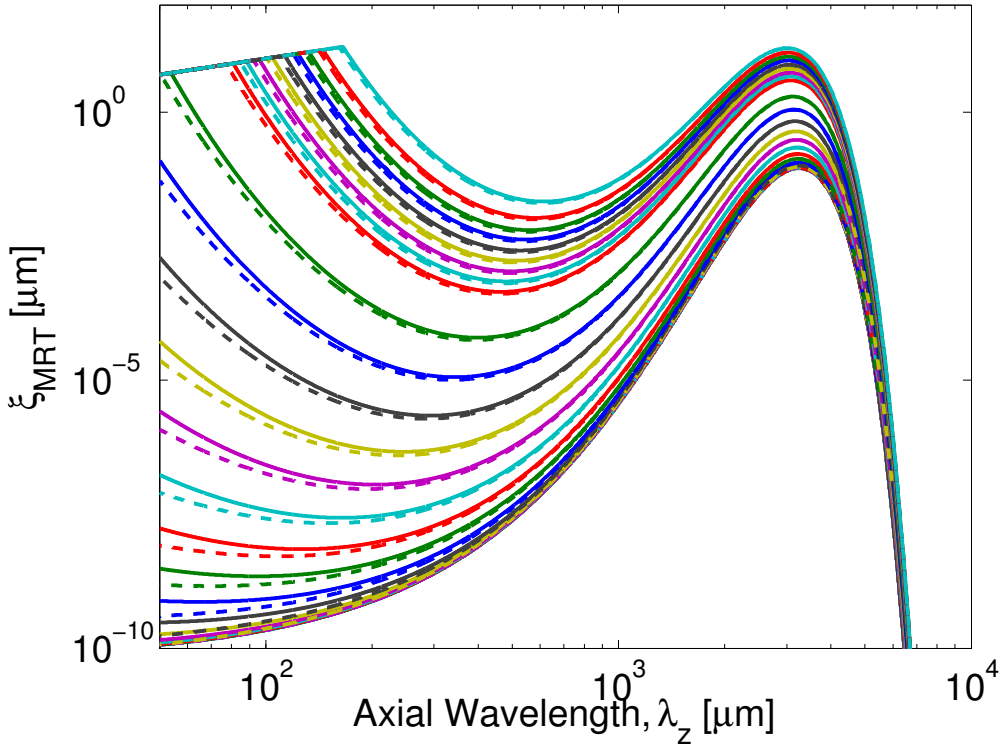

Figure 2.25: An initially gaussian spectrum peaked at 3 mm is evolved using our MRT growth rates, with and without a 10 T axial magnetic field. The solid curves set $B_z = 0$ and the dashed use $B_z = 10$ T. Each color is separated by 10 ns. The mild difference in amplitude between the solid and dashed curves indicates the slower growth of the mode due to the axial magnetic field.

In Fig. 2.25, the total gain for the relatively long wavelengths observed in experiments (0.5 to 1 mm), independent of an axial field, is overall lower than expected. The initial amplitude at the peak ($\lambda = 3$ mm) is 0.1 μm and the amplitude after 140 ns is roughly 4 μm, yielding a gain of 40. For wavelengths around 700 μm, the gain is a much more violent and unrealistic 3×10^4. If the growth were completely linear, this would correspond to a 15 nm amplitude perturbation growing to 500 μm. Surface finish data from experimental targets shows that long wavelengths like 700 μm are not present at large amplitudes, if at all. *In general, it is difficult to obtain sufficient growth of long wavelengths from an initially unseeded liner amplitude without considering contributions from shorter wavelengths.*

2.4.4.2 Effect of ripple phase of two surfaces

Equations 2.59-2.60 are general enough to allow for different initial phase perturbations to be on the two liner surfaces. Two limiting cases are considered: (1) completely out of phase, where the peaks on one surface line up with the troughs on the other, and (2) completely in phase, where the peaks line up at the two surfaces, leading to a thick sinusoidal plasma slab. For these two cases, the phase is adjusted by the sign of ξ_{α_0} relative to ξ_{β_0}, where it will be assumed $\xi_{\beta_0} > 0$. Once again, the Sinars et al. [51] parameters are considered with $\lambda = 400$ μm (Fig. 2.26(a))and 1.5 mm (Fig. 2.26(b)). The α interface will be the surface experiencing feedthrough, while the β surface is the highly unstable MRT surface. The results of these three calculations is shown in Fig. 2.26 which displays the inner surface (feedthrough surface) as a function of time for the two different wavelength perturbations..

The results are very clear in showing that the relationship between the initial phase of the dominant MRT mode and the state of the feedthrough surface can be very important as well as wavelength dependent. While this is a highly idealized case, it can be imagined that once longer wavelength MRT has developed on the exterior

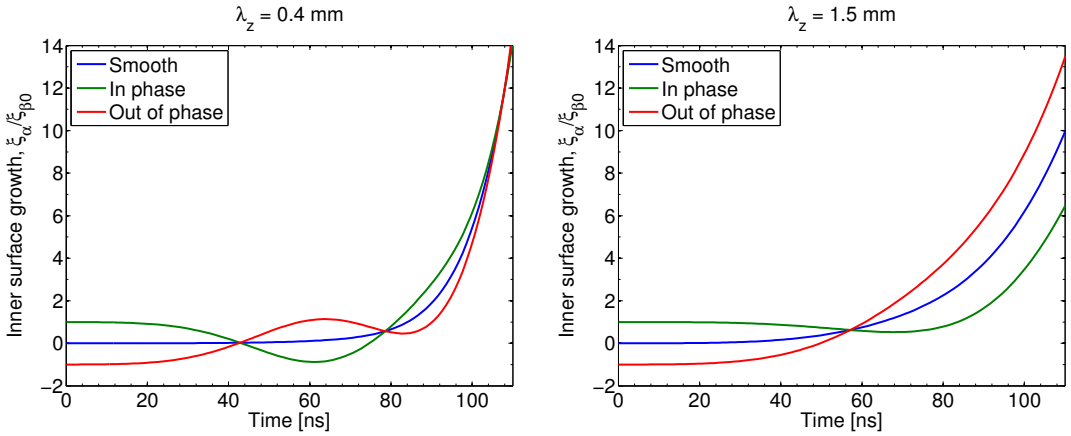

(a) Evolution of a 0.4 mm axial wavelength perturbation seeded on the inner surface (α) with phase relative to the 0.4 mm perturbation on the outer surface (β). $\xi_{\alpha 0} = 0$ corresponds to a smooth inner surface.

(b) Evolution of a 1.5 mm axial wavelength perturbation seeded on the inner surface (α) with phase relative to the 1.5 mm perturbation on the outer surface (β). $\xi_{\alpha 0} = 0$ corresponds to a smooth inner surface.

Figure 2.26: Inner and outer surface evolution of different combinations of 400 μm and 1.5 mm perturbations on the inner and outer liner surface.

of a target it can interact with any large scale perturbations on the inner surface that could have arisen from poor machining or other instabilities (such as Richtmyer-Meshkov instability that may be shock-excited during laser preheat in MagLIF, as in section 4.3 of this thesis). These results reveal the interesting possibility that there could be an optimum for the relationship between the two surfaces in order to minimize feedthrough. Meanwhile, the growth of MRT on the unstable surface remains independent of the state of the α surface for the 0.4 mm wavelength because of the small feedthrough factor; the analytic result for ξ_β similar to Fig. 2.26 would yield the same curves (not shown). This is confirmed by 2D HYDRA simulation results using the various seeds just discussed. The results for the MRT growth on the exterior are plotted in Fig. 2.27(a), clearly showing the MRT growth to be independent of the condition of the inner surface when the large perturbation is present. The inner surface evolution is plotted in Fig. 2.27(b). 2D HYDRA simulations show very similar qualitative behavior as found in the analytic results (Fig. 2.26). The smooth inner surface case has a medium amount of growth while the out of phase case shows the

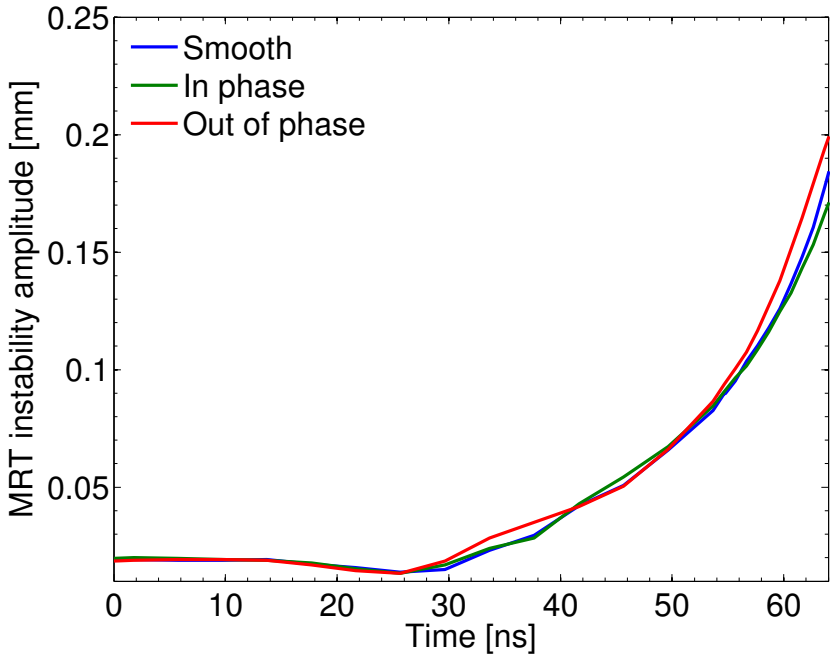

(a) Evolution of a seeded 400 μm perturbation on the outer liner surface for various seeding on the inner surface.

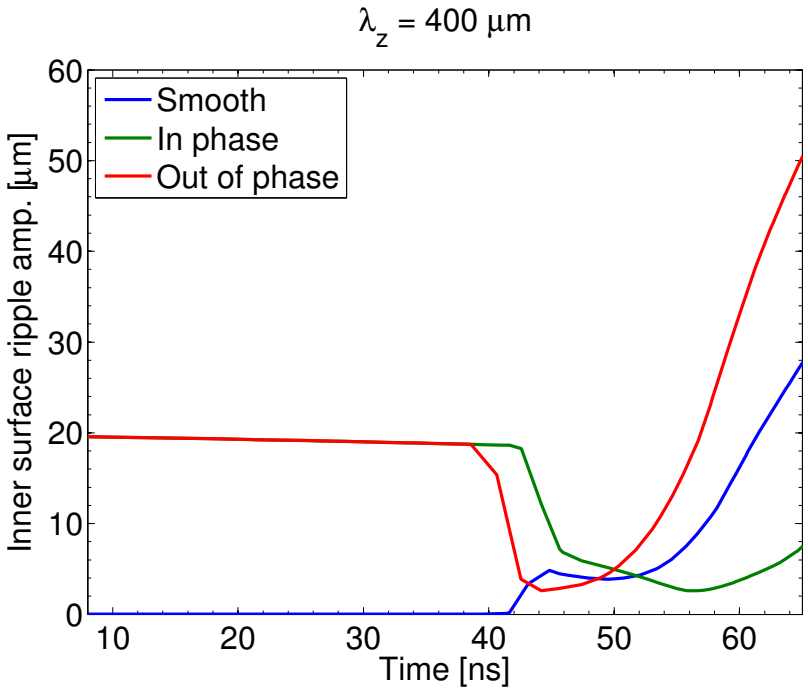

(b) Evolution of inner surface ripple with 400 μm wavelength at two phases relative to the 400 μm perturbation on the exterior. Smooth corresponds to seeding only on the liner exterior.

Figure 2.27: HYDRA 2D simulation of the inner and outer surface evolution of different combinations of 400 μm perturbations on the inner and outer liner surface.

most growth and the in phase case, the least amount of growth. Important to keep in mind for the 2D simulations is that the liner was still shock compressed. Despite this, the analytic model is still able to predict the qualitative behavior at both surfaces. A more detailed look at inner surface seeding will be presented in Chapter 4.

2.4.4.3 Magnetic flux compression and feedthrough reduction

Typically, generation of a large axial magnetic field from a small seed field is accomplished by compressing the flux contained in an imploding liner. The planar model is capable of describing this sort of compression as the axial magnetic field in the gas or vacuum region can take on an arbitrary value. In this way, an imploding liner will be modeled. Chapter 3 will be devoted to this sort of geometry and look at additional effects expected when $1/r$ or $1/r^2$ dependences are important. For now, it is again assumed that $k_z r$ is sufficiently large and consider the faster growing modes, which are aligned axially ($m = 0$ or $k_y = 0$). Long wavelengths are again the most important as they have the largest feedthrough factor so 1.5 mm is selected as the axial wavelength. Dominant wavelengths observed in experiment vary from 500 μm to 1500 μm. As these results are intended to directly illustrate effects relevant to experiment, a mild 10 T field is used as the initial seed field. 1D simulations have no difficulty running such a problem and can capture the flux compression that occurs. The large B_z generated is then used in the analytic planar model in region III, while region I remains at 10 T (no flux compression). These 1D HYDRA simulations then are fed into Eqs. 2.59-2.60. The reader is again reminded, that while this calculation is performed over the entirety of the implosion for a particular wavelength, nonlinear effects as well as magnetic diffusion can easily affect the overall amplitude after such a substantial time. However, the qualitative behavior introduced by the axial magnetic field is anticipated to remain. Results of the full calculation are shown in Fig. 2.28 which shows the growth factor for the inner surface, α, of the liner as a function of the

strength of the compressed axial magnetic field. The MRT growth factor is shown, in Fig. 2.28(a) as the blue curves.

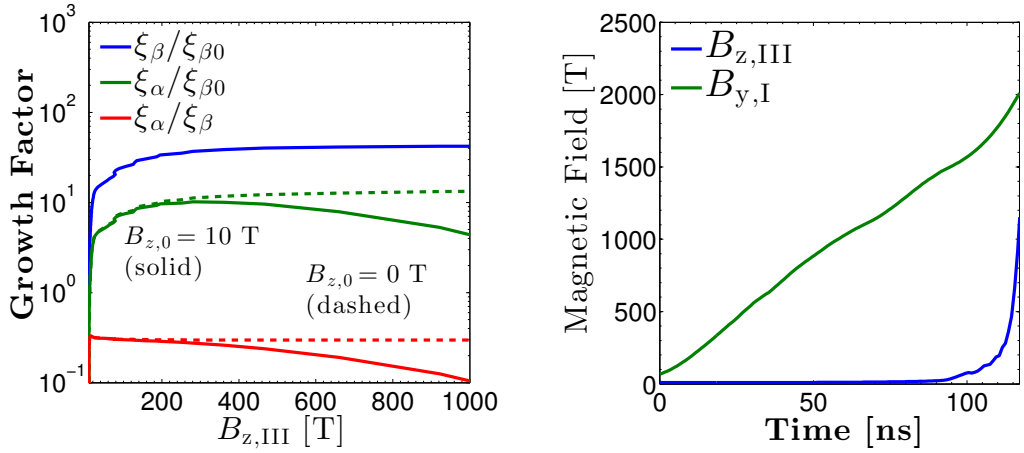

(a) Evolution of inner and outer liner surface for 1500 μm axial wavelength perturbation seeded on the β liner surface. The solid curves were generated with an initial 10 T field, and the dashed obtained with $B_z = 0$ T (no premagnetization).

(b) Magnetic field as a function of time. $B_{z,III}$ is the flux compressed field.

Figure 2.28: Comparison of inner surface rippling evolution of a 1.5 mm perturbation with and without an applied B_z.

The solid curves are for $B_{z,0} = 10$ T, while the dashed curves depict the zero axial field case. The evolution of the magnetic fields is shown in Fig. 2.28(b). As expected, the axial magnetic field does not impact the MRT growth on the outer surface, β, whereas for high flux compression, the feedthrough can be substantially reduced. From Fig. 2.28(b), this reduction only occurs past 100 ns, otherwise the azimuthal field is much too large (and hence acceleration). Nonetheless, during this short time period, the compressed axial magnetic field is able to significantly reduce feedthrough even for relatively long wavelengths. Shorter wavelengths are increasingly stabilized as shown earlier.

2.5 Concluding remarks

This chapter has presented an analytic planar model describing MRT growth and feedthrough in magnetically accelerated targets. The planar model makes use of 1D HYDRA simulation results as input to the model. This allows for a more realistic evaluation of the instantaneous MRT growth rate. Applying this method to seeded aluminum liner experiments by Sinars et al. [51] showed excellent agreement between the models, 2D HYDRA simulations and Sinars' experiments. The 200 μm wavelength seemed to be the lower limit for long time scale linear theory growth. Calculations also predict significant stabilization of MRT and feedthrough with a strong axial magnetic field. 2D resistive MHD simulations show the axial field has the strongest impact on feedthrough, while MRT stabilization could be much less effective due to diffusion of the magnetic field lines. Feedthrough in seeded targets is more challenging to understand when the target is shock compressed, but in the absence of a strong shock, analytic feedthrough theory agrees well with the 2D MHD simulations. Lastly, the analytic solutions combined with 1D HYDRA data were used to determine the temporal evolution of surface ripples of any wavelength. Significant reduction in feedthrough was shown to be present in flux compression platforms, while only modest reduction in MRT on the outer surface was shown. Feedthrough is also affected by any perturbations already present on the feedthrough surface. The relative phase between the initial MRT and feedthrough perturbations can strongly affect the overall evolution of the feedthrough surface. Ideally, the perturbations are in phase, to minimize feedthrough. A more detailed look at inner surface perturbations will be discussed in chapter 4.

While not without its limitations, the planar model contains a vast amount of information particularly when integrated with advanced 1D resistive, compressible, MHD simulations. The simulations help ameliorate the major weaknesses of the model particularly in constructing the equilibrium. 2D simulations help illustrate the

regimes the model works best and the model also provides some simple benchmarking problems for the 2D simulations. Non-sharp boundary solutions of the planar model are possible as well that can also help to mitigate the weaknesses of the model. Such solutions require numerical methods, which substantially increases the calculation time. On the other hand, the planar ODE is much better behaved than the equivalent in cylindrical geometry. This is of course true for the sharp boundary model as well. The next chapter will tackle one of the weaknesses of the planar model: cylindrical geometry, especially in the coupling of MRT, kink and sausage modes.

CHAPTER III

MRT Growth on a Cylindrical Liner

3.1 Introduction

The main reason for an analytic formulation of MRT in cylindrical geometry is that when $g = 0$ in the planar formulation, there is no unstable mode under the ideal MHD approximation. Plasma instabilities known as the sausage and kink modes were the killers of equilibrium Z-pinch fusion in the early days [70]. So in one of the most common scenarios in cylindrical geometry, even when $g = 0$ there exists the possibility of instability. This is purely due to the current carried in the cylindrical plasma column. Such instabilities are prime examples of MHD instabilities. Of course, an equilibrium Z-pinch is designed to operate and burn for very long time scales. This gives the MHD instabilities ample time to grow. Liner implosions occur on a much faster time scale ($\sim$ 100 ns) so the purpose of this work is to include sausage and kink effects on MRT so that the instability calculation is valid, whether or not g is zero (i.e., whether or not the liner is moving). For an ICF implosion, $g \approx 0$ occurs at two key times: (1) initially, as the current ramps up, the liner remains mostly motionless due to inertia and (2) near stagnation, when the liner stops accelerating inward and begins to decelerate on a hot fusion fuel. These two periods are certainly not restricted to ICF type implosions, but it is a particularly relevant and important application.

The calculations presented here build on the seminal work by Harris [6] and more recent work by Bud'ko [7]. Harris' early work focused on a thin shell model concentrating on MRT and only considered very specific magnetic field orientations. His description of feedthrough was similarly limited, and not presented in cylindrical geometry. The work by Bud'ko developed a MRT model for a thick liner, but the solutions of his equations relied heavily on a self-similar model of a liner implosion and subsequent numerical integration of the governing equations (of unknown derivation). The model that will be presented here will be completely analytic, allowing for substantially more insight than can be found in a purely numerical solution. The magnetic field geometry will be fairly arbitrary and the acceleration can be provided by any combination of magnetic and kinetic pressure (as in the planar model).

This section will develop in a manner similar to that of chapter 2. The governing equations will first be discussed and appropriate boundary conditions developed. An analytic dispersion relation will be derived along with the analytic feedthrough factor for the growing mode. Simple scaling of the dispersion relation will again be examined for a variety of magnetic field orientations and accelerations. The 1D HYDRA calculations will again support calculation of instability growth rates through a typical liner implosion, including magnetic flux compression.

3.2 Ideal MHD model of the Magneto-Rayleigh-Taylor Instability

3.2.1 Equilibrium

As in Chapter 2, we begin with defining the equilibrium. The equilibrium describes the balance of magnetic and kinetic pressures with the addition of an effective gravitational force that may be positive, negative or zero but assumed to be a constant. Similar to the planar model, an initial assumption is that the equilibrium radial

magnetic field B_r is zero and variations in the equilibrium quantities occur only in the radial variable, which is typical for a Z-pinch. The equilibrium magnetic field is then $\vec{B} = \langle 0, B_{\theta,0}(r), B_{z,0}(r) \rangle$. We assume that calculations are performed in the rest frame of the fluid so that $v_0 = 0$. Simplification of the $\vec{J} \times \vec{B}$ force, in cylindrical coordinates, leaves the magnetic pressure term and all but a single quantity from the magnetic tension term described by the last term on the left hand side of Eq. 3.2. In the radial direction,

$$\nabla p_0 = \vec{J} \times \vec{B} + \rho \vec{g} = -\frac{B_\theta(r)}{\mu_0} \frac{d}{dr} B_\theta(r) - \frac{B_\theta^2(r)}{\mu_0 r} - \frac{B_z(r)}{\mu_0} \frac{d}{dr} B_z(r) + \rho g, \tag{3.1}$$

$$\rightarrow \frac{d}{dr} \left[p_0(r) + \frac{(B_\theta^2(r) + B_z^2(r))}{2\mu_0} \right] + \frac{B_\theta^2(r)}{\mu_0 r} = \rho(r) g. \tag{3.2}$$

In this case, a positive g will correspond to inward radial acceleration ($g = -dv_r/dt$), and a negative g could correspond to deceleration due to stagnation in a Z-pinch or perhaps an exploding liner (Fig. 3.1). In general, Eq. 3.2 states that the pressure (kinetic + magnetic) is supported by the pressure due to gravity. For this work we will assume g is essentially uniform for the instantaneous equilibrium described above. We may assume that $p_0(r)$ is adjusted so that g = const. is an acceptable solution to Eq. 3.2 as in the planar model. 1D HYDRA simulations of beryllium and aluminum liners indicate this not unreasonable for the majority of the implosion. The generality of the equilibrium again allows for arbitrary distributions of ρ, $\vec{B}$, etc. which could come from a self-similar model as in Bud'ko et al.[7] or 1D simulations as will be the case for this work (for additional discussion of self-similar models for Z-pinches see Liberman et al.[21]). Such models can include additional physics not found in ideal MHD.

The equilibrium equation can be simplified for the rather general geometry shown in Fig. 3.1. This is an example of a three region problem, where for $0 < r < r_i$ there is a low density gas (fuel) with an embedded axial magnetic field (though either the

density or magnetic field may be zero in this region). The region $r_i < r < r_e$ contains the metallic liner with embedded axial magnetic field, and $r > r_e$ is a vacuum region containing only magnetic field. The prototypical sharp boundary model that will be used throughout the remainder of this chapter is depicted in Fig. 3.1. All three

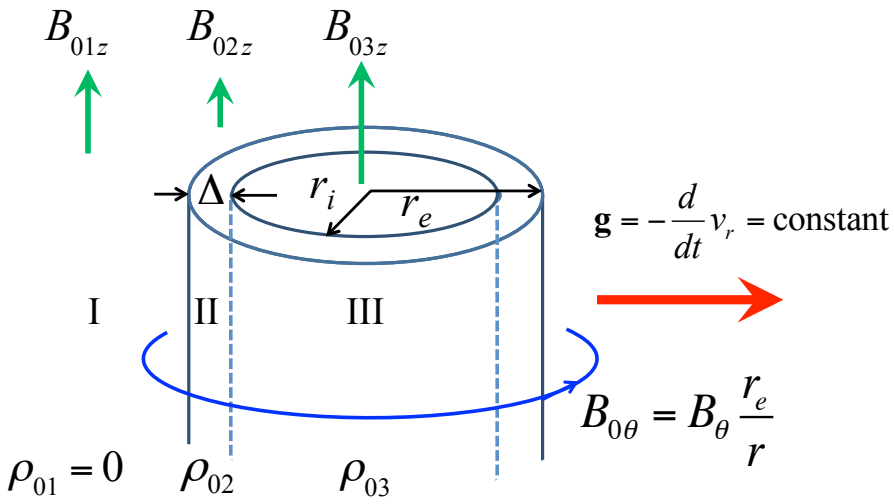

Figure 3.1: Three region sharp boundary model for cylindrical liners including arbitrary axial magnetic fields.

regions will allow an arbitrary constant axial magnetic field. Region I is assumed to be vacuum, so that $\rho_{01} \to 0$ and $B_{0\theta} = B_\theta r_e/r$. Regions II and III allow for arbitrary constant densities and assume that there is no diffusion of azimuthal field (B_θ is entirely confined to region I). In the limit that $r_i \to 0$ the plasma fills the entire cylinder and some simple solutions can be recovered that will be shown later on. The model can further be reduced to the equilibrium Z-pinch with an axial magnetic field. This is the classic case of a hot conducting plasma column confined by an azimuthal magnetic field ($r_i \to 0$) and is well known. Equation. 3.2 can be integrated across the plasma-vacuum interface ($r_\beta = r_e$ in nomenclature similar to Chapter 2). This produces a two-region sharp boundary model. The result of the integration across

the outer surface is given by Eq. 3.3

$$\frac{B_\theta^2}{2\mu_0} + \frac{B_{z,\mathrm{v}}^2}{2\mu_0} = \left(p_\mathrm{p} + \frac{B_{z,\mathrm{p}}^2}{2\mu_0}\right), \tag{3.3}$$

as the last two terms of Eq. 3.2 do not contribute as the integration is carried out across an infinitesimally thin region. In such a case, the plasma pressure is completely supported by the magnetic pressure if the axial magnetic fields in each region are the same. A more general equilibrium for a three region sharp boundary model is given by Eq. 3.4, obtained by applying the integral operator, $\int_{r_{i^-}}^{r_e^+} \mathrm{d}r$ to Eq. 3.2 assuming $\rho(r)$ is constant between r_i and r_e. The sharp boundary model assumes the axial magnetic fields and densities are constant in each region. The axial current is assumed to flow completely on the outer liner surface under the ideal MHD approximation.

$$\rho_0 \Delta g = \left[\frac{B_\theta^2}{2\mu_0} - \left(p_\mathrm{fuel} + \frac{B_{z,\mathrm{fuel}}^2}{2\mu_0}\right)\right]. \tag{3.4}$$

In Eq. 3.4 and hereafter, the vacuum (I), liner (II), and fuel (III) regions, are defined with subscripts, v, l, and f, respectively. Here, when B_θ is large, $g > 0$ which corresponds to an implosion driven by an azimuthal magnetic field. Once the compressed fuel pressure or axial magnetic field exceeds the azimuthal magnetic field pressure, the acceleration switches sign ($g < 0$) and the equilibrium describes deceleration. Generally, g is dominated by either the large driving pressure, or the strong pressure in the fuel (be it magnetic or kinetic). In order to determine the analytic instability growth rates for an imploding (or stationary) cylindrical liner a sharp boundary model will again be considered.

The largest difference between the cylindrical formulation and planar model, is the $1/r$ dependence for the azimuthal magnetic field. This means that the magnetic pressure gradient is weakened (strengthened) as the outer interface expands radially outward (inward), which is the physical mechanism driving the sausage and kink

mode. This behavior comes directly solution of Ampère's law for an axial current confined to the liner surface and is markedly different than the planar case where $B_y = \text{const.}$ (neglecting any anode/cathode or edge effects). The implication is that, even if there is no gravity, it is energetically favorable to move down the gradient (increasing r). Such a feature is often used to understand the physical origin of the sausage and kink modes in Z-pinches [70] and will be briefly discussed later. As a final point, this model also describes RT in cylindrical geometry where $B_\theta = B_{0z} = 0$ (currents are small, as in radiation driven implosions, where g is not required to be driven from magnetic pressure gradients). We next linearize the ideal MHD equations.

3.2.2 Linearization and Perturbation

The linearization procedure for the ideal MHD equations in cylindrical geometry is no different than in planar geometry but the results are far more complicated. We begin with the same equations as in Chapter 2. They are quoted next, for convenience, first for the force law,

$$\rho \frac{\partial^2 \vec{\xi}}{\partial t^2} = -\nabla p_1 + \vec{J}_0 \times \vec{B}_1 + \vec{J}_1 \times \vec{B}_0 + \rho_1 \vec{g}, \tag{3.5}$$

$$\begin{aligned} -\omega^2 \vec{\xi} = &-\nabla p_1 + (\nabla \times \vec{B}_0) \times [\nabla \times (\vec{\xi} \times \vec{B}_0)]/\mu_0 \\ &+ \{\nabla \times [\nabla \times (\vec{\xi} \times \vec{B}_0)] \times \vec{B}_0\}/\mu_0 + \rho_1 \vec{g}. \end{aligned} \tag{3.6}$$

The equilibrium quantities are denoted by a subscript of $'0'$. We shall assume $e^{i\omega t - i(m\theta + kz)}$ dependence for the perturbation quantities, designated with subscript $'1'$. Squares and higher powers of perturbation quantities are ignored. Besides the form of the equilibrium the difference between planar and cylindrical geometry enters only in the form of the gradient in Eq. 3.6. The "frozen-in law", Faraday's law, and Ampère's law in linearized form are used to express the perturbation magnetic field, $\vec{B}_1$ and

current density, $\vec{J}_1$ in terms of the perturbation displacement, $\vec{\xi}$:

$$\vec{E}_1 = -\vec{v}_1 \times \vec{B}_0 = -i\omega\vec{\xi} \times \vec{B}_0, \tag{3.7}$$

$$\vec{B}_1 = -\nabla \times \vec{E}_1/(i\omega) = \nabla \times (\vec{\xi} \times \vec{B}_0), \tag{3.8}$$

$$\nabla \times \vec{B}_1 = \mu_0 \vec{J}_1. \tag{3.9}$$

The above equations are applicable to the plasma regions. In vacuum, the magnetic field perturbations take the general form:

$$\vec{B}_1 = \nabla\phi, \tag{3.10}$$

$$\nabla \cdot \vec{B}_1 = 0 \Rightarrow \nabla^2\phi = 0. \tag{3.11}$$

Additionally, the incompressible condition ($\nabla \cdot \vec{\xi} = 0$) is again used as the equation of state (EOS). The linearized continuity equation defines the perturbation density, ρ_1 in terms of $\vec{\xi}$,

$$\frac{d}{dt}\rho_1 = -\nabla \cdot (\rho_0 \vec{v}_1), \tag{3.12}$$

$$\rho_1 = -\vec{\xi} \cdot \nabla\rho_0. \tag{3.13}$$

Up until this point everything is the same as in planar geometry. The link to planar coordinates involves letting $k_y = m/r$. Formally, the planar limit is obtained by letting $m \to \infty$ and $r \to \infty$ so that $k_y = m/r =$ constant. The perturbation is then $e^{i\omega t - i\vec{k}\cdot\vec{x}} = e^{i\omega t - i(m\theta + kz)}$. As with the planar case the value of $\omega(m, k)$ determines the growth or decay for a particular mode (m, k). A growing mode is found when there is a solution for ω where Im(ω)< 0. The application of the spatial Fourier transform to Eq. 3.6 removes the remaining spatial derivatives and what is left is three equations for the vector components of $\vec{\xi}$ in terms of ω, m, k, and the equilibrium quantities. Unlike planar geometry, the equations are significantly more complex. Nevertheless,

the three unknowns with three equations can be combined into one governing ODE for the radial displacement, ξ_r.

The most straightforward way to determine this relation begins with Eq. 3.7 by calculating the cross product, $\vec{E}_1$ can be directly substituted into Faraday's law, Eq. 3.8. This completely defines $\vec{B}_1$ in terms of $\vec{\xi}$. Calculating the curl of $\vec{B}_1$ then completely determines $\vec{J}_1$ in terms of ξ (Eq. 3.9). These results were then substituted into Eq. 3.5 to give Eq. 3.6. ρ_1 is defined in terms of ξ by Eq. 3.13 and also substituted into the force law. The incompressible condition then closes the set of three vector equations by determining ξ_z in terms of ξ_r and ξ_θ (see Eq. 3.23 below). Though, the equations are long and cumbersome, the procedure to reduce these equations down to one is easy to describe.

1. Taking the $\hat{z}$ component of the linearized force law (Eq. 3.6) and substituting the incompressible condition for ξ_z (Eq. 3.23), p_1 can be determined in terms of ξ_r and ξ_θ.

2. The $\hat{\theta}$ component of the linearized force law is then simplified using the incompressible condition for ξ_z and substituting the value of p_1 just determined. ξ_θ is then determined in terms of ξ_r.

3. The incompressible condition is substituted into the $\hat{r}$ component of the force law, followed by p_1 from (1) and lastly ξ_θ from (2). This leaves ξ_r (and its derivatives) defined purely by the equilibrium variables.

The remaining work is to cast the second order ODE in either the form of Eq. 3.14, or Eq. 3.15, or Eq. 3.16. Either form can be numerically integrated easily, however, Eq. 3.16 is much easier to work with when computing analytic derivatives. Equations 3.15 and 3.16 are directly related by expanding the derivative of Eq. 3.16. $A(r)$

can be recognized as $P(r)$ and $C(r)$ and $D(r)$ are related to $Q(r)$,

$$\frac{d^2}{dr^2}\xi_r = f(r, \vec{B}_0(r), \rho_0(r), g, m, k, \xi_r, \xi_r'), \tag{3.14}$$

$$A(r)\frac{d^2}{dr^2}\xi_r + C(r)\frac{d}{dr}\xi_r + D(r)\xi_r = 0, \tag{3.15}$$

$$\frac{d}{dr}\left[\frac{P(r)}{r}\frac{d}{dr}\left(r\xi_r(r)\right)\right] + Q(r)\xi_r(r) = 0. \tag{3.16}$$

The third formulation, Eq. 3.16, resembles the form of the planar ODE albeit with a much more complicated $Q(r)$. $P(r), Q(r)$ are functions of the equilibrium quantities and perturbation wavevector. They are defined next

$$P(r) = \frac{\mu_0 r^2\omega^2\rho_0 - (mB_{0,\theta}(r) + krB_{0,z})^2}{(k^2r^2 + m^2)}, \tag{3.17}$$

$$\begin{aligned} Q(r) =& \frac{2B_{0,\theta}'(B_{0,\theta}(m - kr)(kr + m) + krmB_{0,z})}{r\left(k^2r^2 + m^2\right)} \\ &+ \frac{2kmB_{0,\theta}B_{0,z}'}{k^2r^2 + m^2} \\ &+ \frac{\beta B_{0,\theta}B_{0,z} + \alpha B_{0,\theta}^2 + \kappa B_{0,z}^2}{r^2\left(k^2r^2 + m^2\right)^2} \\ &- \frac{4k^2B_{0,\theta}^2(mB_{0,\theta} + krB_{0,z})^2}{\left(k^2r^2 + m^2\right)\left((mB_{0,\theta} + krB_{0,z})^2 - \mu_0 r^2\omega^2\rho_0\right)} \\ &+ \mu_0 g\rho_0' - \mu_0\omega^2\rho_0, \end{aligned} \tag{3.18}$$

$$\alpha = k^4r^4\left(m^2 + 2\right) + 2k^2r^2m^2\left(m^2 - 2\right) + \left(m^2 - 2\right)m^4, \tag{3.19}$$

$$\beta = 2krm\left(k^4r^4 + k^2r^2\left(2m^2 - 3\right) + m^2\left(m^2 - 1\right)\right), \tag{3.20}$$

$$\kappa = k^2r^2\left(k^2r^2 + m^2\right)^2, \tag{3.21}$$

where a prime denotes differentiation with respect to r. This formulation for $\xi_r(r)$ remains sufficiently general to determine $\omega(m, k)$ for any arbitrary equilibrium profile $(\rho_0(r), B_{0\theta}(r), B_{0z}(r))$ with appropriate boundary conditions. It is important to note that the equilibrium pressure profile, $p_0(r)$ does not enter Eq. 3.16, so that $p_0(r)$ may be adjusted to satisfy the equilibrium condition, Eq. 3.2, as in planar geometry.

We now have the same sort of boundary value problem (BVP) as in the planar case. As an example of suitable boundary conditions consider that $r\xi_r|_{r=0}$ ($\xi_r(r=0)$ is finite) and $\xi_r(r=r_{\text{wall}})=0$ at a wall boundary (if there is a wall). Numerical solution of Eq. 3.16 requires sufficiently smooth equilibrium profiles so that the derivatives behave reasonably well, otherwise no ODE solver can provide a reliable result for ω or the feedthrough. Shooting methods or finite differencing can again be used to solve the BVP however, solving the ODE itself is more difficult (takes longer) due to the increased complexity of the equation. To continue the analysis of the solution of this equation, the sharp boundary model will be invoked. Beginning with the derivation of the appropriate boundary conditions linking the three regions shown in Fig. 3.1. Region III will be referred to as the fuel or fill gas region (often with subscript $'f'$), Region II will be the liner region (often with subscript $'l'$), and Region I will be the vacuum region (often with subscript $'v'$). Alternatively, as in the planar formulation of Chapter 2, the dispersion relation can be obtained directly from integration of Eq. 3.16 across the interfaces at r_i and r_e. This method is outlined in Appendix B.

We now consider the sharp boundary model with constant ρ_0 and B_{0z} in each region. Starting with regions III (fuel) and II (liner), the spatial derivatives in ρ_0 and $B_{0z}(r)$ and $B_{0\theta}$ terms are zero (no axial current in fuel or liner). Following the procedure outlined to determine Eq. 3.16, ξ_z and ξ_θ are

$$\xi_\theta(r) = -\frac{im\left(\xi_r(r)+r\xi_r'(r)\right)}{k^2r^2+m^2}, \tag{3.22}$$

$$\xi_z(r) = \frac{-m\xi_\theta(r)-i\left(\xi_r(r)+r\xi_r'(r)\right)}{kr}. \tag{3.23}$$

Equation 3.31 (below) is the perturbation plasma pressure (which is also given in terms of ξ_r) and used in combination with Eqs. 3.22-3.23 to evaluate the $\hat{r}$ component

of the force law. This yields a single ODE for ξ_r, i.e., Eq. 3.16 simplifies to read,

$$\xi_r'' = \frac{\xi_r(r)\left(k^4r^4 + k^2r^2\left(2m^2+1\right) + m^2\left(m^2-1\right)\right) - r\left(k^2r^2+3m^2\right)\xi_r'(r)}{r^2\left(k^2r^2+m^2\right)}. \quad (3.24)$$

Perhaps the best feature of this equation is that it has an exact analytic solution given by Eq. 3.25 [9],

$$\xi_r(r) = C_1 I_m'(kr) + C_2 K_m'(kr), \quad (3.25)$$

where I_m and K_m are, respectively, the modified Bessel functions of order m of the first and second kind, a prime denotes a derivative with respect to the argument and C_1 and C_2 are arbitrary constants. The relatively simple expressions, Eqs. 3.22, 3.23, 3.25, 3.30, and 3.31 are obtained relatively easily for the liner region, region II, with the assumption that $\rho_{02} = \text{const.}$, $B_{02z} = \text{const.}$, and $B_{0\theta} = 0$ in Eqs. 3.6 and 3.13.

These solutions would no longer be valid in region I if $\rho_{01} > 0$ (since we have assumed the vacuum solution for $B_{0\theta}$). However, for the current sharp boundary model with $\rho_{01} = 0$, the vacuum solutions are required, which are given by Eqs. 3.10-3.11. ϕ is determined by the solution to the Laplacian in cylindrical coordinates which is just the modified Bessel's functions. The I_m solution is thrown out as it is not bounded as $r \to \infty$. If a conducting wall at some larger radius were included, I_m must be kept. The appropriate boundary condition would then be a perfect conductor at the wall. Proceeding on the infinite domain, for region I ($r > r_e$), the vacuum solutions are then

$$\phi(r,\theta,z,t) = \phi_0 \frac{K_m(kr)}{K_m(kr_e)} e^{i\omega t - im\theta - ikz}, \qquad r > r_e. \quad (3.26)$$

which then directly determines $\vec{B}_1$ in terms of ϕ_0 as

$$\vec{B}_{1,v} = \nabla \left(\phi_0 \frac{K_m(kr)}{K_m(kr_e)} e^{i\omega t - i(\theta m + kz)} \right), \qquad r > r_e. \tag{3.27}$$

ϕ_0 must then be determined by enforcing the perfect conductor condition at the liner/vacuum interface. This will be discussed in the following section.

3.2.3 Boundary Conditions

The boundary conditions for each region are very similar to the planar formulation. At the fuel-liner and liner-vacuum interface continuity of total pressure is enforced. Secondly, the normal component of the perturbation magnetic field at these two surfaces must be zero to satisfy the ideal MHD condition. In Appendix B, an alternate derivation of the boundary conditions is presented using the governing differential equation, Eq. 3.16, however, both methods yield the same final expressions.

3.2.3.1 Region III: Fuel Region

The fuel/fill gas region (region III) occupies $0 \leq r \leq r_i$. As stated earlier, for the sharp boundary model, the density and axial field are assumed uniform and that no azimuthal field is present (no current in the region). The validity of this assumption is briefly discussed next. While it is assumed that both the gas and magnetic field compress uniformly, 1D HYDRA MHD simulations have shown that the density and axial magnetic field can build up near the inner liner surface. This can be imagined as a snowplow like effect where the material and field cannot get out of the way of the liner fast enough as the liner implodes onto it. For constant values in the fuel, this means we may either take the average field and density or peak values. Peak values tend to overestimate such physics as field line bending stabilization, while the average value may underestimate it. The build-up of axial field also induces strong

currents in the azimuthal direction at the interface that can enhance expansion of the inner liner surface into the fuel region. Of course, this is accounted for in the 1D simulations but the net effect makes the averaging procedure more challenging. Nonetheless, the sharp boundary model solution is continued.

As stated earlier, the eigenfunction solution for region III is derivative of the modified Bessel's functions. The first boundary condition for this region requires regularity at the origin which eliminates the K'_m solution, leaving, (c.f. Eq. 3.25)

$$\xi_r(r) = \xi_\alpha \frac{I'_m(kr)}{I'_m(kr_i)}, \qquad r < r_i \tag{3.28}$$

where ξ_α will be used to determine the feedthrough factor, as with the planar model. Next, this region must be matched to region II so that ξ_r is continuous at the inner interface, $r = r_i$. The first matching condition requires continuity of total pressure across the interface, which includes, the kinetic, magnetic, and gravitational pressures. This is determined by linearizing the equilibrium condition, which is then evaluated just within the fuel region (r_i^-), together with the perturbation pressure and set equal to the same expression evaluated just within the liner region r_i^+. The result of the total perturbation pressure reads:

$$\begin{aligned} &\left[p_{1,f} + \left(\vec{\xi} \cdot \nabla \vec{B}_{0,f} + \vec{B}_{1,f} \right) \cdot \frac{\vec{B}_{0,f}}{\mu_0} + \rho_f g \xi_r \right]_{r=r_i^-} \\ &= \left[p_{1,l} + \left(\vec{\xi} \cdot \nabla \vec{B}_{0,l} + \vec{B}_{1,l} \right) \cdot \frac{\vec{B}_{0,l}}{\mu_0} + \rho_l g \xi_r \right]_{r=r_i^+} \end{aligned} \tag{3.29}$$

where the subscripts f correspond to the fuel/fill gas side of the interface and subscripts l correspond to the liner side. The expression for the perturbed magnetic field is $B_1 = \nabla \times \left(\vec{\xi} \times \vec{B}_0 \right)$ in the two regions as derived earlier. Of course $\vec{B}_{0,f} = \langle 0, 0, B_{z,f} \rangle$. Since $\vec{B}_1$ is defined in terms of ξ_r for regions III and II, no additional boundary conditions are needed. By construction, the perturbed magnetic field sat-

isfies the perfect conductor condition (plasma is perfect conductor). Lastly, the perturbed plasma pressure can be written as

$$p_1 = i\rho_0\omega^2\xi_z/k, \tag{3.30}$$

$$p_1 = \frac{r\omega^2\rho\left(\xi_r + r\xi_r'\right)}{m^2 + k^2r^2}, \tag{3.31}$$

where $\rho = (\rho_f, \rho_l) = (\rho_{03}, \rho_{02})$ depending upon the region. Equation 3.31 is determined from substitution of Eq. 3.23 and then Eq. 3.22. As a reminder, these expressions are valid only when derivatives of ρ_0 and B_{0z} in the radial direction are zero together with $B_{0\theta} = 0$. With all of the terms in Eq. 3.29 determined, the matching condition between regions III and II can be derived.

Equation 3.29 using Eq. 3.31 gives a restriction on the slope of the eigenfunction at the inner boundary in region II in terms of the eigenvalue and equilibrium quantities. This is possible because we have also used the condition $\xi_r(r_\alpha^-) = \xi_r(r_\alpha^+)$ which ensures continuity of velocity (since we have neglected viscosity, the fluids should remain in contact). Combining the above results, the boundary condition for total pressure continuity (Eq. 3.29) across the fuel/liner interface reads (defining $\frac{d}{dr}\xi_r|_{r=r_i^+} = \frac{d}{dr}\xi_l|_{r=r_i}$)

$$\begin{aligned}\frac{d}{dr}\xi_l|_{r=r_i} = &\frac{\xi_\alpha\left(k^2r_iB_{z,f}^2 - k^2r_iB_{z,l}^2 + \mu_0\left(\rho_l - \rho_f\right)\left(gk^2r_i^2 + gm^2 + \omega^2r_i\right)\right)}{r_i^2\left(k^2B_{z,l}^2 - \mu_0\omega^2\rho_l\right)} \\ &+ \frac{\xi_f'(r_i)\left(k^2B_{z,f}^2 - \mu_0\omega^2\rho_f\right)}{k^2B_{z,l}^2 - \mu_0\omega^2\rho_l},\end{aligned} \tag{3.32}$$

where ξ_f is the region III eigenfunction solution (fuel/fill gas region) and ξ_l is the region II eigenfunction solution (liner region). The derivatives, ξ_r' arise from Eq. 3.31. This boundary condition can be further simplified using the derived solution in region

III given by Eq. 3.28

$$\frac{d}{dr}\xi_r|_{r=r_i^+} = \frac{\xi_\alpha\left(-B_{z,l}^2k^2r_i+\nu_0+B_{z,f}^2k^2r_i+\mu_0(\rho_l-\rho_f)\left(g\left(k^2r_i^2+m^2\right)+r_i\omega^2\right)\right)}{r_i^2\left(B_{z,l}^2k^2-\mu_0\rho_l\omega^2\right)}, \tag{3.33}$$

$$\nu_0 = \frac{kr_i^2(I_{m-2}(kr_i)+2I_m(kr_i)+I_{m+2}(kr_i))\left(B_{z,f}^2k^2-\mu_0\rho_f\omega^2\right)}{2(I_{m-1}(kr_i)+I_{m+1}(kr_i))}. \tag{3.34}$$

While this is seemingly a complicated expression, the form of the RHS is no more than $\xi_\alpha f$ where f is just a constant depending upon the equilibrium values and the mode under consideration. This completes the derivation for one boundary condition for region II, given by Eq. 3.33. The second and final boundary condition is determined via matching the liner/vacuum interface, described next.

3.2.3.2 Region I: Vacuum Region

In the vacuum, there is no material or currents, so there is only magnetic pressure as discussed earlier. $\vec{B}_1$ is given by, $\vec{B}_{1v} = \nabla\phi$ (determined by Eq. 3.26) in region I for $r_e < r < \infty$. The total pressure balance across the outer liner surface ($r = r_e$) then reads (compare Eq. 3.35 with Eq. 3.29; for the vacuum region, $p_{1,v} = \rho_v = 0$)

$$\left[p_{1,l}+\left(\vec{\xi}\cdot\nabla\vec{B}_{0,l}+\vec{B}_{1,l}\right)\cdot\frac{\vec{B}_{0,l}}{\mu_0}+\rho_l g\xi_r\right]_{r_e^-} = \left[\left(\vec{\xi}\cdot\nabla\vec{B}_{0,v}+\vec{B}_{1,v}\right)\cdot\frac{\vec{B}_{0,v}}{\mu_0}\right]_{r=r_e^+}. \tag{3.35}$$

$\vec{B}_{1,l}$ remains the same as in the liner region, defined in terms of the perturbation displacement. $\vec{B}_{1,v}$ is given by the Bessel function solution, Eq. 3.27, with unknown coefficient. The boundary condition on the magnetic field must now be explicitly invoked. A perfect conductor requires that the magnetic field to be aligned along the conducting surface (magnetic field normal to the perturbed surface is zero). Mathe-

matically this is stated as:

$$\vec{B}_1 \cdot \hat{n}_0 + \vec{B}_0 \cdot \hat{n}_1 = 0, \tag{3.36}$$

where $\hat{n_0} = \hat{r}$ is the unperturbed surface normal of the conducting plasma. Expanding the perturbed field, this can be re-written as

$$\left[\vec{B}_{1,v} + \vec{\xi} \cdot \nabla \vec{B}_{0,v}\right] \cdot \hat{n}_0 + \vec{B}_{0,v} \cdot \hat{n}_1 = 0. \tag{3.37}$$

The perturbation normal vector reads

$$\hat{n}_1 = -\frac{\nabla \xi_r}{|\hat{r} + \nabla \xi_r|} = -\nabla \xi_r = -\left\langle \xi_r', -\frac{im\xi_r}{r_e}, -ik\xi_r \right\rangle, \tag{3.38}$$

which may be obtained by linearizing the normal vector to the rippled β-surface, $r_\beta = r_0 + \xi_r(\theta, z)$, i.e., $\hat{n} = \nabla r_\beta / |\nabla r_\beta| \equiv \hat{n_0} + \hat{n_1}$. The expression, Eq. 3.36, then links the unknown coefficient, ϕ_0 with the equilibrium magnetic field in the vacuum, $\vec{B}_{0,v} = \langle 0, B_\theta r_e/r, B_{z,v} \rangle$ and the perturbation displacement, $\xi_\beta = \xi_r(r = r_e)$ as shown by Eq. 3.39

$$\phi_0 = \frac{i\xi_\beta K_m(kr_e)(kr_e B_{z,v} + B_\theta m)}{mK_m(kr_e) + kr_e K_{m-1}(kr_e)}. \tag{3.39}$$

With ϕ_0 determined, $\vec{B}_{1,v}$, given by Eq. 3.27, can be plugged back into Eq. 3.35 and worked into a similar form as Eq. 3.33,

$$\frac{d}{dr}\xi_l|_{r=r_{e^-}} = \frac{\xi_\beta\left(-k^2 r_e^2 B_{z,l}^2 + (k^2 r_e^2 + m^2)(B_\theta^2 + i(\phi_0/\xi_\beta)(kr_e B_{z,v} + B_\theta m)) + \mu_0 r_e \rho_l (gk^2 r_e^2 + \omega^2 r_e + gm^2)\right)}{r_e^3\left(k^2 B_{z,l}^2 - \mu_0 \omega^2 \rho_l\right)}, \tag{3.40}$$

where ϕ_0/ξ_β is given by Eq. 3.39. Now, with the boundary conditions at both interfaces determined, the eigenfunction in region II is fully defined. All that remains is another fair amount of algebra. As a reminder, Eqs. 3.32 and 3.40 are also obtained with a slightly different derivation method in Appendix B.

3.2.4 Sharp Boundary Model Solutions

The eigenfunction solution has already been determined in the liner region, as given by Eq. 3.25. Recalling the requirement that $\xi_r(r)$ be continuous, the solution in region II can be written directly in terms of ξ_α, ξ_β which are the unknown coefficients in the boundary conditions,

$$\xi_r(r_i) = \xi_\alpha = C_1 I'_m(kr_i) + C_2 K'_m(kr_i), \tag{3.41}$$

$$\xi_r(r_e) = \xi_\beta = C_1 I'_m(kr_e) + C_2 K'_m(kr_e). \tag{3.42}$$

This effectively determines, the coefficients C_1 and C_2 in terms of ξ_α and ξ_β. The derivative of $\xi_l(r)$ can then be computed from Eq. 3.25 and matched with the two boundary conditions Eqs. 3.33 and 3.40. As with the planar model, these two boundary conditions become two equations of the familiar form

$$\xi_\alpha = \xi_\beta F_{a,b}(\omega^2) \tag{3.43}$$

where ω is a function of m, k and the equilibrium quantities and F is again interpreted as the feedthrough factor from the β-surface ($r = r_e$) to the α-surface ($r = r_i$) for a particular eigenvalue, ω. The dispersion relation is again found by setting $F_a = F_b$. In this case, the result is not so easily written down. The structure of the dispersion

relation remains the same though, a quadratic equation in ω^2.

$$A\omega^4 + B\omega^2 + C = 0 \tag{3.44}$$

$$= A\sigma^2 + B\sigma + C = 0 \tag{3.45}$$

The dispersion relation also has the same property where ω^2 is real-valued. In the limit $\rho_{03} = \rho_f = 0$, the analytic expression for A, B, and C were obtained independently by Dr. Peng Zhang which was recorded in Eqs. 3-4 of our joint paper [9]. Dr. Zhang and I have done extensive checks that out independent numerical results are virtually identical. Most of the dispersion plots in the liner modes section such as Fig. 3.3 can be directly compared to those figures in [9], generated by Dr. Zhang. Most importantly, the coefficients A, B, C of Eq. 3.44 are remarkably complicated and thus makes our checks all the more important. Note that in [9] the small signal dependence, $e^{i\omega t+im\theta-ikz}$ was used so that the $m = 1$ mode is the most unstable kink mode. In this thesis $e^{i\omega t-im\theta-ikz}$ is used and $m = -1$ is the unstable kink mode. Unless results are explicitly stated for both $m = \pm 1$, reference to the $m = 1$ mode corresponds to the fastest growing kink mode, or kink-MRT mode.

3.3 Some solutions of the cylindrical sharp boundary model

In general, the dispersion relation and feedthrough factors are very complicated. In order to limit human error, the two roots for $\sigma = \omega^2$ were imported directly from Mathematica to Matlab. For reference, σ_1 takes up 140 lines in the standard Matlab editor. To begin discussion on the properties of the equations, some simple examples will be provided. The first place to begin is with the classic sausage and kink modes, which are well-known.

3.3.1 Traditional Sausage and kink modes

The traditional sausage and kink modes of a plasma column are special cases of the dispersion relation just derived, where $r_i \to 0$. This turns the problem into a two region sharp boundary problem with well known solutions when $g = 0$. The important point here being that instabilities can still exist despite $g = 0$ in this simple scenario. The pure sausage mode corresponds to $m = 0$ (pure referring to $g = 0$) and the kink, $m = \pm 1$ ($\pm m$ may have different growth rates with $m = -1$ being the dominant one with $J_z > 0$). The appropriate limit from the general dispersion relation is found by setting $r_i = 0$ with uniform B_z that may take on different (constant) values inside and outside the plasma. Additionally, B_θ is excluded from the plasma region. The analytic dispersion relation that results from these simplifications is given by

$$\frac{\omega^2}{k^2} = \frac{B_z^2}{\mu_0 \rho} - \frac{[kr_\beta B_{z,e} + mB_\theta(r_\beta)]^2}{\mu_0 \rho (kr_\beta)^2} \frac{I'_m(kr_\beta)K_m(kr_\beta)}{I_m(kr_\beta)K'_m(kr_\beta)} - \frac{B_\theta^2(r_\beta)}{\mu_0 \rho} \frac{I'_m(kr_\beta)}{kr_\beta I_m(kr_\beta)}. \quad (3.46)$$

For the sake of differentiating this case from the finite thickness case, take $r_\beta = r_e$. The primes indicate differentiation with respect to the quantity kr_β. While this is a fairly simple case, this dispersion relation illustrates many important aspects of the more general dispersion relation for a finite thickness liner, without the cumbersome algebra.

The necessary and sufficient condition for instability is $\omega^2 < 0$. With that in mind, the interpretation of Eq. 3.46 is then straightforward. The first term is stabilizing due to the axial magnetic field present in the plasma column. The mechanism of stabilization is the same as in the planar case; magnetic field tension prevents perturbation growth. The second term is also stabilizing, as the ratio of the Bessel functions is negative. This represents the $(\vec{k} \cdot \vec{B})^2$ term for the vacuum region which now includes magnetic field line bending in the azimuthal direction via the B_θ term. This stabilization term is also scaled by a geometrical factor in terms of the Bessel

function ratio, which has a limit of -1 for $kr_\beta \to \infty$ (the planar limit). The last term is something new due to the cylindrical formulation. The last term is destabilizing and is the source of the finite growth rate when $g = 0$. Note that unlike the stabilizing terms, there is very limited dependence on azimuthal mode number, m. Consider $B_z = B_{z,e} = m = 0$, then there is no magnetic field line bending and the only remaining term is the third in the RHS of Eq. 3.46. This is the growth rate for the sausage mode. Note that when considering the sausage mode, $m = 0$, therefore no azimuthal field line bending is present. The sausage mode grows because of the form of the magnetic pressure. At smaller radii, the magnetic pressure is higher (larger pinch force), while at larger radii the magnetic pressure is smaller. Thus, if a plasma element is displaced by $r-\delta$ the element feels a larger magnetic pressure (larger force) and continues to displace inward. Since the fluid is incompressible this requires fluid to move away from the constriction. Thus the plasma element displaced by $r+\delta$ continues outward since the force decreases with increasing radius. This is the essence of the sausage mode instability. The troughs $(r - \delta)$ of a sinusoidal perturbation are pushed inward, while the peaks $(r + \delta)$ expand outward. This is much like the physical basis behind MRT where system with a heavy fluid supported by a light fluid minimizes its potential energy via interchange of the heavy and light fluid elements (forming larger ripples from an initial ripple). A sufficiently strong axial magnetic field can of course suppress the sausage mode. The well-known result for tokamaks being $B_z > \sqrt{2}B_\theta$ to achieve stability to the sausage mode, may be obtained from the small kr_e limit of Eq. 3.46.

The kink mode is a slightly more interesting example. Consider again, $B_z = B_{z,e} = 0$ and $m = \pm 1$. For this case $m = \pm 1$ yields the same growth rate. The kink mode retains a stabilizing term that reduces the growth rate, but can never completely suppress the mode unless $k = 0$. Thus, the kink mode will have a smaller growth rate than the sausage mode in this case, even though the growth rate remains

relatively large. Adding a B_z can stabilize the kink mode to a certain extent, as is the case for the sausage mode. This is well known in the tokamak community as the Kruskal-Shafranov condition (stabilization of the kink mode) which is incredibly important to steady-state operation of a tokamak [22]. Stabilization occurs when

$$kr_\beta \frac{B_z}{B_\theta} > 1, \tag{3.47}$$

in the limit $kr_\beta << 1$. The LHS of Eq. 3.47 becomes the calculated tokamak safety factor, q, if we use $(1/R)$ for k where R is the major radius of the tokamak and r_β is the minor radius of the tokamak. Equation 3.47 then becomes $q = (r_\beta/R)B_z/B_\theta > 1$ for stability. However, with a non-zero kB_z term, the sign of m becomes important. The stabilizing term, the middle term on the RHS of Eq. 3.46, is maximized for positive m so the largest growing kink mode will correspond to $m = -1$. For the sake of simplifying the discussion, for the remainder of this work, any reference to the kink mode will use the fastest growing solution. One of the the most interesting features of Eq. 3.46 is the relative growth rate of the sausage and kink mode when an axial magnetic field is present. *This will be important later on, but the result is that the kink mode generally has a larger growth rate than the sausage mode when an axial magnetic field is included.* This makes sense from the tokamak perspective as well, since the sausage mode is typically stabilized before the kink mode. Most importantly, a similar result is obtained for a finite thickness liner as will become clear later. Thus, in MagLIF with a seeded axial magnetic field, the kink mode may dominate in the initial stage (similar to a tokamak), before the azimuthal magnetic field is ramped up from the current rise.

For larger values of m (short azimuthal wavelengths) the stabilizing term begins to dominate and eventually higher mode numbers are completely stabilized, assuming $B_\theta > 0$. As a Z-pinch typically has a very large azimuthal magnetic field throughout

an implosion, large m numbers are stabilized according to this model, leaving the major instability growth aligned more or less aligned with the z axis. For this reason the sausage and kink modes will be the main focus of this work. These robustly growing instabilities are also visible (most visible in beryllium at 6.151 keV) in many liner implosion experiments at Sandia [53][37][55]. This effect does have interesting consequences for laser-imploded cylinders where there is no strongly stabilizing azimuthal field for large azimuthal mode numbers. In such a scenario, we would anticipate more isotropic RT mode structure to develop.

Unlike a pre-seeded axial magnetic field that is initially uniform throughout the domain of the problem, the azimuthal magnetic field must first diffuse into the liner region. The current cylindrical model assumes this diffusion to be small on the timescales of interest (and exactly zero for ideal MHD). Nonetheless, as the field diffuses into the liner there is large competition between stabilization due to azimuthal field line bending, reduction of this stabilization because of a magnetic diffusion, and de-stabilization due to current present in the liner. This is a highly complicated scenario that will be addressed later via 2D simulations and additional calculations.

Thus far in these discussions, MRT itself has been left out. So as a final example of a simplified dispersion relation, again consider the sausage mode, setting $B_z = B_{z,e} = 0$ and include a finite g. The resulting dispersion relation is

$$\omega^2 = -k\left(\frac{B_\theta^2}{\mu_0 \rho_0 r_\beta} + g\right)\frac{I_1'(kr_\beta)}{I_0(kr_\beta)} \tag{3.48}$$

where the Bessel function ratio is always positive. If $B_\theta = 0$, Eq. 3.48 gives the result for pure MRT when $g > 0$. $g < 0$ provides a stabilizing influence. The major point however, is when there is a finite azimuthal field, the sausage mode is introduced and the instability growth rate increases. Similar behavior occurs for the kink mode. Thus, in cylindrical geometry, MRT growth rates can be enhanced in comparison to

planar geometry. The instability growth rate of the sausage and kink modes can also be considered to be enhanced by acceleration, if g is small. Additionally, the sign of g can again make the difference between a stable or unstable configuration. With these concepts in mind, growth rates for finite thickness liners are investigated in great detail next.

However, before moving on, it is important to note that the growth rate from Eq. 3.48, where $r_i = 0$, can be much different than the growth rate where $r_i > 0$ as in the next section. In other words, introducing even the slightest sized fuel region can change the behavior of the growth rates. Consider the deceleration (or explosion case) where $g < 0$. If there is no fuel region, only a filled column, this is a stable configuration for MRT. Now consider a finite fuel region at very small radius. When $g < 0$, an RT unstable interface is now present and this small radius interface is highly unstable. This is a dramatically different scenario than the filled column. As such, it is difficult to directly compare Eq. 3.48 to some of the dispersion curves that follow in the next section. Instead an asymptotic result will be given to better illustrate the difference between $r_i = 0$ and $r_i > 0$. These subtleties were corroborated in the numerical results in Dr. Zhang's independent calculations.

3.4 Liner modes

It was shown in the last section that current carrying instabilities known as the sausage and kink modes could increase MRT growth rates. A strong azimuthal field can also significantly stabilize large m modes, which is common to Z-pinches. For $B_z = 0$, the sausage mode has the largest growth rate for any k under nearly any circumstance, as it has the smallest amount of magnetic field line bending (none). When both B_z and B_θ are non-zero, axial kink modes generally have larger growth rates than the sausage mode. Lastly, the sign of g can significantly impact the stability of the system.

The aspect ratio for a liner is defined as the ratio of the liner's outer radius to its thickness,

$$AR = \frac{r_e}{\Delta} = \frac{r_e}{r_e - r_i}. \tag{3.49}$$

A typical value is $AR = 6$ for liner experiments on the Z-machine and is the point design for a MagLIF liner [12]. $AR = 1$ is the limit of filled column of plasma and $AR \to \infty$ is infinitely thin. The effective gravity for the following plots will be defined in terms of the driving magnetic pressure so that $g = g_{\max} = B_\theta^2/2\mu_0\rho_0\Delta$ (this assumes the fuel pressure is negligible, c.f. Eq. 3.4). When $|g|$ is maximized (including the stagnation phase in which the pressure in the fuel region is dominant in Eq. 3.4), we call the modes pure MRT modes. These modes with $g = |g|_{max}$ couple the current carrying modes with the MRT modes. When $g = 0$, the equilibrium condition requires that $p_{\text{III}} = B_\theta^2/2\mu_0$ where p_{III} is the total pressure in the fuel region so that the liner is motionless. The $g = 0$ case will be considered the pure sausage and kink modes that are not present in planar geometry. Since $|g|$ is typically between 0 and its maximum value, the mode is somewhere between pure MRT and pure sausage-kink mode.

For comparison with the previous section, where $r_i = 0$ for the filled column, the asymptotic growth rate for $k_z = 0$, $B_{0z} = 0$ for the liner sausage mode is presented (in the absence of an axial field) in Eq. 3.52. This form was calculated by using the small argument (small k_z) expansion in place of the full Bessel's functions I and K. The major details of this calculation are provided in the appendix B.

$$\omega^2 = -\frac{B_{0\theta}^2 r_i - g r_e \Delta\mu_0\rho_0 + |B_{0\theta}^2 r_i - g r_e \Delta\mu_0\rho_0|}{2r_e^2 r_i \mu_0\rho_0 \ln q}, \tag{3.50}$$

$$q = \frac{r_e}{r_i} = \frac{AR}{AR - 1}. \tag{3.51}$$

For direct comparison to the next section with normalized growth rates, the growth

rate can be re-written as

$$\bar{\omega}^2 = \frac{-1 + \bar{g}q - |1 - \bar{g}q|}{2 \ln q}, \tag{3.52}$$

$$\bar{\omega}^2 \equiv \omega^2 / (B_{0\theta}^2 / \mu_0 \rho_0 r_e^2), \tag{3.53}$$

$$\bar{g} \equiv g / (B_{0\theta}^2 / \mu_0 \rho_0 \Delta), \tag{3.54}$$

where $\bar{g} = 0.5$ for $g = g_{\max}$. The normalized growth rates using Eq. 3.52 are plotted as a function of aspect ratio in Fig. 3.2. The appropriate limit of $AR = 1$ is recovered for $k_z = 0$ which is $\omega = 0$ as expected by Eq. 3.48. Additionally, for finite thickness liners the reduced growth for $g > 0$ is observed. We next consider the results using

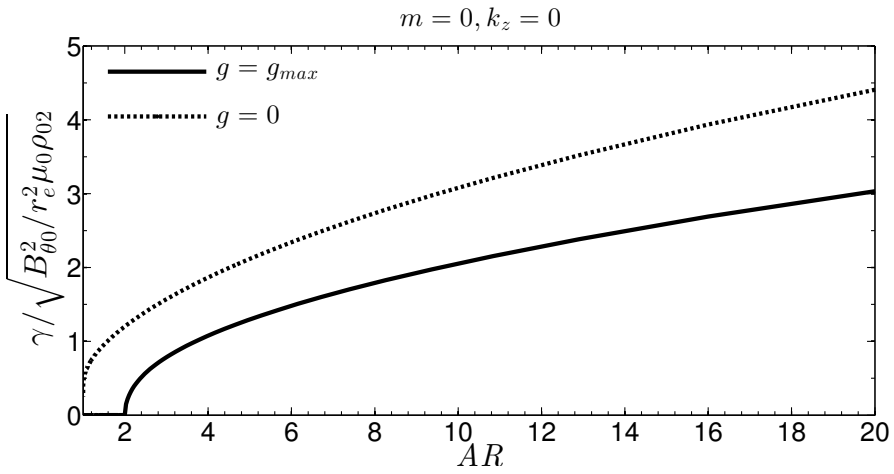

Figure 3.2: $k_z = 0$ limit for the sausage mode growth rate as a function of liner aspect ratio, AR.

the full analytic solutions.

As a direct analog to the previous section, a scan of the pure sausage and kink modes was performed for increasing axial magnetic field. The axial field in regions I, II, III was assumed equal and varied from 0 to $B_z = B_\theta$ to identify the points of marginal stability ($\omega = 0$) as function of axial field and wavenumber, for $g = 0$. Figure 3.3 shows the normalized growth rates for the two instabilities ($\bar{\gamma}$) on a logarithmic color scale for an $AR = 6$ liner. The jaggedness is purely an artifact of the

finite grid to which the growth rates are mapped. The transition from reddish to deep blue indicates a transition from instability to stability. In the long wavelength limit

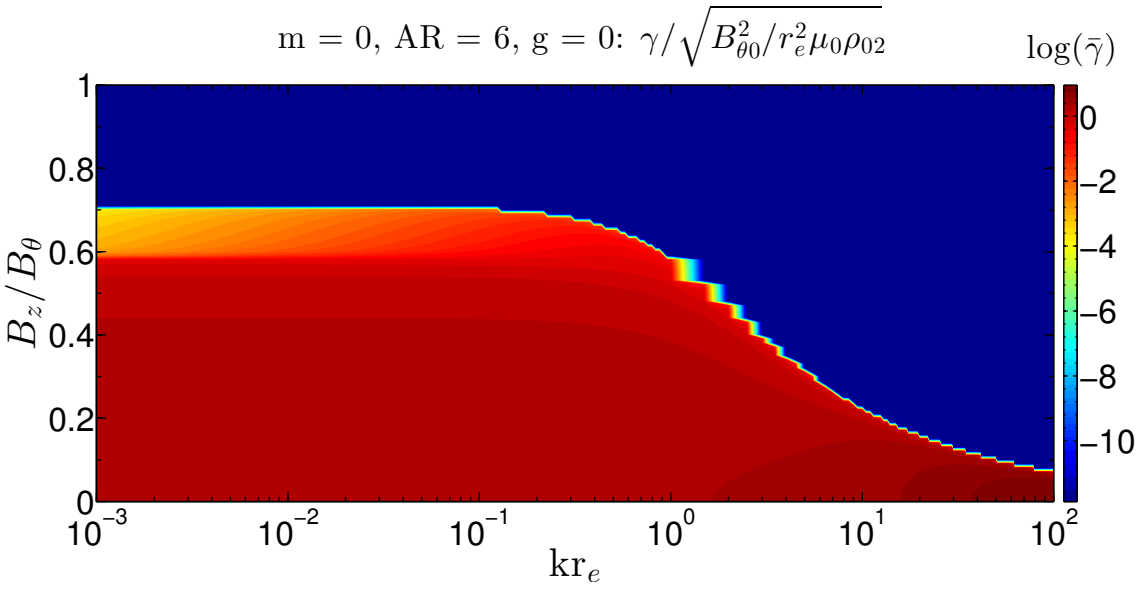

(a) $m = 0$ Pure sausage mode growth rate for $AR = 6$ liner with increasing axial magnetic field.

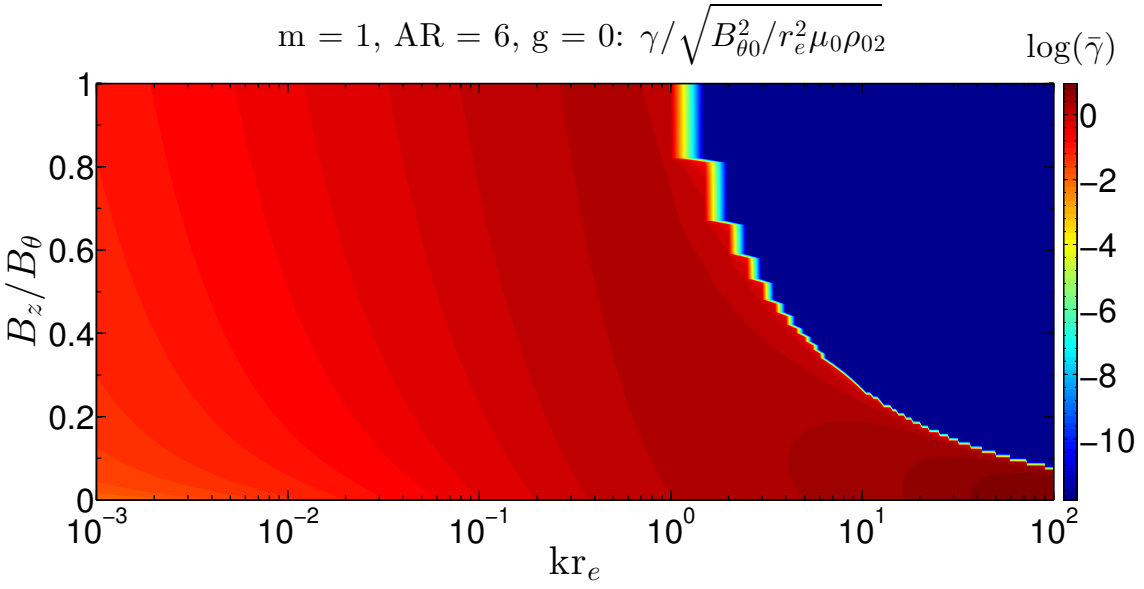

(b) $m = 1$ Pure kink mode growth rate for $AR = 6$ liner with increasing axial magnetic field.

Figure 3.3: Instability growth rates for the pure sausage and kink modes ($g = 0$) in an $AR = 6$ liner with increasing axial magnetic field. $B_z = B_{z,\mathrm{I}}, B_{z,\mathrm{II}}, B_{z,\mathrm{III}}$.

for the sausage mode, the liner is stable for $B_z > 0.7B_\theta$ which is in excellent agreement with the well-known stability criterion, $B_z > (1/\sqrt{2})B_\theta$. As the wavelength becomes shorter, the simple sausage mode stability criterion no longer holds as expected. The

kink mode also shows reasonable agreement with the kink stability criterion. The liner, under these circumstances, behaves similarly to the plasma column with regard to the cutoffs in the growth rate, although the growth rates themselves are higher. We note that the required B_z for these cutoffs increases as g increases (must stabilize MRT modes as well as sausage or kink modes), as well as if the axial field is strong only in one region (the fuel region for example). Note also that Fig. 3.3 sets $g = 0$ to examine the pure sausage and kink modes.

During the main implosion phase of a pre-magnetized liner implosion, $B_z << B_\theta$. In any un-magnetized liner implosion this condition holds throughout the current pulse. The normalized growth rates for the sausage and kink modes under these conditions are shown in Fig. 3.4. The growth rates are normalized to the Alfvén time and the wavenumber normalized to the liner outer radius (which is always non-zero). The solid curves show the pure sausage and kink mode growth rates for various aspect ratios while the dashed lines take $g = g_{\max}$. $AR = 1.0101$ is the approximately filled plasma column, $AR = 2$ is a very thick liner, while $AR = 10$ is a rather thin liner. Both g and the aspect ratio have the most significant effect on the growth rates for

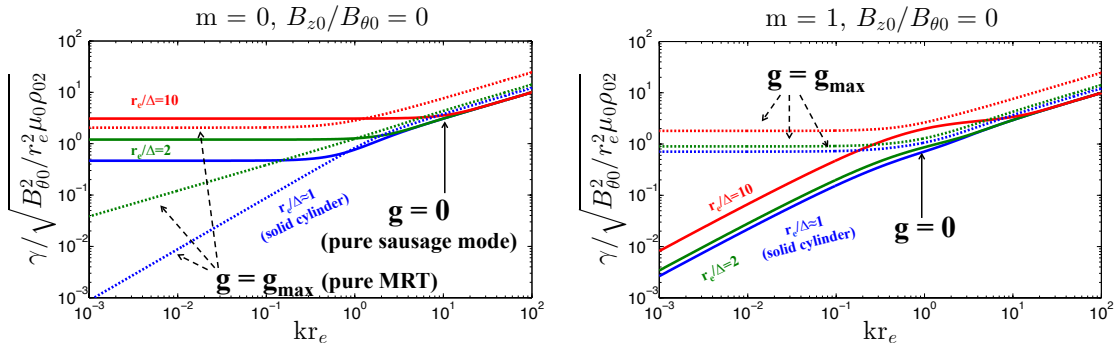

(a) $m = 0$ MRT/sausage mode growth rate for $B_z << B_\theta$ and $g \geq 0$ (implosion).

(b) $m = 1$ MRT/kink mode growth rate for $B_z << B_\theta$ and $g \geq 0$ (implosion).

Figure 3.4: Instability growth rates for various aspect ratios including both $g = 0$ and $g > 0$ and $B_z << B_\theta$.

small kr_e. All the curves behave similarly for large kr_e with the thinnest liner being the most unstable in all cases. Shorter wavelengths are less sensitive to cylindrical

geometry and the growth rate looks very much like $\sqrt{kg}$. This limit was also shown in Eq. 3.48 for the sausage mode. For small kr_e, drastically different behavior is observed between the sausage and kink modes. When $g = 0$, the sausage mode has a finite growth rate in the limit as $kr_e \to 0$, making its growth rate significantly larger than the pure kink mode growth rate which goes to zero. When g is turned to $g_{\max}$ this behavior is flipped. *The kink mode is substantially destabilized by finite g, while the sausage mode is actually somewhat stabilized except for the thinnest liner which retains a finite growth rate in the long wavelength limit (Figs. 3.4(a)-3.4(b)).* The long wavelength limits are given by Eqs. 8,9 of [9].

Next an axial magnetic field is introduced in each region, where $B_{z,1} = B_{z,2} = B_{z,3} = 0.1B_\theta$. The results are shown in Fig. 3.5. The shortest wavelengths begin to be stabilized with an axial field, as was found in planar geometry for MRT. Shown in Figs. 3.3, 3.5, the axial field also stabilizes the pure kink and sausage modes as well. The effect on the longer wavelengths is minimal, particularly for $g > 0$, though the $AR = 2$ liner appears to be more stable to the sausage mode. This is a case that

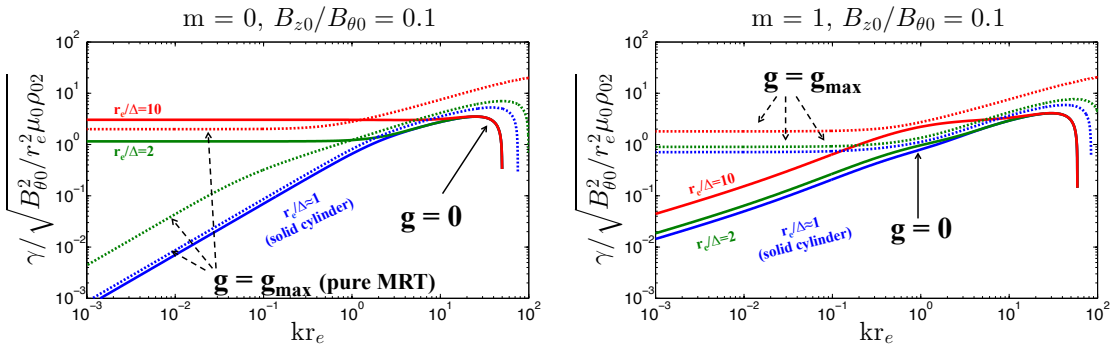

(a) $m = 0$ MRT/sausage mode growth rate for $B_z = 0.1B_\theta$ and $g \geq 0$ (implosion).

(b) $m = 1$ MRT/kink mode growth rate for $B_z = 0.1B_\theta$ and $g \geq 0$ (implosion).

Figure 3.5: Instability growth rates for various aspect ratios including both $g = 0$ and $g > 0$ and $B_z = 0.1B_\theta$.

is likely to occur early in an implosion as the axial current is ramping up and B_z is not yet negligible compared with B_θ. The influence of non-zero g also shows for large kr_e. For $g = 0$ the cutoff at short wavelengths, due to the finite B_z, occurs at

nearly the same kr_e for all three aspect ratios. When $g > 0$, the cutoff wavenumber depends more strongly on the aspect ratio of the liner and no longer resembles the Kruskal-Shafranov and sausage mode stability criteria.

Further increasing the axial field so that $B_{z,1} = B_{z,2} = B_{z,3} = B_\theta$ is a case that occurs very early in an implosion. Azimuthal fields in excess of 10 T do not take much time to develop (less than 30 ns, but depends on the current pulse) but before that time the kink mode is easily the most dangerous instability as shown by Fig. 3.6. Short wavelengths are essentially cut off because of the strong field line bending, which is very much related to the Kruskal-Shafranov condition. Meanwhile the sausage mode is completely stabilized at longer wavelengths as well, as $B_z > 0.7B_\theta$ (sausage stability criterion is met), save for the thinnest liner that is under strong inward acceleration ($g = g_{max}$). This relationship between the axial and azimuthal

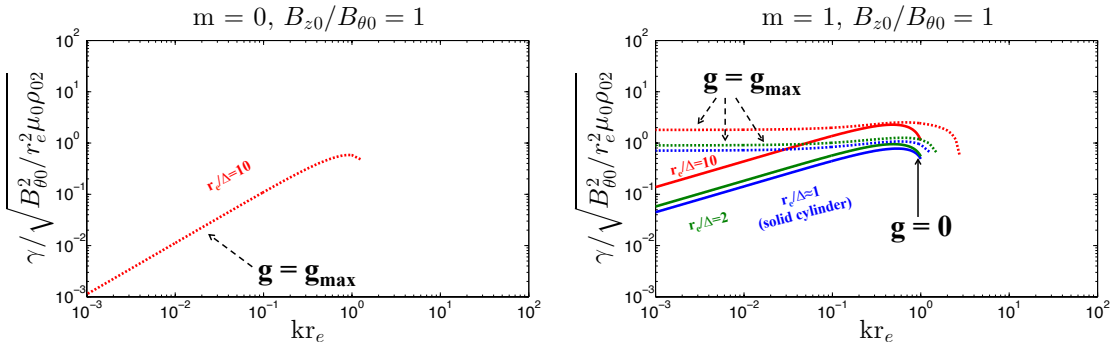

(a) $m = 0$ MRT/sausage mode growth rate for $B_z = B_\theta$ and $g \geq 0$ (implosion).

(b) $m = 1$ MRT/kink mode growth rate for $B_z = B_\theta$ and $g \geq 0$ (implosion).

Figure 3.6: Instability growth rates for various aspect ratios including both $g = 0$ and $g > 0$ and $B_z = B_\theta$.

fields also can occur very late into an implosion once the liner has significantly compressed the axial field. Since our instantaneous equilibrium allows for compressibility and arbitrary distribution of magnetic fields, we can account for axial magnetic field compression in the fuel and liner region. The field in the liner can also be mildly compressed, but for simplicity Fig. 3.7 assumes $B_{z,3} = B_\theta$ and $B_{z,2} = B_{z,1} = 0$ (i.e., a large B_z only in the fuel region). This reduces the overall stabilization of the growth

rates. However, the long wavelength sausage modes remain significantly depressed and kink mode growth remains robust at long wavelengths. Thus, the kink mode is likely to be dominant during both the very early phase and highly compressed phase in pre-magnetized MagLIF.

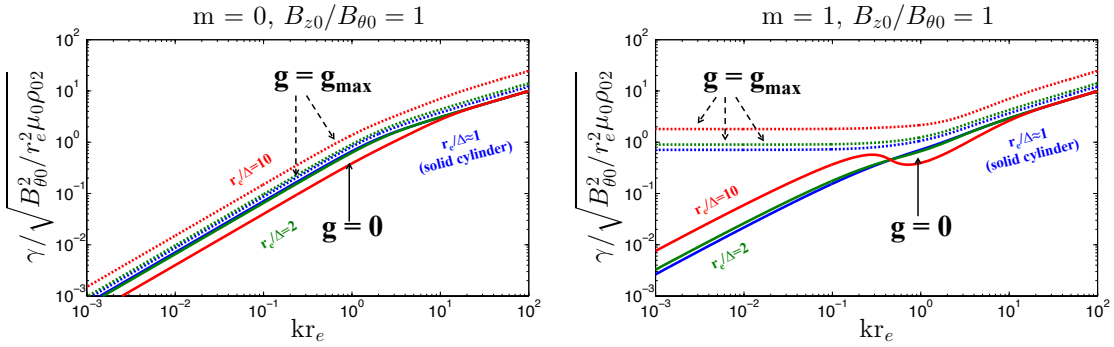

(a) $m = 0$ MRT/sausage mode growth rate for $B_z = B_\theta$ in region III (fuel) only and $g \geq 0$ (implosion).

(b) $m = 1$ MRT/kink mode growth rate for $B_z = B_\theta$ in region III (fuel) only and $g \geq 0$ (implosion).

Figure 3.7: Instability growth rates for various aspect ratios including both $g = 0$ and $g > 0$ and $B_z = B_\theta$ in the fuel region only ($B_{z,2} = B_{z,1} = 0$ T).

Often coincident with, or shortly after the above conditions of $B_{z,fuel} \approx B_\theta$, as the liner begins to decelerate onto a hot/dense fuel region, g switches sign. The MRT unstable interface then becomes the fuel/liner interface. In the absence of feedthrough or other instabilities, the inner surface should be nearly pristine. Thus, MRT would be expected to begin growing at very short wavelengths as MRT generally does on the exterior. However, any feedthrough of MRT could seed larger wavelengths on the inner surface, thus making these wavelengths important as well. Aside from simulations, there is little knowledge as to the state of the inner surface as the deceleration phase begins, so a large wavenumber space will be surveyed. The deceleration phase of an ICF implosion can be analyzed by the cylindrical model by setting $g < 0$. The liner decelerates primarily due to increasing fuel pressure in region III (assuming that $p_f >> B_z^2/2\mu_0$, such that the RHS of Eq. 3.4 is negative). To quantify this scenario, we assume that the RHS of Eq. 3.4 equals $-B_\theta^2/\mu_0$ so that $g = -|g_{\max}| = -B_\theta^2/\mu_0\rho_0\Delta$.

Figure 3.8 shows the growth rates for no pre-magnetization $B_{z,1} = B_{z,2} = B_{z,3} = 0$ for the deceleration phase as well as the pure sausage and kink modes for reference. The kink mode was already unstable over the whole domain plotted for $g > 0$ (Fig. 3.4(b)) and the kink mode remains this way for $g < 0$ (Fig. 3.8(b)). The long wavelength sausage mode is found to be much more unstable for $g < 0$ (Fig. 3.8(a) as compared to $g > 0$ (Fig. 3.4(a)). The sausage and kink mode growth rates are also

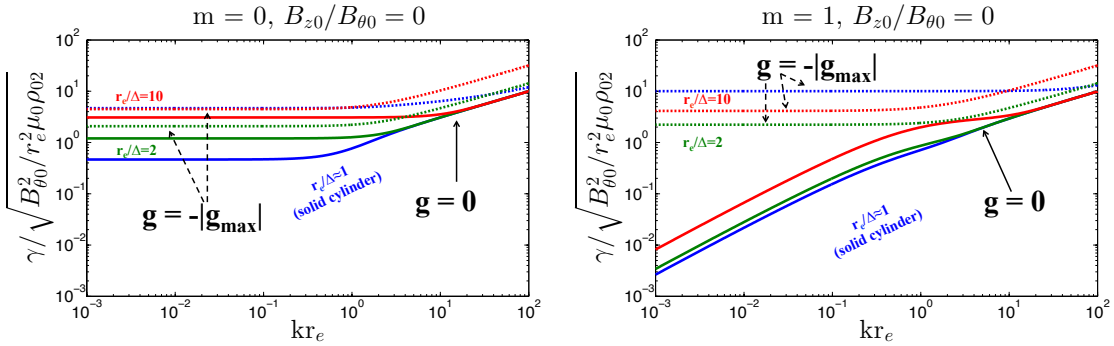

(a) $m = 0$ MRT/sausage mode growth rate for $B_z = 0$ and $g \leq 0$ (decel.).

(b) $m = 1$ MRT/kink mode growth rate for $B_z = 0$ and $g \leq 0$ (decel.).

Figure 3.8: Instability growth rates for various aspect ratios including both $g = 0$ and $g < 0$ and no pre-magnetization ($B_{z0} = B_{z1} = B_{z2} = B_{z3} = 0$ T).

very similar with no pre-magnetization and non-zero deceleration.

The effect of high axial field compression case can again be considered. It is natural to use $B_{z,3} = B_\theta$ and $B_{z,2} = B_{z,1} = 0$ as it is the most physically realizable case. The results are shown in Fig. 3.9. The kink mode remains unstable for long wavelengths while the sausage modes that were unstable in the previous un-magnetized case are now significantly stabilized. Only the thinnest liner, $r_e/\Delta = 10 = AR$, remains unstable for $g = -|g|_{\max}$, but the growth rate is much reduced, particularly for long wavelengths, as there is no longer a finite limit for $kr_e \to 0$ as in Fig. 3.8(a). The kink mode remains unstable for $kr_e < 10$ with a strong finite growth rate for long wavelengths as well as growth rates larger than the sausage mode for all r_e/Δ (c.f., Fig. 3.9(a) and Fig. 3.9(b)). To summarize, Figs. 3.8 and 3.9 show that the deceleration phase appears to be dominated by the kink mode for all $kr_e \lesssim 1$ in

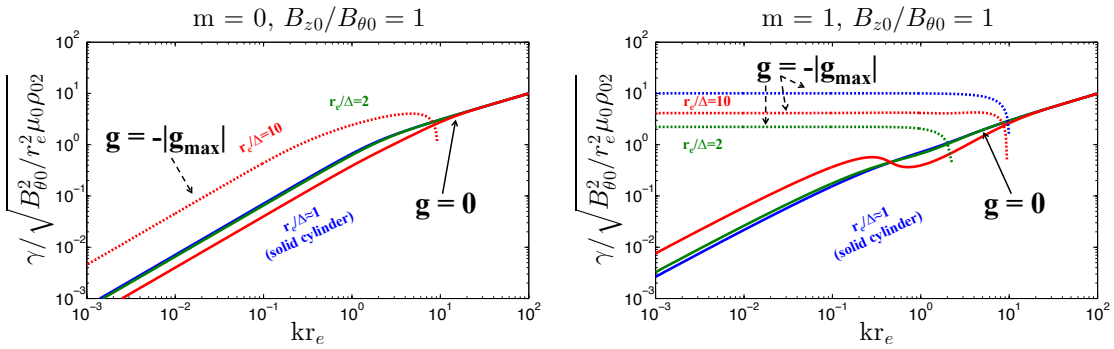

(a) $m = 0$ MRT/sausage mode growth rate for $B_{z3} = B_\theta$ and $g \leq 0$ (decel.).

(b) $m = 1$ MRT/kink mode growth rate for $B_{z3} = B_\theta$ and $g \leq 0$ (decel.).

Figure 3.9: Instability growth rates for various aspect ratios including both $g = 0$ and $g < 0$, $B_{z1} = B_{z2} = 0$ T, and $B_{z3} = B_\theta$.

pre-magnetized implosions while the sausage and kink are comparable without pre-magnetization. Since the $m = 0$ minimizes field line bending, it is likely to dominate over the kink mode without pre-magnetization. This is particularly true if the sausage mode feeds through. The implication in either scenario is that if larger wavelengths are seeded on the inner surface of the liner, they have significant potential to grow during the deceleration phase. These wavelengths are also the most dangerous as they can significantly impact the liner integrity. Unfortunately, while the axial field significantly reduces the sausage mode growth rate, the long wavelength kink mode remains unaffected despite the large axial magnetic field. If this instability becomes a problem, it is then best managed by reducing the initial seed. Feedthrough during the implosion phase is naturally the next consideration.

Feedthrough is most important in the implosion stage where $g > 0$ as the undesired rippling of the inner surface causes poor target performance at the stagnation phase for a variety of reasons. The primary reason is that rippling on the inner surface is the seed for deceleration RT. Many of the same lessons learned in the planar formulation remain here, such as stabilization due to strong field bending. The sausage and kink mode do introduce some complications, however, as they are intrinsically long wavelength instabilities ($k_y r = m = 0, 1$ for sausage and kink modes) but are totally

absent in the planar geometry. Figure 3.10 shows the feedthrough factors for the sausage and kink modes with $B_z << B_\theta$. Also plotted as the dashed teal (black) curve is the pure hydro feedthrough factor $e^{-k\Delta} = e^{-kr_e/AR}$ for $AR = 10$ ($AR = 2$). Unlike the planar case, when $g = 0$ there can still be instability and hence a well-defined feedthrough factor exists. The behavior it exhibits is quite different from the typical MRT feedthrough factor. For both the sausage and kink mode and $AR = 2$, $F(\omega) > 1$ for $kr_e \lesssim 1$. In this regime, the feedthrough is 'backward' so $F(\omega) = 2$ means that the inner surface ripple amplitude is twice that of the outer surface. This effect is most prominent for thicker liners and is due to the fact that thicker liners have an inner surface at a smaller radius, which accentuates the cylindrical effects. When g becomes large, this behavior disappears in the kink mode, but remains for the sausage mode to a somewhat smaller extent (Fig. 3.11(a)). In fact, for the kink mode, $g > 0$ brings both AR feedthrough factors below unity and results are not much different than the planar feedthrough factor. It is unlikely this effect makes an appearance in experiments unless the inner surface is somehow rippled early on (when g is small) with a long wavelength outside of feedthrough.

A possible physical interpretation of this somewhat unanticipated result is that there is a competition between MRT and a bulk sausage mode while the acceleration is small. A typical eigenfunction for MRT shows exponential decay away from the MRT unstable surface where the peak is. Introduction of the sausage and kink modes modifies the behavior of the eigenfunction such that the peak may no longer occur at the interface, but somewhere in the liner (hence bulk). Then, as g becomes large enough, the MRT at the outer interface dominates such that the peak has moved from the liner interior to the outer surface.

During the majority of a pre-magnetized implosion $B_z << B_\theta$ and as shown in the planar results the feedthrough factor is not much affected in this case. The most important case is $B_{z,f} \approx B_\theta$, particularly for $g > 0$. These conditions occur as the

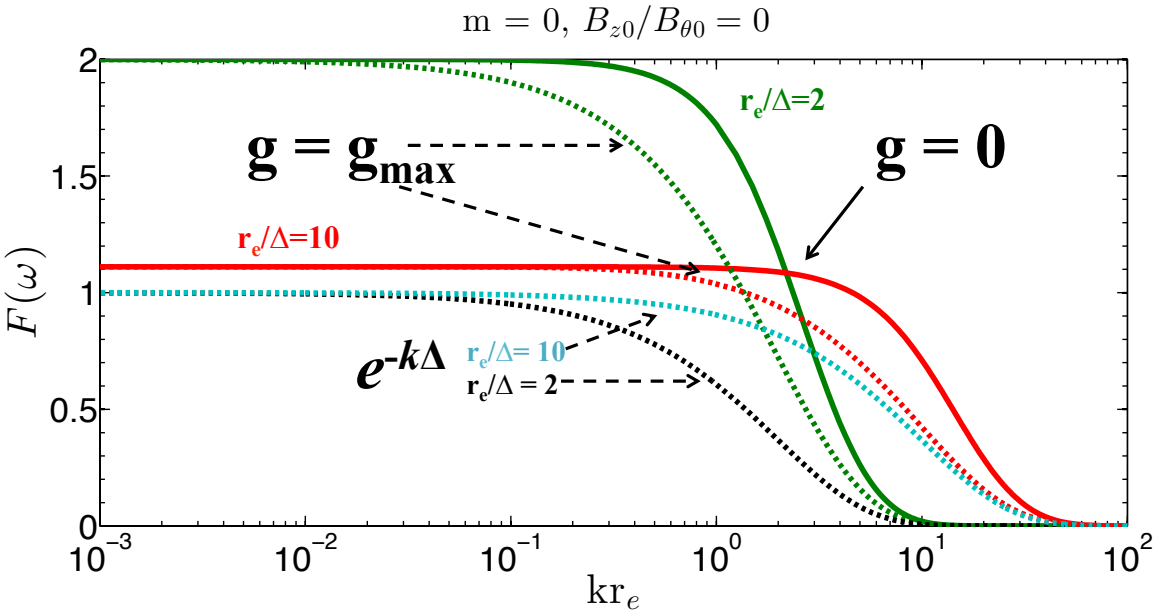

(a) $m = 0$ MRT/sausage mode feedthrough factor for $B_z << B_\theta$ and $g \geq 0$ (implosion).

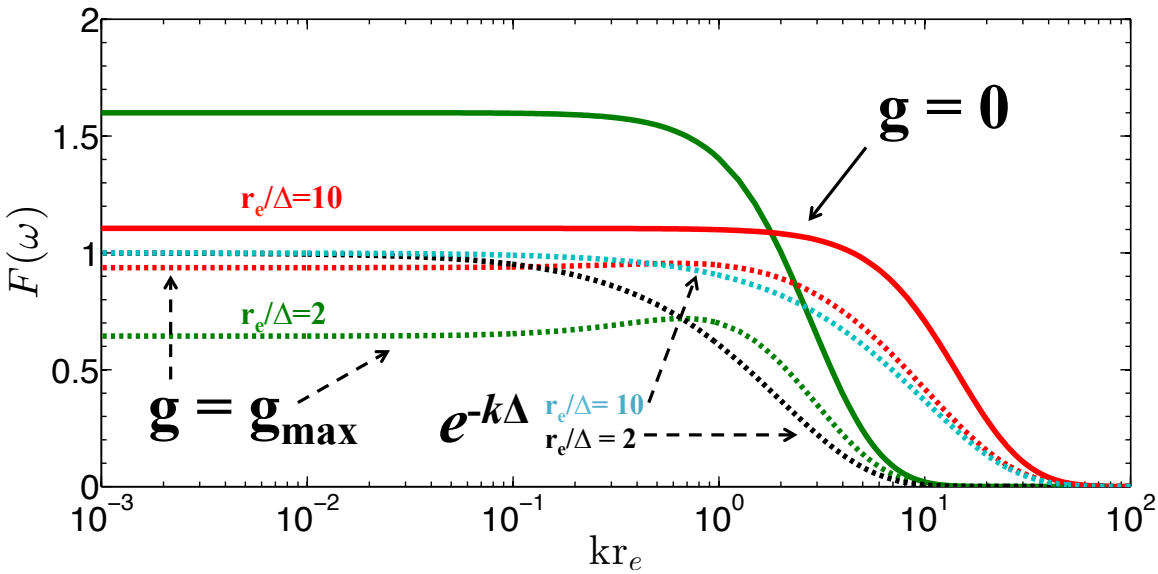

(b) $m = 1$ MRT/kink mode feedthrough factor for $B_z << B_\theta$ and $g \geq 0$ (implosion).

Figure 3.10: Feedthrough for $AR = 2, 10$ including both $g = 0$ and $g > 0$. The pure hydro feedthrough factor is included as the dashed teal (black) curve using $AR = 10$ ($AR = 2$). $B_{z1} = B_{z2} = B_{z3} = 0$ T. $AR = r_e/\Delta$ is the aspect ratio.

liner nears the deceleration phase and has begun to compress axial magnetic field in the fuel region significantly, but is still accelerating inward. In general this also means that $(B_{z1},\ B_{z2}) << B_\theta$. This scenario is considered next in Fig. 3.11. The axial field has the greatest impact on the sausage mode as it brings the feedthrough factor below unity for all k. Compared to the sausage mode, the kink mode feedthrough is insensitive to the axial field. Only the shortest wavelengths have some reduction in feedthrough. Interpreting these results in the context of experiments is more challenging. Experimental images (Fig. 1.4) show evidence of kink-like MRT growth that has developed during the main phase of the implosion (where $B_z << B_\theta$) [54][55]. Since the feedthrough factors for both the sausage and kink are similar, it is difficult to say whether feedthrough of the kink mode, or sausage mode or both occurs. However, as the axial field is compressed, feedthrough of the kink mode becomes the most important. X-ray measurements of the hottest fuel region in MagLIF experiments also indicate a helical shape [38][39]. Whether this is from feedthrough of helical perturbations, growth of a kink-MRT mode or something else, is a subject of ongoing research.

3.4.1 Application of analytic solutions to 1D liner implosions

As an important check, the derived growth rates can be compared to the benchmark problem from Sinars et al.'s experiments from Chapter 2 [51]. The same 1D simulation used for the planar equilibrium parameters can easily be adapted for the cylindrical model as well. The MRT amplitude can then be computed in exactly the same way as for the planar model. The 400 μm axial wavelength calculation for $m = 0$ is shown in Fig. 3.12 along with the planar calculation ($k_y = 0$), 2D HYDRA simulation and experiment. As expected, the cylindrical model gives slightly larger overall growth than the planar model. While not a direct test of the cylindrical effects

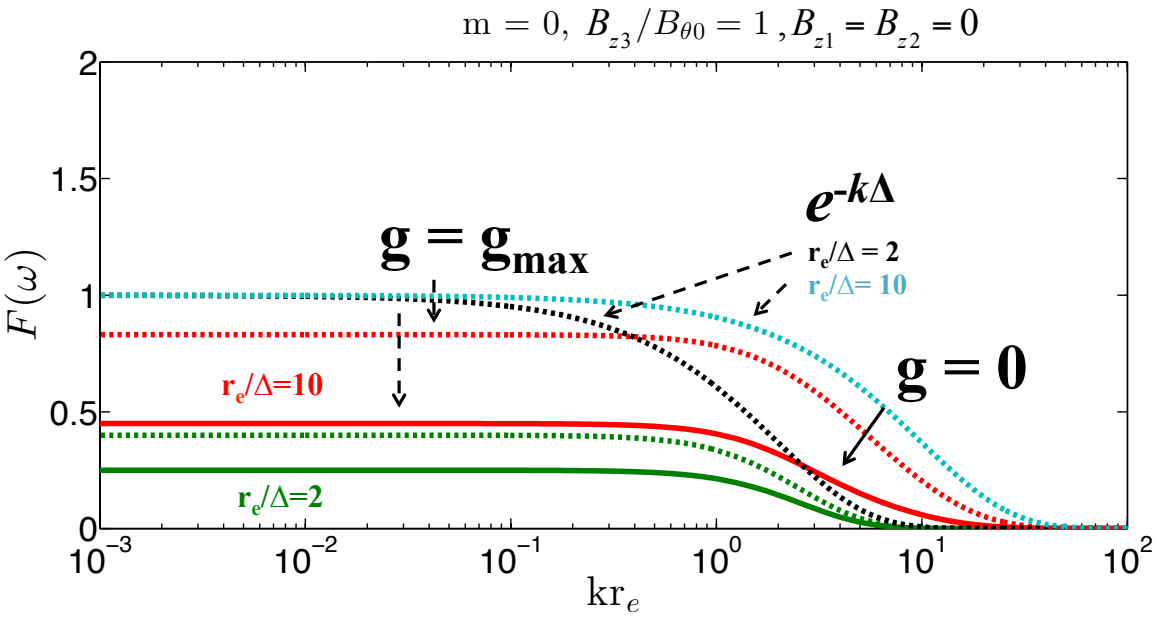

(a) $m = 0$ MRT/sausage mode feedthrough factor for $B_z = B_\theta$ and $g \geq 0$ (implosion).

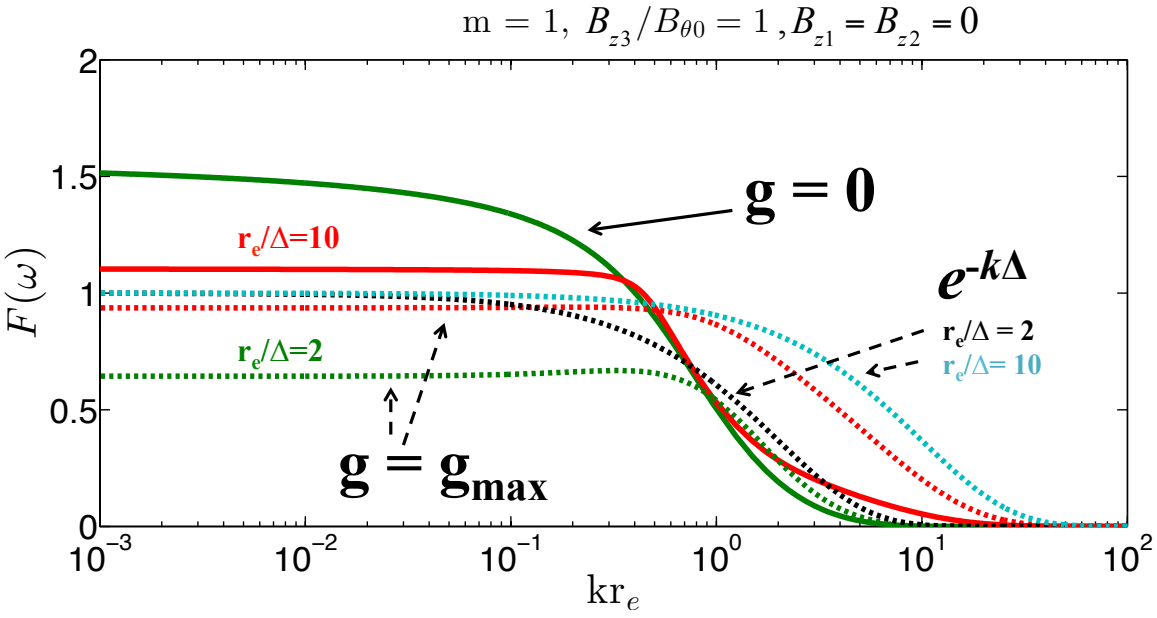

(b) $m = 1$ MRT/kink mode feedthrough factor for $B_z = B_\theta$ and $g \geq 0$ (implosion).

Figure 3.11: Feedthrough for $AR = 2, 10$ including both $g = 0$ and $g > 0$. The pure hydro feedthrough factor is included as the dashed teal (black) curve using $AR = 10$ ($AR = 2$). Only the fuel region is highly magnetized,$B_{z3} = B_\theta$, $B_{z1} = B_{z2} = 0$ T. $AR = r_e/\Delta$ is the aspect ratio.

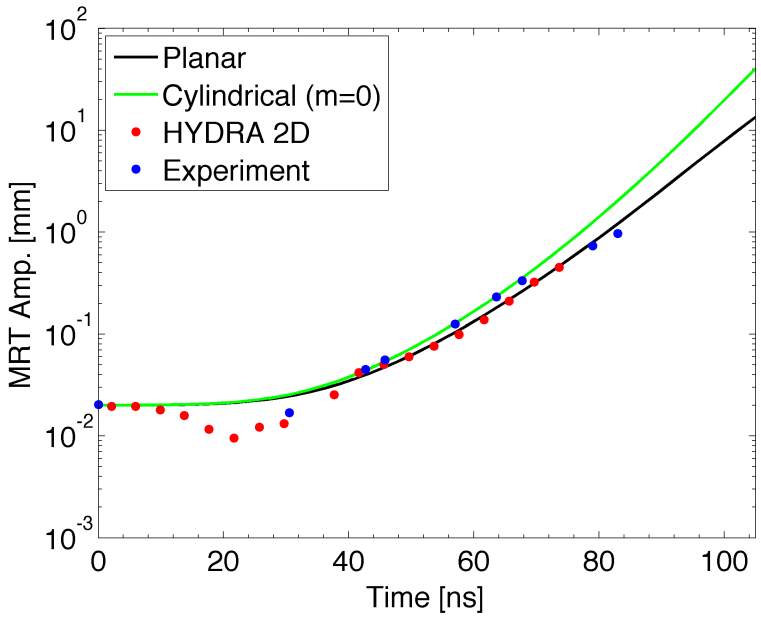

Figure 3.12: Three region sharp boundary model calculation of MRT growth of a 400 μm perturbation on a cylindrical liner using both planar and cylindrical ($m = k_y = 0$) with 2D HYDRA data [8] and Sandia experimental data from Sinars et al.[51].

of the sausage mode, the model gives the appropriate limit. It is very computationally expensive to simulate a seeded kink mode with $k > 0$ since it is a fully 3D calculation; nevertheless, efforts to do this are underway (see Appendix C). Instability growth in the (r, θ) plane will be considered later in this chapter.

As with the planar model, 1D HYDRA simulations can be used to calculate appropriate equilibrium quantities for the analytic model. In order to analyze both $g > 0$ (implosion) and $g < 0$ (explosion or stagnation), a full ICF style implosion is modeled in 1D HYDRA. This is necessary to establish a deceleration phase at high convergence. This could also be accomplished by using a higher density material such as liquid deuterium or even water to achieve stagnation at larger radii. Plotted in Fig. 3.13 are the results of these 1D HYDRA simulations averaged to generate equilibrium quantities. The initial fuel density is 2.5 mg/cc and initial axial field is 10 T. The drive current used is the Sandia z1965 pulse [51] shown in Fig. 2.8. The fuel is preheated to roughly 250 eV on average. The liner itself is a beryllium liner with

$AR = 6$, initially at a smaller radius than the Sinars et al.[51] aluminum liner (from 3.168 mm to 2.79 mm). The azimuthal and axial magnetic fields are only comparable

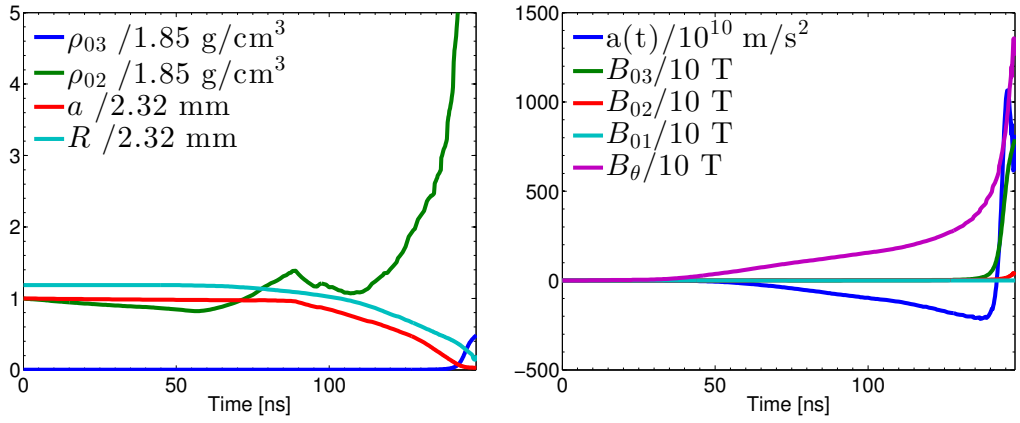

(a) Beryllium liner trajectory including the temporal evolution of the average liner (ρ_{02}) and fuel densities (ρ_{03}).

(b) Magnetic field and acceleration history for pre-magnetized ICF style implosion. Initially, at $t = 0$, $B_{z1} = B_{z2} = B_{z3} = 10$ T and $B_{0\theta} = 0$. For $a(t) < 0$, the liner is imploding. For $a(t) > 0$, the liner is decelerating.

Figure 3.13: Time history of equilibrium quantities from 1D HYDRA simulations for an ICF style implosion.

early on and very late into the implosion, around the time g changes sign. Recall $a(t) = -g(t)$. Also, $\rho_2 >> \rho_3$ which means the Atwood number is essentially unity. Using the values from Figs. 3.13(a)-3.13(b), the instantaneous growth rate can be calculated for a given (m, k). Of particular interest are the sausage and kink modes which will be compared directly at each moment in the implosion. A map of this comparison is plotted in Fig. 3.14 along with some annotations. The green dashed curve highlights an axial wavelength of 1 mm, which is roughly the dominant axial mode observed in liner implosion experiments [53][55]. The results can be roughly divided into three phases for the purposes of these calculations: (1) initial current rise ($g \approx 0, t < 55$ ns), (2) implosion ($g > 0, 55$ ns $< t <$ 140 ns), and (3) deceleration ($g < 0, 140$ ns $< t <$ 148 ns). The first phase is the current ramp phase, which includes $B_z > B_\theta$ until $B_z \approx 0.1 B_\theta$. During this phase g remains small as the magnetic drive pressure must first overcome the inertia of the liner. The shortest wavelengths

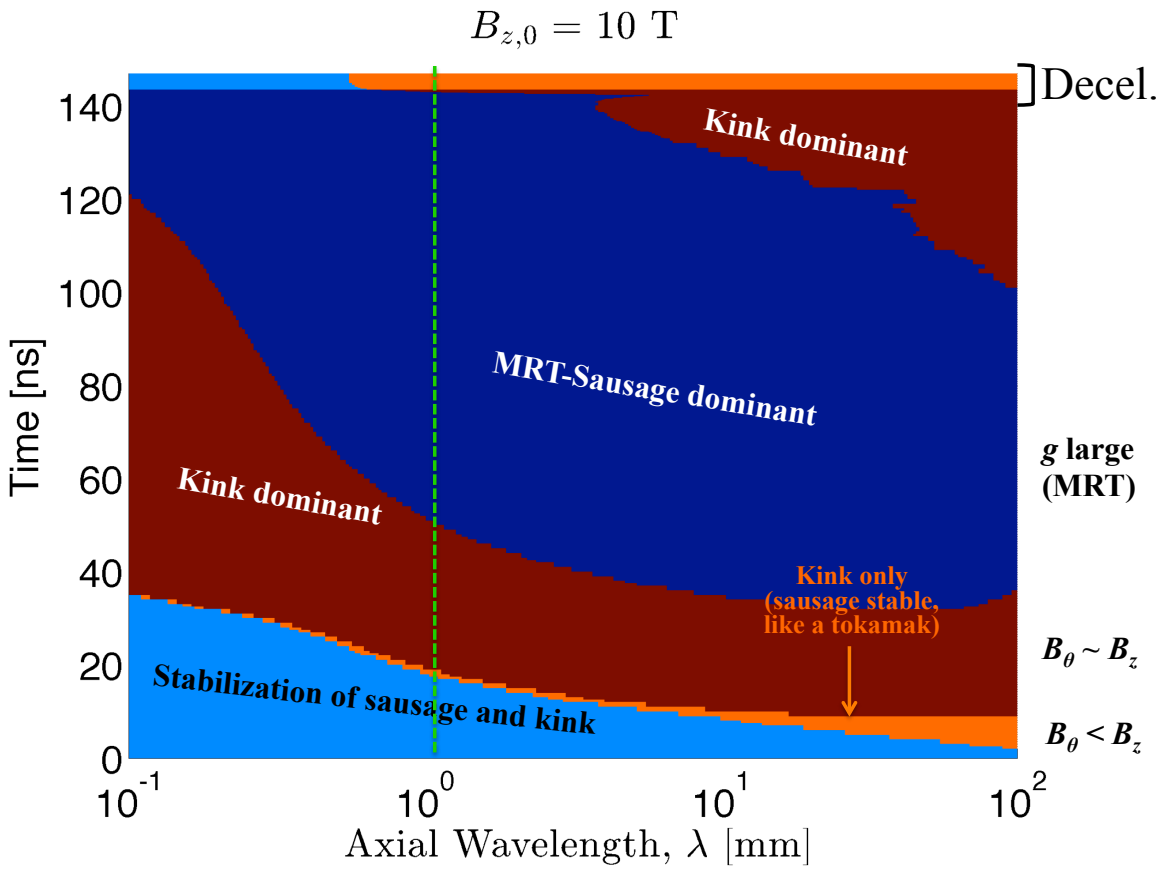

Figure 3.14: Relative importance of sausage and kink modes throughout a typical ICF liner implosion. The final approximately, 7 ns of the implosion is the deceleration phase where the sign of g flips. In our model, MagLIF again behaves like a tokamak where the sausage mode is completely stabilized by the axial magnetic field but the kink mode remains.

of both sausage and kink modes are initially stabilized by the relatively strong axially magnetic field. This is a regime that does not last long. While the thickness of the liner and wavelength do have a marginal effect on the sausage stability criterion, once $B_z < 0.7B_\theta$, the sausage mode turns on, even though the kink mode remains the dominant mode like a tokamak. Once g becomes large, the shortest wavelengths are still the most unstable to the kink mode (see Figs. 3.4, 3.5). MRT is known to evolve from short wavelengths to long wavelengths through nonlinear effects. Nonetheless, nearly every axial wavelength of interest begins as stable to the sausage and kink mode, transitions to period of growth dominated by the kink mode, followed by sausage dominated growth in the second, implosion, phase. Thus, the character of MRT has the potential to be a mixture of the sausage and kink mode.

The main portion of the implosion phase is dominated by MRT with the growth rate mostly determined by g. When g is small, the absolute growth rate of the (nearly) pure sausage and kink modes is relatively small using the sharp boundary model at solid density. Since the growth rate scales with $1/\sqrt{\rho}$ (see Eqs. 3.46, 3.48), ablated plasma could exhibit faster growth. Very important to note is that if this same case were run with no axial magnetic field, the vast majority of the implosion is dominated by the sausage mode and it is never stabilized, as $(k_z B_z)^2 = 0$. Additionally, with no B_z, the kink mode enters only in the stagnation phase where both the sausage and kink modes are comparable, with slight preference to the kink. The effect of the axial magnetic field on this stage is discussed next.

The final stage occurring in the last 8 ns of Fig. 3.14 is the deceleration phase where g switches sign. At this point in the implosion the axial magnetic field is highly compressed in the fuel region and is comparable with the azimuthal magnetic field. This is sufficient to stabilize the sausage mode, however the kink mode remains strong, and has almost constant growth rate over a wide range of wavelengths (Fig. 3.9). The dominant MRT mode is experimentally observed to be between 500 to 1500 μm which

also has a relatively large feedthrough factor. Thus, these are the modes most likely to seed the inner liner surface. The subsequent deceleration growth is then dominated by the kink mode due to the highly compressed B_z. The effective $|g|$ during the deceleration phase is about an order of magnitude larger than the implosion phase. While the deceleration phase occurs only for a limited time, a significant number of e-folds can occur leading to substantial instability growth. Such a calculation was done for the sausage and kink mode and is displayed in Fig. 3.15. The amplitude

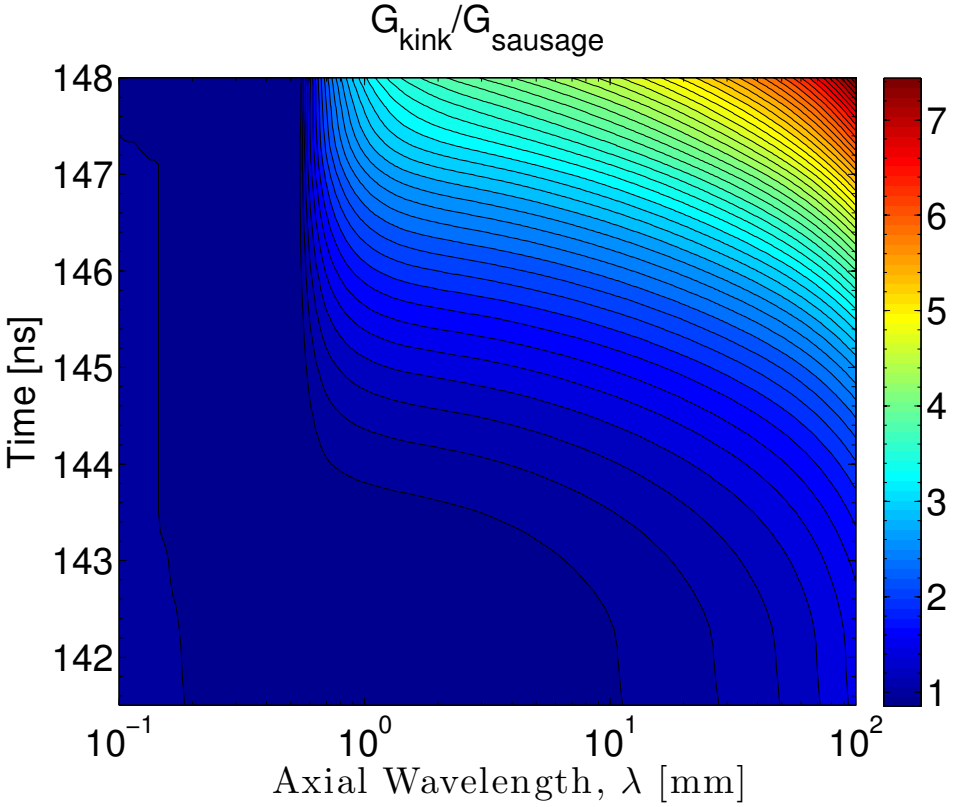

Figure 3.15: Comparison of MRT amplitude gain for sausage and kink modes. $G = \exp(\int \gamma dt)$ when the axial magnetic field is strongly compressed.

gain is defined as $G = \exp(\int_{t_0}^{t} \gamma(m, k, t')dt')$ where the exponent is just the number of e-folds and t_0 is the beginning of the deceleration phase ($\sim$ 141 ns). The sausage mode is stabilized so the amplitude gain for the sausage mode is unity. A typical liner is on the order of 1 cm tall, which limits the maximum wavelength. So the total

amplitude gain for the kink mode is around 5 or less which is still quite substantial. The gain is sensitive to the value of g and the compressed B_z. The axial magnetic field also affects where the plateau occurs at which the gain goes to unity for both kink and sausage modes (wavelengths shorter than ~ 1 mm in this case). If the axial magnetic field is less successfully compressed, the kink mode is no longer stabilized for slightly shorter wavelengths and additional amplitude gain can be found there. For larger axial fields, the longer wavelengths can be stabilized, so the plateau moves to the right. In reality, these 1D calculations likely overestimate the compressed B_z since the B_z in the fuel region is radially averaged. HYDRA also does not yet include the Nernst effect (see Slutz et al. for discussion of the impact of the Nernst term [12]), which is another way field can leak from the fuel region through the combination of a temperature gradient and low magnetization. Increasing the axial magnetic field tends to decrease the Nernst effect [12]. This is one of the possibly more important pieces of physics missing from HYDRA but is in development. However, if the 1D profiles are sufficiently well known, they can be used to numerically integrate the governing ODE. This would be able to account for gradients in density and axial magnetic field, as well as any azimuthal magnetic field leaking into the fuel.

The focus of this chapter has thus far been on the $m = 0, 1$ modes. Unfortunately, it is difficult to determine the true mode structure of a 3D liner from 2D radiographs. The sausage and kink modes are effectively very long wavelength modes and very robust, if slow growing. As m becomes larger, modes grow fastest in the absence of an azimuthal magnetic field (just like large k_z), assuming g is provided by other means. However, in a Z-pinch, since B_θ is large, it is anticipated these modes play a very small role, because $(k_\theta B_\theta)^2$ becomes large. While it is unlikely modes as high as $m = 20$ appear, the difference between $m = 1$ and $m = 2$ is not particularly large. To illustrate this, the number of MRT e-folds for 80 ns and over the entire implosion phase was calculated for $|m| \leq 20$. These calculations used the same data as for the

previous plots so that 80 ns corresponds roughly to the beginning of the implosion phase. Direct comparison of Figs. 3.16(a)-3.16(b) shows that as time goes on the

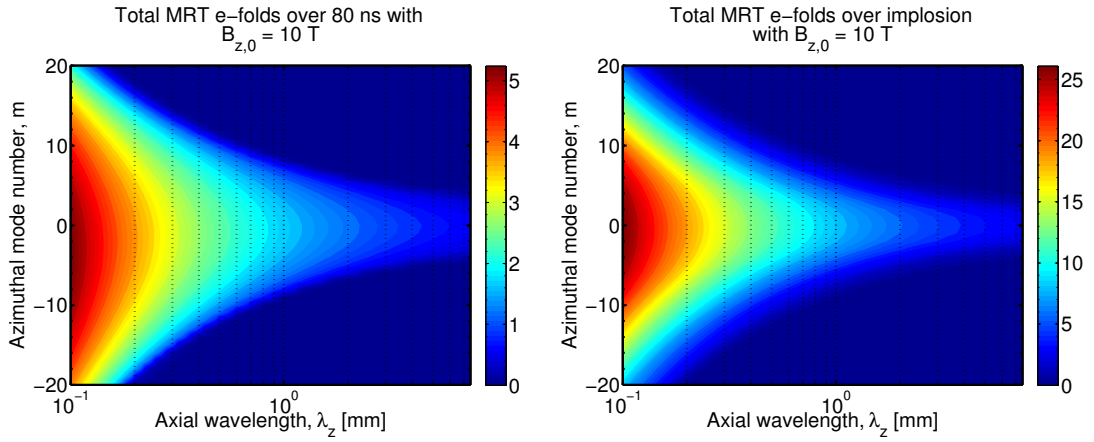

(a) Total number of MRT e-folds over the first 80 ns of an implosion.

(b) Total number of MRT e-folds over the entire implosion phase.

Figure 3.16: Total number of e-folds for instability growth for $-20 \leq m \leq 20$.

largest gain is concentrated towards smaller m numbers. Nonetheless, in the first 85 ns, B_θ has already risen to 1100 T (Fig. 3.13(b)) yet the larger m numbers still show a substantial number of e-folds. Figure 3.16(a) also illustrates the effect of the axial magnetic field on the dominant MRT mode. As was shown in the comparison of the sausage and kink mode, including an axial field pre-disposes the liner to the kink mode. Careful investigation of Fig. 3.16(a) shows the e-folds are not symmetric about $m = 0$ as would be found if $B_z = 0$. Instead the peak is off-center. As time goes on the sausage mode begins to dominate the growth and hence Fig. 3.16(b) becomes more symmetric. Figure 3.17 shows the total e-folds for $-20 < m < 20$ for two fixed values of $\lambda_z = 300,\ 1000$ μm after 57 and 85 ns to better illustrate these points. The green curves plot the results for $B_z = 0$ T showing the symmetry of the modes about m when no magnetization is present. At 57 ns the current is in the ramp up phase and highlights the early dominance of the kink mode. After 85 ns, the asymmetry begins to be overwhelmed by the sausage mode as the liner enters the implosion phase. While it is difficult to say whether early growth of the kink

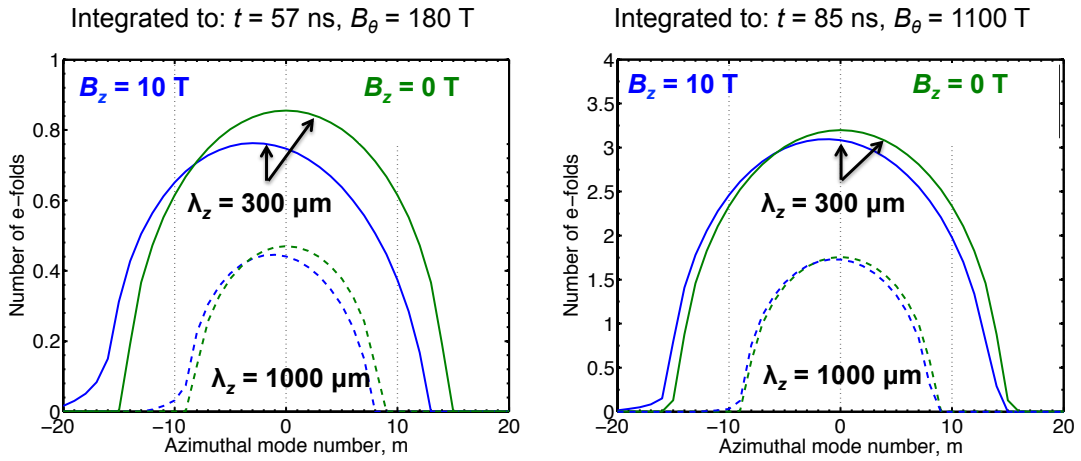

(a) Total number of MRT e-folds for fixed λ_z after 57 ns elapsed.

(b) Total number of MRT e-folds for fixed λ_z after 85 ns elapsed.

Figure 3.17: Comparison of the asymmetry of azimuthal mode instability growth for long and short axial wavelengths, and with and without pre-magnetization.

mode will persist, experimental radiographs directly comparing two cases with and without an axial field do show the presence of kink-like modes with the axial field present. Without the axial field, the images look much more azimuthally symmetric [53][37][55]. Radiographs have not been taken during the current ramp up phase when an axial field is present so it is currently unknown how early this kink-like structure appears. Nonetheless, based on the present study, the presence of the kink mode is not totally unexpected. The effect of magnetic diffusion is an important consideration that remains, particularly in the azimuthal direction. If there is sufficient diffusion, the stabilization of MRT can be significantly reduced even with large magnetic fields. This allows for greater growth of any mode with $|m| > 0$. From a scaling standpoint, the planar model could fairly easily be modified to include a parameter that scales the $(\vec{k} \cdot \vec{B})^2$ terms based on fitting to HYDRA data. The cylindrical model expressions are far more complicated and such a simple procedure is not possible.

3.4.2 2D (r, θ) HYDRA simulations of purely azimuthal modes

In the previous chapter, the effect of finite resistivity on axially oriented modes was considered (where $m = 0$). Here, the effect of finite resistivity on the growth of purely azimuthally oriented modes will be examined. As 3D calculations are too computationally expensive, the following section will resort to 2D (r, θ) simulations where $k = 0$. As was seen in the previous section, the issue with this type of simulation is that these growth rates tend to be small (according to ideal MHD). This geometry also requires additional consideration as to measuring the instability growth. To facilitate this, a very simple transformation to transmission measure is applied to the 2D data.

$$T(r, \theta) = e^{-\kappa \rho(r,\theta) L}. \tag{3.55}$$

Here κ is the opacity of the aluminum (assumed to be a constant 102 cm^2/g) and L is the axial length of the liner (0.75 cm). To model the full 2π of the liner 2048 zones were used in the $\hat{\theta}$ direction. This is significantly more total zones than the previous (r, z) simulations and are thus more computational expensive. At the initial radius of 3.168 mm, this gives an azimuthal resolution of ~ 10 micron. Two azimuthal modes were considered, $m = 1, 6$ (note that the sign does not matter in 2D, with $k = 0$) and seeded on the exterior of the same liner that has been considered for the majority of this thesis. The instability amplitudes for $m = 1, 6$ are shown in Fig. 3.18.

The jaggedness in the $m = 1$ result is a consequence of significant ablation and higher frequency modulation. The MRT growth plotted in Fig. 3.18 is determined from the 38 % transmission contour. This contour level was selected to image the same density as the 50 % contours did in the (r, z) simulations (similar path lengths). It should be noted that results were very similar over a wide range of contour levels. While not the highest fidelity simulations, it is clear that both the $m = 1$ and $m = 6$

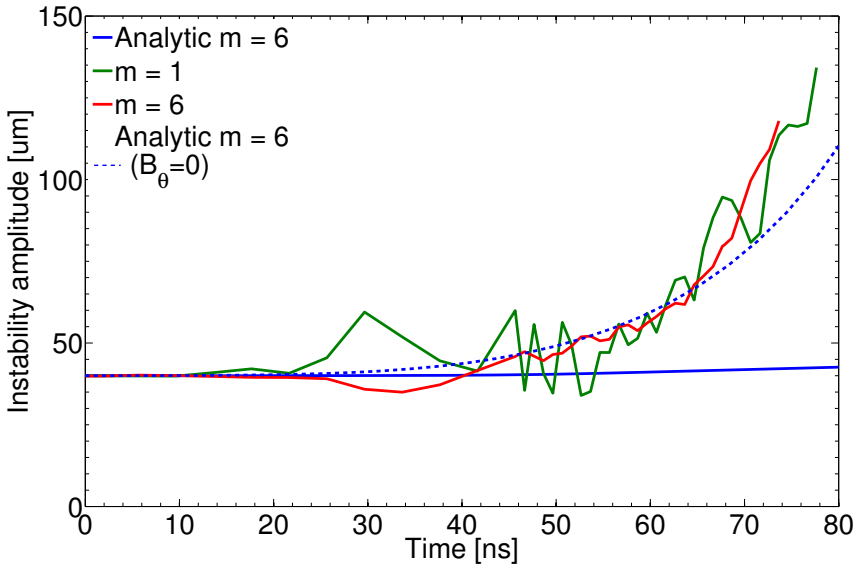

Figure 3.18: Comparison of instability growth for $m = 1, 6$ modes with $k_z = 0$ from 2D HYDRA simulations. The dashed analytic line sets $B_\theta = 0$ so there is no stabilization in the $\hat{\theta}$ direction, and the liner is imploded by other means.

modes grow significantly more than the analytic predictions using the ideal MHD sharp boundary model. More interestingly, both modes grow at roughly the same rate, both showing a gain in amplitude of approximately by a factor of 3. This is a very unexpected result based on the analytic calculations which predict high stabilization of the $m = 6$ mode since $(k_\theta B_\theta)^2 = (mB_\theta/r)^2$ is large when $m = 6$. The analytic result for the $m = 1$ mode is not shown as it reaches an amplitude of only 52 μm at 80 ns.

Growth of both $m = 1, 6$ modes scale in interesting ways. The $m = 6$ mode behaves as though there are no magnetic field effects ($B_\theta = 0$ as shown by the dashed curve, g is assumed to be produced by other means) such that only MRT grows ($\sim \gamma^2 = \sqrt{k_\theta^2 + k_z^2} g$). The kink mode does not behave in this manner as k_θ is six times smaller. Thus, for the kink mode, the magnetic terms cannot be neglected but does not solve the discrepancy, as the analytic growth rates remain too small. The chosen density value may influence the growth rate value, particularly since the

wavelength is long, MRT stabilization via a density gradient is relatively unimportant. Based on the form of Eq. 3.48 for the sausage mode, the smaller density regions may grow faster for the kink mode as the kg term is relatively small as compared to the $m = 6$ case (where k_θ is large). Nonetheless, there are many confounding effects making agreement between analytic and simulation results very challenging.

As anticipated, there is significant diffusion of the azimuthal magnetic field into the liner. While it is known that a finite current distribution in an ideal MHD Z-pinch reduces the growth of pure sausage and kink modes, an analysis including MRT has not been done. Since a finite g has been shown to affect sausage and kink growth rates, a calculation including diffused azimuthal field is considered next.

In order to model this effect for ideal MHD, a technique similar to that employed by Zhang et al. [66] is used. A sharp boundary model is still used, however, a finite distribution of azimuthal magnetic field is allowed in the liner region but it is assumed that $B_{0\theta}$ is not lowered as a result of diffusion. This requires numerical solution of the governing ODE, however, for constant density and constant axial magnetic field, the solver is still quite fast. To model the azimuthal magnetic field in the liner, a simple diffusion profile is used, that is parameterized via δ, which measures the distribution of B_θ within the liner. This profile is described by Eq. 3.56 and plotted for various values of δ in Fig. 3.19,

$$B_\theta(r,t) = B_{\theta,0}\frac{\sinh\left[\left(1-\left(r_e-r\right)/\Delta\right)/\delta\right]}{\sinh\left(1/\delta\right)}. \tag{3.56}$$

In physical units, δ is closely related to, $\sqrt{D_m}$, where D_m is the magnetic diffusion constant. Increasing values of δ correspond to increased azimuthal magnetic field within the liner as shown by Fig. 3.19. This model assumes that the peak B_θ is not lowered as a consequence of the diffusion. The liner outer radius for Fig. 3.19 is located at $r_e = 3.168$ mm (at the rightmost of the figure) and the liner inner

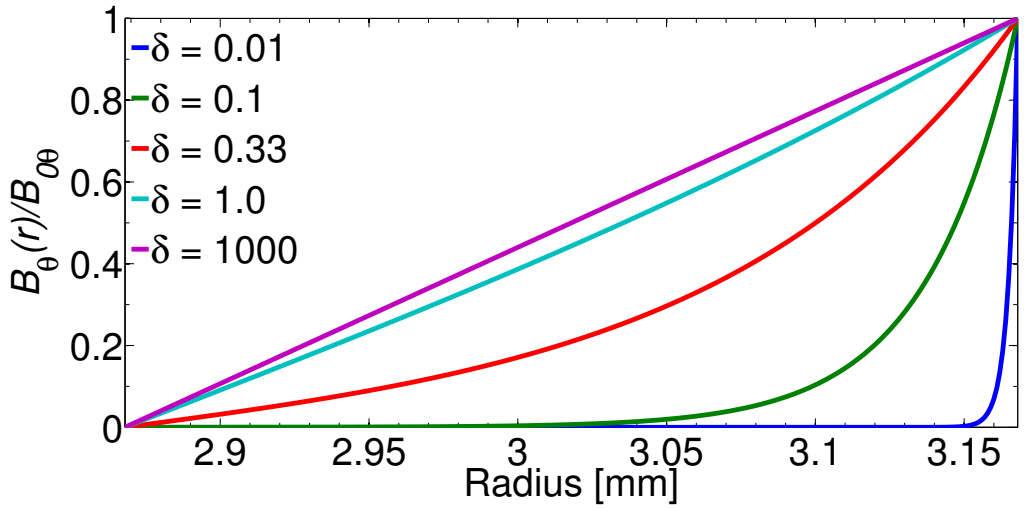

Figure 3.19: The assumed analytic profile for the azimuthal magnetic field within a liner with outer radius located at $r_e = 3.168$ mm, with thickness, $\Delta = 0.3$ mm. The magnetic field is normalized to the value at the liner exterior.

surface is located at $r_e - 0.3$ mm (leftmost side of plot). The azimuthal magnetic field equals to zero at the inner liner surface ($r_e - \Delta$). This formulation accounts for magnetic diffusion in time, which is found in the 2D simulations while the analytic treatment of unstable modes still uses ideal MHD. To model this, the resistivity, η, is fixed and the diffusion length increases as time increases. Though this is still a substantial simplification as D_m varies with r and t in resistive MHD simulations. Also important to keep in mind, is that while the field is 'diffused' into the liner, the field lines still fully bent in ideal MHD. In resistive simulations the bending of the magnetic field lines may be reduced somewhat because of magnetic diffusion which reduces the effective $(\vec{k} \cdot \vec{B})^2$ term.

The results for the finite current distribution in our analytic framework are shown as the solid curves in Fig. 3.20 and the purely analytic calculation (no current in liner) as the dots. Here there is no axial magnetic field (since k_z is so small it should not affect results anyway). These results indicate that presence of azimuthal field within the liner has a significant impact on the $m = 6$ mode, while the sausage and kink

mode growth remains nearly the same (dots are on top of solid curves). On the log scale, the dip in the $m = 6$ result corresponds to a brief period of stability ($\sigma^2 = 0$). The sausage mode has a very small growth rate ($\sigma \sim 10^9 s^{-2}$), but is also unaffected by the finite current. This is a result that is difficult to interpret in the context of the 2D simulations given the large number of variables in the problem. Nonetheless, the ideal MHD results show that the presence of azimuthal field in the liner is generally a stabilizing configuration for these (r, θ) perturbations.

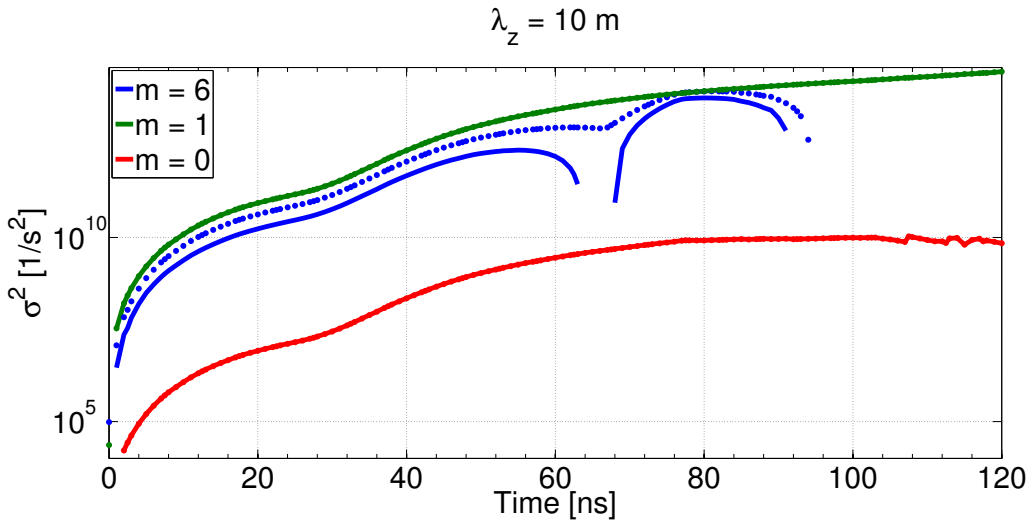

Figure 3.20: Comparison of instability growth rates for $m = 0, 1, 6$ modes with $k_z = 0$. The solid curves include a finite current distribution in the liner using our analytic framework, while the dots are the completely analytic model with no current in the liner. Note that the analytic results are nearly identical for $m = 0, 1$. $m = 6$ shows smaller growth including the finite current distribution.

An additional calculation was performed for $\lambda_z = 400$ μm, which is a 3D mode when $|m| > 0$ (Fig. 3.21). Again, the dotted curves are from the completely analytic case (no current in the liner), while the solid curves use the diffusion model (including current in the liner). $B_z = 0$ again. Results again show that finite current in the liner reduces the growth rates for all modes. Like the kink mode, for the $k \approx 0$ case the sausage mode growth was negligible though the diffusive and surface current case showed nearly the same growth rate. The shorter axial wavelengths of the

sausage and kink mode appear to be more affected by the diffusive model as the results diverge quite a bit. The $m = 6$ mode shows substantial growth for a shorter axial wavelength (400 μm) but it is similarly reduced by finite current. Based on these analytic calculations, the overall trend seems to be that the larger m modes are affected by finite current for both long and short axial wavelengths, whereas the sausage and kink modes are most affected by finite current for shorter axial wavelengths.

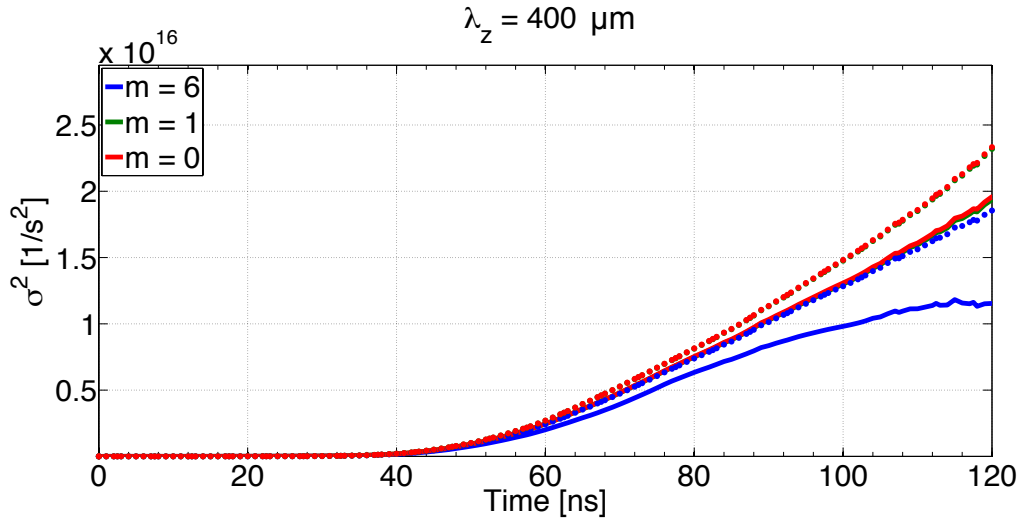

Figure 3.21: Comparison of instability growth rates for $m = 0, 1, 6$ modes with $\lambda_z = 400$ μm and $B_z = 0$. The solid curves include a finite current distribution in the liner using our analytic framework, while the dots are the completely analytic model with no current in the liner.

Lastly, a growth rate calculation was performed at a single time using the full 1D profiles from a HYDRA simulation. The governing ODE was solved using a finite difference formulation in an attempt to incorporate magnetic field and density gradients since the various azimuthal modes scale differently with each. The time selected was 77 ns (roughly halfway through the current pulse). The density and azimuthal magnetic field are plotted in Fig. 3.22. $B_z = 0$ for these calculations. Strong and weak density gradients are apparent and significant diffusion of azimuthal magnetic field is present. Because of the distribution of density and magnetic field

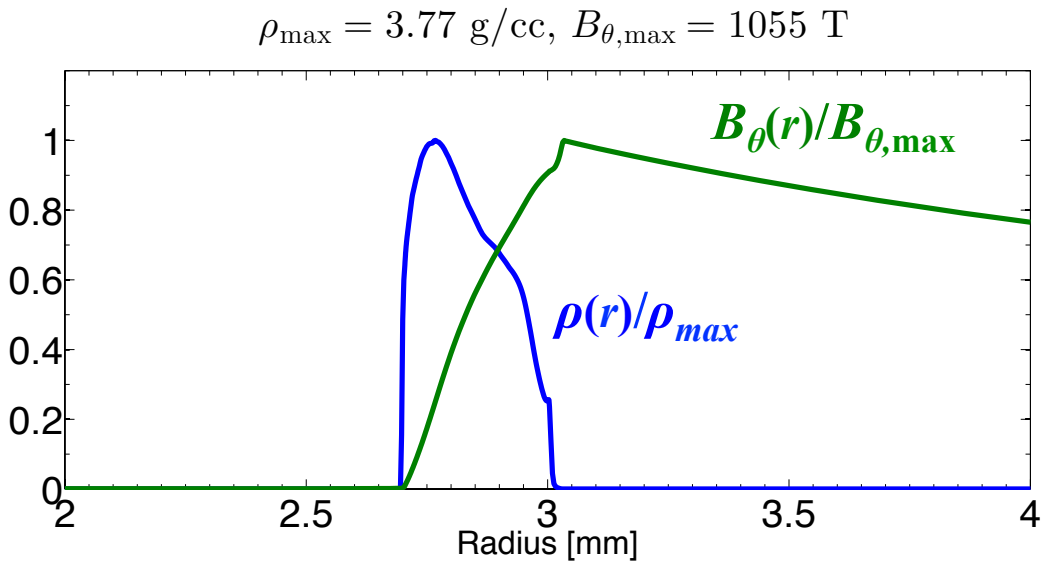

Figure 3.22: Density and azimuthal magnetic field distribution in an aluminum liner at $t = 77$ ns from 1D HYDRA simulation. At this time $g = 6.8 \times 10^{11}$ m/s^2 and $B_z = 0$.

there is the possibility of more solutions to the eigenvalue problem than just the four modes given by Eq. 3.45. This will quickly become apparent in the following plots and makes finding the correct eigenvalue much more challenging. To solve the eigenvalue problem, the governing ODE is discretized and solved via matrix methods. The boundary conditions are homogeneous the eigenvalue that solves the problem creates a singular matrix. Numerically it is not so simple to determine whether a matrix is singular. The method selected in this work is to compute the condition number of the matrix. An infinite condition number corresponds to a singular matrix.

Figure 3.23 shows the first of these calculations with $m = 6$. The value, $\omega^2 = \sigma$, in the title of the figure corresponds to the sharp boundary model solution of $\sigma = 1.07 \times 10^{16}$ in units of s^{-2}. For $\lambda_z = 400$ μm, the computed $\sigma = 8.27 \times 10^{15}$ which is slightly smaller than the sharp boundary model solution. However, for $\lambda_z = 10$ m ($k_z \approx 0$) the computed $\sigma = 3.75 \times 10^{13}$ is slightly larger than the sharp boundary model of $\sigma = 3.31 \times 10^{13}$.

Figure 3.24 shows the results for the kink mode. The value, $\omega^2 = \sigma$ in the title

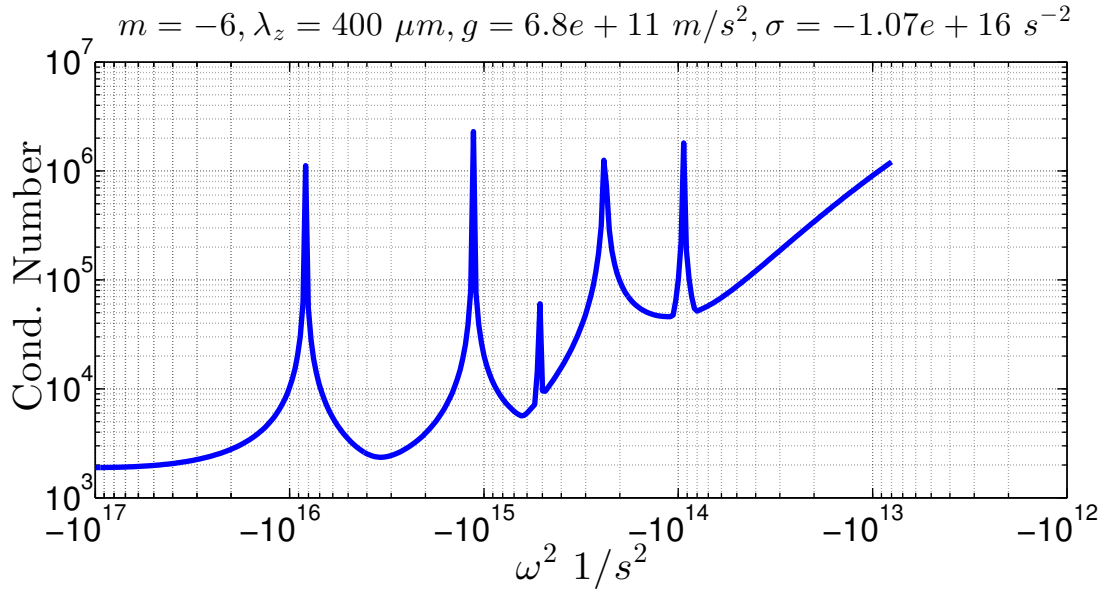

(a) Plot of matrix condition number for $m = 6$ and $\lambda_z = 400$ μm. The peaks correspond to solutions of the eigenvalue problem. The largest $\sigma = 8.27 \times 10^{15}\ s^{-2}$.

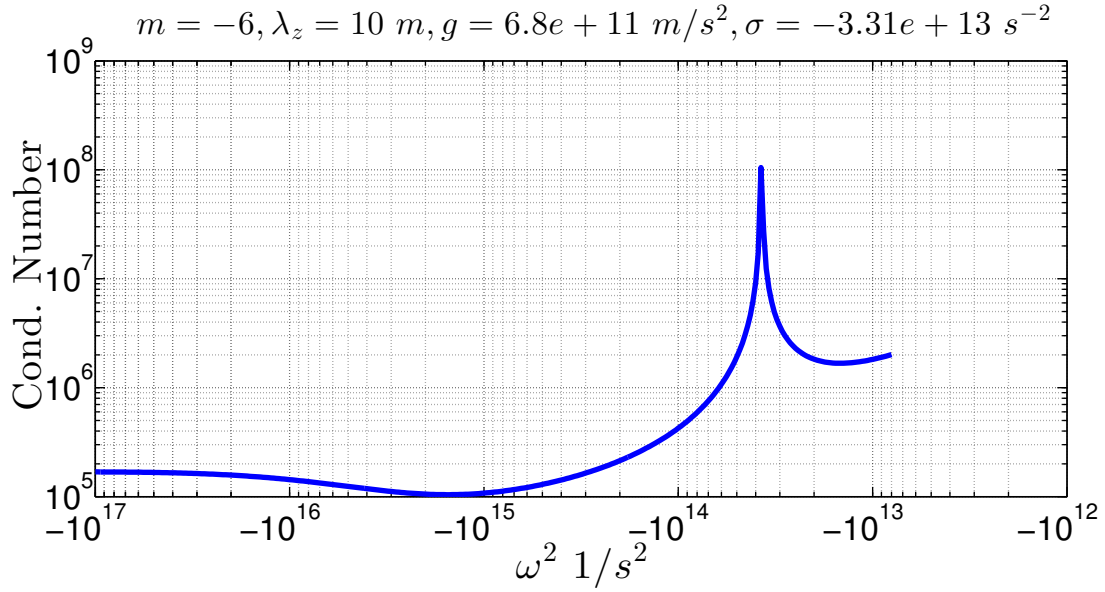

(b) Plot of matrix condition number for $m = 6$ and $\lambda_z = 10$ m. The peaks correspond to solutions of the eigenvalue problem. The largest $\sigma = 3.75 \times 10^{13}\ s^{-2}$.

Figure 3.23: Complete eigenvalue problem solution using a 1D HYDRA profile for density and azimuthal magnetic field for $m = 6$.

of the figure again refers to the sharp boundary model solution. For $\lambda_z = 400$ μm the computed $\sigma = 9.7 \times 10^{15}$ in units of s^{-2}, is again slightly smaller than the sharp boundary model solution of $\sigma = 1.2 \times 10^{16}$. More interestingly, for $\lambda_z = 10$ m ($k_z \approx 0$) the computed $\sigma = 2.13 \times 10^{13}$ is significantly smaller than the sharp boundary model result of $\sigma = 1.4 \times 10^{14}$. The growth rate is, in fact, quite similar to the $m = 6$ growth rate shown in Fig. 3.23(b). From the standpoint of the 2D (r, θ) simulations this is good news as the $m = 1, 6$ modes were observed to grow at roughly the same rate. Of course, this is only at one particular time however, this result makes much more sense when compared with the simulations (Fig. 3.18).

Lastly, Fig. 3.25 shows the results for the sausage mode. The two peaks at the largest values of σ are at 2.13×10^{16} and 1.17×10^{16}. Note that this corresponds directly to the benchmark case that was considered earlier in this chapter and in chapter 2. This means that the sharp boundary model solution in this case should work remarkably well and corresponds to the second peak. The first peak is thus, surprisingly large. Additionally, the $m = 0$, $k_z \approx 0$ case also shows a larger computed $\sigma = 6.67 \times^{10}$ than the sharp boundary model which is 8.96×10^9. This is another subtlety of using such a general solution technique. Examination of the eigenfunction solution for each mode shows different behavior. The eigenfunction solution for the first peak $\sim 2kg$ actually shows a peak in the low-density region of the profile. Essentially, this growth rate seems to correspond to growth in the lower density material as opposed to the bulk. The solution resembling kg shows an eigenfunction that more closely resembles the eigenfunction for the sharp boundary model, with a peak near the steep gradient and a decay into the bulk of the liner density. This is the main reason growth rates were calculated for one point in time. Calculations at additional times would likely best be served by recording multiple eigenvalues and the corresponding eigenfunctions as well as the location of the peak of the eigenfunction to determine more information about the mode. It is also clear that the shorter

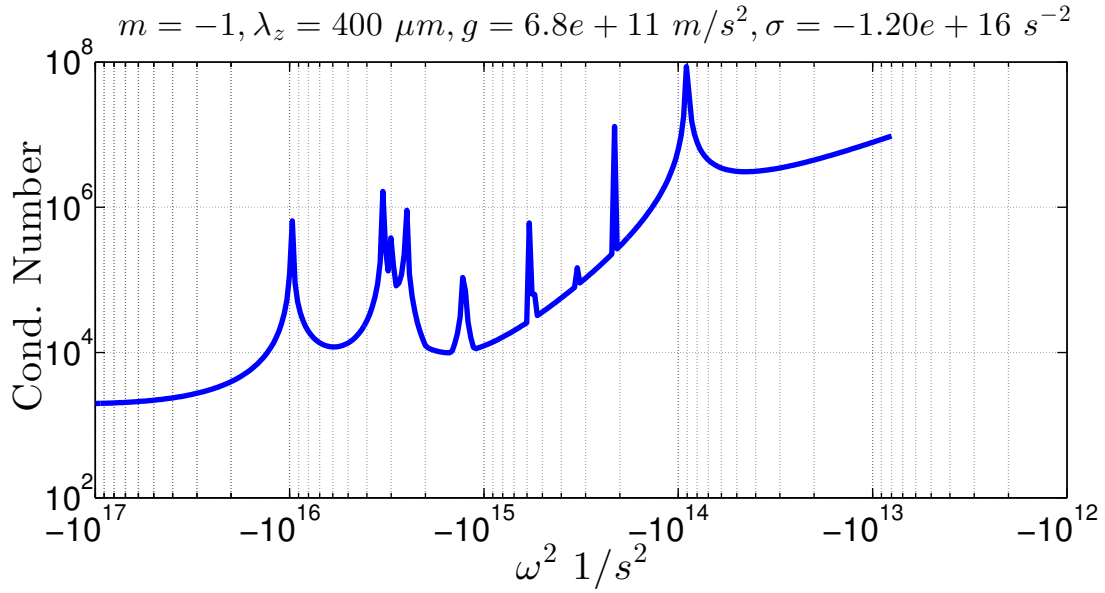

(a) Plot of matrix condition number for $m = 1$ and $\lambda_z = 400$ μm. The peaks correspond to numerical solutions of the eigenvalue problem. The largest $\sigma = 9.7 \times 10^{15}\ s^{-2}$.

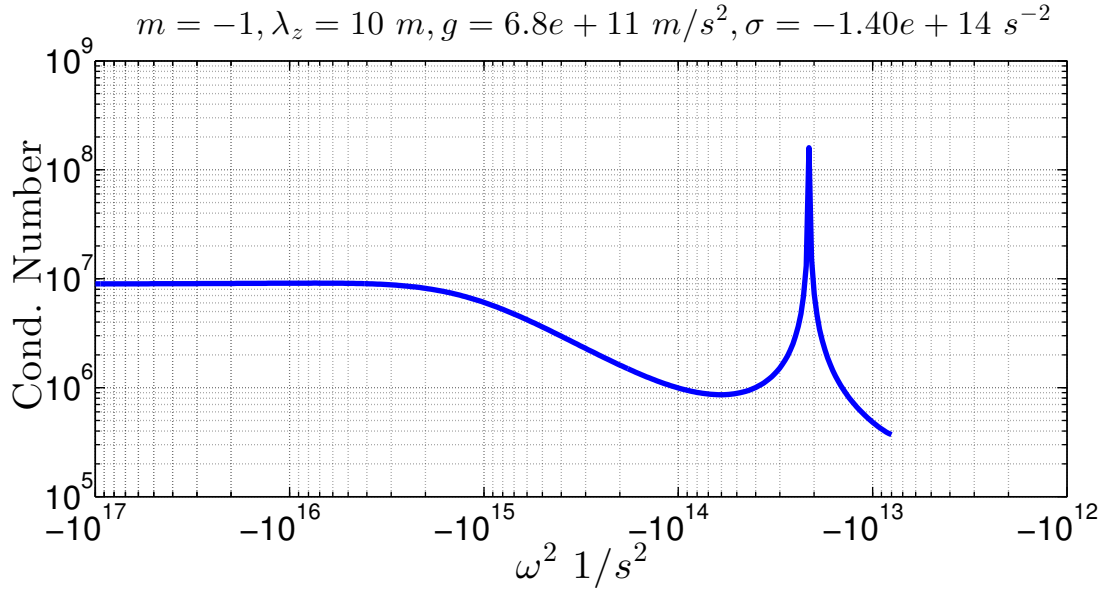

(b) Plot of matrix condition number for $m = 1$ and $\lambda_z = 10$ m. The peaks correspond to solutions of the eigenvalue problem. The largest $\sigma = 2.13 \times 10^{13}\ s^{-2}$.

Figure 3.24: Complete eigenvalue problem solution using a 1D HYDRA profile for density and azimuthal magnetic field for $m = 1$.

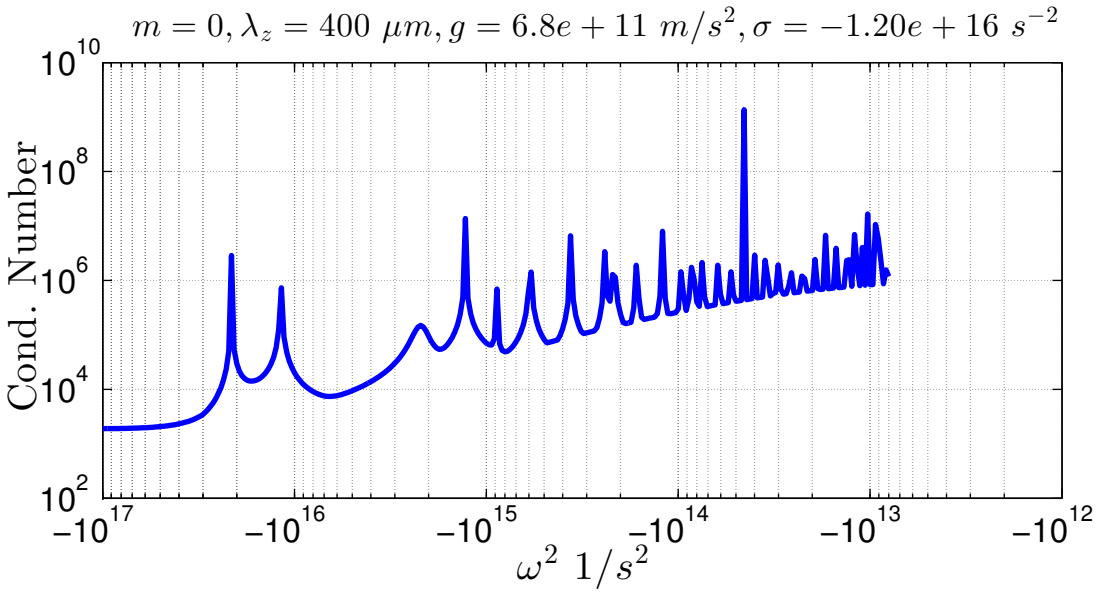

(a) Plot of matrix condition number for $m = 0$ and $\lambda_z = 400\ \mu$m. The peaks correspond to solutions of the eigenvalue problem. The two peaks at the largest values of σ are at 2.13×10^{16} and $1.17 \times 10^{16}\ s^{-2}$.

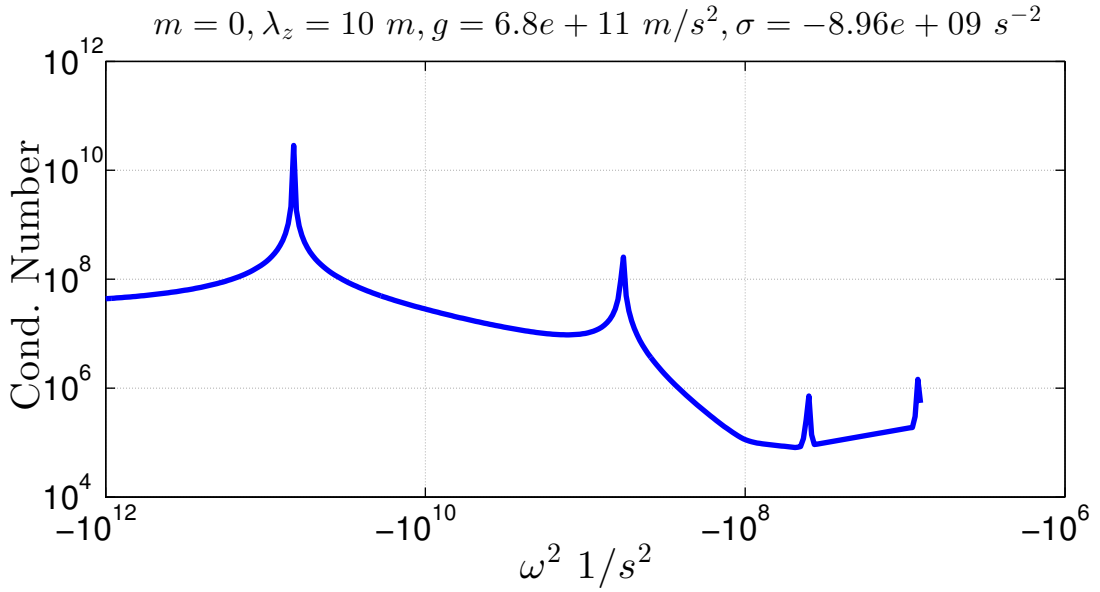

(b) Plot of matrix condition number for $m = 0$ and $\lambda_z = 10$ m. The peaks correspond to solutions of the eigenvalue problem. The largest $\sigma = 6.67 \times^{10}\ s^{-2}$.

Figure 3.25: Complete eigenvalue problem solution using a 1D HYDRA profile for density and azimuthal magnetic field for $m = 0$.

wavelengths show much more complicated solutions.

This is perhaps one of the most advanced calculations possible using a linearized ideal MHD model. However, the calculations are also significantly more involved and it is not clear the obtained growth rates are significantly more accurate. Certainly, we have found some significant differences in growth rates between the two calculations. The largest differences in the maximum growth rate were observed for long axial wavelengths and for $m = 0$ or $m = 1$. Including just the finite current into the sharp boundary model for these same modes (Fig. 3.20) did not show these differences. However, Fig. 3.20 used a simple diffusion model as opposed to the actual HYDRA calculated diffusion. Fig. 3.20 also did not account for the lower density material at the exterior of the liner. If the full profile growth rate calculations can accurately model the azimuthal modes, the method would be of substantial benefit but more work is needed on that front. Nonetheless, the longer axial wavelengths seem more influenced by finite azimuthal magnetic field in the liner. In these cases, the effect of density gradients is also minimized for MRT since the effect enters the dispersion relation as $kg/(1 + kL)$ where L is the density scale length. Lastly we note for the shorter 400 μm axial wavelength, a large number of eigenmode solutions are introduced.

3.5 Conclusion

This chapter introduced, developed, and applied a cylindrical three-region sharp boundary model to understand the coupling of MRT and the sausage and kink modes in a finite thickness liner. As in the planar description, magnetic field line bending can reduce MRT growth and feedthrough. The azimuthal magnetic field, unlike the planar case, can also drive additional instability. In general, this effect increases the overall instability growth rate as compared to the Cartesian formulation especially for short axial wavelengths. With only an azimuthal magnetic field, the $m = 0$ sausage mode has the dominant MRT growth rate. Introduction of an axial magnetic field

reduces the overall growth rate of instability but makes the dominant MRT mode helical ($m > 0$). As anticipated, the thinnest liners are overall the most unstable regardless of B_z and g. High compression of an axial magnetic field in the central region of the implosion can significantly suppress the sausage mode, however the kink mode growth remains very robust. Thus, at high compression, the kink mode is expected to dominate. In some sense, this is like a tokamak, where a strong axial magnetic field is present.

Because of finite conductivity in the liner, it is possible that $m = 2$ and larger modes may also be important. As was thoroughly discussed within this chapter, the higher m numbers are stabilized in ideal MHD field due to line bending stabilization. As azimuthal field diffuses into the liner, this current may drive instability. Yet if there is now additional field line bending in the liner, this is also stabilizing, but again, finite conductivity reduces this stabilizing effect. 2D (r, θ) simulations have shown that the azimuthal modes do indeed grow faster than anticipated by ideal MHD. However, it is difficult to separate out the effects contributing to instability growth at this point. Finite current within an imploding liner was considered via numerical integration of the linearized ideal MHD equations in cylindrical geometry using both an idealized model and the full 1D radial profiles from 1D HYDRA simulations. Many more unstable modes were obtained for the numerical results when using the full 1D profiles than the (at most) two from the analytic theory (Eq. 3.44). The analytic ideal MHD results predict a larger growth rate for the kink mode than for $m = 6$. However, the fully integrated calculation gives very similar growth rates for both modes as was found in 2D simulations.

Based on the challenges with the purely azimuthal modes, more work is needed to determine how well the analytic equations describe the evolution of fully 3D modes. Additionally, while feedthrough of the sausage mode is fairly straightforward to simulate, the kink mode is the more dangerous one when B_z is present but also may

be more difficult to model due to the same problems with modeling MRT. What is required to make these comparisons are accurate 3D simulations. The sharpness of the helices and very specific mode numbers (in m and k) that were observed in the experiments by Awe et al. [55] present the biggest challenge in comparing (unseeded) 3D simulations and experiments. We remark that, using the eigenmode solution, we have resolved a major puzzle [9] on why the observed helices in Awe et al. [54][55] did not wind up despite the ratio B_z/B_θ becoming increasingly smaller as the current increased. There is still more work that can be done with understanding feedthrough. The next chapter will change focus from the evolution of instability on the liner outer surface to the stability of the inner surface.

CHAPTER IV

Study of Liner Inner Surface Stability

4.1 Introduction

In the previous chapters, the magneto-Rayleigh-Taylor (MRT) instability in planar and cylindrical geometry has been studied in depth in magnetically driven pulsed power loads. Many of the cases were idealized to best understand the link between the linear theory and simulation results. This chapter will focus on a number of non-ideal and nonlinear effects in liner implosions, in particular, the effect of shock compression on feedthrough, the generation of long wavelength MRT, subsequent feedthrough from surface roughness, and some considerations related to the impact of the MagLIF preheat on the inner surface. The first two physical processes are beyond our ideal MHD model because of the incompressible equation of state (EOS) and linearized equations used. The incompressible EOS implies an infinite sound speed in the material such that the inner surface is instantly aware of the conditions on the outer surface. In many cases however, loads on pulsed power machines, such as Z, are shock compressed while concurrently accelerated. The incompressible assumption has actually worked quite well for the MRT unstable surface as was presented in the previous two chapters, even if a more sophisticated EOS is used in the simulations. However, a sufficiently strong shock would create a very different scenario at the inner surface depending upon its initial conditions. Such a shock effectively isolates

the perturbed and accelerating material from un-perturbed material. This, in essence, limits the communication between the outer and inner surface until the shock reaches the inner surface, at which point feedthrough can occur between the two interfaces. The net effect is to introduce a time delay to feedthrough. Additionally, when a shock is driven non-uniformly in the material, whether from initial surface perturbations or non-uniform drive, more complications are introduced at the inner surface. Lastly, in the MagLIF concept, preheating the fuel deposits 0.1-4 kJ of energy into a deuterium fill gas, launching a blast wave towards the liner surface [38][39][27]. This hot gas can then deposit considerable energy in the liner inner surface when the blast wave reaches it. The heating itself can lead to ETI [17]-[19] if there is significant axial or induced azimuthal current at the surface. Non-uniform heating of the surface can introduce large perturbations to the inner surface due to ablation of material. From our results in Chapter 2, we know that perturbations on the inner surface can feed back to the outer surface seeding additional MRT growth. These issues will be examined in this chapter.

Once again, aluminum will be the material of choice though a few beryllium simulations will be presented to understand some material dependent effects. The organization of this chapter is as follows. (1) First we will examine feedthrough of MRT in roughened liners, where the roughness emulates that found in machined liners with wavelengths on the order of 1-10 micron. These wavelengths are too short to feedthrough, for sufficiently thick liners, but as the liner is accelerated, nonlinear effects cause the dominant wavelength to increase to the point where the feedthrough factor becomes large. Feedthrough will be compared with and without an axial magnetic field, as this field is found to reduce feedthrough from ideal MHD calculations. (2) We will consider pre-seeded liners in concert with shock compression, with well-defined wavelengths machined on the inner surface. For long enough wavelengths, this can drastically alter the stability of liner. The effect of a water fill to hasten deceleration

RT, as well as other effects will also be reported.

Lastly, as we will be considering a variety of different initial conditions on the inner surface, it is best to provide early definitions here. In this chapter, we will use 'seeded liners' when relatively large amplitude, long wavelengths are seeded sinusoidally on one or both of the liner surfaces ($\lambda_z \sim$ 100s of microns). For our purposes, a 'seeded liner' will have, at most one or two seeded wavelengths present. When the seeded sinusoidal perturbation is not present on the surface we will call the surface 'smooth'. If necessary, we can also 'roughen' any smooth surface to include the quasi-random small amplitude, short wavelength perturbations naturally found on a liner. We will avoid use of the word 'seed' as related to these random perturbations and do not consider additional roughening of sinusoidal perturbations. Lastly, a 'clean' surface is a surface with absolutely no perturbations present on the surface.

4.2 Rough liners

In 2D (or 3D) simulations, a perfectly smooth liner is a liner without any initial surface perturbations. Liners fielded in experiments always have some sort of initial roughness depending on the material and method used to prepare the liner. In laser fusion, the ultimate goal is to produce a spherical capsule with as small perturbations as possible, on both inner and outer surfaces, to reduce the initial seed for the Rayleigh-Taylor instability [30]. Liner implosions at Sandia have shown that the initial surface condition may not be so important due to the presence of other early-time instabilities such as the electrothermal instability (ETI) [17][18]. However, the ability of 3D codes to show the same insensitivity is somewhat in question [55]. In order to obtain the helical structure observed in experiments [55], 3D simulations had to be initially seeded with the helix. Additionally, the resolution requirements to model ETI growth are substantial due to the very short wavelengths intrinsic to ETI and the following simulations will not attempt to model this effect. The goal of

this section is to then understand whether feedthrough of MRT can be reduced by an axial magnetic field. It will be shown this can be accomplished so long as reasonable long wavelength MRT appears on the liner exterior. This is captured in 2D HYDRA simulations by the nonlinear evolution of MRT from short to long wavelengths.

Roughening a liner surface may provide a seed for ETI. This instability may be the precursor to MRT, however resolving the instability is beyond the resolution of the simulations presented for the most part as already mentioned. The shock breakout can also heat the inner surface; perhaps driving ETI if axial current diffuses to the surface, or it is also possible that ablation may effectively anneal the inner surface. Some simulations of this sort of scenario are presented in Peterson et al. [18]. ETI at the inner surface could lead to mix of liner material into the gas leading to subsequent Bremsstrahlung losses. An in-depth study of ETI at the inner surface is necessary to determine whether it can be more detrimental than feedthrough. Our focus is on feedthrough of longer wavelengths on the order of the liner thickness, where $e^{-k\Delta}$ is appreciable. These modes are the most dangerous for the overall liner integrity since they can significantly deform the whole liner; as opposed to smaller λ_z which have much smaller feedthrough and affect only the outer surface. In these rough liners, feedthrough is initially predicted to be quite small as MRT wavelengths are very short and the liner is thick. Over the course of the implosion, MRT tends to evolve to longer wavelengths, on the order of 0.5 to 1 mm [53][55]. These wavelengths have much larger feedthrough factors and are also the most dangerous MRT modes as the wavelengths are of the order of the liner thickness. In general, this requires following the liner implosion through fairly large convergence ratios while maintaining resolution in the liner, increasing the computational requirements. The result is that these simulations are the most computationally taxing presented thus far.

The common materials of interest for MagLIF are aluminum and beryllium. Both have been used extensively for direct study of MRT, though beryllium is the current

material of choice for ICF implosions. There are many benefits to using beryllium. It is low-Z (smaller Bremsstrahlung losses if material mixes into the fuel), can be made thicker for the same mass (more robust to feedthrough), and can have a higher implosion velocity (more energy into the fuel) [12]. A useful property of Be for the purposes of studying MRT is that both the inner and outer surface of the liner are visible to the 6.151 keV x-ray radiography used on the Z-accelerator due to its much lower opacity (2.24 cm^2/g compared to 102 cm^2/g).Beryllium does tend to have higher amplitude surface irregularities due to machining the liner [51]. The surfaces of targets made out of both materials have been extensively characterized [51][53] and show typical wavelengths on the order of microns, with RMS amplitudes on the order of 10s-100s of nanometers, with larger divots on the order of microns. Beryllium typically has overall larger amplitude modulations [51]. HYDRA 2D simulations will be extensively employed so we will assume azimuthal (m = 0) symmetry for all axially machined modes, or $\lambda_z \to \infty$ for (r,θ) simulations.

Before progressing further, some limitations of 2D (r, z) simulations are acknowledged. The first being $m = 0$ azimuthal symmetry is strictly enforced. Implosions of these targets also show no discernible azimuthal symmetry [51][53] early on, before the long wavelengths develop. In essence, these 2D simulations likely overestimate short wavelength MRT growth and as such we consider this the worst case for these liner implosions [53]. The goal of these 2D simulations is to show enhanced stability to the feedthrough of MRT when an axial magnetic field is compressed. Flux compression of the field is the main method of achieving such high field strengths on MagLIF without covering the whole experiment in high current coils to achieve 100s of Tesla throughout the experiment. As was shown in the previous chapter, the sausage mode is affected most strongly by B_z. However, the kink mode is known to be extremely important for pre-magnetized implosions and cannot be modeled in 2D. The importance of the kink mode has been extensively discussed in chapter 3, in our

paper [9], and shown in Sandia experiments [54][55].

4.2.1 Simulations of roughened cylindrical liners

We begin with 2D (r,z) simulations of 'roughened' Al liners with inner radius, $r_i = 2.876$ and outer radius, $r_e = 3.168$ mm which gives a thickness of $\Delta = 292$ μm, the same as in Sinars et al. [51]. The liners are also driven with the same current pulse from Z-machine (Fig. 2.8). Redrawn in Fig. 4.1, shot z1965 obtained a peak current of nearly 20 MA pulse in 150 ns. *Note that all times in subsequent figures in this chapter refer to the current timing in Fig. 4.1.* The tube is filled with a 2.5 mg/cc deuterium gas at room temperature. As in previous chapters, this pulse will

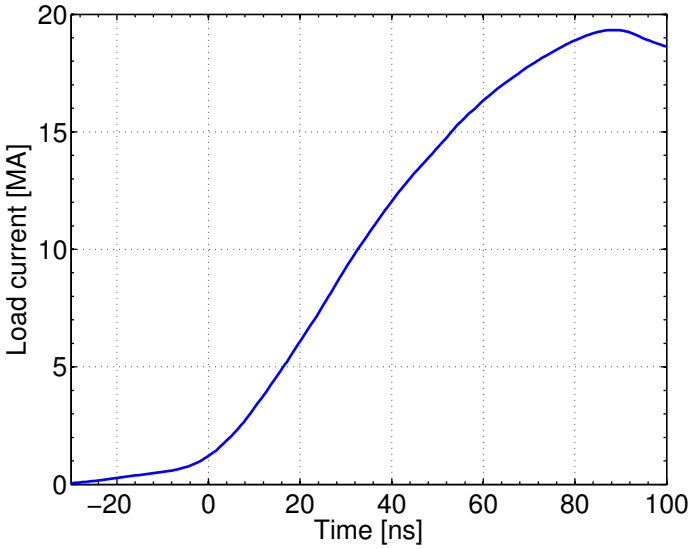

Figure 4.1: Current drive of shot z1965 [51].

be used for the remainder of the paper as it is representative of a typical pulse on Z. To impose a surface roughness on the liners we simply deform the mesh slightly at the outer boundary (or inner for roughness on both sides) along the axial direction, according to either random noise, or assigned from an FFT spectrum. We will present the results of two different resolution simulations using a random surface. By virtue of the different resolution, this effectively compares two very different initial surfaces.

The lower resolution simulations were designed to be fast and a proof of concept. They used an axial length of 1.2 mm with an axial resolution of $\sim$10 μm. The higher resolution simulation had an axial length of 0.8 mm with axial resolution of $\sim$1.5 μm. For the high-resolution case, this is sufficient to resolve wavelengths as short as 15 μm taking at least 10 zones/wavelength. For low resolution, the shortest wavelength resolved is $\sim$ 100 μm. This low resolution case still has higher axial resolution than most 3D simulations [53][55]. The first simulation includes longer possible wavelengths to feedthrough, while the second better simulates the evolution of shorter wavelengths to longer. It is possible the high resolution simulation can capture some amount of ETI [17] at early times. The random surface was constructed by the formula $r = r_0 + a_0(2\zeta - 1)$ where $r_0 = 3.168$ mm is the unperturbed radius, $a_0 = 37.5$ nm and ζ is a random number between 0 and 1. The lower resolution simulation used $2a_0$ to accommodate better gridding. The result is a very small initial random perturbation on the liner outer surface, sufficient to initiate MRT from very small amplitude, short wavelength perturbations. The two surface spectra are presented in Fig. 4.2. Note, these spectra are not from actual measurements.

Based on the results found in previous chapters, the 10 T magnetic field is expected to minimally impact the development of axial MRT modes on the exterior of the liner in 2D. The greatest potential for impact exists for the shortest wavelengths since they exhibit the strongest stabilization. Though it is possible magnetic diffusion effects could overwhelm this. Consider an initial wavelength perturbation with amplitude $\xi =\sim 5$ μm, then the diffusion time is $(\eta_{Al}/(\mu_0\xi^2))^{-1} \approx 1$ ns. As the aluminum heats, increasing the resistivity, the diffusion time reduces further and subsequent field line bending is reduced. Experimental results for beryllium liners also show a fairly consistent axial wavelength, independent of the applied axial magnetic field. Of course, the axial magnetic field does affect the overall MRT development in 3D, but such interesting problems are outside the scope of this chapter.

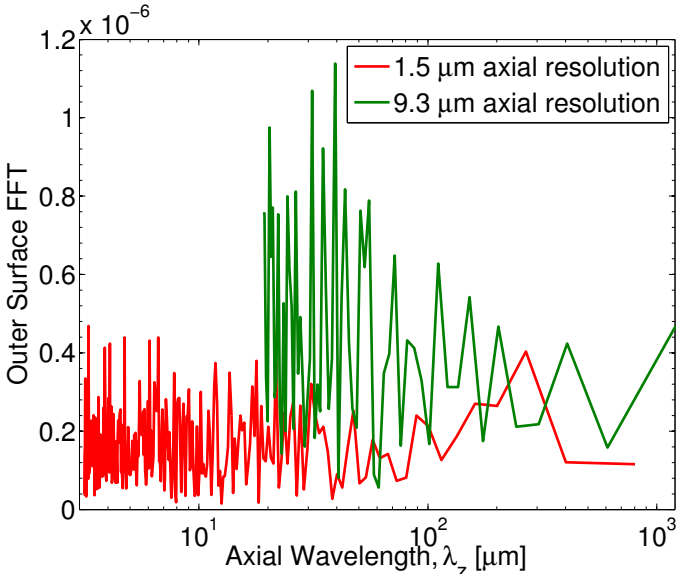

Figure 4.2: Initial liner surface spectra used as seeds for roughened liner implosions. FFT units are cm^{-1}.

We begin by examining the early time growth of MRT as the current begins rising and the bulk of the liner is not yet moving. During this phase there is rapid heating of the rough liner surface and azimuthal field begins to diffuse through the liner. As the current ramps up through to 45 ns (Fig. 4.1), initial evolution of the outer surface remains nearly identical with and without an axial field. If we neglect stabilization by magnetic tension, MRT unstable regions require $\nabla p_{tot} \cdot \nabla \rho < 0$. This condition is satisfied through the majority of the liner surface due to very large magnetic pressure exterior to the liner. This is a complicated period of growth as the liner is expanding and being decelerated by magnetic field which eventually becomes large enough to implode the material. The ablating/expanding material can carry axial magnetic field. This induces a small azimuthal current on the order of 10^6 $\mathrm{A/cm}^2$, corresponding to $\nabla \times \vec{B}$, however, this seems to contribute very little to the overall heating of the liner exterior. However, this could contribute to the larger amplitudes at longer wavelengths for the $B_z = 30$ T case. This is evidenced in Fig. 4.3 where the MRT is again analyzed by looking at a 50 % transmission contour and subse-

quent FFT plotted. The data are analyzed directly from the HYDRA simulation so as not to include any instrumental resolution limits though the resolution is bounded by the grid resolution. As anticipated, the shortest wavelengths grow the quickest but transition to longer wavelengths as the current continues to ramp. By 45 ns, the largest perturbations have wavelengths just under 100 μm. Thus, in about 25 ns the dominant wavelength has moved from $\sim$ 10 μm to $\sim$ 100 μm. At 45 ns, the

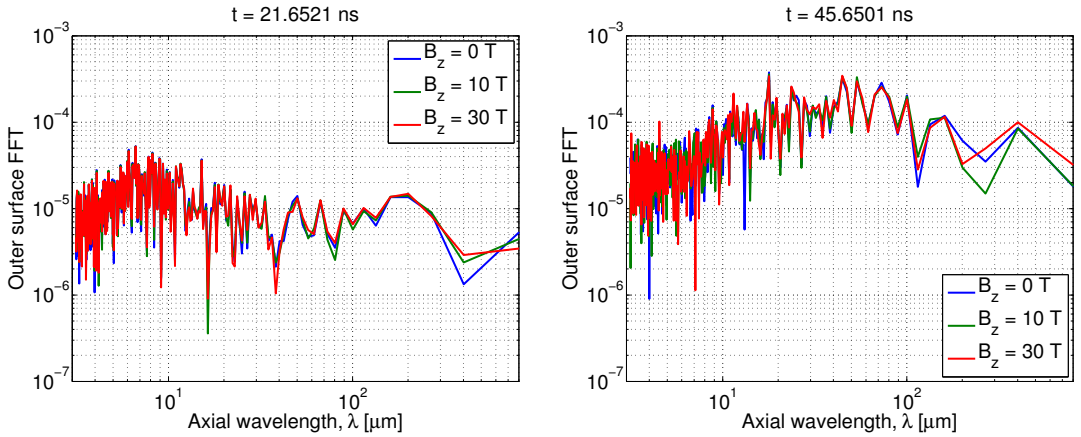

(a) FFT of liner outer surface at $t = 21$ ns ($\sim$ 6 MA) for high resolution case (1.5 μm axial resolution).

(b) FFT of liner outer surface at $t = 45$ ns ($\sim$ 12 MA) for high resolution case (1.5 μm axial resolution).

Figure 4.3: Structure of outer surface perturbations during current ramp up phase for high resolution case (1.5 μm axial resolution).

only difference between three cases occurs for very long wavelengths (where the 10 T case shows slightly less growth) and for very short wavelengths where the 30 T case shows overall smaller mode amplitudes if the spectra are integrated. The effect seems negligible at this point. Otherwise the differences between the simulations for the MRT structure are minute this early in time.

As the MRT is developing over this time period, a shock wave develops from the liner exterior and propagates through the bulk of the liner. *For these rough liners with random small seeds, the shock is relatively unimportant from the standpoint of feedthrough.* However, it is important in the sense that our feedthrough theory is incompressible, which precludes a shock. Only once the shock has broken out of the

inner surface can we consider the two surfaces linked. Ahead of the shock the inner surface is motionless and unaware of the shock compression of the liner. Hence, there is an intrinsic delay time for feedthrough to begin. In the incompressible limit, there is no shock (the sound speed, $c_s \to \infty$) and the two surfaces are in communication instantly. Additionally we note that upon shock breakout the liner inner surface temperature is raised to roughly 0.1 eV (4x ambient temperature) in 4 ns which is above the melting temperature of aluminum. In terms of Fig. 4.1, shock breakout occurs at roughly 45 ns. The remainder of the discussion of the shock dynamics is deferred to the section on seeded liners.

Once the shock breaks out, feedthrough can occur at the inner surface. Figure 4.4 plots the FFT of the inner surface just after shock breakout (at the same time as Fig. 4.3(b)). Keep in mind, just before this time, the inner surface is completely flat. While it is possible that some longer wavelengths could ride on the shock front (see next section), the short wavelengths present on the exterior are effectively cutoff by the thickness of the liner and cannot feedthrough. The very short wavelengths observed in the FFT cannot be differentiated between noise and ETI, however the inner surface is RT stable at this point. The axial current density is on the order of $\sim 0.5 \times 10^7$ A/cm^2 near the interface. The axial field marginally reduces the inner surface amplitudes at this point. The differences at longer wavelengths are nearly imperceptible. Long wavelengths are also near the axial length of the simulation so the amplitudes are likely somewhat under-estimated but nonetheless are indicative of the start of feedthrough.

The effective feedthrough factor is the ratio of the inner surface FFT to the outer surface FFT and would roughly scale as $F(k) = \exp(-k\Delta)$, neglecting any magnetic field line bending. Although the rippling on the inner surface is very low amplitude, it is clearly dominated by long wavelengths, as we would expect. These long wavelengths are much harder to see in the MRT structure as it is still dominated

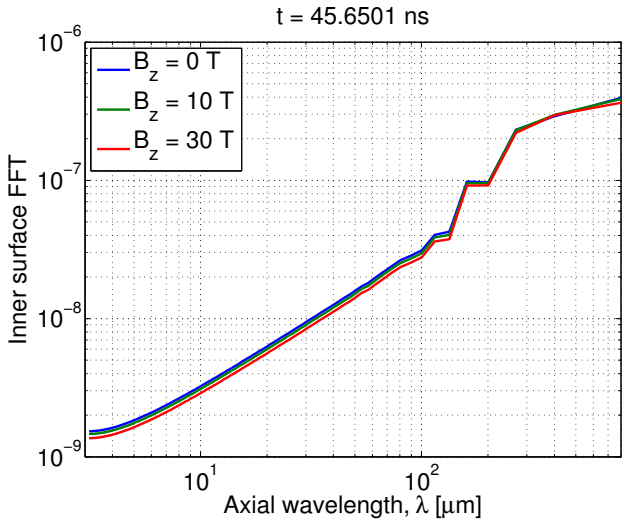

Figure 4.4: Liner inner surface FFT after shock breaks out for the high resolution case (1.5 μm axial resolution). The long wavelengths present are traced to feedthrough, while the short wavelengths are likely a combination of ETI from the shock heated surface and grid noise. The axial current density is on the order of $\sim 0.5 \times 10^7$ A/cm^2 near the interface. Note that wavelengths shorter than 100 μm cannot feedthrough substantially. Note, there is no preheat, just fill gas as in Awe et al. [55].

by large wavenumbers. Nonetheless, the ratio of the 400 μm mode amplitude from inner to outer surface is 0.75 % $\approx F(\omega(k))$. This is essentially the instantaneous feedthrough factor for the 2D simulation at 400 μm wavelength. Because the liner expands and compresses in these simulations the density is non-uniform, making the determination of Δ for the analytic feedthrough factor difficult. This is particularly a problem when MRT can deform the liner enough via mass redistribution, such that the thickness significantly varies with axial position (something not captured in a 1D simulation). Plugging in $F(400 \text{ um}) = 0.0075$ the effective thickness is 311 μm (293 μm) for the uniform roughness (peaked) case, which is quite reasonable. The analytic feedthrough factor also goes to zero much faster for short wavelengths than found in the simulations which is consistent with the conjecture that they are present due to a combination of ETI and grid resolution limits. Direct comparison between the analytic feedthrough factor and simulation results becomes more difficult as the

MRT bubble and spikes grow and become more diffuse (as time increases). When this happens the concept of a liner 'thickness' becomes more ambiguous which reduces the efficacy of our sharp boundary model. This not only introduces additional uncertainty into what we call the liner thickness, but also the true MRT amplitude. The longest wavelengths' amplitude are also the most difficult to measure accurately via the FFT.

Another useful metric for the inner surface is the time evolution of the RMS amplitude. Since HYDRA can maintain a Lagrangian interface and the inner surface is not very diffuse, this is a simple calculation. This is plotted in Fig. 4.5(a) and displays some rather interesting features, some best illustrated by plotting versus the convergence ratio, CR, (see Fig. 4.5(b))

$$CR = \frac{r_i(t=0)}{r_i(t)}. \tag{4.1}$$

Over the majority of the implosion, the RMS amplitude does not vary much between the magnetized and un-magnetized cases. In fact, there is a short period of time where the magnetized cases exhibit larger amplitude perturbations. The mechanism behind this appears to rely on the additional ohmic heating of the inner surface by azimuthal current induced by spatially (and temporally) varying axial magnetic field. This tends to heat and ablate the inner surface leading to additional motion and larger density gradient scale lengths. As time continues on, the axial magnetic field is compressed and the RMS amplitude of the un-magnetized case overtakes the magnetized cases as anticipated. When plotted against CR, it is very clear that the axial field can strongly suppress growth of ripples on the inner surface. The highest published CR of a liner implosion observed via radiography thus far at Sandia is $CR = 7$ and included a 10 T axial magnetic field [55]. Recent experiments have reached $CR = 20$ (via private communication with Kyle Peterson). However, even for aluminum at

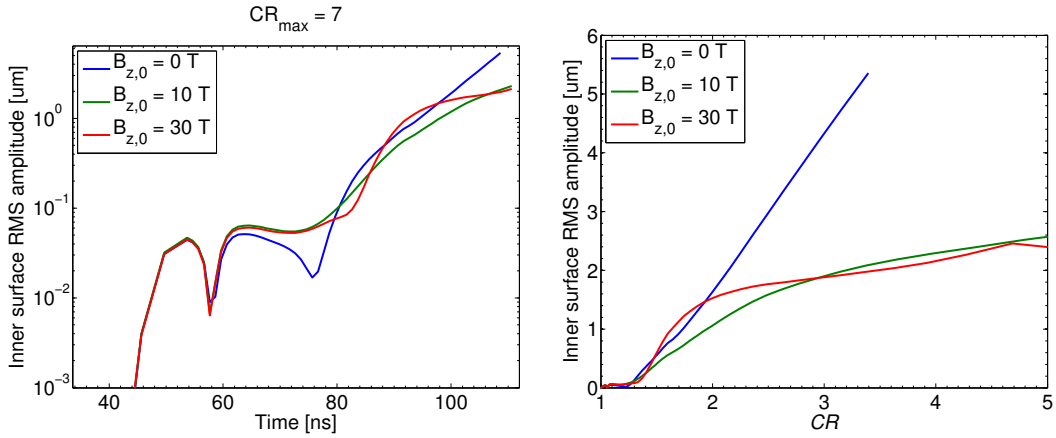

(a) RMS amplitude of inner liner surface as a function of time for high resolution case (1.5 μm axial resolution).

(b) RMS amplitude of inner liner surface as a function of convergence ratio, CR for high resolution case (1.5 μm axial resolution).

Figure 4.5: RMS amplitude of liner inner surface of the high resolution case over duration of the liner implosion for various degrees of pre-magnetization. Note, there is no preheat, just fill gas as in Awe et al. [55].

$CR = 3.4$ there is a noticeable impact on the inner surface evolution. For the slower aluminum implosion, the 30 T case begins to affect the overall implosion dynamics of the simulations (i.e., the three simulations have slightly different CR at the exact same time). This means that the magnetic pressure due to the compressed axial magnetic field (for 30 T) in the fuel region begins to slow the implosion. This is one potential explanation for why the 30 T case does not show significantly more stabilization of the inner surface. Additionally, the consequences of finite resistivity may also play a role in allowing the tension in the bent magnetic field lines to relax. Lastly, the distribution of axial magnetic field is different between the 10 and 30 T cases.

In order to directly compare the three simulations we will compare the inner surface conditions at $CR = 3.4$. Figure 4.6 shows the inner surface FFT at $CR = 3.4$ for all three axial field levels and shows markedly different behavior than observed early on in the implosion (c.f., Fig 4.4). An important feature of the simulations is that the axial magnetic field is not distributed uniformly in the fuel region. On

average, the 10 T field is compressed to $\sim$ 100 T and the 30 T case is compressed to roughly 340 T. The peak axial field is actually found to be largest for the 10 T case, however, the average axial field is smaller. This is because, for the 10 T case, the magnetic pressure remains a smaller fraction of the total pressure in the fuel region is thus easier to compress. Despite a three-times larger axial field for the 30 T case, both 10 and 30 T cases' surfaces look nearly the same as shown in Fig. 4.5(b). The

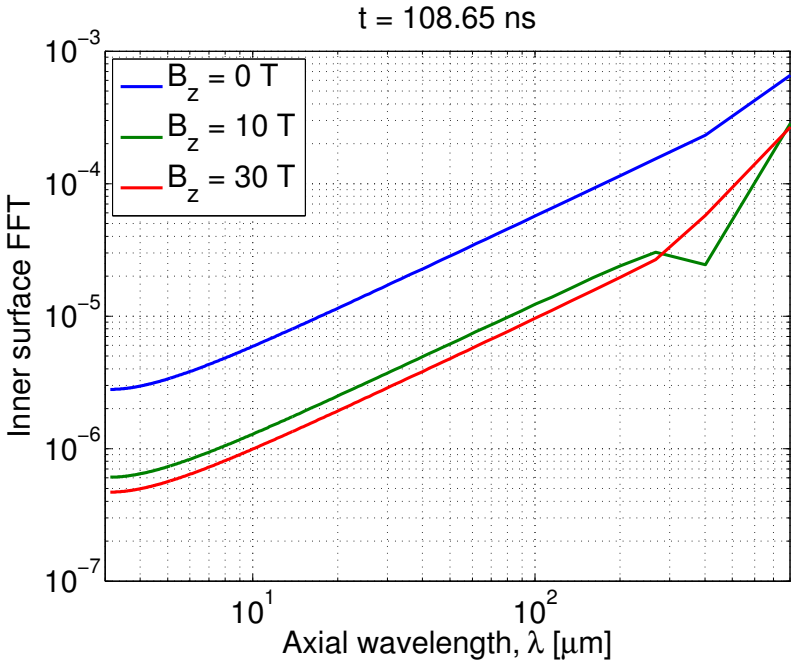

Figure 4.6: FFT of inner surface of aluminum liner at $CR = 3.4$ for $B_z = 0, 10, 30$ T for high-resolution case (1.5 μm axial resolution). Note, there is no preheat, just fill gas as in Awe et al. [55].

initial flux in the fuel region, $B_{z,0}\pi r_i^2$ can be compared to the flux in the fuel region at $CR = 3.4$ for an estimate of flux compression efficiency. For both $B_{z,0} = 10, 30$ T, at $CR = 7$, the fuel retains 80 % of the initial flux. This does not account for losses due to the Nernst effect [12] which could be present in a pre-heated MagLIF experiment where the temperature gradients between the fuel and liner can be large. The net result is that the axial magnetic field strength could overall be smaller in the fuel region in a fully integrated experiment; for these cases without preheat, this is a

small effect. As discussed in Chapter 3, the kink mode could be the most dangerous mode feeding through, but these results show that feedthrough of the sausage mode is reduced for pre-magnetized implosions. For the sausage mode, both growth rate and feedthrough are less than the kink mode. So the kink mode dominates at stagnation. This is most important for seeding perturbations that may grow during deceleration. Additional complications may arise when preheat of the fuel is considered and will be briefly discussed later in this chapter.

Similar trends are obtained for the lower resolution case where the axial resolution is 10 μm instead of 1.5 μm. Figure 4.7(a) shows the FFT of the inner surface again at $CR = 3.4$ and once again shows that with increasing axial magnetic field strength mode amplitudes are reduced. However, the $B_z = 10$ T is significantly different from the 30 T case unlike the higher resolution case (Fig. 4.6). The RMS amplitude of the inner surface also shows somewhat different results for the two magnetization levels, shown in Fig. 4.7(b). Additionally, the lower resolution case, Fig. 4.7(b), shows amplitudes rough twice that of the higher resolution case (Fig. 4.5(b)). This is likely due to a few factors. First, the lower resolution simulation contains a larger axial extent, allowing longer wavelength MRT to develop and to feedthrough (longer wavelengths feedthrough more). Secondly, the initial surface seeds were different. The average RMS amplitude of the initial perturbations was about a factor of two larger for the low-resolution case. The initial factor of two could persist to later times and could contribute to the difference between the two simulations. A factor of two would be apparent in linear theory, however it is more difficult to predict the nonlinear interactions. Lastly, the lower resolution simulation implosions were slightly faster, marginally changing the dynamics of the implosion (higher acceleration for the lower resolution case). In this respect, one way the resolution can influence the implosion is by affecting the magnetic pressure felt by the liner which then affects the trajectory of the liner (i.e., if the peak field is slightly larger, this results in larger acceleration).

Certainly, additional high-resolution simulations should be performed with varying

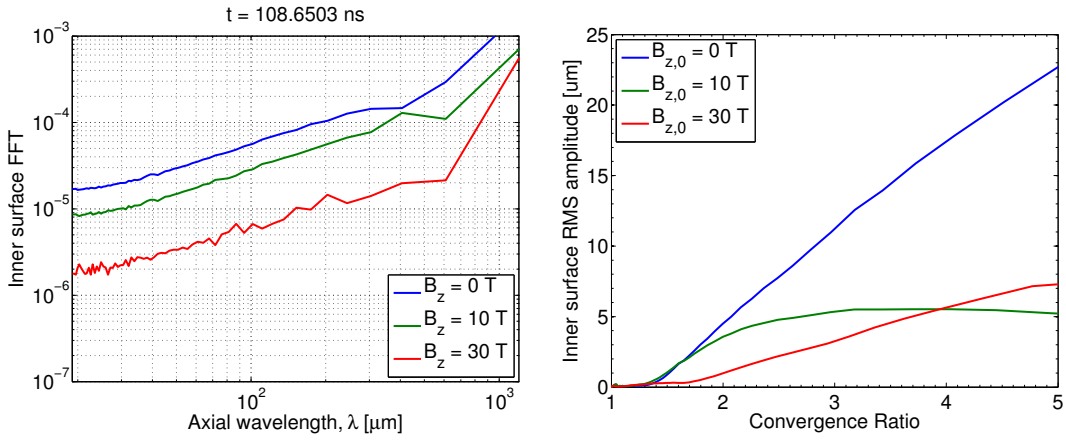

(a) RMS amplitude of inner liner surface as a function of time for low resolution case (10 μm axial resolution).

(b) RMS amplitude of inner liner surface as a function of convergence ratio, CR for low resolution case (10 μm axial resolution).

Figure 4.7: RMS amplitude of liner inner surface of the low resolution case over duration of the liner implosion for various degrees of pre-magnetization. Note, there is no preheat, just fill gas as in Awe et al. [55].

surface seeds to test how sensitive the amplitudes are to the simulation resolution. The expected result is that the same large wavelengths would appear, however, noticeable differences may be important if inner surface ripple amplitudes can be reduced by a significant fraction (i.e. the seed for deceleration RT is reduced by 1/2). Nonetheless, these two very different resolution simulations do confirm that highly compressed axial magnetic fields can reduce the ripples on the inner liner surface.

The results shown in this section are certainly encouraging, but in a MagLIF implosion, the kink mode is present and may also feedthrough, the danger of which must be assessed. Despite the presence of the kink mode, feedthrough reduction is one explanation for the improved stability of magnetized liners (no pre-heat) observed by Awe et al [55]. Though, stabilization by the axial field on feedthrough does not necessarily guarantee a successful implosion with high yield. With current axial magnetic field strengths it may be possible to reduce the aspect ratio of the liner without detrimental performance. However, with stronger fields, it may be possible

to reduce the aspect ratio of the liner to take advantage of this feedthrough reduction to achieve higher yield. It will be necessary to develop a metric that can determine how the perturbations on the inner liner surface influence the final yield of a MagLIF implosion. At present, the stability of the MagLIF inner surface in integrated experiments may be influenced strongly by feedthrough or other sources of perturbations; the relative importance is unknown. Some possible scenarios are: (1) other deleterious effects emerge despite any mitigation of ripple growth from feedthrough reduction, such as ETI or preheat effects, (2) other 3D modes may be more dangerous, or (3) feedthrough reduction is indeed helping improve target performance. Future experiments are needed to address these possibilities and quantify a sufficiently small amplitude on the inner surface to maximize target performance.

4.3 Seeded liners - Effect of shocks

While whole chapters could be devoted to the above topics relating to roughened liners, the simulations are very computationally expensive. To further the discussion and analysis of feedthrough in liner implosions, we return to pre-seeded liners as there are some crucial questions from the previous chapters requiring answers. The terminology 'seeded liner' again refers to sinusoidal seeds of a single wavelength on one or both of the liner surfaces. This section will more thoroughly examine the effect shock waves have on feedthrough, particularly on long wavelength perturbations present on the liner outer and inner interfaces.

4.3.1 Shock waves in metallic liners

Shock compression of the liner coincides with the initial ramp up of the drive current. This occurs before bulk motion of the liner begins. From the rise of the voltage pulse an axial current is driven on the exterior of the metallic cylindrical liner that induces an azimuthal magnetic field. Initially, the current is confined to the skin

depth and rapid deposition of energy in this small area heats and ablates a layer of material. Ohmic heating ($P = IR \rightarrow \eta J^2$) raises the resistivity, which allows faster diffusion of the azimuthal magnetic field. This positive feedback mechanism drives a nonlinear magnetic diffusion wave into the liner, the timescale of which is determined by the resistivity of the material [37]. Meanwhile, on the liner exterior, there is a rapid increase in magnetic pressure that eventually overtakes the material pressure, truly beginning the implosion. The magnetic drive pressure launches a stress wave into the liner that forms a shock that propagates to the inner liner surface. In quasi-ideal MHD simulations, there would be minimal magnetic field diffusion as the current is confined to the outer surface. Material choice also plays a part, as the resistivity and sound speed strongly contribute to the formation of the magnetic diffusion wave and shock wave. We begin our analysis with the initial surfaces perturbations present on the liner exterior.

4.3.2 Seed on liner exterior

A very useful way to study MRT, as we have seen, is to pre-seed a liner with known wavelengths. For example, the work by Sinars et al. [51], multiple sinusoidal perturbations were machined on the exterior of cylindrical aluminum liner such that each wavelength could grow nearly independently and compared easily with linear theory. At the same time, feedthrough can also be studied. As the liner implodes the inner surface is MRT stable while the exterior surface is subjected to MRT. The longest wavelength examined, 400 μm, is predicted to feedthrough to the greatest extent, as classic RT theory has feedthrough scaling like $\sim e^{-k\Delta}$ where k is the wavenumber of the perturbation and Δ is the thickness of the liner. However, the interior surface of the aluminum liner is opaque to the 6.151 keV x-rays used to image the implosion and unfortunately masks the evolution of that surface. We have already used the MRT data provided to benchmark our analytic MRT growth rates and MHD

code, HYDRA so we turn our attention to the inner surface.

As in chapter 2, the simulations will consider a 1.2 mm long aluminum liner with two wavelengths a piece of 400 and 200 μm sinusoids defining the exterior surface, the peak-to-valley amplitudes being 20 μm and 10 μm respectively (5 % their wavelength). The maximum radius for both ripples is the same, so the center of the two sinusoids is offset. The average radius of the 400 μm section is then located 5 μm inward as compared to the 200 μm section. Without the sinusoidal part of the perturbation, just the offset, the outer surface of the liner would then take the form

$$r(z) = 3.158 \text{ mm} \qquad 0 < z < 0.8 \text{ mm}, \tag{4.2}$$

$$r(z) = 3.163 \text{ mm} \qquad -0.4 < z < 0 \text{ mm} \tag{4.3}$$

whose Fourier coefficients will contribute to the Fourier spectrum when including the sinusoidal perturbations. The 400 μm data was extensively studied by Sinars et al. [51]. The 200 μm MRT growth is more difficult to analyze due to jetting that occurs, however, this does not affect the feedthrough greatly, as we will see. The axial zoning maintained greater than 30 zones/200 μm wavelength, and ratioed zoning within the liner kept the radial resolution at $\sim$1 μm. The simulations are again driven with the z1965 (see Fig. 4.1) current pulse.

Our analytic ideal MHD model (both in cylindrical and planar geometry) allows us to calculate the evolution of the inner and outer surface ripple as a function of time. Here we may use the planar or cylindrical model interchangeably. It was shown in Chapters 2 and 3, that the perturbations, being azimuthally symmetric ($m = 0$ or $k_y = 0$) and satisfy the planar limit where $k_z r >> 1$. Thus, the sausage mode only slightly contributes to the instability growth (c.f., Fig. 3.12 and Fig. 3.4(a) in Chapter 3). The simulation begins with the two wavelength perturbations described above applied to the liner outer surface. The inner surface is assumed completely

smooth initially. A direct comparison of the inner surface ripple amplitude straight from 2D HYDRA simulations with our analytic model shows dismal agreement, with the HYDRA results showing some striking features. The remainder of this section

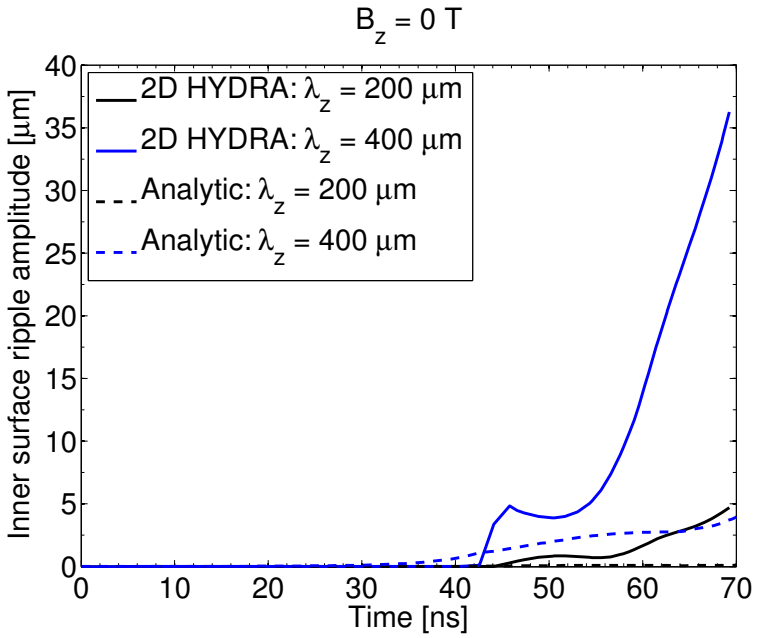

Figure 4.8: Comparison of growth of 400 and 200 μm perturbations on the inner liner inner surface using analytic feedthrough theory and 2D HYDRA simulations.

addresses the differences observed in more detail. The quick summary is that the large magnetic pressure drives a rippled shock wave and the ripple on the shock persists to the inner surface on which the ripple is subsequently seeded. The rapid increase in amplitude just after 40 ns (around 12 MA current, c.f. Fig. 4.1) corresponds to the shock breakout time (or the time when the shock reaches the inner surface).

Additional simulations were run with the LEOS 130 EOS for aluminum to confirm the shock seeding. Figure. 4.9 shows a comparison of the growth of both 400 and 200 μm perturbations on the inner liner surface for both SESAME and LEOS tabular EOSs. Results are relatively independent of EOS used, though the LEOS tables seem to exhibit slower growth at later times. Prior to $\sim$40 ns, the amplitude is approximately zero. Up until this time, a rippled shock is propagating through the

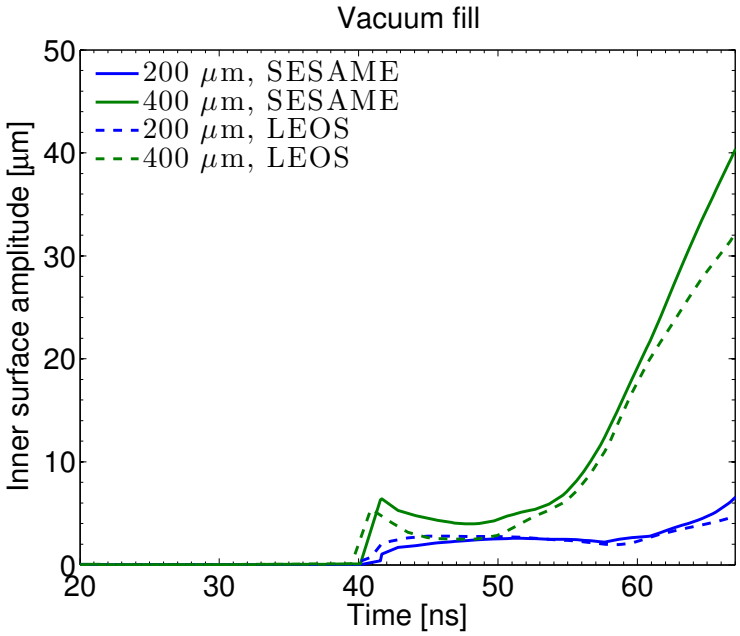

Figure 4.9: Comparison of growth of 400 and 200 μm perturbations on the inner liner surface for both the SESAME 3719 and LEOS 130 tables.

liner. The survival of the perturbation on the shock is highly dependent upon the wavelength. As was shown in the previous section, the RMS amplitude of the inner surface of the randomly seeded liners at shock breakout was well below 1 micron. As the current ramps up on the liner's exterior, a shock develops as in the 'rough' case, however the larger wavelength perturbations cause the shock to be significantly deformed to the shape of the perturbations. Thus, the shock is initially strongly rippled as it begins to propagate inward. The initial ripple amplitude of the shock is roughly the amplitude of the perturbation it came from. There is some uncertainty as to the initial position of the shock front and the exact amplitude of the ripple, as we will show below. Both ripples decay as the shock moves through the liner but the 200 μm case clearly decays faster. This observation is in line with predictions from classical fluid theory, discussed next. The initial ripple amplitude is also much larger than expected from feedthrough theory. The ratio of the inner surface to outer surface amplitude, $F(\omega, k) = 0.25 >> \exp(-2\pi\Delta/\lambda_z)$. The corresponding effective thickness

would have to be 88 μm (not 292 μm) to satisfy feedthrough theory. There is a rapid increase in ripple amplitude on the inner surface after 40 ns seconds when the rippled shock arrives at the inner surface. The amplitude seeded on the inner surface is roughly 60 % the amplitude of the shock as it just reaches the inner surface. As the shock is moving from metal to the central region, there is competition between a transmitted (depending on the fill material or whether the central region is vacuum) and reflected shock, as well as sound waves at the interface, reducing the effective seed. The magnitude of these effects is also tied to the tabular EOS as well as ablation and heating of the inner surface. Following the breakout of the shock, the inner surface continues to evolve and the ripple amplitude increases with time.

We will consider next the three phases of this process in more detail: (1) propagation of the rippled shock in the liner, (2) rippled shock breakout, (3) post-shock evolution of the interface.

4.3.2.1 Details of the propagation of a magnetically driven rippled shock in a liner

We first focus on the propagation of a rippled shock in metallic liners, driven by a magnetic pressure. In this subsection, we assume no axial magnetic field. Similar to laser driven targets, the ripple amplitude decay rate increases with wavenumber as well as with propagation distance. Thus, the effect of this seeding mechanism for the inner surface for a typical 'smooth' liner target is negligible if the liner is sufficiently thick.

Stability of a rippled shock has been studied for more than half a century in fluid dynamics. Early work in the 50s by D'yakov [77] and Kantorovich [78] showed the conditions for which ripples on shocks grow. More recent work has focused on application laser driven targets. Work by Bates [79] has shown exact solutions for shocks in aluminum to be stable. In other materials, this is not necessarily true

and the amplitude of a rippled shock can grow. For ideal materials, the superstable behavior of a propagating shock is due to the flow fields set up in the post-shock material. For a shock propagating in the ± x direction in the x-z plane, flow is also generated in the z direction due to pressure variations directly behind the shock front. This axial flow directs material away from the peaks of the ripple into the troughs, essentially smoothing the shock ripple. We also point out that this flow is primarily along an imposed axial magnetic field, such as in MagLIF, weakening the effects of an axial field on this behavior. This is illustrated in a later subsection in Fig 4.17(b).

Depending on the timescale of the shock propagation, this flow can cause inversion of the ripple amplitude, and hence, the ripple tends to oscillate while its overall amplitude decays. In laser driven experiments, this can be a very important and pronounced effect [80]. This effect is accentuated at small wavelengths giving the faster decay. Linearized solutions have been developed for laser driven targets where the additional complication of magnetic fields is not needed. These models rely on an ideal gas equation of state with an arbitrary specific heat ratio (γ). We quote an asymptotic solution from Goncharov et al. [80] in Eq. 4.5. These are derived from the linearized, purely, hydrodynamic equations allowing for a compressible fluid. In this case, the perturbations have an e^{-ikz} dependence (no temporal Fourier transform). The perturbation pressure is described by the wave equation

$$\frac{\partial^2 p_1}{\partial t^2} = c_s^2 \frac{\partial^2 p_1}{\partial x^2} - k^2 c_s^2 p_1. \tag{4.4}$$

After applying the linearized shock jump conditions at the free surface and shock front to Eq. 4.4, the temporal evolution of the shock ripple amplitude, $\xi_s(t)$, is determined. The analytic solution for $\xi_s(t)$ is given by Eq. 4.5. As the solutions are made up of a superposition of Bessel's functions, the solutions admit a number of zeros corresponding to the oscillations of the shock ripple surface, as well as an amplitude

decaying in time.

$$\xi_s(t) \cong \eta_0 \left[J_0(r_s) + \frac{2(M_s^2+2)}{3M_s^2+1} J_2(r_s) \right],$$

$$= \eta_0 \left[J_0(r_s) + a J_2(r_s) \right]. \tag{4.5}$$

$$r_s = k c_{ps} t \sqrt{1 - [(v_s - v_{ps})/c_{ps}]^2} \tag{4.6}$$

Here J_n is the Bessel function of order n, and $M_s = v_s/c_0$ is the Mach number, where v_s is the shock speed, and c_0 is the un-shocked material's sound speed. The subscript 'ps' refers to post-shock values. The quantity, $r_e - v_s t$ gives the average position of the shock front as a function of time. For a finite thickness liner, the shock position is bounded by $v_s t \leq \Delta$.

Analysis of these equations shows that with increasing Mach number and post-shock sound speed, the ripple decay rate increases. Similarly, with increasing wavenumber, the ripple decay rate increases. While the structure of Eq. 4.5 allows for damped oscillations, we will see that for our current problem, the liner is much too thin to observe these. The times of interest thus occur before the first zero of the sum of the above Bessel's functions. The derivation of Eq. 4.5 also requires that the various sound speeds and Mach numbers remain constant in time. For the liner implosions of interest, this is not the case, as we will show next.

In order to determine the shock dynamics, without considering any non-uniformity, 1D HYDRA simulations were run. First we present the drive pressure (from the azimuthal magnetic field) as well as the shock front trajectory in Fig. 4.10. The shock develops over a finite distance just within the liner and the initial start time of the shock is difficult to pinpoint. From Fig. 4.10 the shock forms at roughly 8 ns. The initial compression wave appears approximately 45 μm inside the aluminum, with the material behind it, compressed by a factor of 1.04. This region is initially moving subsonically ($c_{s,0} \approx 5300$ m/s but quickly surpasses the sound speed within 10 ns.

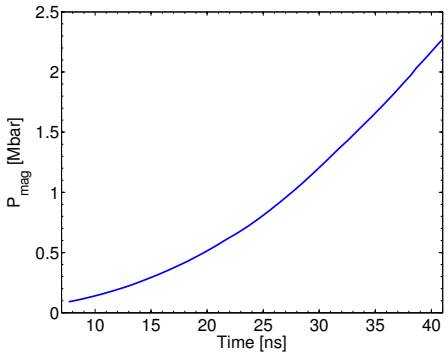

(a) Magnetic pressure drive (B_θ).

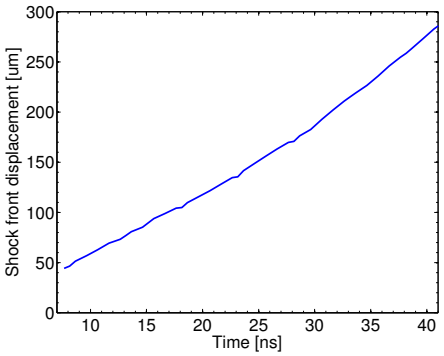

(b) 1D shock displacement from liner exterior.

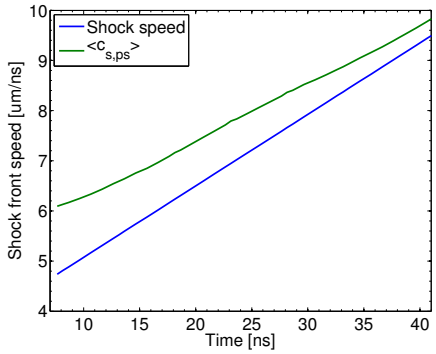

(c) 1D shock speed from liner exterior.

Figure 4.10: Shock parameters from 1D simulations for z1965 current, times correspond to Fig. 4.1. The shock begins roughly at time, $t = 8$ ns.

Post-shock values such as the sound speed, $c_{s,ps}$ must be averaged in the post-shock region to determine a uniform value as a function of time.

As we can surmise from Fig. 4.10, the post-shock quantities evolve in time. During this timeframe the current rises linearly in time, so the magnetic pressure (square of the current) increases quadratically. If we again reference averaged post-shock quantities, their scaling in time is easily obtainable from these 1D results based on the quadratic pressure drive. Equations 4.7-4.12 reflect these scalings.

$$r_s(t) \propto t^2, \tag{4.7}$$

$$v_s(t) \propto t, \tag{4.8}$$

$$P_{mag}(t) \propto t^2, \tag{4.9}$$

$$P_{ps}(t) \propto t^2, \tag{4.10}$$

$$c_{s,ps}(t) \propto t^2, \tag{4.11}$$

$$\rho_{ps}(t)/\rho_0 \propto t^2. \tag{4.12}$$

Because these physical quantities vary significantly in time, Eq. 4.5 cannot be expected to give accurate results as it assumes only non-temporally evolving quantities. Some of these quantities do exhibit different regimes, where the quadratic scaling is weak, but all vary at least linearly in time.

Time averaged values of all of the relevant physical quantities required in Eq. 4.5, $\xi_s(t)$ can be computed. With the aforementioned in mind, we first directly compare $\xi_s(t)$, derived from the averaged 1D HYDRA data, to our 2D simulations for aluminum in Fig. 4.11(a). The calculation for the 400 and 200 μm perturbations overestimates the damping of the perturbations in comparison to the 2D HYDRA results shown as the dots. As the various parameters have been averaged, there is clearly some "wiggle room" for the appropriate weighting of the averaging. Introducing a simple scaling factor, κ, and then scanning κM_{ps} as input into Eq. 4.5 shows $\kappa = 1.47$ results in

a much better fit of $\xi_s(t)$ (see Fig. 4.11(b)). Similarly, the post-shock velocity and post-shock sound speed can also be modified. The overall requirement to obtain better agreement is that M_{ps} must be increased from the mean value. Additionally, c_{ps} increases faster in time than $v_s - v_{ps}$, hence, the Mach number early on is much larger than later in time. The temporal dependence of the decay for both 400 and

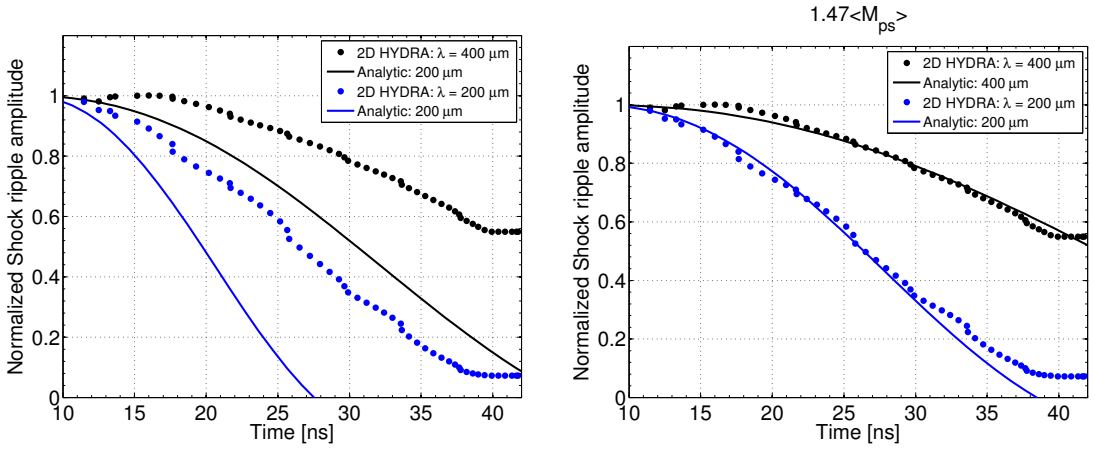

(a) Application of Eq. 4.5 using averaged physical parameters from 1D HYDRA simulations. Solid curves are computed from Eq. 4.5, while the dots are from 2D HYDRA simulations.

(b) Application of Eq. 4.5 using averaged physical parameters from 1D HYDRA simulations, with the post-shock Mach number increased by a factor of 1.47. Solid curves are computed from Eq. 4.5, while the dots are from 2D HYDRA simulations.

Figure 4.11: Comparison of 2D HYDRA and analytic calculations describing the temporal evolution of the shock ripple amplitude for both 400 and 200 μm axial wavelengths, as it moves through an aluminum liner.

200 μm are fit quite well by a quadratic function during the main propagation of the shock. The initial startup up of the shock occurs more slowly. The fits are given by Eqs. 4.13 and 4.14,

$$\xi_{400}/\xi_0 = -4.39 \times 10^{-4} t^2 + 5.27 \times 10^{-3} t + 1.027 \qquad 10 < t < 40 \text{ ns}, \tag{4.13}$$

$$\xi_{200}/\xi_0 = -2.19 \times 10^{-4} t^2 - 0.0255 t + 1.34 \qquad 10 < t < 40 \text{ ns}. \tag{4.14}$$

where the time, t is in nanoseconds and directly corresponds to the simulation times that have been presented. If we extrapolate the HYDRA results of Fig. 4.11 to shorter

wavelengths, it is anticipated that wavelengths shorter than 200 μm will quickly reach the point where they do not shock seed the inner surface. An example of this is shown next in Fig. 4.13.

While there appears to be a finite seeding amplitude for the 200 μm perturbation, wavelengths shorter than this become increasingly difficult to properly resolve with 2D simulations. However, keeping in mind the analytic calculations tend to over predict the damping rate for the temporally changing drive pressure, we perform the same calculation for 100 μm and 50 μm perturbations. These calculations are shown in Fig. 4.12 with the 400 and 200 μm HYDRA data shown for comparison. Clearly,

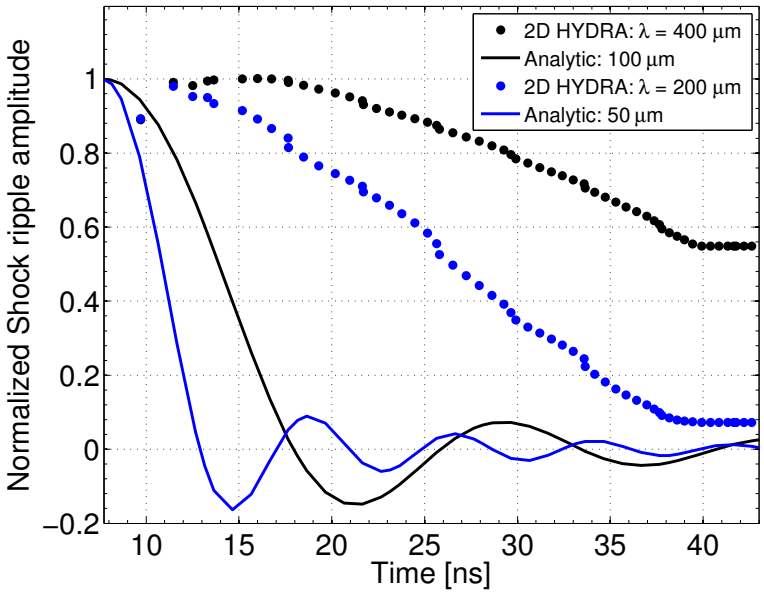

Figure 4.12: Application of Eqn. 4.5 using averaged physical parameters from 1D HYDRA simulations for 100 and 50 μm perturbations.

the 100 and 50 μm perturbations damp much faster than the longer wavelengths we have looked at in depth. As additional evidence, we also present a density plot from a 2D simulation at 21 ns, when the ripples are anticipated to be damped. (Fig. 4.13). From Fig. 4.13 we can see limited rippled structure remaining on the shock and any remaining structure is on the order of 1 μm, which is the approximate radial resolution. Based on these results it is unlikely that any random surface perturbations

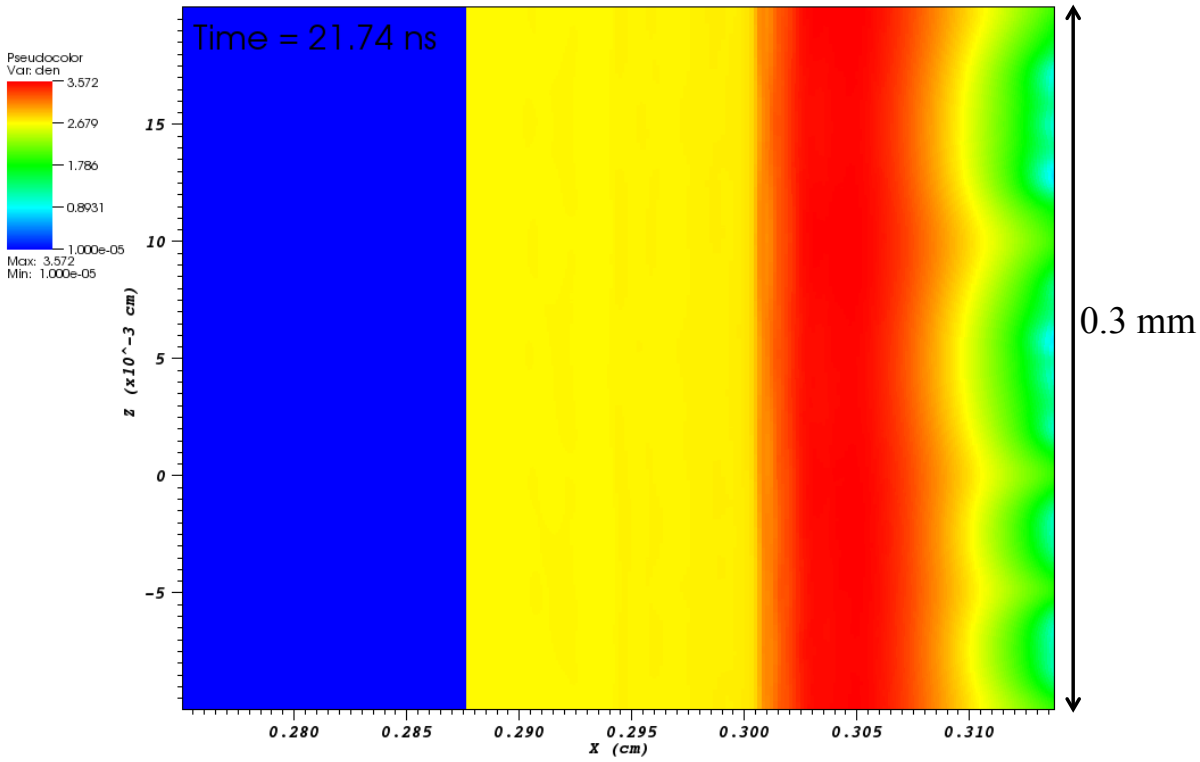

Figure 4.13: Color plot of density, in units of g/cm^3, from a 2D HYDRA simulation showing the 'rippled' shock at 21.7 ns with 100 and 50 μm perturbations initially seeded on the liner exterior. The shock front is located just past 0.3 cm and is nearly smooth.

of short wavelength could shock seed the liner interior. Axial non-uniformities seem to require wavelengths greater than 100 μm to have any impact. Unfortunately, this cutoff is not a completely general result, as the survival of the ripples depends not only on the liner thickness, but the material properties and the drive current as well.

Additional non-uniformities in pressure, density, and magnetic field, may also contribute to the discrepancy beyond the time dependent drive. The radial non-uniformity of the post-shock region also poses a significant challenge for analyzing the shock behavior. In particular, a large fraction of the post-shock region is unstable to magneto-Rayleigh-Taylor instability. There are a few distinct regions where the $\nabla p_{tot} \cdot \nabla \rho < 0$ condition for MRT instability holds. These regions are highlighted in the liner density plot in Fig. 4.14 with the purple hue and purple arrows. The rippled shock front is located at the transition from green to red (~ 0.296 cm). The liner density is overlaid with the color blue in the MRT unstable regions yielding the purple-ish color. The MRT stable regions are the bright red and green regions over most of the left side of Fig. 4.14. There is also a small localized area unstable to MRT where the axial current density contour concentrate, just past 0.3 cm. The liner inner and outer radii are off the scale, at $r_i = 2.876$ mm and $r_e \approx 3.168$ mm (approximate due to ablation). The shock front itself is stable to MRT, however, the post-shock region is almost completely unstable to MRT all the way through to the liner exterior (minus the bright red region already mentioned in Fig. 4.14). In the post-shock region, the magnetic pressure is significantly higher than the fluid pressure and since the post-shock $d\rho(r)/dr < 0$, this leads to the MRT instability which can help slow the ripple decay rate on the shock. MRT drives material into the peaks/troughs and perpetuate the ripple as in any other instance of MRT. Behind the shock front, the fluid pressure gradient is such that material is directed from the peaks to the trough, smoothing the ripple. The blue arrows detail the axial fluid velocity, v_z that directs material away from the bulges at the shock front. This is the

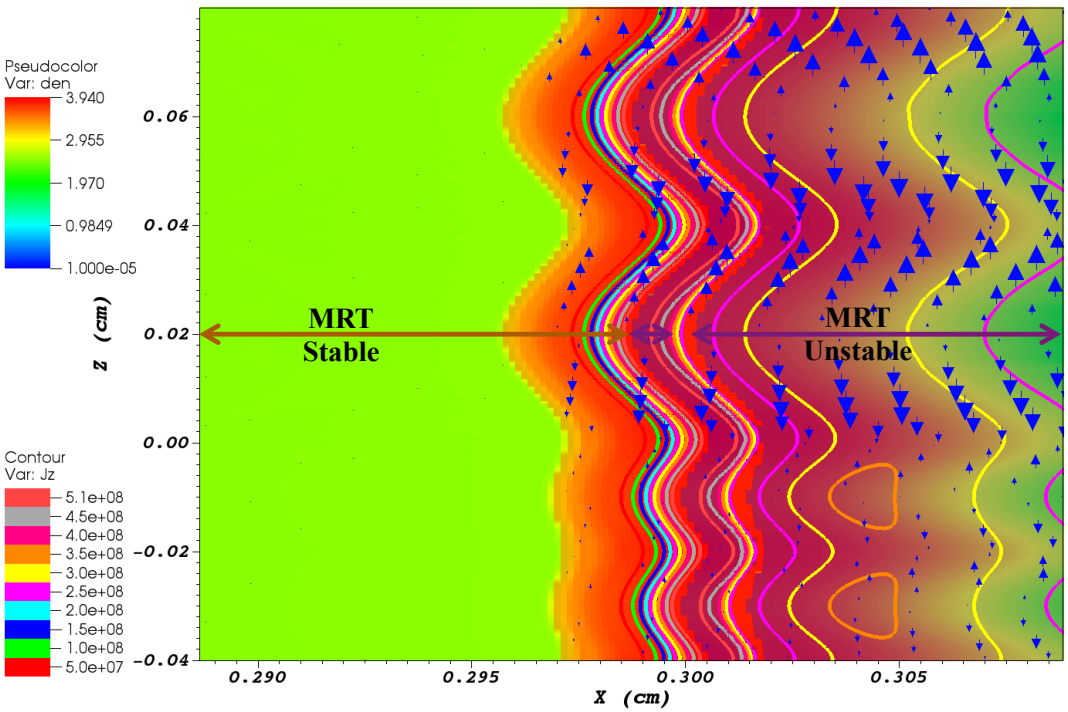

Figure 4.14: Color plot of liner density in 2D, at 30 ns, showing the MRT stable and unstable regions according to $\nabla p_{tot} \cdot \nabla \rho < 0$. The contours plot the axial current density J_z in units of A/cm^2. The MRT unstable regions are overlaid with the color blue, creating the purple-ish regions in the color plot. Bright red regions are MRT stable, as well as the green region on the left (the un-shocked liner material). The density is in units of g/cc. Initially, $r_i = 2.876$ mm and $r_e = 3.168$ mm. The blue arrows show the fluid velocity in the $\hat{z}$ direction which directs fluid away from the bulges at the shock front. Note that the z-velocity in the 200 μm section is much smaller since the ripple amplitude is significantly damped already.

typical mechanism responsible for smoothing ripples on shocks [81]. In the post-shock region the fluid flow is also directed radially inward and can reinforce the ripples. Thus, there is competition between destabilization by MRT and stabilization by the flow patterns. Complicating matters is the diffusion of the azimuthal magnetic field which is illustrated by the strong axial current density contours in Fig. 4.14. The azimuthal magnetic field can retard velocity in the $\hat{z}$ direction and strong compression of azimuthal field lines can launch magneto-sonic waves.

The above issues also appear when a roughly constant (in time) drive pressure is used. In this case, the important variables such as the post-shock sound speed, are also roughly constant in time. However, it is not simple to keep the magnetic pressure perfectly constant in time. As the current diffuses into the liner and ablates material the peak magnetic pressure at the liner/vacuum interface can change. Nonetheless, again using 1D HYDRA simulations to determine the shock parameters, Eq. 4.5 can be evaluated, now for nearly constant in time parameters. For these simulations a drive pressure of 0.3 Mbar was selected. This corresponds to $\rho_s/\rho_0 \approx 1.2$, $c_{s,ps} \approx 7.9$ μm/ns, and $v_s \approx 8.5$ μm/ns. Figure 4.15 plots $\xi_s(t)/\xi_0$ for analytic formula (solid curves) and 2D HYDRA (dots). In this case, the 2D HYDRA simulations show faster decay of the ripples. The agreement between the analytic results and HYDRA data is good early on, but deteriorates later on. In particular, the oscillation for 200 μm perturbation observed in HYDRA is not captured by the analytic model. In this constant drive case, reducing the post-shock Mach number results in slightly better agreement with the 400 μm perturbation, but not the 200 μm case. The shock decay for both wavelengths can again be parameterized rather well by quadratic fits. For the 200 μm case, this fit works only for the non-oscillatory phase. The fit of the

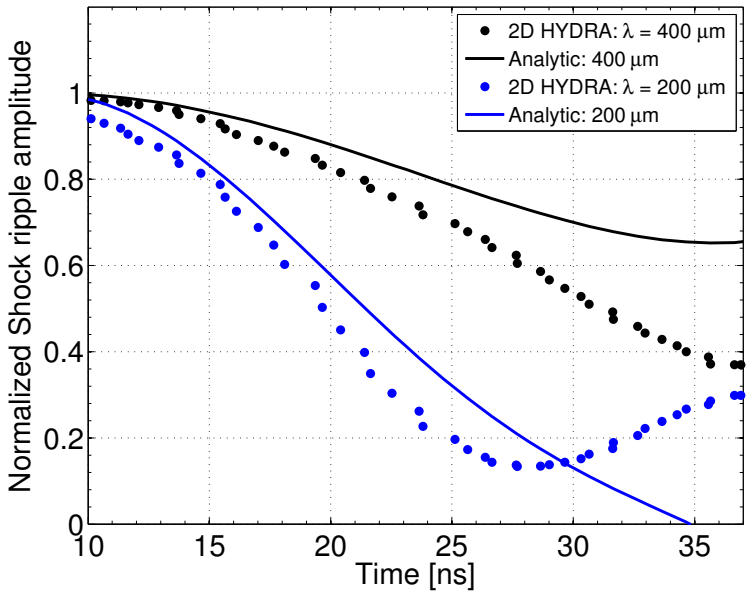

Figure 4.15: Application of Eqn. 4.5 using averaged physical parameters from 1D HYDRA simulations and a temporally constant magnetic drive. 2D HYDRA results are shown as the dots.

HYDRA results in Fig. 4.15 read (t in ns),

$$\xi_{400}/\xi_0 = -5.078 \times 10^{-4} t^2 - 1.78 \times 10^{-3} t + 1.06 \qquad 7 < t < 35 \text{ ns}, \tag{4.15}$$

$$\xi_{200}/\xi_0 = -1.23 \times 10^{-3} t^2 - 7.21 \times 10^{-3} t + 1.15 \qquad 7 < t < 25 \text{ ns}, . \tag{4.16}$$

Overall, the shock ripples decay faster with the reduced drive pressure (and constant in time) of 0.4 Mbar, as compared to the increasing drive pressure case (Fig. 4.11).

Our 2D simulations also show that the amplitude of the shock ripple just as it reaches the inner surface is not the same as the seeded amplitude there. This is due to the transition from nearly solid aluminum to a low-density gas (or vacuum). As we discussed above, the effective transmission for the 400 μm perturbation is roughly 60 %, that is, a 10 μm ripple amplitude just before reaching the interface will impart a 6 μm seed after breakout. The breakout time for the 200 and 400 μm perturbations is also not precisely the same but very small ($\sim$ 0.5 ns), since the

400 μm perturbation has a larger amplitude by 5 μm (10 μm peak to valley). This means the average position of the 400 μm wave is slightly ahead of the 200 μm wave since the perturbation itself is machined 5 μm deeper. Thus, it is best to compare the shock amplitude before any interface complications can occur.

The shock propagation described in the preceding paragraphs in (r,z) geometry is also found in (r,θ) geometry. Here, $k = 0$ effectively due to the 2D symmetry of the problem. Again, these calculations assume a relatively large initial seed on the liner outer surface. In this case, the sinusoid modulating the outer surface is determined by $\sim e^{im\theta}$ and for our current problem take $m = 6$. Another example would be $m = 1$ which effectively corresponds to more mass on one side of the liner as compared to the other. For these (r, θ) problems we may consider this also as a case of non-uniform drive current. As we saw in the (r, z) plane, the longer the wavelength,

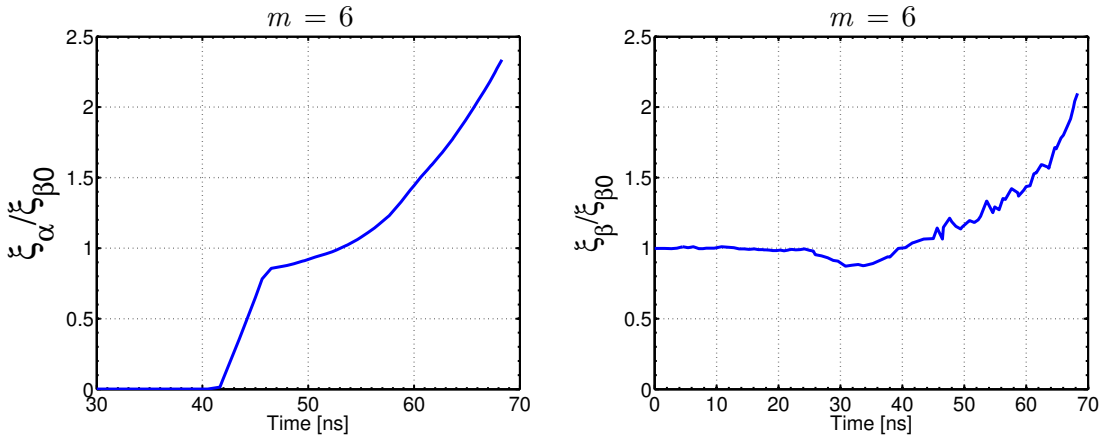

(a) Shock seeding of $k = 0$, $m = 6$ mode and evolution of liner inner surface.

(b) Corresponding growth of MRT on liner outer surface for $k = 0$, $m = 6$ mode.

Figure 4.16: Shock seeding of the inner surface from azimuthal perturbations.

the larger the shock seed amplitude, all things being equal. The equivalent planar mode is $k_y = m/r_0 = 6/(3 \text{ mm})$ and thus $\lambda_y = \pi$ mm >> 400 μm. This mode should then seed much stronger than the previous modes we considered and this is exactly what we observe in Fig. 4.16(a). The amplitude has been normalized to the initial $m = 6$ ripple seeded on the liner exterior. While the shock seeding remains strong,

the overall growth of the shock seeded ripple on the inner surface is observed to be much slower than in the (r, z) case. Similarly, Fig. 4.16(b) shows very slow MRT growth as well, though this is somewhat expected given the liner is only beginning to implode and $k_y = k_\theta$ is small. In fact, the inner surface grows marginally faster than the outer surface, indicating Richtmyer-Meshkov-like instability is responsible and will be discussed further in the next section.

Besides the long wavelength being considered, the other major difference is that these simulations include bending of the azimuthal magnetic field lines though k_θ is relatively small. As mentioned earlier, the azimuthal magnetic field diffuses in directly behind the shock front and these field lines, depending on the magnetic diffusion time, can be rippled as well, adding to the stabilization. Again, as shown in the previous chapter, the presence of current within the liner can affect the $m = 6$ mode growth. Most importantly, the azimuthal field is also much stronger than the 100 T axial field we considered earlier for the (r, z) simulations. As the shock begins to form, the azimuthal field, $B_\theta = 120$ T and increases to nearly 750 T at the shock breakout time. This is a far more realistic scenario than a constant 100 T axial magnetic field. Despite all of these complicated effects, qualitatively, the shock seeding is strong as expected and could be an important effect if there is something like a non-uniform current drive.

4.3.2.2 Effects of axial magnetic field, fill density, and material on the shock seeded amplitude of liner inner surface

The previous sub-section focused on the dynamics of shock propagation within a metallic liner up until shock breakout. A primary result showed that the wavelength strongly affected the strength of the seed on the inner liner surface. In particular, longer wavelengths tend to lead to larger amplitude shock seeding. In this section we will investigate the effects of an axial magnetic field, fill density, and material on the

amount of shock seeding.

The first result we will show is that under a variety of circumstances, the shock seeding mechanism is very robust. Common scenarios for imploding liners include a fill gas and a seed magnetic field. 2D HYDRA simulations using a D2 fill gas of various densities were run, as well as with and without an axial magnetic field. The expectation for the fill gas is that increasing the fill density can reduce the amplitude of the shock seed since the Atwood number at the gas/liner interface is reduced. The magnetic field may affect the propagation of the shock, via generation of magneto-sonic waves, and perhaps the amplitude of the shock seed due to strong bending of field lines.

Results for these two cases are shown in Fig. 4.17(a). These curves, around 45 ns, show nearly the exact same shock seeding amplitude over two orders of magnitude of fill gas density (D2). The fill density does have an effect on the evolution of the interface, post shock breakout. This is similar to what is expected from Richtmyer-Meshkov instability (RMI), however this is not the exact definition of RMI since we have a rippled shock interacting with a smooth surface. Nonetheless, a simple scaling for the RMI growth rate is $d\xi_s(t)/dt = kAv_{ps}\xi_{s0}$, where k is the wavenumber, ξ_{s0} the initial seeded ripple amplitude, and v_{ps} is the post-shock velocity[81]. For the highest fill density, 100 mg/cc corresponds to the Atwood number, $A = 0.93$ which is sufficient to reduce the surface growth by almost 58 % as shown in Fig. 4.17(a) for the 2D simulation. We can estimate the product, $kAv_{ps}\xi_{s0}$ from 1D simulations as well. Both 1D and 2D simulations show the average inner surface velocity for the 100 mg/cc fill is roughly 80 % the 2.5 mg/cc case and 2D simulations show that $\xi_{s0} = 5$ μm (1 μm smaller). Then the product $kAv_{ps}\xi_{s0} = 0.62$ μm/ns for the 100 mg/cc fill and is in reasonably good agreement with the growth reduction observed in our 2D simulations which capture much more complicated physics.

A final point is that a 100 mg/cc fill density also begins to interfere with the

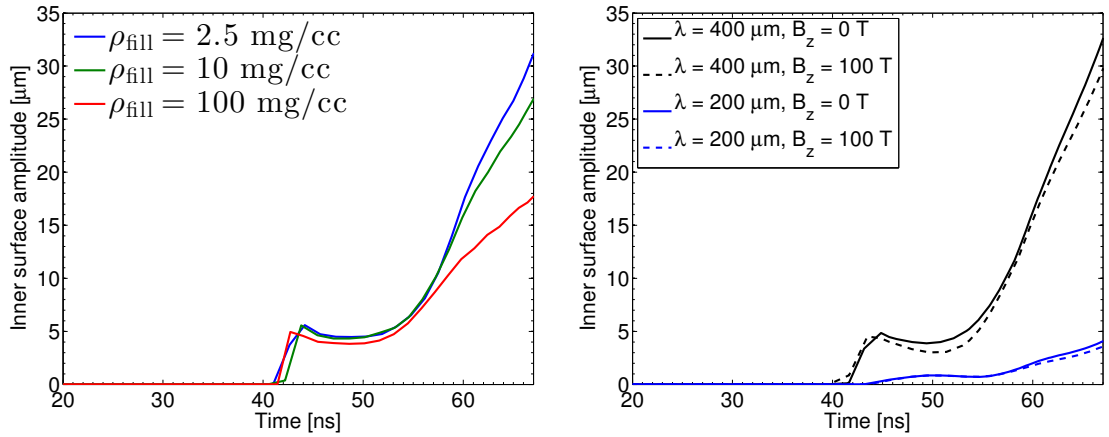

(a) Comparison of growth of 400 μm perturbations on the inner liner surface for increasing fill density.

(b) Comparison of growth of 400 and 200 μm perturbations on the inner liner surface with a 100 T axial magnetic field with $\rho_{fill} = 0$.

Figure 4.17: Even relatively extreme conditions show shock seeding is very robust and consistent.

implosion dynamics of the liner. Cryogenic deuterium is liquid with a density of 0.163 g/cc. This material can provide a substantial backpressure that can stagnate an implosion far earlier. A potential application of this is for study of deceleration RT [82]. In such a case, a magnetically imploded liner stagnates on a relatively cool dense fluid as opposed to a hot compressed plasma in a typical inertial fusion experiment. Clearly, such a liner will implode to a larger radius, which is easier to diagnose via radiography. If the shock seed can be applied, with limited growth due to RMI, then this would provide an excellent surrogate for seeding the inner liner interior. The key piece of knowledge is knowing how appreciable the RMI-like growth is and whether deceleration RT growth observed is truly attributable to it. The inner liner surface could also be seeded initially, though this would still lead to RMI growth, and such seeding may be more mechanically difficult to apply.

An axial magnetic field plays a very small roll in the evolution of a shock seeded surface (Fig. 4.17(b)). We consider a 100 T seed field with no fill gas to emphasize this. As we see in Fig. 4.17(b) such a B_z does very little to the evolution of the interface as well as the shock seed itself. The negligible impact on the shock seed

also suggests that the rippled shock propagation is minimally impacted. A finite B_z could slow the shock since the axial field is being slightly compressed (magnetosonic waves) or damp the ripple via field line bending (Alfvén wave). Additional axial magnetic field cases were also run including a fill gas and a fill gas with an artificially high conductivity. The high conductivity was intended to mimic preheating of the fuel without any additional effects introduced with the blast wave. We have already seen magnetic diffusion can severely impact the effect the axial magnetic field has on instabilities in these liners. A more conductive fuel helps keep the field better tied to the gas and comes closer to expected results from ideal MHD. Figure 4.18 again

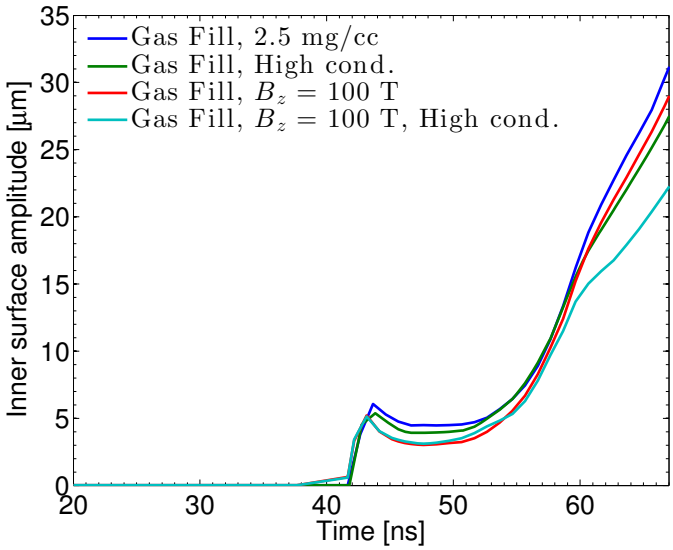

Figure 4.18: Comparison of growth of 400 μm perturbations on the inner liner surface with 100 T axial magnetic field, fill gas, and highly conductive fill gas.

shows minimal change in seed amplitude for all cases, the maximum reduction is no more than a micron at about 43 ns. However, the conductivity of the fuel does play an important role in the evolution of the interface at later times, similar to what we saw for increasing fill densities. HYDRA runs also suggested the diffusion of B_θ into the interior increases the growth rate past 50 ns, than when B_θ exists only in the exterior region.

Next, we move on to beryllium targets. For the same liner dimensions there will be roughly half the mass in a Be target as compared to Al. This means that the liner will implode faster and experience higher acceleration. In addition, important parameters for this problem such as sound speed and electrical resistivity are different. The electrical resistivity of beryllium at room temperature is roughly 30 % larger than Al, and has a sound speed twice that of Al. From a materials standpoint, the bulk, shear, and Young's modulus of Be are all much larger than Al, but such material properties will not be considered here. However, the material strength of beryllium may be important for longer pulse lengths, when it is attempted to keep the beryllium in the solid phase. We will assume, as with aluminum, that the material strength is quickly exceeded. We can directly compare the decay of the two ripple wavelengths in the two materials since the target dimensions and current pulse are the same. This is plotted in Fig. 4.19. The results are consistent with the level of shock seeding. The

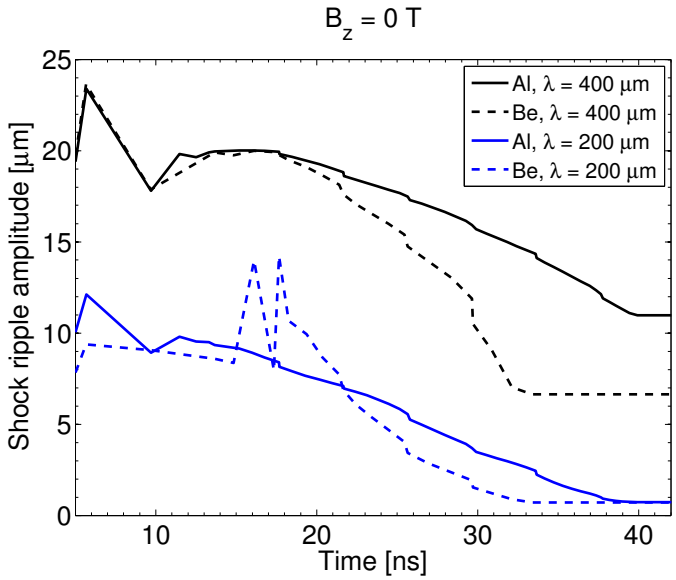

Figure 4.19: Comparison of the evolution of the two shock ripples as they move through aluminum and beryllium liners. The horizontal portion of the curve illustrates the amplitude of the ripple just before shock breakout.

200 μm perturbations actually decay quite similarly in both materials early on and

eventually reach nearly the same amplitude upon reaching the inner liner surface. The difference between the materials with the 400 μm perturbation is much starker. The uncertainty in the amplitudes is on the order of 1 μm, limited by the radial resolution in the liner and uncertainty in determining the exact shock front as the shock is spread over a few zones. The most interesting and useful result would have been the case where beryllium, because of its higher resistivity and sound speed, would show predominantly feedthrough behavior as opposed to shock-dominated behavior. *We stress that persistent shock dominated behavior is observed in both materials. Of course, liners could be made thicker to reduce these shock effects but this would require more current to drive the implosion if the liner remains at its original radius. Increased current of course potentially strengthens the shock.*

4.3.2.3 Post-shock evolution in seeded targets

We now consider the evolution of the inner liner surface after the shock has reached and rippled the inner surface. This time also corresponds roughly to the beginning of bulk implosion of the liner. In general, no more shocks are generated during the implosion and one might expect feedthrough to dominate the evolution of perturbations on the inner surface. Important to keep in mind is that these targets were initially seeded with very long wavelengths and much larger amplitude perturbations than those found naturally. Such targets are typically designed for the study of MRT and feedthrough (depending upon material and imaging capability). For a given material and drive conditions, the amplitude of perturbation seeded on the interior was found to be in nearly all cases dependent only on the perturbation wavelength, amplitude, and liner thickness. Figures 4.17-4.18 also show the subsequent evolution of the inner surface post-shock breakout.

Since the beginning of the current pulse, the liner has been shock compressed. The material ahead of the shock is unaware of any material motion, hence the inner

surface remains motionless. This all changes once the shock reaches the inner surface and the two interfaces finally can communicate at the post-shock sound speed. As the liner implodes it is continually accelerated and no more shocks are driven. This is not to say the original shock does not partially reflect from the inner surface interface, but any effect is much reduced given the large perturbations already on the liner exterior. Focusing on the inner surface ripple amplitude after 55 ns, we find the scaling to be roughly linear, shown in Fig. 4.20. Upon closer inspection of the various

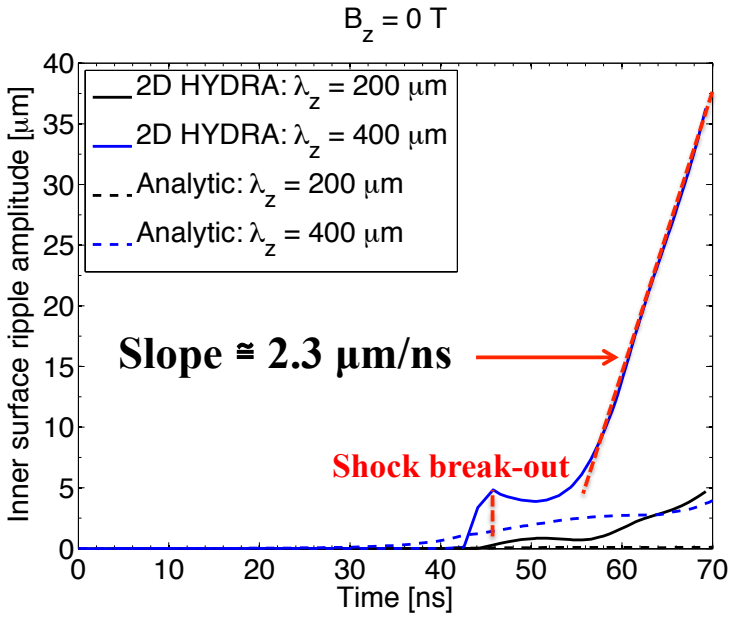

Figure 4.20: Simple linear fit of the post-shock evolution of the inner surface 400 μm shock-seeded perturbation.

fill gas/magnetic field combinations shown in Fig. 4.18 of the previous section, the inner surface evolution post-shock breakout is remarkably similar. All cases show the dip in amplitude, which is a transient not found in simple RMI theory. The dip occurs as the interface briefly rebounds after the shock breaks out and then is partially reflected. This is followed by rapid growth for about 10 ns, and then the slope changes and growth is somewhat slower only for the high conductivity fill gas. The combination of high conductivity and strong axial magnetic field is the only

configuration that affects the amplitude at later times in any significant way. This is expected in the sense that the high conductivity maximizes stabilization due to magnetic field line tension.

Depending on the exact timeframe fit, arguments can be made for $\xi_s(t) \sim t,\ t^2,\ e^t$. Linear-in-time scaling agrees with Richtmyer-Meshkov like instability, while $\sim e^t$ is similar to feedthrough scaling. The slope indicated on Fig. 4.20 agrees fairly well with RMI scaling:

$$\frac{d\xi_\alpha}{dt} = A v_{ps} k \xi_0 = 1.8\ \mu\text{m/ns}, \tag{4.17}$$

where A is the Atwood number at the interface, k the axial wavenumber, v_{ps} the post-shock velocity, and ξ_0 the initial amplitude. This sort of scaling does not account for the dip that occurs just after shock breakout, but the overall scaling of the interface growth. This dependence on the Atwood number and post-shock velocity help explain the results with increasing fill density. (The dependence on wavenumber can also be viewed in (r, θ) geometry where $k = m/r$. The more rapid growth of the inner surface shown in Fig. 4.16 as compared to the MRT is also explainable by additional RMI growth).

Beryllium implosions can be faster and thus illustrate the faster RMI growth due to increased post-shock velocity. Figure 4.21 directly compares the previous aluminum results for 200 and 400 μm perturbations with the target material switched to beryllium. A number of features are quickly apparent. First, the shock speed is much higher in the beryllium target as evidenced by the shock seeding occurring about 7 ns earlier. Second, the seeded amplitudes for the 200 μm perturbation are roughly the same between the two materials, while the 400 μm shows slightly larger seeding in aluminum. The post-shock evolution of the surface follows an opposite trend. The 200 μm perturbation shows larger growth in beryllium at later times. The 400 μm

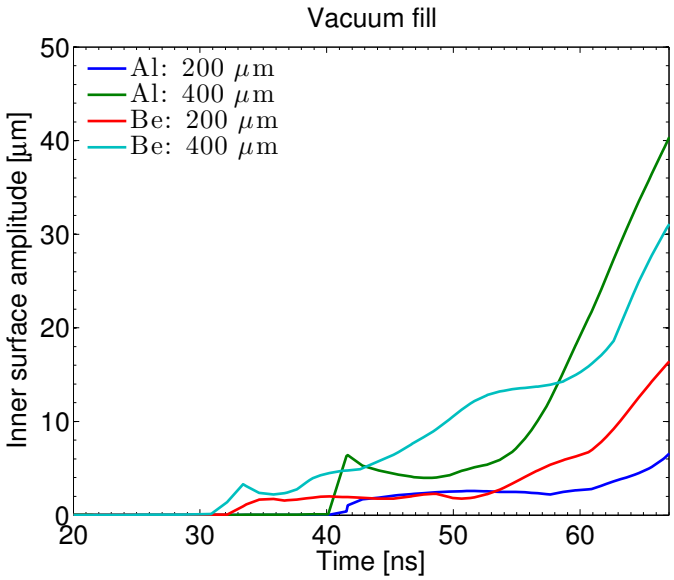

Figure 4.21: Comparison of evolution of inner surface for both beryllium and aluminum pre-seeded targets from 2D HYDRA simulations.

perturbation behaves a bit more erratically, with mild oscillation in beryllium.

A hallmark of classic Richtmyer-Meshkov (RMI) growth is that axial fluid flow directs material from the troughs to the peaks, causing the overall amplitude to grow [81]. The classic Richtmyer-Meshkov problem has a flat shock interacting with a rippled surface. However, our cases examined rippled shocks interacting with flat surfaces. Our 2D HYDRA simulations show that the flows are observed to be directly opposite that typically found in classic RMI. Minimizing the diffusion of the driving azimuthal field that otherwise follows the shock shows a dramatic reduction in growth of perturbations on the inner surface (Fig. 4.22). The low η cases model ideal MHD and show the shock seed remains but the subsequent growth of the perturbations once shock-seeded is minimal. We will show in the next section that this shock-seeded scenario is actually the more dangerous as compared to classic RMI. Nonetheless, these simulations indicate that these liners should **not** be multiply shocked, especially once MRT has begun to grow on the exterior of the liner. Shock seeded perturbations are found to be incredibly robust and grow quite quickly. In the next section we

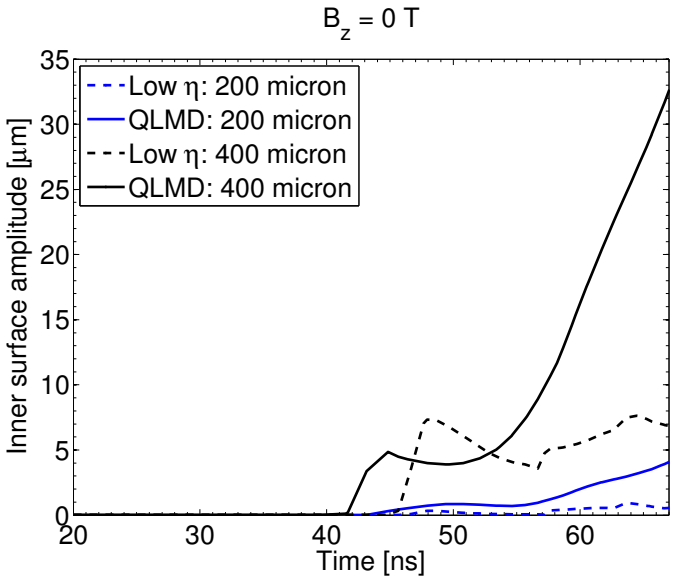

Figure 4.22: Comparison of evolution of inner surface aluminum pre-seeded targets from 2D HYDRA simulations using both realistic resistivities (LMD) and approximately ideal MHD.

will see how perturbations seeded on the inner surface are also dangerous but behave much differently.

4.3.3 Other seeds on liner interior

We next consider how perturbations located only on the liner inner surface affect the stability of implosions. Removing the large single sinusoidal perturbation from the liner exterior but keeping a seeded inner surface is, comparatively, a more stable configuration. This is because the inner surface is MRT stable during the implosion phase unlike the outer surface. A ripple on the inner surface of the liner can develop in a number of ways unrelated to MRT. In an ICF-like implosion this could be through electrothermal instability (ETI) or via interaction with a preheated gas. The preheat may be an important consideration because anywhere from 100 - 2000 J of energy is expected to be deposited in the fusion fuel in about 2 ns, right before the liner begins to implode [27]. The preheat generates a blast wave in the fuel that can

interact with the inner surface. Depending upon the degree of non-uniformity of the preheat, the blast wave can non-uniformly interact with the inner surface. This can perturb the surface with large wavelengths (significant fractions of the liner height). If the circumstances are right, this can even lead to RT development if the preheat is effectively pressing on the liner. However, bulk implosion of the liner is likely to overwhelm this. Modeling this in a completely consistent way is very challenging [27] so we settle on a simple case where the inner surface is pre-seeded and no preheat is present. This neglects many effects such as ablation and heating of the inner surface. Heating of the inner surface can initiate ETI, which can ripple the inner surface with much shorter wavelengths. We anticipate, that the surface being MRT stable and the initial ripple amplitude being very small, these very short wavelengths will not be subject to much growth via RMI. Our focus will be on longer wavelength seeds as we have seen in the previous section. The ripples on the inner surface can not only directly degrade the fuel/liner interface of MagLIF but can also impact the exterior surface as well. This is a situation analogous to 'feedout' in laser driven capsules where roughness on the DT ice layer inside the capsule can feedback to the outer surface which are subsequently amplified by the unstable RT surface [80]. Unless stated otherwise, the outer liner surface in this subsection will be of the 'rough' variety, with small random perturbations. The conditions of the inner surface will either be sinusoidally seeded (200 or 400 μm axial wavelength) or perfectly smooth. We will not consider small random perturbations on the inner liner surface.

The presence of an initial seed on the inner liner surface and subsequent interaction with, in this case, a uniform shock wave subjects the interface to Richtmyer-Meshkov instability (RMI). This is in direct contrast to the previous section where a rippled shock interacted with a smooth surface. With a smooth (or even mildly rough) exterior the propagating shock front should be nearly smooth based on the arguments earlier in this chapter (short wavelengths on the shock front damp very quickly). Once

the shock interacts with the interface, RMI is initiated. The potential danger to the outer liner surface is then a rippled reflected shock and feedback from the inner surface. Three cases will be considered with the same 400 and 200 μm perturbations now seeded on the aluminum liner inner surface. The first contains a 2.5 mg/cc fill gas (D2), the second adds a 100 T field to the gas, and the last fills the fuel region with water and no axial field. Based on the results from the previous section, it is anticipated that the fill gas will have a very limited impact on growth of the inner surface. Since the implosion should be more stable, it should also reach a higher CR which should accentuate any effects due to compression of the axial field or fill gas. The water fill serves a duel purpose: first, to see how it might affect RMI growth early on (whether the reduced Atwood number quenches RMI) and second to determine how the implosion speed affects the inner surface growth. The original goal was to also capture some deceleration growth. Unfortunately, to see that phase, the liner had to be moved to too large a radius to be adequately compared to the other cases. Lastly, an unseeded liner compressing a 2.5 mg/cc fill gas will be used as a control case and is denoted as 'smooth'. The 'smooth' case has only small random perturbations on the exterior, as with the seeded liners.

Figure 4.23 shows the temporal evolution of the 400 and 200 μm sinusoidal ripples on the liner inner surface for the various seeded cases discussed (outer surface has only small random perturbations). The two gas fill cases, overall, behave quite similarly, despite the strong axial field present in one case. Both simulations show oscillations of the inner surface, with the oscillation frequency dependent on the wavenumber of the perturbation. See Eq. 4.18 below. The first peak for the 200 μm perturbation occurs roughly 10 ns before the peak of the 400 μm perturbation. While there is clearly a strong influence of the shock, the shock may also excite the stable RT oscillations (recall the general dispersion relation and feedthrough factors contain both the unstable and stable mode solutions, ω_3 denotes the stable mode). RT oscillations

would then scale as,

$$\xi_{osc} \propto \sin(\omega_3 t) = \sin\left(\sqrt{|kg|}t\right) \tag{4.18}$$

The axial magnetic field enters in ω_3 via $(k_z B_z)^2$ terms and modify the oscillation frequency. For the water fill, the Atwood number is significantly less than unity at the inner surface, which can reduce the oscillation frequency further.

The overall amplitudes of the two modes are relatively small in comparison to the shock seeded cases considered in the previous section (Fig. 2.27(b)). By 70 ns the 400 μm shock seeded perturbation already attained an amplitude of over 30 μm (c.f. Figs. 4.20) where as the inner seeded case is still oscillating. The important difference in the shock seeded case is that there is very substantial MRT growth at 400 μm by that point as well. It takes longer for the random perturbations to develop to such long wavelengths with substantial amplitude. The axial magnetic field does damp

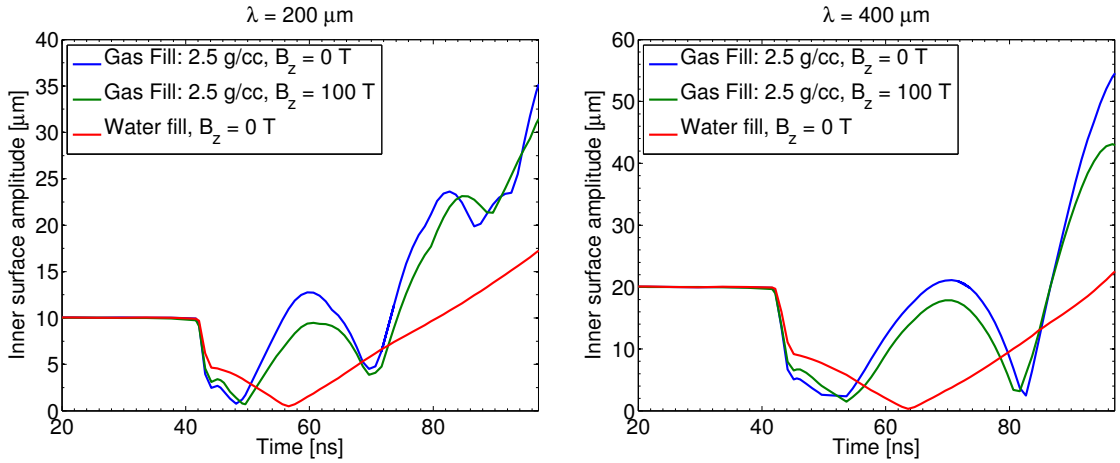

(a) Comparison of growth of 200 μm perturbation on the inner aluminum liner surface.

(b) Comparison of growth of 400 μm perturbation on the inner aluminum liner surface.

Figure 4.23: Evolution of seeded ripples on the inner liner surface. Only the water fill shows substantial reduction of RMI.

the amplitude of the ripples on the inner surface and also marginally modifies the phase of the oscillations with respect to the $B_z = 0$ T case. In this case, the strong

100 T field affects the short wavelength MRT growth on the exterior (Fig. 4.25(a)) but does not significantly alter wavelengths such as 400 μm (see Fig. 2.17(a)). The impact of the axial field on the two different wavelengths appears very similar. As in Ref. [8], magnetic diffusion can also reduce the stabilizing effect of a strong axial magnetic field. We have also seen that a strong axial magnetic field did not impact the shock seeded perturbation (Fig. 4.18), so the minimal impact on the inner surface is not too surprising with that in mind. The water fill behaves much differently once the shock breaks out from the inner surface due to the high density and relatively incompressible nature of the water. While the inner surface of the liner is free to expand somewhat into the fill gas, the water severely restricts this motion. This also seems to tamp the growth of perturbations on the inside surface as well for the water fill (see Figs. 4.25(b),4.26(b)). Overall, we find in the gas fill cases, the amplitude of the inner surface ripples grow in time via RMI but the ripples slowly oscillate due to MRT and feedthrough effects. The presence of the water fill is enough to reduce the oscillations but not RMI.

Figure 4.24 compares the average (axially averaged) density gradient in the radial direction over the first few liner zones of the inner surface. At the shock breakout time the water fill and gas fill cases behave very similarly. At later times, as the liner moves inward, there is significantly more pile-up of aluminum at the liner inner radius due to the water pressure. This maintains a much steeper density gradient than for the gas fill, where the liner material is still free to expand into the low-density gas.

We next introduce the 'smooth' liner (roughened liner exterior but completely *smooth interior*) as a comparison case for how much long wavelength growth occurs naturally on the liner exterior (unrelated to feedout or the perturbation on the interior). Figure 4.25 shows the inner and outer surface FFT just after shock breakout. Already the smooth liner and seeded liner exhibit much different structure. This is a fairly surprisingly result given the thickness of the liner and theoretically small

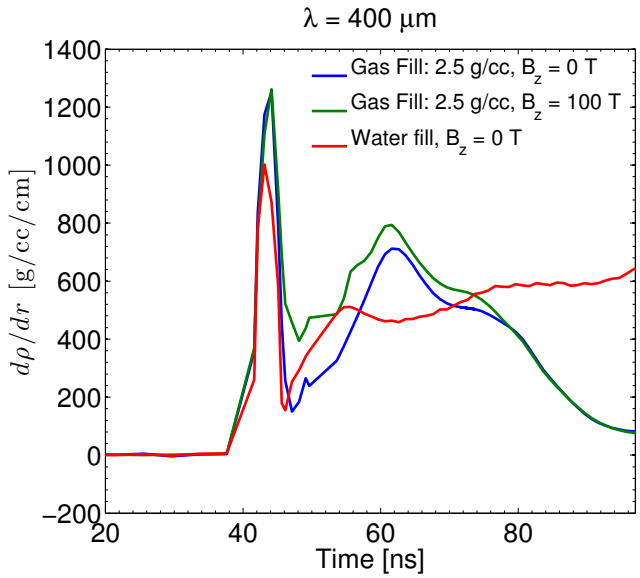

Figure 4.24: Comparison of the density gradient of the inner liner surface, quantifying expansion of the surface.

feedthrough. Downstream of the shock there are significantly larger axial pressure modulations in the inner seed case which can be propagated to the outer surface, a process known as feedout. Passage of the shock excites smaller wavelength perturbations on the inner surface but the dominant perturbations are certainly the seeded ones. At this point the inner surfaces of the three seeded cases are all very nearly the same, whereas significant feedthrough has not yet occurred for the 'smooth' case. The smooth liner and seeded liner also already exhibit much different structure on the liner exterior. This is a fairly surprisingly result given the thickness of the liner and theoretically small feedthrough. As mentioned earlier, downstream of the shock there are significantly larger axial pressure modulations in the inner seed case which can be propagated to the outer surface, a process known as feedout. There is also reduction in the short wavelength mode strength on the liner outer surface for the 100 T axial magnetic field case as expected since $(k_z B_z)^2$ is very large. Nevertheless, the long wavelength modes on the outer surface are much stronger for the inner seeded case, than just the randomly seeded perturbations ('smooth' in Fig. 4.25).

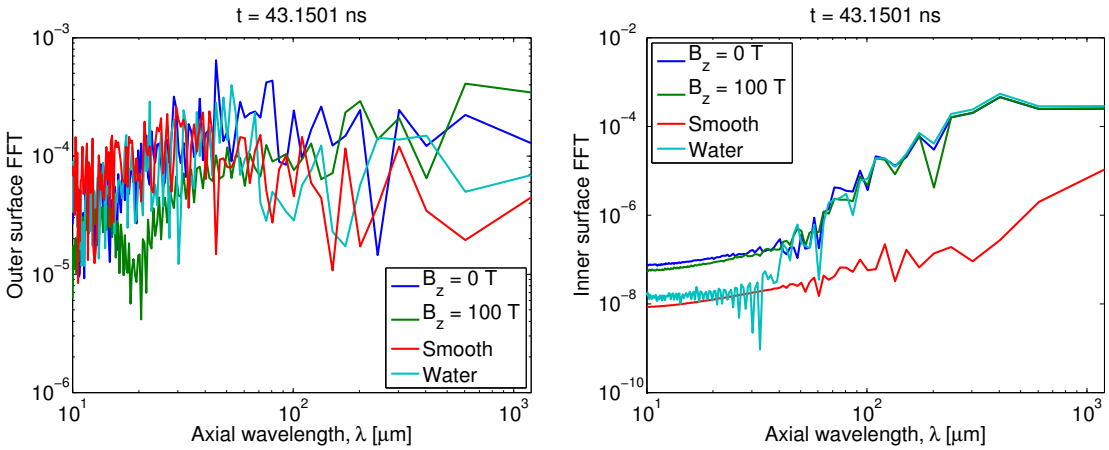

(a) FFT of MRT growth on liner outer surface for inner surface sinusoidally seeded and 'smooth' liners at shock breakout. Only the 'smooth' liner has no perturbations on the inner surface and only random surface roughness on the outer surface.

(b) FFT of liner inner surface including both seeded and non-seeded liners at shock breakout. Only the 'smooth' liner has no perturbations on the inner surface and only random surface roughness on the outer surface.

Figure 4.25: FFTs of inner and outer liner surface comparing seeded and unseeded cases at shock breakout.

One of the main goals of these simulations was to assess whether perturbations on the inner surface can strongly affect liner stability during an implosion. Over the timescale shown in Fig. 4.23, g remains positive, thus the growth of the inner surface in these cases can be accounted for primarily by RMI or feedthrough. The inner surface should otherwise be stable. We also performed what will be referred to as a 'clean' simulation of the $B_z = 0$ T sinusoidally seeded case (dashed blue in Fig. 4.26(a)), where the outer surface of the inner seeded liner was completely smooth but inner surface seeded. This substantially reduces the short wavelength perturbations that naturally evolve to longer wavelengths on the outer surface and completely isolates the feedout effects.

Plotted in Fig. 4.26 are the inner and outer surface FFTs at roughly peak current. Overall, the MRT growth shown in Fig. 4.26(a), is actually quite similar at longer wavelengths for most of the wavelength space, though larger in the inner seed case with a fill gas (up to 50 % larger). The 'clean' case shows dramatically reduced short

wavelength growth as expected, but very similar 400 μm growth (the feedout effect) as the other cases. Because the 'clean' case has much less mode structure, feedout of the 200 μm perturbation is also noticeable. Based on these results it is also possible that feedout can be washed out by naturally occurring MRT, depending on the wavelength, but should nonetheless still add to any MRT growth as opposed to subtract. Including the surface roughness in the solid curves shows that the liner is quite unstable, as expected, but the feedout mechanism at the seeded wavelengths on the interior, is a very important contribution to the MRT structure on the exterior. Most importantly,

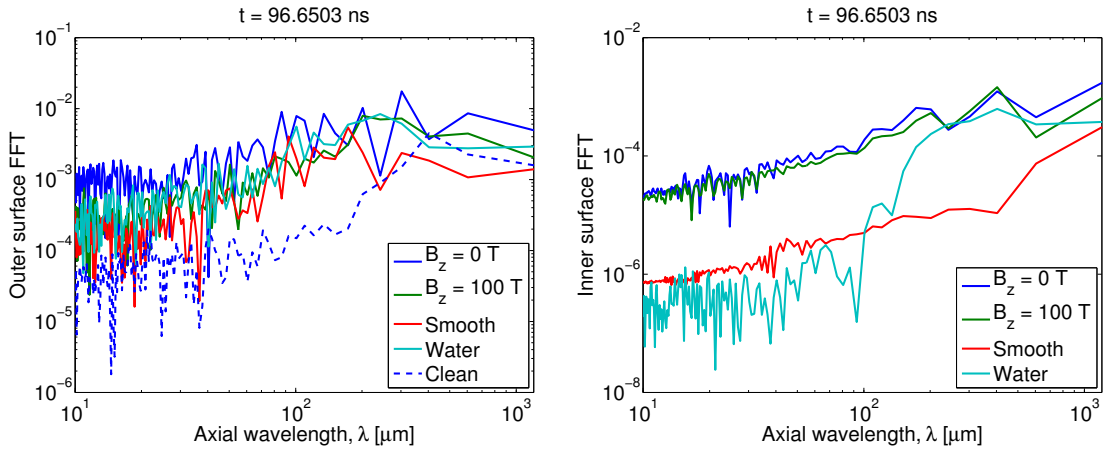

(a) Outer surface FFT near peak current for seeded liner interior. The solid curves utilize a small surface roughness on the liner exterior. The dashed curve is initially completely smooth on the liner exterior with $B_z = 0$ T ('clean case'). Only the 'smooth' liner has no perturbations on the inner surface and only random surface roughness on the outer surface.

(b) Inner surface FFT near peak current for seeded liner interior. The solid curves utilize a small surface roughness on the liner exterior. The 'clean' case is nearly identical to solid case, so it was not included. Only the 'smooth' liner has no perturbations on the inner surface and only random surface roughness on the outer surface.

Figure 4.26: Late time FFTs of liner inner and outer surfaces. The initially smooth liner is observed to be significantly more stable than the inner seeded liners.

the inner surface of the smooth liner is far more stable as expected; the growth of the longer wavelengths from feedthrough does not catch up to the seeded case. From these results it is clear that the presence of inner surface perturbations before shock breakout can significantly reduce the stability of a liner implosion by both generating instability at the seeded interface as well as increasing MRT growth on the exterior.

The second mechanism is a manifestation of feedout, where the reflected shock from the rippled inner surface "seeds" the MRT at the liner outer surface during implosion. There can also be a contribution from feedthrough from the inner to outer surface. Such a process is only visible when the inner surface perturbations are initially much larger than any perturbations on the outer liner surface. Under these circumstances, we can take $\xi_\alpha = 20$ μm and $\xi_\beta = 0$ μm for our analytic formulation (via Eqs. 2.59,2.60 or see Eqs. 36 and 37 of Ref. [8]). The evolution of the two surfaces, $\xi_\beta(t)$ and $\xi_\alpha(t)$ is then plotted for this case in Fig. 4.27 including other, very small, initial conditions for $\xi_{0\beta}$. In this case, the feedthrough contribution is small. However, it does not require a very large perturbation at all to instigate strong MRT growth (40 nm initial amplitude was sufficient to show similar growth purely due to MRT). Here we've used the 'clean' case for the 2D HYDRA simulation, which has the most accurate estimate for the amplitude of the perturbation. The perturbations, as introduced

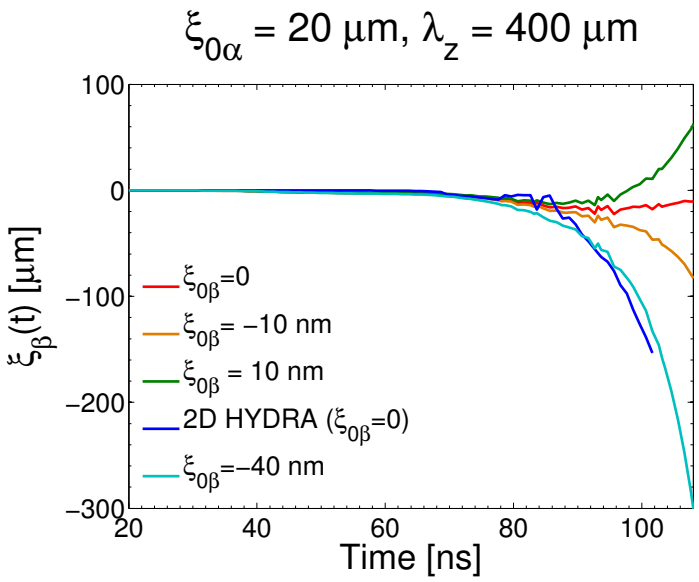

Figure 4.27: Temporal evolution of outer surface 400 μm perturbations using Eqs. 2.59,2.60 for various initial conditions on the outer surface. The initial condition on the inner surface is $\xi_{0\alpha} = 20$ μm in all case.

in these simulations, are entirely artificial, understanding the impact of the preheat

(in addition to ETI and feedthrough) on the liner for these purposes is thus the next frontier. From this standpoint it is easy to see that the timing, uniformity, and energy of the laser preheat could have a substantial impact on liner stability. In particular, uniformity of the preheat is key. Figures 4.23-4.26 point out the potential danger when the liner is perturbed by non-uniform preheat of a long wavelength nature, or some other mechanism before shock breakout. This is likely the worst-case scenario for liner stability as RMI can grow alongside perturbations from feedthrough. It is currently unknown whether the relative phase between the feedthrough perturbations and RMI could impact one another. Some indication of the importance of the phase effect was shown in Figs. 2.26, 2.27(b) of Chapter 2.

4.4 Conclusions

Feedthrough was examined in 2D randomly seeded aluminum liner implosions with increasing amounts of pre-magnetization. These 2D simulations show that stronger axial magnetic fields can significantly reduce the amplitude of ripples forming on the inner liner surface. For initial axial magnetic field strengths of 10 and 30 T, reduction of these ripples began to manifest past $CR = 2$. One major difficulty of applying these results to experiments is that 2D limits results to $m = 0$ modes only. Based on the results from Chapter 3, the sausage mode is anticipated to be the fastest growing mode when $B_z = 0$ T. For increasing strength of axial magnetic field the dominant MRT mode tends to shift from azimuthally symmetric to helically oriented modes. Feedthrough for these helically oriented modes is also larger than for $m = 0$ with pre-magnetization present. Thus, while the sausage mode can be somewhat stabilized by an axial magnetic field, it is not clear how significantly the kink mode can be stabilized, particularly with respect to feedthrough. Also unknown is the link between feedthrough reduction and overall target performance. If the inner surface rippling is reduced by 10 % how much better does the target perform? This is one of

many open questions remaining.

Studying MRT is particularly straightforward in liners with perturbations seeded on the liner exterior as seen in Chapters 2 and 3. Studying feedthrough in these liners is much more challenging. This is due to seeding of perturbations by a rippled shock. Rippled shocks in aluminum were found to be superstable, however the longer the wavelength the perturbation, the slower the ripple decays. This is in agreement with laser fusion simulations and experiments. 400 and 200 μm wavelengths were found to survive to the inner surface of 300 μm thick liners and seed ripples of those wavelengths on the inner surface. These ripples then proceeded to grow robustly and quickly independent of axial magnetic field and fill gas. Only fills nearing liquid deuterium densities affected the post-shock evolution of the perturbations.

The seeded perturbation was then imposed on the inner surface with the outer surface smooth. Such a scenario may actually be quite important for integrated MagLIF-like experiments. Sources of perturbations on the inner surface could arise from shock heating of the inner surface and pre-heat non-uniformity. These perturbations on the inner surface can also perturb the smooth exterior based on our feedthrough theory of Chapters 2 and 3 as well as the "feedout" effect explored in this chapter. This can lead to the development of longer wavelengths on the liner exterior, seeding additional MRT growth. Additionally, if there are perturbations on the liner interior before shock breakout, RMI can occur. After shock breakout, the inner surface ripples are found to oscillate, with a general increase in the amplitude of the ripples. The maximum amplitude grows slower than the shock seeded perturbations from the liner exterior (which did not oscillate at all). A water fill was not found to be sufficient to eliminate the growth of the inner surface, despite the high density. However, the amplitude was found to oscillate only once and then grow monotonically in time. If the liner can enter the deceleration phase before significant growth can occur on the inner surface, it may be possible to observe deceleration RT

growth. Future work will have to examine rippling applied to the liner inner surface after shock breakout either via an accurate preheat model or artificially depositing energy at the inner surface. This would eliminate any RMI growth and hopefully focus on the feedthrough like physics from the inner to the outer surface.

CHAPTER V

Conclusion

5.1 Conclusions and Future Work

This thesis describes the development, application, and results of an ideal MHD model of the magneto-Rayleigh-Taylor instability and its feedthrough in planar and cylindrical geometries. Between the planar and cylindrical model, the vast majority of pulsed power driven targets can be analyzed for stability. Most importantly, in cylindrical geometry, both MRT and Z-pinch instabilities such as the sausage and kink mode were combined for a more complete description of the dominant instabilities in imploding liners. Under the assumptions of ideal MHD, the linear growth rates and feedthrough factors for the sharp boundary model are calculated exactly. Both geometries were thoroughly tested against 2D resistive magneto-hydrodynamics simulations using the HYDRA code as well as experimental results where available. The analytic models were further used to interpret results of simulations and experiments where non-ideal effects are prevalent. Chapter 2 provided detailed benchmarking of the MRT and feedthrough theory and introduced the concept of mitigation of feedthrough via strong magnetic field line bending. Chapter 3 merged MRT with the intrinsic current carrying instabilities in cylindrical liners, known as the sausage and kink mode, and showed the combined MRT-kink mode to be most important in magnetized implosions. Chapter 4 exercised the HYDRA MHD code to test our

linear ideal MHD models. These models showed feedthrough reduction is a real possibility for strongly compressed axial magnetic fields. Simulations of aluminum liners showed over a factor of two reduction in the RMS amplitude of inner surface ripples at $CR = 3.4$. Several novel scenarios were presented to show that inner liner surface perturbations can impact the overall liner stability, despite being present at a stable interface.

5.1.1 On magneto-Rayleigh-Taylor instability in planar systems

Exact growth rates for the development of magneto-Rayleigh-Taylor instabilities (MRT) were formulated from the linearized ideal MHD equations in a Cartesian coordinate system. The analytic growth rates were computed for an equilibrium configuration consisting of an arbitrary combination of magnetic and kinetic pressure in an effective gravity. The equilibrium is formulated in the most general form, without some of the simplifying assumptions of the linearized equations, such as an incompressible equation of state. This allows the equilibrium quantities to be determined from 1D HYDRA simulations, which incorporate resistivity, thermal conductivity, and advanced equations of state. Post-processing of the simulations averages the equilibrium quantities in the plasma and vacuum regions of interest. The instantaneous growth rate and feedthrough factor of MRT can then be determined as a function of the simulation times for realistic, evolving plasma and magnetic fields. Some example applications of these growth rates are to experiments using accelerated planar foils and low convergence metallic liner implosions. The form of the analytic growth rates and feedthrough factors show that magnetic fields aligned with a perturbation wave vector, $\vec{k}$ have a tendency to reduce growth of that perturbation due to the additional energy required to bend the field lines. This is a direct consequence of the frozen-in law of ideal MHD. Finite resistivity reduces this effect [8].

The results of Chapter 2 show that our growth rate estimates can be most suc-

cessfully applied to experiments with strong initial seeds on the MRT unstable surface. The first direct application of the theory was to seeded aluminum liners where $k_z r >> 1$. For single wavelength perturbations of 200 μm or longer, the growth was very well modeled by linear theory. Agreement was reached between experiments on the Z-machine at Sandia National Laboratories and 2D HYDRA simulations of these experiments. Simulations show that pre-magnetization (B_z) of these long wavelength seeded liners has limited impact on MRT growth (for 2D perturbations) due to strong magnetic diffusion of the axial field. For these same liners, feedthrough was complicated by shock compression, which is not modeled with our incompressible analytic calculations. To validate our feedthrough calculations, the same seeded liners were used but the current pulse modified to reduce the shock strength. Using this new pulse, the evolution of the inner surface in 2D simulations was found in excellent agreement with the analytic theory. Additionally, feedthrough was significantly reduced by strong axial magnetic fields in these simulations. Though the stabilizing effect was weaker than predicted by the analytic ideal MHD formulation, the model's insight was still viable.

The analytic growth rates were also applied to arbitrary 3D surface perturbations on both plasma surfaces under the linear approximation. Initial perturbations on both interfaces were considered and showed that the phase of the perturbations can strongly affect MRT growth and feedthrough, particularly with longer wavelengths. One implication of this is that, perturbations present on the otherwise stable liner inner surface during implosion can instigate MRT growth on an otherwise pristine unstable surface. The growth rates were also applied to quasi-random surfaces finishes to show that an axial magnetic field could slow the typical transition of short wavelength MRT to long wavelength MRT.

The ideal MHD sharp boundary model of MRT growth and feedthrough was found to be a very insightful tool for examining liner implosions and other magnetically

accelerated targets. Its most accurate results are for those situations where relatively large and well-defined perturbations are present on the unstable surface. The model produces only qualitative results when strong magnetic field line bending is present in resistive materials and with very short wavelength initial perturbations (which can quickly become nonlinear). Similarly, feedthrough was most accurately modeled with longer wavelength perturbations on the liner exterior and without shock compression. An isentropic or at least quasi-isentropic pulse would be an ideal platform for studying feedthrough and even deceleration phase RT.

The most apparent future work for this model is to mitigate some of its weaknesses. Accounting for the effect of resistivity is important, particularly for the case of diffusion of the driving magnetic field and strongly compressed axial field. Since the driving field is strong, it may substantially reduce growth rates of perturbations aligned with it, making perturbations closer to 2D (in $r - z$). The effect of finite resistivity could be determined empirically from 2D simulation comparisons with the ideal MHD growth rates. For cases where two different magnetic field orientations of different strength are present, this is an increasingly important calculation. It would also be interesting to continue to add a number of seeded perturbations to determine how long the linear aspects of the model apply. Good success has been achieved with two different wavelength perturbations but of course there can be an arbitrary number on any given pulsed power target.

5.1.2 On magneto-Rayleigh-Taylor and current driven instabilities in cylindrical systems

As an important extension of the results of Chapter 2, an ideal MHD formulation containing the combination of MRT and current driven instabilities of a Z-pinch was presented (such as sausage and kink modes which cannot be accounted for in the planar model). Growth rates are completely analytic and dependent on the same set

of equilibrium quantities, including density, magnetic field and effective gravity, now in cylindrical force balance. The majority of the calculations were performed with a three-region sharp boundary formulation with a fuel, liner, and vacuum region, with the current confined to the outer liner surface. The most important feature of this model is that when there is no acceleration ($g = 0$) there can still be instability if there is axial current flow. The well-known instabilities are the sausage and kink modes ($m = 0$ and $m = 1$), and when $g = 0$ we call these the pure sausage and kink modes. In the planar formulation when $g = 0$, the growth rate, $\gamma = 0$ and the pure sausage and kink modes are completely absent. In cylindrical geometry, growth rates of these instabilities are reduced by substantial magnetic field line bending, but are increased due to the current driving the liner in addition to the instability caused by the acceleration of the liner (when applicable). In general, this tends to increase the growth rate of instability for any given (k_θ, k_z), in comparison to the planar formulation.

The model was applied to magnetized liner implosions on the Z-machine, similar to MagLIF, again using results from 1D HYDRA simulations to determine the required equilibrium parameters of the model. The kink mode was found to be particularly important in magnetized liner implosions where there is a strong azimuthal magnetic field imploding a liner with an initially uniform, 10 T axial magnetic field. In the equilibrium Z-pinch, the sausage mode can be stabilized by a strong axial magnetic field, and the kink mode can be stabilized if it satisfies the Kruskal-Shafranov condition. In a magnetized liner implosion, the kink mode is found to be the dominant mode early on due to stabilization of the sausage mode by the axial magnetic field. During this period the acceleration is small which means the MRT growth is small. As the axial current increases, the azimuthal magnetic field increases as well and continues to destabilize the sausage and kink modes. The increasing azimuthal field also corresponds to an increase in acceleration and as the liner implodes at high acceleration

the MRT-sausage mode is the dominant mode. At high compression, the initial axial magnetic field is significantly compressed (scaling with $\sim 1/r^2$ as opposed to $1/r$ for B_θ) in the fuel region and again begins to stabilize the sausage mode. The liner then decelerates on the highly compressed fuel and the acceleration changes direction. At this point the sausage mode is completely stabilized and kink mode remains. Over the entire deceleration phase, the kink mode is found to grow by roughly a factor 4 depending upon the axial wavelength present. These results appear in agreement with experimental results from the Z-machine. The MRT growth on the exterior is observed to be helically oriented and the stagnating fuel column is possibly helical as well.

In order to extend the cylindrical results beyond the sharp boundary model, the governing ODE for the linearized ideal MHD equations was numerically integrated incorporating the full 1D HYDRA radial profile. While significantly more computationally expensive, the results are theoretically more accurate given that they account for finite density and magnetic field gradients as found in HYDRA and experiment. Presence of finite current in the liner is particularly important in the $\hat{\theta}$ direction as that is where the strongest field is. 2D (r, θ) simulations were run with $m = 1$ and $m = 6$ to test the numerical integration. The sharp boundary results predict the kink mode to have the faster growth over $m = 6$, due to strong stabilization for high azimuthal mode numbers, however both modes grew roughly the same in simulation. This is also what the numerical integration indicates; however this methodology has not yet been applied to the entire 1D simulation. Future work with this upgraded model requires a sensitivity study of these growth rates to the profile used. However this numerical approach does seems to be a feasible method to determine more sophisticated growth rates, certainly much faster than any 2D or 3D MHD simulation. Seeded 3D simulations would be ideal test cases for these more advanced growth rate calculations, as well as for the sharp boundary model. A preliminary set of 3D HY-

DRA simulations with seeded perturbations is given in Appendix C. Additionally, effects of finite resistivity are likely again important, particularly in the azimuthal direction due to the strong diffusion of the azimuthal field. Quantifying this would be exceedingly useful to better understand the dominant mode at any given time.

The sausage, kink and other non-axisymmetric MHD modes ($m \geq 2$) are not the only instabilities that occur when $g = 0$. There is additionally the electrothermal instability. Proper inclusion of ETI requires the energy equation of MHD as ETI is driven by temperature perturbations and the dependence of resistivity on temperature. As such it is significantly more difficult to include in the linearized fluid equations. It is nonetheless extremely important to liner implosions, as it is believed to seed MRT. Incorporating ETI with the sausage and kink modes even with $g = 0$ may be very beneficial in understanding how MHD modes in magnetized liner implosions are seeded.

5.1.3 On the 2D simulation of fuel/liner interface stability in magnetized liner implosions

Chapters 2 and 3 of this thesis have illustrated both the strengths and weaknesses of the ideal MHD models. Chapter 4 was devoted to the use of these limited models to understand some of the more complex and non-ideal behavior that is observed in experiments and resistive MHD simulations. The workhorse of this chapter was HYDRA, run in 2D (r, z) geometry.

The first approximation addressed was the linear approximation. Based on the results of Chapters 2 and 3 it was clear that the most dramatic and successful effect of the axial magnetic field (outside of 3D structure since we are considering 2D only) was to reduce feedthrough. Reducing feedthrough is tantamount to reducing the seed of deceleration RT on the inner surface. A typical MagLIF liner is shock compressed and only machining roughness modulates the surfaces. The key physics here is the

evolution of instabilities from short to long wavelengths. Initially, the feedthrough is small due to the short wavelengths, but as the longer wavelengths develop over time, the inner surface can become increasingly rippled by stronger feedthrough. This transition from short to long wavelengths is a nonlinear process that the code handles. Two very different initial surface perturbations were run for aluminum liner implosions with increasingly levels of pre-magnetization (0, 10, 30 T). Even at very small convergence ratio ($CR = 3.5$) significant reduction in ripple amplitude on the inner surface was observed in all magnetized simulations as anticipated by analytic theory. Interestingly, the 30 T field did not seem to give significantly more benefit than the 10 T field (for the purposes of feedthrough). However, additional beryllium simulations are needed to assess this effect at higher CR. Due to the lower mass of beryllium these liners implode faster and could exhibit additional differences between the 10 and 30 T at higher CR. Some future work is to examine the feedthrough of 3D modes which are likely very important to magnetized implosions. As it stands, only the sausage mode was determined to be stabilized by the axial magnetic field via 2D simulations, however, we know the kink mode is present in these implosions. Nonetheless, this was a highly encouraging result given that the experimental evidence points to the axial magnetic field as increasing the stability of the implosion.

The second half of Chapter 4 was devoted to the shock compression of the liner. In seeded liners, shock compression introduces the complexity of the Richtmyer-Meshkov instability in various forms. It was found that shock waves in liners with long wavelength seeds on the exterior are driven non-uniformly and can significantly deteriorate the liner interior. The non-uniform shock wave is initially rippled with the seeded wavelength and amplitude and then propagates towards the liner interior. Shorter wavelengths damp faster than long, but any left over amplitude seeds the inner liner surface with a ripple that then proceeds to grow linearly in time. This is very similar to traditional RMI growth. Both the amplitude of the seed and growth rate of the

perturbation were found to be quite insensitive to the strength of the axial magnetic field and fill gas density. Only significant impact on the seed and growth was observed for fill densities near liquid water and highly conductive fluid. The high Atwood number reduces RMI and highly conductive fluid increases the field line bending. Overall, this could be a very dangerous perturbation for the fuel/liner interface.

In order to include an initial perturbation but also in a more stable configuration, the initial rippling was instead imposed on the inner surface (leaving the outer surface smooth). The inner surface ripples were expected to grow due to RMI as well as oscillate due to feedthrough and stable MRT effects (oscillating solutions are the stable form of feedthrough/MRT). This was observed in 2D simulations and additionally, the overall growth of the ripples was observed to be smaller than the previous shock seeded case. Trading a fill gas for water fill substantially increases the Atwood number at the inner liner surface, which can reduce both feedthrough and RMI. We found the water fill in the central region was able to eliminate the oscillations from feedthrough, however, it could not completely subdue the RMI growth. In the future, it may be interesting to investigate the potential to use a water fill with a larger radius liner to examine deceleration RT in detail. The deceleration phase would ideally begin before any RMI growth is significant as maintaining the initial condition of the surface is imperative. The larger radius reduces the magnetic pressure and liner velocity, which can reduce RMI. The inner surface perturbation was also observed to increase MRT growth on the liner exterior, which may be very important for MagLIF. This is particularly the case if the laser preheat is non-uniform. However, in a well-implemented implosion shock breakout occurs before the non-uniform preheat would interact with the liner surface. At least in the worst-case scenario, the presence of perturbations on the liner interior can lead to destabilization of a liner implosion. Better modeling of the preheat phase will likely lead to better understanding of the influence of the preheat on the liner inner surface.

HYDRA has many capabilities beyond just the resistive MHD package. As a multi-physics code its material strength models and radiation diffusion packages could also introduce important (neglected) physics in certain scenarios. For example, one of the primary reasons to isentropically compress targets (besides not introducing a shock) is to keep the material as close to the solid phase as possible. In such a scenario, material strength may play a significant role. Radiation generated in the preheat could also heat the liner inner surface (if it does not escape and cool the fuel). The effect of radiative cooling on ETI has also been examined [17] but not in the context of a MagLIF target. All of these packages require additional computing time and the physical models are just that, models, and may not necessarily represent the true physics occurring. Similarly, the resistive MHD package has its own limitations due to its neglect of the Nernst term and some of the underlying framework of the MHD package itself. The simple Ohm's law of resistive MHD neglects many terms that could be important in a wide variety of pulsed power experiments. Extended MHD models that can eliminate the "floor" density values and can better model lower density plasma is a very important goal to move towards. This can hopefully improve the robustness of such codes.

5.1.4 Future work and possible experiments

Finally, avenues for future work and experimental considerations for key results can now be summarized. Both Chapters 2 and 3 analytically predicted the stabilization of MRT and feedthrough, dependent upon the perturbation wavenumber $\vec{k}$, due to the stabilizing influence of bent magnetic field lines. Ideal MHD can over predict the amount of stabilization that occurs even in seeded liners. Seeded experiments with a pre-imposed axial magnetic field can then give confidence to our simulation results and further our understanding of the impact of finite resistivity on our ideal MHD model. The ultimate goal then is to improve the accuracy of the linear model by

incorporating finite resistivity and answering the question, for a given axial magnetic field, what modes are actually stabilized?

For liners where there is only initial surface roughness, it is would also be extremely valuable to determine how early the helical MRT structure appears in experiments. This refers not only to the early tokamak-like behavior of MagLIF but perhaps the interplay between MRT and ETI that would be present early in the current pulse. Such studies could also illuminate the extent of nonlinear generation of modes in 3D when a helical magnetic field is present. Further quantifying the effect of the axial magnetic field on the stability of the inner liner surface as well the 3D nature of feedthrough that occurs is also important for MagLIF. Identifying any difference between feedthrough at high and low CR also would provide valuable insight into the true impact of modes introduced by cylindrical geometry. This could be done by moving the liner to an initially larger radius; however, the thickness of the liner and corresponding acceleration history would have to be carefully considered. A larger initial radius would also allow for more axial magnetic field compression if there were a central metal rod that confines the axial flux in an annulus. The other major question is whether or not feedthrough is the dominant mechanism responsible for perturbations on the inner surface. One culprit could be the preheat blast wave, however, this phase requires significantly more investigation.

APPENDICES

APPENDIX A

A note on the Taylor instability

In his classic paper [2], Taylor considered the instability on the surfaces of a fluid slab of a finite thickness that is accelerated by a much lighter fluid on either side of the fluid slab. He found that there is always an unstable mode in which the ripples on both surfaces of this fluid slab grow exponentially in time. This is called the Taylor instability or the Rayleigh-Taylor instability (RT). The RT growth rate of the unstable mode is given by,

$$\gamma = \sqrt{ka} \tag{A.1}$$

where k is the wavenumber of the surface ripples and a ($a > 0$) is the acceleration. This growth rate is independent of Δ, the thickness of this accelerating fluid slab. For the unstable mode, the amplitude of the ripple at the back surface of the accelerated fluid slab is a factor of $e^{-k\Delta}$ smaller than the amplitude of the ripple at the front surface of this accelerated fluid slab, and this factor is known as the "feedthrough factor" in the literature of RT [6][30][57]. Thus, over a time t, the slab will undergo a distance $s = at^2/2$, during which the unstable mode will gain an amplitude on both

surfaces of the fluid slab,

$$G = e^{\gamma t} = e^{\sqrt{2ks}}. \tag{A.2}$$

In writing Eq. A.2, we have assumed that the fluid slab does not have any initial velocity. As written, Eq. A.2 is independent of a, independent of Δ, but depends only on the accelerated distance, s, and the wavenumber, k. Equation A.2 was in fact given by Taylor [2]. We shall next show that Eq. A.2 actually gives the bound on the maximum amplitude gain over a distance s. This bound depends only on k and s, and is independent of the magnitude or sign of a.

Suppose now that at $t = 0$, there is an initial velocity v, $v > 0$, in the fluid slab. After a time t, the slab travels a distance, $s = vt + at^2/2$. We may easily solve for t in terms of s, and the amplitude gain during time t may then be expressed as,

$$G = e^{\gamma t} = e^{\sqrt{2ks} f(\xi)}, \tag{A.3}$$

where $\xi = v/\sqrt{2as}$, and $f(\xi) = \sqrt{1+\xi^2} - \xi$. Figure A.1 plots $f(\xi)$ as a function of ξ, showing that $f(\xi) \leq 1$, regardless of the value of v, a, or s. Comparing Eq. A.3 with Eq. A.2, we see that Eq. A.2, is the bound for the RT growth over a distance s, regardless of v, a, or s. Suppose that a changes sign, so that $a = -|a|$. Assume that at $t = 0$, the slab also has an initial velocity v, $v > 0$. After a time t, this slab travels a distance, $s = vt - |a|t^2/2$. This slab will be decelerated to zero velocity at time $t_{st} = v/|a|$, after traveling the distance $s_{st} = v^2/2|a|$. Likewise, we may solve for t in terms of s for this $a < 0$ case. During time t, before s reaches s_{st}, the amplitude gain may be expressed as,

$$G = e^{\gamma t} = e^{\sqrt{2ks} h(\xi)}, \tag{A.4}$$

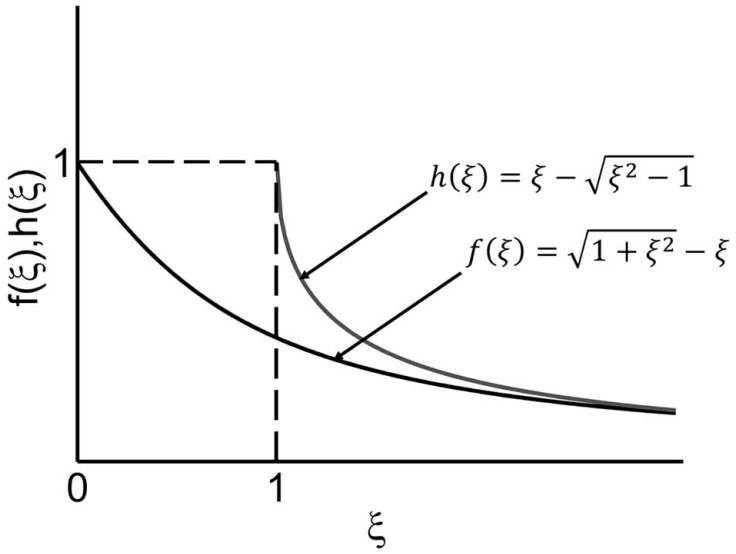

Figure A.1: The functions $f(\xi)$ and $h(\xi)$. Both $f(\xi)$ and $h(\xi)$ approach $(1/2)\xi$ for $\xi >> 1$.

where $\xi = v/\sqrt{2|a|s} = \sqrt{s_{st}/s} > 1$, and $h(\xi) = \xi - \sqrt{\xi^2 - 1}$. Figure A.1 plots $h(\xi)$ for all $\xi > 1$, showing that $h(\xi) \leq 1$, regardless of the value of v, a, or s ($< s_{st}$). Comparing Eq. A.4 with Eq. A.2, we see that Eq. A.2 is again the bound for RT growth over a distance$s$, regardless of v, a, or s ($< s_{st}$). After t_{st}, Eq. A.2 applies because the slab has a zero velocity at $t = t_{st}$.

In general, acceleration of a fluid slab, a in the lab frame, may be provided by a magnetic pressure [6], a kinetic pressure [2][30], or some combination of the two [57]. Regardless of what causes the acceleration of this slab, the maximum growth rate, γ, is still given by $\sqrt{ka}$, when all stabilization mechanisms are absent. Stabilizing influence may come from surface tension [30], magnetic tension [6][57], magnetic shear [66], etc. The maximum amplitude gain in the unstable mode after the slab travels a distance s is, therefore, always bounded by Eq. A.2, regardless of the magnitude or sign of a, of the magnitude or sign of the initial velocity v of the slab, of the thickness of the fluid slab, and of the degree of the stabilization influence, according to the linear theory.

The simple scaling described in this appendix can sufficiently describe the evolution of single mode MRT with one modification. We return to the simple single mode MRT experiments run by Sinars et al. [51] for the 400 μm axial wavelength perturbation. Using the 1D HYDRA implosion data, the trajectory of the individual fluid elements of the liner can be tracked. The position of the fluid then feeds directly into the estimate of the MRT growth rate, $\gamma = \sqrt{2k(r(t) - r_0)}$ and then the overall MRT gain. The MRT gain can be calculated with the exponential as shown by Eq. A.2 but can also be more accurately calculated using the hyperbolic cosine function, cosh instead [51][57]. Figure A.2 shows this comparison for the MRT amplitude evolution, using the hyperbolic cosine function in Fig. A.2(a) and the simple exponential function (Eq. A.2) in Fig. A.2(b). The calculation plots the MRT growth for every five zones. The evolution is best estimated by the central zones of the liner as opposed to the ablating regions near the liner exterior and interior interfaces. These ablating zones are annotated in Fig. A.2. These fluid elements tend to be very low density and strongly accelerated but do not contribute to MRT growth in the bulk mass of the liner. One implication of this result is that g can be substituted in both the planar and cylindrical models described in Chapters 2 and 3 by the transformation to the displacement of the fluid elements. As a result this technique works not only for RT but the pure MRT as well (in the absence of stabilizing mechanisms and of the sausage and kink modes).

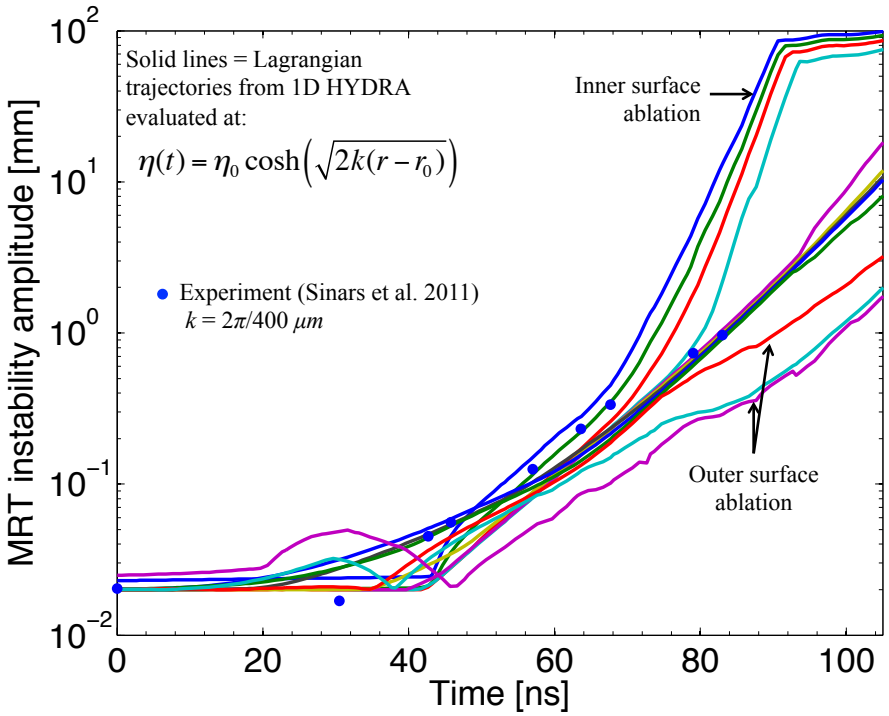

(a) Calculation of MRT growth for 400 μm axial wavelength by the formula $\cosh(\sqrt{2k(r-r_0)})$

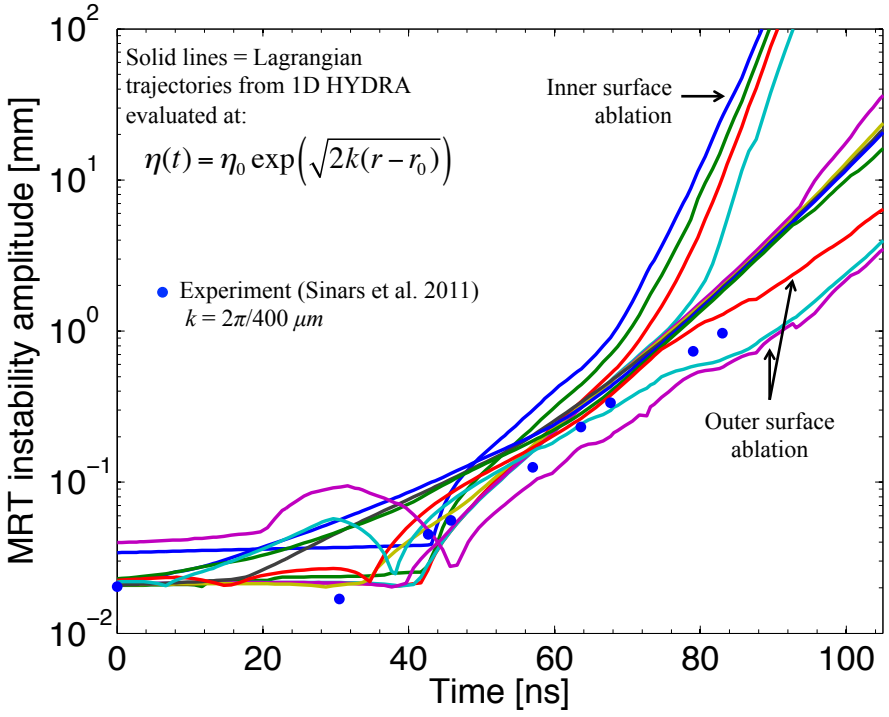

(b) Calculation of MRT growth for 400 μm axial wavelength by the formula $\exp(\sqrt{2k(r-r_0)})$

Figure A.2: Comparison of MRT growth estimates for the 400 μm perturbation of the experiment by Sinars et al. [51]. The exponential scaling clearly shows the largest growth. Curves are plotted for every five zones in the liner.

APPENDIX B

Alternate derivations and details of the cylindrical eigenmode solutions

B.1 Alternate derivation of boundary conditions for cylindrical MRT formulation

It is possible to construct the boundary conditions for the cylindrical sharp boundary model directly from the governing ODE in cylindrical coordinates. The ODE recorded in Chapter 3 is given by (c.f.,. Eq. 3.16)

$$\frac{d}{dr}\left[\frac{P(r)}{r}\frac{d}{dr}\left(r\xi_r(r)\right)\right] + Q(r)\xi_r(r) = 0, \tag{B.1}$$

$$P(r) = \frac{\mu_0 r^2 \omega^2 \rho_0 - (mB_{0,\theta}(r) + krB_{0,z})^2}{(k^2r^2 + m^2)}, \tag{B.2}$$

$$\begin{aligned} Q(r) =& \frac{2B'_{0,\theta}(B_{0,\theta}(m - kr)(kr + m) + krmB_{0,z})}{r\left(k^2r^2 + m^2\right)}, \\ &+ \frac{2kmB_{0,\theta}B'_{0,z}}{k^2r^2 + m^2} \\ &+ \frac{\beta B_{0,\theta}B_{0,z} + \alpha B^2_{0,\theta} + \kappa B^2_{0,z}}{r^2\left(k^2r^2 + m^2\right)^2} \\ &- \frac{4k^2B^2_{0,\theta}(mB_{0,\theta} + krB_{0,z})^2}{\left(k^2r^2 + m^2\right)\left((mB_{0,\theta} + krB_{0,z})^2 - \mu_0 r^2\omega^2\rho_0\right)} \\ &+ \mu_0 g\rho'_0 - \mu_0\omega^2\rho_0, \end{aligned} \tag{B.3}$$

$$\alpha = k^4r^4\left(m^2 + 2\right) + 2k^2r^2m^2\left(m^2 - 2\right) + \left(m^2 - 2\right)m^4, \tag{B.4}$$

$$\beta = 2krm\left(k^4r^4 + k^2r^2\left(2m^2 - 3\right) + m^2\left(m^2 - 1\right)\right), \tag{B.5}$$

$$\kappa = k^2r^2\left(k^2r^2 + m^2\right)^2, \tag{B.6}$$

It is difficult to verify whether the ODE in Bud'ko et al.[7] is similar to or the same as the one derived here (after taking the limit of their gas index, $\gamma \to \infty$), given there is no explanation of the derivation. There also seems to be at least one typo in Eq. 3 of Bud'ko, otherwise the limit of $\gamma \to \infty$ is unbounded. The limit can be repaired by changing the right square bracket around $\rho^2\sigma^2$ (first term on second line) to encompass all terms up until the $-r\frac{d}{dr}$ term. However, the author cannot guarantee this is the ODE that Bud'ko intended. The boundary conditions there take a much different form as well. Additionally, when all derivatives are set to zero for the equilibrium quantities, a fairly complex ODE remains, requiring numerical integration. It is possible there are some "tricks" that could provide an analytic result, though there is nothing obvious to the author.

The derivation of the boundary conditions in Chapter 3 summed the perturbation kinetic, magnetic and gravity pressures at both sides of each interface and then set equal. The perturbation quantities were determined from simplifying the governing ODE, Eq. B.1, using the fact that the densities and magnetic fields were constant.

Like the planar formulation of Chapter 2, Eq. B.1 can be integrated across the two interfaces over an infinitesimally thin region. The appropriate operator for this procedure is

$$\lim_{\epsilon \to 0} \int_{r_0-\epsilon}^{r_0+\epsilon} dr, \tag{B.7}$$

where r_0 is the radial position of the interface (either r_i or r_e for the liner problem). Calculation of this integral is fairly straightforward. Applying the integral to the first term of Eq. B.1 at r_e (interface of regions I and II), yields

$$\frac{P(r_{e^+})}{r_e}\frac{d}{dr}(r\xi_r(r))\bigg|_{r_{e^+}} - \frac{P(r_{e^-})}{r_e}\frac{d}{dr}(r\xi_r(r))\bigg|_{r_{e^-}}, \tag{B.8}$$

where r_{e^+} corresponds to evaluating the equilibrium quantities in the vacuum region (region I), and r_{e^-} corresponds to the liner region (region 2). In this case, for example, $B_{0\theta}(r_{e^-}) = 0$, $\rho_0(r_{e^+}) = 0$. The same procedure can be applied to the interface at r_i. Recall that $\xi_{r,f}$ is known in the fuel region and that $\xi'_{r,v}$ must be determined from the condition $\vec{B_1} \cdot \hat{n}_0 + \vec{B_0} \cdot \hat{n}_1 = 0$ and $\vec{B_1} = \nabla \times (\vec{\xi} \times \vec{B_0})$ (linearized Faraday's law). Using the definitions provided in chapter 3, $\xi_v(r)$ in region I is (compare with the simple planar solution, e^{-kx})

$$\xi_v(r) = \frac{\xi_\beta r[krK_{m-1}(kr) + mK_m(kr)](mB_{0\theta} + B_{z,v}kr_e)}{[kr_eK_{m-1}(kr_e) + mK_m(kr_e)]\,(mB_{0\theta}r_e + B_{z,v}kr^2)}, \tag{B.9}$$

where $\xi_v(r_e) = \xi_\beta$.

Application of Eq. B.7 to $Q(r)\xi_r(r)$ of Eq. B.1 at the vacuum/liner interface (regions I and II) retains only the first two terms of $Q(r)$, and the last term with ρ'_0, as only those terms contain derivatives in Eq. B.3. The simplified terms of $Q(r)$ at

the liner/vacuum interface then become

$$\frac{2B'_{0,\theta}(B_{0,\theta}(m-kr)(kr+m)+krmB_{0,z})}{r\left(k^2r^2+m^2\right)} \rightarrow \frac{B_{0\theta}\left[(B_{z,l}+B_{z,v})kr_im+B_{0\theta}(m^2-k^2r_i^2)\right]}{r_i(m^2+k^2r_i^2)}, \tag{B.10}$$

$$\frac{2kmB_{0,\theta}B'_{0,z}}{k^2r^2+m^2} \rightarrow \frac{kmB_{0\theta}(B_{z,v}-B_{z,l})}{k^2r_e^2+m^2}, \tag{B.11}$$

$$\mu_0 g\rho'_0 \rightarrow -\mu_0 g\rho_{0,l}. \tag{B.12}$$

Equations B.10 and B.11 are identically zero at the fuel/liner interface (i.e. terms proportional to $B_{0\theta}$, which is zero in the liner and fuel region). At the fuel/liner interface the final term yields

$$\mu_0 g\rho'_0 \rightarrow \mu_0 g\rho_{0,l}-\mu_0 g\rho_{0,f} \tag{B.13}$$

The form of the boundary conditions found in Chapter 3 is then found by combining Equations. B.8,B.10,B.11,B.12 or Eq. B.13 for the appropriate interface. Keeping in mind that $d\xi_{r,l}(r)/dr$ is the remaining unknown, while the eigenfunction $\xi_r(r)$ is known in regions I and III.

The result of the integration at the fuel/liner interfaces gives

$$\frac{(\xi_\alpha+r_i\xi'_l(r_i))\left(\mu_0\rho_l r_i^2\sigma-B_{z,l}^2k^2r_i^2\right)}{r_i\left(k^2r_i^2+m^2\right)}-\frac{\left(\xi_\alpha+r_i\xi'_f(r_i)\right)\left(\mu_0\rho_f r_i^2\sigma-B_{z,f}^2k^2r_i^2\right)}{r_i\left(k^2r_i^2+m^2\right)} + g\mu_0\xi_\alpha(\rho_l-\rho_f)=0, \tag{B.14}$$

and the result at the liner/vacuum interface

$$-\frac{(\xi_\beta + r_e\xi_v'(r_e))\,(B_{0\theta}m + B_{z,v}kr_e)^2}{r_e\,(k^2r_e^2+m^2)} - \frac{(\xi_\beta + r_e\xi_l'(r_e))\left(\mu_0\rho_l r_e^2\sigma - B_{z,l}^2k^2r_e^2\right)}{r_e\,(k^2r_e^2+m^2)} + \xi_\beta\left(\frac{B_{0\theta}km(B_{z,v}-B_{z,l})}{k^2r_e^2+m^2} + \frac{B_{0\theta}\,(B_{0\theta}\,(m^2-k^2r_e^2)+kmr_e(B_{z,l}+B_{z,v}))}{r_e\,(k^2r_e^2+m^2)} - g\mu_0\rho_l\right) = 0. \tag{B.15}$$

Plugging in the expressions for $\xi_f'(r_i)$ (from Eq. 3.28) and $\xi_v'(r_e)$ (Eq. B.9) and solving for ξ_l' then give the boundary conditions developed in Chapter 3 (Equations. 3.32, 3.40) but derived in a completely different manner.

B.2 Derivation of long wavelength ($k_z << 1$) limit of $m = 0$ mode with $B_z = 0$

To derive the long wavelength limit $m = 0$ dispersion relation, series expansions are needed for the modified Bessel's functions, I_m and K_m. These are found in most any mathematical physics reference and can also be computed to arbitrary order in the Mathematica program as was done here. The appropriate long wavelength expansions are

$$I_0(kr) = 1 + \frac{(kr)^2}{4} + O((kr)^3), \tag{B.16}$$

$$K_0(kr) = \left(-\log(kr) - \log\left(\frac{1}{2}\right) - \gamma\right) + \frac{1}{4}(kr)^2\left((-\log(kr)) - \gamma + 1 - \log\left(\frac{1}{2}\right)\right) + O\left((kr)^3\right), \tag{B.17}$$

where $\gamma \approx 0.577216$ is the Euler's constant. Recalling the exact solution for $\xi_r(r)$ in the liner region is with boundary conditions is given by

$$\xi_r(r_i) = \xi_\alpha = C_1 I'_m(kr_i) + C_2 K'_m(kr_i), \tag{B.18}$$

$$\xi_r(r_e) = \xi_\beta = C_1 I'_m(kr_e) + C_2 K'_m(kr_e), \tag{B.19}$$

the asymptotic solution for $\xi_r(r)$ in the liner region can be computed as

$$\begin{aligned}\xi_l(r) = &\frac{\xi_\alpha r_i \left(k^2 r^2 r_e^2 \log(r_e/r) + 2r^2 - 2r_e^2\right)}{r\left(k^2 r_e^2 r_i^2(\log(r_e/r_i)) - 2(r_e - r_i)(r_e + r_i)\right)} \\ &+ \frac{\xi_\beta r_e \left(k^2 r^2 r_i^2 \log(r/r_i) - 2r^2 + 2r_i^2\right)}{r\left(k^2 r_e^2 r_i^2(\log(r_e/r_i)) - 2(r_e - r_i)(r_e + r_i)\right)}.\end{aligned} \tag{B.20}$$

The same boundary conditions at r_i and r_e, as found in the main text of Chapter 3 for the sharp boundary (c.f. Equations. 3.32 and 3.40), are applied to B.20 with the asymptotic expressions inserted for the full Bessel's functions. From these two boundary conditions, two equations for ξ_α/ξ_β can again be determined in the long wavelength limit.

$$\xi_\alpha/\xi_\beta = \frac{r_e\omega^2\left(k^2 r_i^2 - 4\right)}{\left(-k^2 r_e^2 r_i(\log(r_e/r_i))\left(gk^2 r_i + 2\omega^2\right) + 2gk^2\Delta(r_e + r_i) + r_i\omega^2\left(k^2 r_e^2 - 4\right)\right)}, \tag{B.21}$$

$$\xi_\alpha/\xi_\beta = \frac{k^2 r_e^2 r_i^2(\log(r_e/r_i))\left(k^2(\chi) + 2\mu_0\rho\omega^2\right) - 2k^2\Delta(r_e + r_i)(\chi) + \mu_0\rho r_e^2\omega^2\left(k^2 r_i^2 - 4\right)}{\mu_0\rho r_e r_i\omega^2\left(k^2 r_e^2 - 4\right)}, \tag{B.22}$$

$$\chi = B_\theta^2 + g\mu_0\rho r_e. \tag{B.23}$$

which are also known as the feedthrough factors. Equations B.21 and B.22 can then be set equal to determine the dispersion relation. For $kr_e << 1$, the dispersion relation, $\omega(m = 0, k)$, remains highly cumbersome even in this limit. The solution of

which is shown in Equations. B.24-B.27.

$$\omega^2 = \frac{-2k^2 r_e^2 r_i \log\left(\frac{r_e}{r_i}\right)\left(B_\theta^2 + g\mu_0\rho\tau\right) + B_\theta^2 r_i\left(k^2 r_e^2 - 4\right) + \Delta g\mu_0\rho r_e\left(k^2 r_e r_i + 4\right) - \sqrt{\psi}}{8\mu_0\rho r_e^2 r_i \log\left(\frac{r_e}{r_i}\right)}, \tag{B.24}$$

$$\begin{aligned}\psi = &\left(B_\theta^2 r_i\left(k^2 r_e^2 - 4\right) + \Delta g\mu_0\rho r_e\left(k^2 r_e r_i + 4\right)\right)^2 \\ &+ 4k^2 r_e^2 r_i\chi\log\left(\frac{r_e}{r_i}\right)\left[B_\theta^2 r_i\left(4 - k^2 r_e^2\right) + g\mu_0\rho r_e\tau\left(4 - k^2 r_e r_i\right) + k^2 r_e^2 r_i\chi\log\left(\frac{r_e}{r_i}\right)\right],\end{aligned} \tag{B.25}$$

$$\tau = r_e + r_i, \tag{B.26}$$

$$\chi = B_\theta^2 + g\mu_0\rho r_e. \tag{B.27}$$

However, at this point the limit of $k \to 0$ can be taken directly, which is quoted in chapter 3 (Eq. 3.52) and reproduced here in Eq. B.28 (un-normalized) and B.30.

$$\omega^2 = -\frac{B_{0\theta}^2 r_i - g r_e\Delta\mu_0\rho_0 + \left|B_{0\theta}^2 r_i - g r_e\Delta\mu_0\rho_0\right|}{2r_e^2 r_i\mu_0\rho_0\ln\left(r_e/r_i\right)}, \tag{B.28}$$

$$q = \frac{r_e}{r_i} = \frac{AR}{AR-1}. \tag{B.29}$$

$$\bar{\omega}^2 = \frac{-1 + \bar{g}q - |1 - \bar{g}q|}{2\ln q}, \tag{B.30}$$

$$\bar{\omega}^2 \equiv \omega^2/(B_{0\theta}^2/\mu_0\rho_0 r_e^2), \tag{B.31}$$

$$\bar{g} \equiv g/(B_{0\theta}^2/\mu_0\rho_0\Delta), \tag{B.32}$$

Similar procedures can be performed for the $|m| > 0$ modes as well, but the solutions become increasingly more complicated.

APPENDIX C

Initial 3D simulations of seeded liners

C.1 Initial simulations of 3D seeded modes

The computational cost of 3D simulations is very high. With the resources at hand it is not possible to perform 3D simulations of the roughened liners of Chapter 4 in a reasonable amount of time. Seeded liners are somewhat more forgiving. Here, we present the initial results of seeded 3D aluminum liner simulations. The setup for these simulations is very similar to the seeded aluminum liners in Chapters 2,3,4 where the aluminum liner is seeded on the exterior with a sinusoidal perturbation. In this case, the axial extent is 1.6 mm, with axially seeded wavelength with $\lambda_z = 800$ μm. We consider both the $m = 0$ and $m = \pm 1$ modes so that the total perturbation is $e^{-im\theta - ikz}$ and the peak-to-valley amplitude is 40 μm. For the $m = \pm$ modes, the perturbation is helical and the sign determines the sense of the helix. The axial resolution is 12.5 μm. In the azimuthal direction, there are 128 zones, which corresponds to 2.8° azimuthal sectors. At the initial liner outer radius (2.79 mm) this corresponds to azimuthal resolution of 136 μm for the full circumference. The liner inner surface is set at 2.325 mm and there is only a vacuum fill. The aspect ratio of the liner is

6 (thicker than the Sinars et al. liner [51] which corresponds to lower acceleration). The radial resolution is highly weighted towards the outer surface of liner to give roughly 10 μm resolution early on. The cells are clearly far from the ideal shape (roughly $dx \approx dy \approx dz$). There are nonetheless, a significant number of cells per seeded wavelength. In total, there are 1.5 million zones, many times larger than the high-resolution 2D simulations presented in the main text. And yet, while the radial and axial resolutions are reasonable, the azimuthal resolution is lower than what would be ideal.

To measure the MRT growth in 3D, the full 3D data is used. For each (r, z) plane the transmission contours are calculated, as was done for the 2D cases where the opacity for aluminum is assumed constant (102 cm^2/g). Since aluminum is very opaque to the X-ray energy considered, this reduces the impact of the azimuthal asymmetry (one cannot see through the aluminum, unlike the beryllium radiographs [55]). The ripple amplitude of the (r, z) plane is computed and the next $\theta + d\theta$ plane is computed. The result is that at each simulation time, we have the ripple amplitude as a function of θ. As in the 2D results measuring the ripple amplitude in this way works quite well so long as the mode of interest is very clean (i.e. no shorter wavelength modulations). Additionally, for each (r, z) plane we can compute the FFT of the surface and store the amplitudes of the wavelengths of interest.

From our linear theory we expect negligible differences between the three different modes, even with a 10 T axial magnetic field, since we initially have $k_z r_e = 21$ for $k_z = 2\pi/800$ μm. The simulation and analytic results are shown in Fig. C.1 including a 10 T axial magnetic field. The analytic results (using 1D HYDRA) for $m = 0, \pm 1$ modes were so similar, we include only $m = 0$ as the dashed curve. The MRT amplitudes for the 3D simulations were computed as briefly discussed above, using 50 % transmission contours. The variation in amplitude between each azimuthal sector remained small, particularly for the sausage mode. Figure C.1(a) shows the

results for the 800 μm ripple computed directly for each azimuthal mode for the 3D simulations. The MRT growth in the 3D HYDRA simulation was observed to be substantially higher for the kink modes, while the analytic result agrees well with the 3D simulation for $m = 0$ mode (the analytic $m = \pm 1$ results were nearly identical to $m = 0$). This was a surprising result given our analytic theory. The result makes more

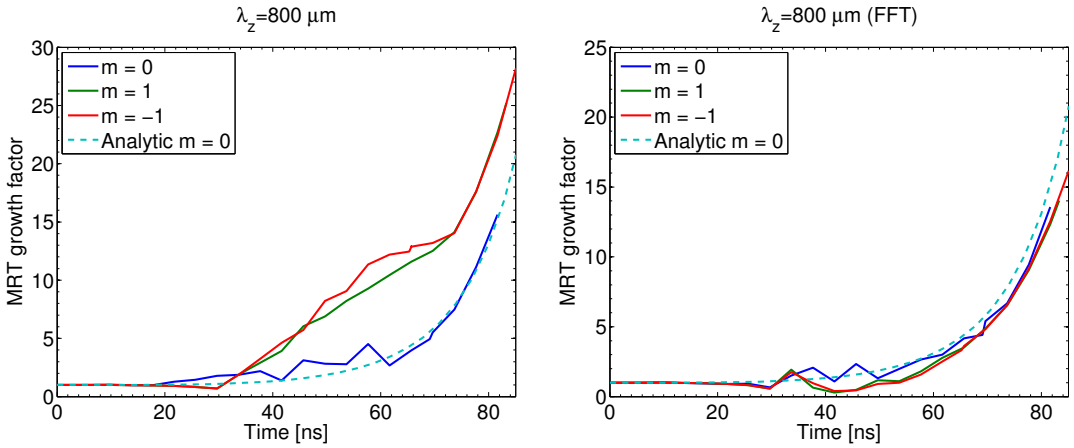

(a) Evolution of MRT amplitude for the $\lambda_z = 800$ μm perturbation for the $m = 0, \pm 1$ modes measured from the minimum to maximum of the 50% transmission contour. The dashed curves show the cylindrical analytic model result for $m = 0$.

(b) Evolution of MRT amplitude for the $\lambda_z = 800$ μm perturbation for the $m = 0, \pm 1$ modes measured from the FFT of the 50% transmission contour. The dashed curves show the cylindrical analytic model result for $m = 0$.

Figure C.1: Evolution of MRT amplitude for the $\lambda_z = 800$ μm perturbation for the $m = 0, \pm 1$ modes measured by two different methods. The initial amplitude is 20 μm so that a growth factor 15 corresponds to 300 μm.

sense when the FFT results are examined. Figure C.1(b) shows the FFT measurement of the 800 μm which shows the growth to be very similar, as expected, between the three modes. The discrepancy between the two measures is easily explainable when the FFT measure of the amplitude at 400 μm is examined (Fig. C.2). Both kink modes show very substantial growth of an additional, apparently nonlinearly generated, 400 μm mode, which is nearly absent in the sausage mode. In fact the 400 μm mode growth is so strong for the kink mode, is on the order of seeded 800 μm mode.

Figure C.3 shows snapshots of the liner density at 77 ns for the three perturbations.

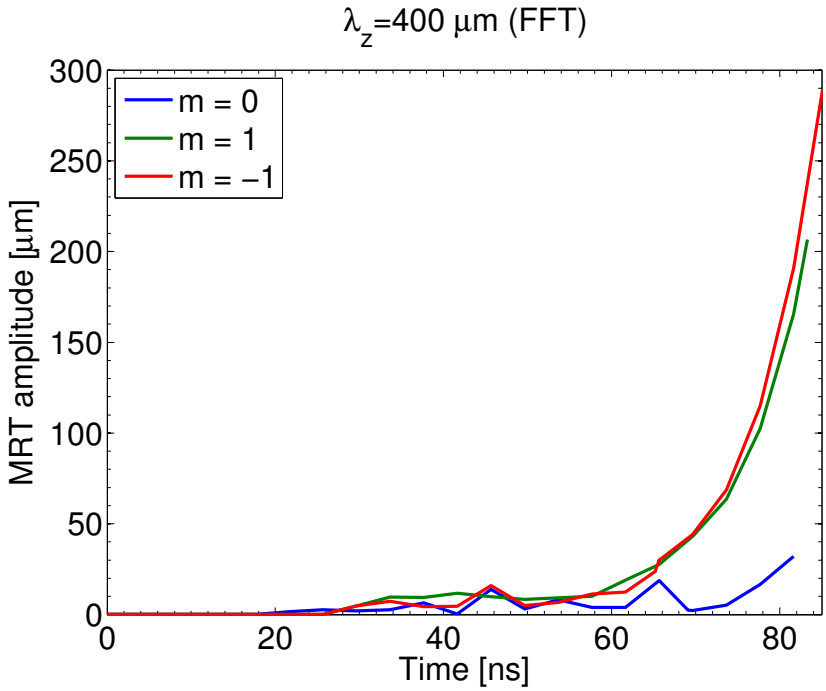

Figure C.2: Evolution of MRT amplitude for the $\lambda_z = 400$ μm perturbation for the $m = 0, \pm 1$ modes measured from the FFT of the 50% transmission contour.

Densities below 1 g/cc were cutoff to better show the MRT structure. As Fig. C.3 shows, the amplitudes are very similar for $\lambda_z = 800$ μm but the helical, unseeded, $\lambda_z = 400$ μm perturbations that have developed are clearly visible. The origin of this $\lambda_z = 400$ μm mode is unknown and higher resolution simulations should be run to verify the result. But nonetheless, it is strongly present only for the kink mode.

The inner surface ripple evolution was also calculated for completeness. The shock seeding in all cases was strong and occurred at 57.5 ns, as shown in Fig. C.4. As a reminder, the initial amplitude on the outer surface was 20 μm. As in the main text, this corresponds to the shock breakout time as well as the beginning of the bulk implosion of the liner. This is also around the time the MRT growth really begins to take off. Interestingly, the kink modes showed slightly stronger shock seeding of the inner surface, by roughly 3 μm. The source of this difference again seems to be related to the additional 400 μm mode present in the kink mode cases. However, this

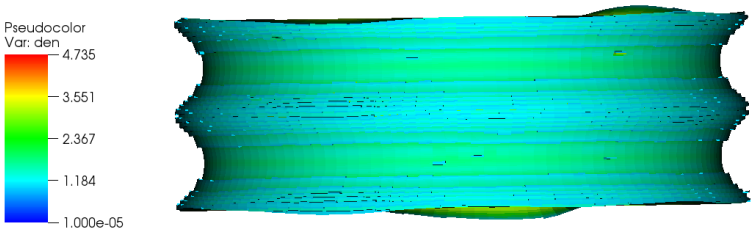

(a) MRT growth of seeded $m = 0$ with $\lambda_z = 800$ μm, $B_z = 10$ T after 77 ns.

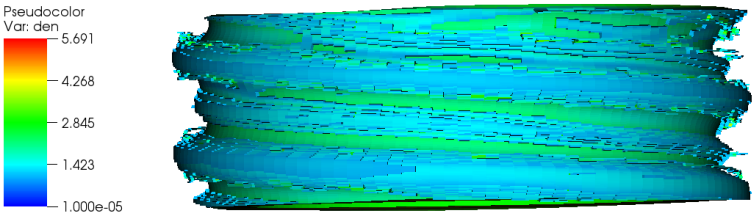

(b) MRT growth of seeded $m = 1$ with $\lambda_z = 800$ μm, $B_z = 10$ T after 77 ns.

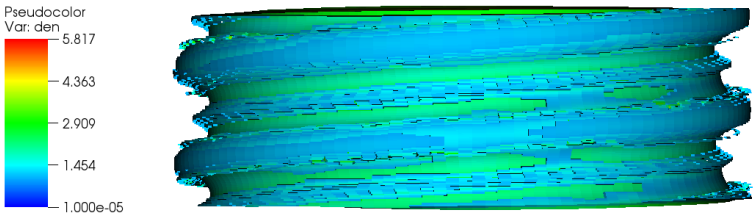

(c) MRT growth of seeded $m = -1$ with $\lambda_z = 800$ μm, $B_z = 10$ T after 77 ns.

Figure C.3: Seeded 3D aluminum liner implosions with an axial 10 T magnetic field. All densities below 1 g/cc were cutoff to better show the MRT structure.

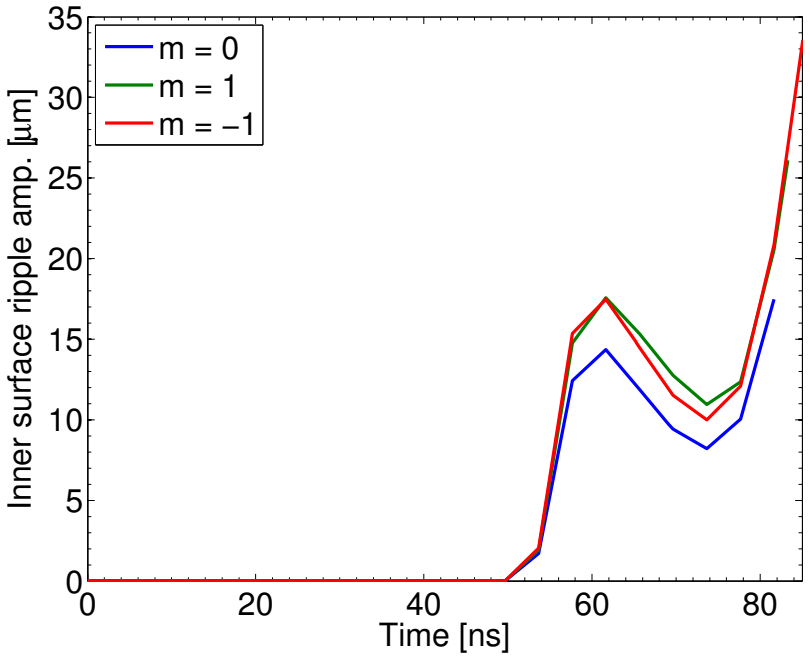

Figure C.4: Evolution of inner surface ripple for the $\lambda_z = 800$ μm perturbation for the $m = 0, \pm 1$ modes.

is a very small difference overall, considering the resolution of the simulations. More importantly, this liner is thicker than the liner in Sinars et al.[51] and yet significant shock seeding remains.

These preliminary results suggest that our analytic models can be successfully applied to 3D scenarios. Additionally, many of the effects we saw in 2D carry over to 3D, such as the shock seeding. Though the 3D simulations themselves are low resolution, results seem consistent with our 2D results as well as our analytic model. Higher resolution simulations should certainly be performed and there are many other modes that can be examined.

Bibliography

[1] Lord Rayleigh. "The Form of Standing Waves on the Surface of Running Water". *Proceedings of the London Mathematical Society* s1-15.1 (1883), pp. 69–78. eprint: `http://plms.oxfordjournals.org/content/s1-15/1/69.full.pdf+html`.

[2] G. I. Taylor. "The Instability of Liquid Surfaces when Accelerated in a Direction Perpendicular to their Planes. I". *Proceedings of the Royal Society of London A: Mathematical, Physical and Engineering Sciences* 201.1065 (1950), pp. 192–196.

[3] J. J. Hester, J. M. Stone, P. A. Scowen, B.-I. Jun, J. S. Gallagher III, M. L. Norman, G. E. Ballester, C. J. Burrows, S. Casertano, J. T. Clarke, D. Crisp, R. E. Griffiths, J. G. Hoessel, J. A. Holtzman, J. Krist, J. R. Mould, R. Sankrit, K. R. Stapelfeldt, J. T. Trauger, A. Watson, and J. A. Westphal. "WFPC2 Studies of the Crab Nebula. III. Magnetic Rayleigh-Taylor Instabilities and the Origin of the Filaments". *ApJ* 456 (Jan. 1996), p. 225.

[4] M. Kruskal and M. Schwarzschild. "Some Instabilities of a Completely Ionized Plasma". *Proceedings of the Royal Society of London A: Mathematical, Physical and Engineering Sciences* 223.1154 (1954), pp. 348–360.

[5] S. Chandrasekhar. *Hydrodynamic and Hydromagnetic Stability*. London, UK: Oxford University Press, 1961, p. 429.

[6] E. G. Harris. "Rayleigh Taylor Instabilities of a Collapsing Cylindrical Shell in a Magnetic Field". *Physics of Fluids* 5.9 (1962), pp. 1057–1062.

[7] A. B. Budko, M. A. Liberman, A. L. Velikovich, and F. S. Felber. "Suppression of RayleighTaylor and bulk convective instabilities in imploding plasma liners and pinches". *Physics of Fluids B* 2.6 (1990), pp. 1159–1169.

[8] M. R. Weis, P. Zhang, Y. Y. Lau, I. M. Rittersdorf, J. C. Zier, R. M. Gilgenbach, M. H. Hess, and K. J. Peterson. "Temporal evolution of surface ripples on a finite plasma slab subject to the magneto-Rayleigh-Taylor instability". *Physics of Plasmas* 21.12, 122708 (2014).

[9] M. R. Weis, P. Zhang, Y. Y. Lau, P. F. Schmit, K. J. Peterson, M. Hess, and R. M. Gilgenbach. "Coupling of sausage, kink, and magneto-Rayleigh-Taylor instabilities in a cylindrical liner". *Physics of Plasmas* 22.3, 032706 (2015).

[10] R. W. Lemke, M. D. Knudson, A. C. Robinson, T. A. Haill, K. W. Struve, J. R. Asay, and T. A. Mehlhorn. "Self-consistent, two-dimensional, magnetohydrodynamic simulations of magnetically driven flyer plates". *Physics of Plasmas* 10.5 (2003), pp. 1867–1874.

[11] R. W. Lemke, M. D. Knudson, C. A. Hall, T. A. Haill, P. M. Desjarlais, J. R. Asay, and T. A. Mehlhorn. "Characterization of magnetically accelerated flyer plates". *Physics of Plasmas* 10.4 (2003), pp. 1092–1099.

[12] S. A. Slutz, M. C. Herrmann, R. A. Vesey, A. B. Sefkow, D. B. Sinars, D. C. Rovang, K. J. Peterson, and M. E. Cuneo. "Pulsed-power-driven cylindrical liner implosions of laser preheated fuel magnetized with an axial field". *Physics of Plasmas* 17.5, 056303 (2010).

[13] D. B. Sinars, S. A. Slutz, M. C. Herrmann, R. D. McBride, M. E. Cuneo, K. J. Peterson, R. A. Vesey, C. Nakhleh, B. E. Blue, K. Killebrew, D. Schroen, K. Tomlinson, A. D. Edens, M. R. Lopez, I. C. Smith, J. Shores, V. Bigman, G. R. Bennett, B. W. Atherton, M. Savage, W. A. Stygar, G. T. Leifeste, and J. L. Porter. "Measurements of Magneto-Rayleigh-Taylor Instability Growth during the Implosion of Initially Solid Al Tubes Driven by the 20-MA, 100-ns Z Facility". *Phys. Rev. Lett.* 105, 185001 (18 2010).

[14] John D. Powell. "Interchange instability in railgun arcs". *Phys. Rev. A* 34 (4 1986), pp. 3262–3269.

[15] M. G. Haines. "An electron thermal instability in a resistive non-equilibrium fully ionised plasma". *Journal of Plasma Physics* 12 (01 Aug. 1974), pp. 1–14.

[16] V. I. Oreshkin. "Thermal instability during an electrical wire explosion". *Physics of Plasmas* 15.9, 092103 (2008).

[17] Kyle J. Peterson, Daniel B. Sinars, Edmund P. Yu, Mark C. Herrmann, Michael E. Cuneo, Stephen A. Slutz, Ian C. Smith, Briggs W. Atherton, Marcus D. Knudson, and Charles Nakhleh. "Electrothermal instability growth in magnetically driven pulsed power liners". *Physics of Plasmas* 19.9, 092701 (2012).

[18] Kyle J. Peterson, Edmund P. Yu, Daniel B. Sinars, Michael E. Cuneo, Stephen A. Slutz, Joseph M. Koning, Michael M. Marinak, Charles Nakhleh, and Mark C. Herrmann. "Simulations of electrothermal instability growth in solid aluminum rods". *Physics of Plasmas* 20.5, 056305 (2013).

[19] Kyle J. Peterson, Thomas J. Awe, Edmund P. Yu, Daniel B. Sinars, Ella S. Field, Michael E. Cuneo, Mark C. Herrmann, Mark Savage, Diana Schroen, Kurt Tomlinson, and Charles Nakhleh. "Electrothermal Instability Mitigation by Using Thick Dielectric Coatings on Magnetically Imploded Conductors". *Phys. Rev. Lett.* 112, 135002 (13 2014).

[20] D. D. Ryutov, M. S. Derzon, and M. K. Matzen. "The physics of fast Z pinches". *Rev. Mod. Phys.* 72 (1 2000), pp. 167–223.

[21] M. A. Liberman, J. S. De Groot, A. Toor, and R. B. Spielman. *Physics of Dense Z-pinches*. New York, NY: Springer-Verlag, 1999.

[22] P. M. Bellan. *Fundamentals of Plasma Physics*. Cambridge, UK: Cambridge University Press, 2006.

[23] John Nuckolls, Lowell Wood, Albert Thiessen, and George Zimmerman. "Laser Compression of Matter to Super-High Densities: Thermonuclear (CTR) Applications". *Nature* 239.5368 (Sept. 1972), pp. 139–142.

[24] John Lindl. "Development of the indirectdrive approach to inertial confinement fusion and the target physics basis for ignition and gain". *Physics of Plasmas* 2.11 (1995), pp. 3933–4024.

[25] R J Tayler. "Hydromagnetic Instabilities of an Ideally Conducting Fluid". *Proceedings of the Physical Society. Section B* 70.1 (1957), p. 31.

[26] J. G. Linhart. "Dynamic Stability of a Conducting, Cylindrical Shell in a Magnetic Field". *Journal of Applied Physics* 32.3 (1961), pp. 500–505.

[27] A. B. Sefkow, S. A. Slutz, J. M. Koning, M. M. Marinak, K. J. Peterson, D. B. Sinars, and R. A. Vesey. "Design of magnetized liner inertial fusion experiments using the Z facility". *Physics of Plasmas* 21.7, 072711 (2014).

[28] C. A. Jennings, M. E. Cuneo, E. M. Waisman, D. B. Sinars, D. J. Ampleford, G. R. Bennett, W. A. Stygar, and J. P. Chittenden. "Simulations of the implosion and stagnation of compact wire arrays". *Physics of Plasmas* 17.9, 092703 (2010).

[29] M. E. Cuneo, R. A. Vesey, G. R. Bennett, D. B. Sinars, W. A. Stygar, E. M. Waisman, J. L. Porter, P. K. Rambo, I. C. Smith, S. V. Lebedev, J. P. Chittenden, D. E. Bliss, T. J. Nash, G. A. Chandler, B. B. Afeyan, E. P. Yu, R. B. Campbell, R. G. Adams, D. L. Hanson, T. A. Mehlhorn, and M. K. Matzen. "TOPICAL REVIEW: Progress in symmetric ICF capsule implosions and wire-array z-pinch source physics for double-pinch-driven hohlraums". *Plasma Physics and Controlled Fusion* 48 (Feb. 2006), p. 1.

[30] S. Atzeni and J. Meyer-Ter-Vehn. *The Physics of Inertial Fusion*. New York, NY: Oxford University Press, 2004.

[31] Michael G. Mazarakis, Michael E. Cuneo, William A. Stygar, Henry C. Harjes, Daniel B. Sinars, Brent M. Jones, Christopher Deeney, Eduardo M. Waisman, Thomas J. Nash, Kenneth W. Struve, and Dillon H. McDaniel. "X-ray emission current scaling experiments for compact single-tungsten-wire arrays at 80-nanosecond implosion times". *Phys. Rev. E* 79, 016412 (1 2009).

[32] C.A. Coverdale, B. Jones, D.J. Ampleford, J. Chittenden, C. Jennings, J.W. Thornhill, J.P. Apruzese, R.W. Clark, K.G. Whitney, A. Dasgupta, J. Davis, J. Guiliani, P.D. LePell, C. Deeney, D.B. Sinars, and M.E. Cuneo. "K-shell X-ray sources at the Z Accelerator". *High Energy Density Physics* 6.2 (2010). ICHED 2009 - 2nd International Conference on High Energy Density Physics, pp. 143 –152.

[33] M. Jones, D. Ampleford, M. Cuneo, C. Jennings, B. Jones, M. Lopez, G. Rochau, M. Savage, and J. Porter. "Total X-Ray Power Improvement on Recent Wire Array Experiments on the Z Machine". *APS Meeting Abstracts*. Nov. 2010, p. 5010.

[34] G. A. Rochau, J. E. Bailey, R. E. Falcon, G. P. Loisel, T. Nagayama, R. C. Mancini, I. Hall, D. E. Winget, M. H. Montgomery, and D. A. Liedahl. "ZAPP: The Z Astrophysical Plasma Properties collaboration". *Physics of Plasmas* 21.5, 056308 (2014).

[35] M. D. Knudson, D. L. Hanson, J. E. Bailey, C. A. Hall, J. R. Asay, and W. W. Anderson. "Equation of State Measurements in Liquid Deuterium to 70 GPa". *Phys. Rev. Lett.* 87, 225501 (22 2001).

[36] M. D. Knudson, M. P. Desjarlais, R. W. Lemke, T. R. Mattsson, M. French, N. Nettelmann, and R. Redmer. "Probing the Interiors of the Ice Giants: Shock Compression of Water to 700 GPa and 3.8 $\mathbf{g}/\mathrm{cm}^3$". *Phys. Rev. Lett.* 108, 091102 (9 2012).

[37] M. R. Martin, R. W. Lemke, R. D. McBride, J. P. Davis, D. H. Dolan, M. D. Knudson, K. R. Cochrane, D. B. Sinars, I. C. Smith, M. Savage, W. A. Stygar, K. Killebrew, D. G. Flicker, and M. C. Herrmann. "Solid liner implosions on Z for producing multi-megabar, shockless compressions". *Physics of Plasmas* 19.5, 056310 (2012).

[38] M. R. Gomez, S. A. Slutz, A. B. Sefkow, D. B. Sinars, K. D. Hahn, S. B. Hansen, E. C. Harding, P. F. Knapp, P. F. Schmit, C. A. Jennings, T. J. Awe, M. Geissel, D. C. Rovang, G. A. Chandler, G. W. Cooper, M. E. Cuneo, A. J. Harvey-Thompson, M. C. Herrmann, M. H. Hess, O. Johns, D. C. Lamppa, M. R. Martin, R. D. McBride, K. J. Peterson, J. L. Porter, G. K. Robertson, G. A. Rochau, C. L. Ruiz, M. E. Savage, I. C. Smith, W. A. Stygar, and R. A. Vesey. "Experimental Demonstration of Fusion-Relevant Conditions in Magnetized Liner Inertial Fusion". *Phys. Rev. Lett.* 113, 155003 (15 2014).

[39] M. R. Gomez, S. A. Slutz, A. B. Sefkow, K. D. Hahn, S. B. Hansen, P. F. Knapp, P. F. Schmit, C. L. Ruiz, D. B. Sinars, E. C. Harding, C. A. Jennings, T. J. Awe, M. Geissel, D. C. Rovang, I. C. Smith, G. A. Chandler, G. W. Cooper, M. E. Cuneo, A. J. Harvey-Thompson, M. C. Herrmann, M. H. Hess, D. C. Lamppa, M. R. Martin, R. D. McBride, K. J. Peterson, J. L. Porter, G. A. Rochau, M. E. Savage, D. G. Schroen, W. A. Stygar, and R. A. Vesey. "Demonstration of thermonuclear conditions in magnetized liner inertial fusion experiments". *Physics of Plasmas* 22.5, 056306 (2015).

[40] J.E. Bailey, P. Arnault, T. Blenski, G. Dejonghe, O. Peyrusse, J.J. MacFarlane, R.C. Mancini, M.E. Cuneo, D.S. Nielsen, and G.A. Rochau. "Opacity measurements of tamped NaBr samples heated by z-pinch X-rays". *Journal of Quantitative Spectroscopy and Radiative Transfer* 81.14 (2003). Radiative Properties of Hot Dense Matter, pp. 31 –45.

[41] J. E. Bailey, T. Nagayama, G. P. Loisel, G. A. Rochau, C. Blancard, J. Colgan, Ph. Cosse, G. Faussurier, C. J. Fontes, F. Gilleron, I. Golovkin, S. B. Hansen, C. A. Iglesias, D. P. Kilcrease, J. J. MacFarlane, R. C. Mancini, S. N. Nahar, C. Orban, J. C. Pain, A. K. Pradhan, M. Sherrill, and B. G. Wilson. "A higher-than-predicted measurement of iron opacity at solar interior temperatures". *Nature* 517.7532 (Jan. 2015), pp. 56–59.

[42] D. V. Rose, D. R. Welch, E. A. Madrid, C. L. Miller, R. E. Clark, W. A. Stygar, M. E. Savage, G. A. Rochau, J. E. Bailey, T. J. Nash, M. E. Sceiford, K. W. Struve, P. A. Corcoran, and B. A. Whitney. "Three-dimensional electromagnetic model of the pulsed-power Z-pinch accelerator". *Phys. Rev. ST Accel. Beams* 13, 010402 (1 2010).

[43] R. M. Gilgenbach, M. R. Gomez, J. C. Zier, W. W. Tang, D. M. French, Y. Y. Lau, M. G. Mazarakis, M. E. Cuneo, M. D. Johnston, B. V. Oliver, T. A. Mehlhorn, A. A. Kim, and V. A. Sinebryukhov. "MAIZE: a 1 MA LTD-Driven Z-Pinch at The University of Michigan". *American Institute of Physics Conference Series*. Ed. by B. R. Kusse and D. A. Hammer. Vol. 1088. American Institute of Physics Conference Series. Jan. 2009, pp. 259–262.

[44] M.R. Gomez, R.M. Gilgenbach, Y.Y. Lau, W. Tang, J.C. Zier, M.G. Mazarakis, M.E. Cuneo, T.A. Mehlhorn, and W.A. Stygar. "Design of a MITL for a 1 MA LTD driving a wire array z-pinch load". *Pulsed Power Conference, 2007 16th IEEE International*. Vol. 1. 2007, pp. 152–155.

[45] A. A. Kim, M. G. Mazarakis, V. A. Sinebryukhov, B. M. Kovalchuk, V. A. Visir, S. N. Volkov, F. Bayol, A. N. Bastrikov, V. G. Durakov, S. V. Frolov, V. M. Alexeenko, D. H. McDaniel, W. E. Fowler, K. LeChien, C. Olson, W. A. Stygar, K. W. Struve, J. Porter, and R. M. Gilgenbach. "Development and tests of fast 1-MA linear transformer driver stages". *Phys. Rev. ST Accel. Beams* 12, 050402 (5 2009).

[46] M. R. Gomez. "Experimental Examination of Plasma Formation and Current Loss in Post-Hole Convolutes". PhD thesis. University of Michigan, Ann Arbor, 2010.

[47] J. C. Zier, R. M. Gilgenbach, D. A. Chalenski, Y. Y. Lau, D. M. French, M. R. Gomez, S. G. Patel, I. M. Rittersdorf, A. M. Steiner, M. Weis, P. Zhang, M. Mazarakis, M. E. Cuneo, and M. Lopez. "Magneto-Rayleigh-Taylor experiments on a MegaAmpere linear transformer driver". *Physics of Plasmas* 19.3, 032701 (2012).

[48] J. C. Zier. "Ablation Dynamics and Instabilities of Metallic Plasmas Generated Using Mega-ampere-scale Current Drivers". PhD thesis. University of Michigan, Ann Arbor, 2010.

[49] I.R. Lindemuth and R.C. Kirkpatrick. "Parameter space for magnetized fuel targets in inertial confinement fusion". *Nuclear Fusion* 23.3 (1983), p. 263.

[50] R. C. Kirkpatrick, I. R. Lindemuth, and M. S. Ward. "Magnetized Target Fusion: An Overview". *Fusion Science and Technology* 27.3 (1995), p. 201.

[51] D. B. Sinars, S. A. Slutz, M. C. Herrmann, R. D. McBride, M. E. Cuneo, C. A. Jennings, J. P. Chittenden, A. L. Velikovich, K. J. Peterson, R. A. Vesey, C. Nakhleh, E. M. Waisman, B. E. Blue, K. Killebrew, D. Schroen, K. Tomlinson, A. D. Edens, M. R. Lopez, I. C. Smith, J. Shores, V. Bigman, G. R. Bennett, B. W. Atherton, M. Savage, W. A. Stygar, G. T. Leifeste, and J. L. Porter. "Measurements of magneto-RayleighTaylor instability growth during the implosion of initially solid metal liners". *Physics of Plasmas* 18.5, 056301 (2011).

[52] D. B. Sinars, M. E. Cuneo, G. R. Bennett, D. F. Wenger, L. E. Ruggles, M. F. Vargas, J. L. Porter, R. G. Adams, D. W. Johnson, K. L. Keller, P. K. Rambo, D. C. Rovang, H. Seamen, W. W. Simpson, I. C. Smith, and S. C. Speas. "Monochromatic x-ray backlighting of wire-array z-pinch plasmas using spherically bent quartz crystals". *Review of Scientific Instruments* 74.3 (2003), pp. 2202–2205.

[53] R. D. McBride, S. A. Slutz, C. A. Jennings, D. B. Sinars, M. E. Cuneo, M. C. Herrmann, R. W. Lemke, M. R. Martin, R. A. Vesey, K. J. Peterson, A. B. Sefkow, C. Nakhleh, B. E. Blue, K. Killebrew, D. Schroen, T. J. Rogers, A. Laspe, M. R. Lopez, I. C. Smith, B. W. Atherton, M. Savage, W. A. Stygar, and J. L. Porter. "Penetrating Radiography of Imploding and Stagnating Beryllium Liners on the *Z* Accelerator". *Phys. Rev. Lett.* 109, 135004 (13 2012).

[54] T. J. Awe, R. D. McBride, C. A. Jennings, D. C. Lamppa, M. R. Martin, D. C. Rovang, S. A. Slutz, M. E. Cuneo, A. C. Owen, D. B. Sinars, K. Tomlinson, M. R. Gomez, S. B. Hansen, M. C. Herrmann, J. L. McKenney, C. Nakhleh, G. K. Robertson, G. A. Rochau, M. E. Savage, D. G. Schroen, and W. A. Stygar. "Observations of Modified Three-Dimensional Instability Structure for Imploding *z*-Pinch Liners that are Premagnetized with an Axial Field". *Phys. Rev. Lett.* 111, 235005 (23 2013).

[55] T. J. Awe, C. A. Jennings, R. D. McBride, M. E. Cuneo, D. C. Lamppa, M. R. Martin, D. C. Rovang, D. B. Sinars, S. A. Slutz, A. C. Owen, K. Tomlinson, M. R. Gomez, S. B. Hansen, M. C. Herrmann, M. C. Jones, J. L. McKenney, G. K. Robertson, G. A. Rochau, M. E. Savage, D. G. Schroen, and W. A. Stygar. "Modified helix-like instability structure on imploding z-pinch liners that are pre-imposed with a uniform axial magnetic field". *Physics of Plasmas* 21.5, 056303 (2014).

[56] D. C. Rovang, D. C. Lamppa, M. E. Cuneo, A. C. Owen, J. McKenney, D. W. Johnson, S. Radovich, R. J. Kaye, R. D. McBride, C. S. Alexander, T. J. Awe, S. A. Slutz, A. B. Sefkow, T. A. Haill, P. A. Jones, J. W. Argo, D. G. Dalton, G. K. Robertson, E. M. Waisman, D. B. Sinars, J. Meissner, M. Milhous, D. N. Nguyen, and C. H. Mielke. "Pulsed-coil magnet systems for applying uniform 1030 T fields to centimeter scale targets on Sandia's Z facility". *Review of Scientific Instruments* 85.12, 124701 (2014).

[57] Y. Y. Lau, J. C. Zier, I. M. Rittersdorf, M. R. Weis, and R. M. Gilgenbach. "Anisotropy and feedthrough in magneto-Rayleigh-Taylor instability". *Phys. Rev. E* 83, 066405 (6 2011).

[58] P. F. Schmit, P. F. Knapp, S. B. Hansen, M. R. Gomez, K. D. Hahn, D. B. Sinars, K. J. Peterson, S. A. Slutz, A. B. Sefkow, T. J. Awe, E. Harding, C. A. Jennings, G. A. Chandler, G. W. Cooper, M. E. Cuneo, M. Geissel, A. J. Harvey-Thompson, M. C. Herrmann, M. H. Hess, O. Johns, D. C. Lamppa, M. R. Martin, R. D. McBride, J. L. Porter, G. K. Robertson, G. A. Rochau, D. C. Rovang, C. L. Ruiz, M. E. Savage, I. C. Smith, W. A. Stygar, and R. A. Vesey. "Understanding Fuel Magnetization and Mix Using Secondary Nuclear Reactions in Magneto-Inertial Fusion". *Phys. Rev. Lett.* 113, 155004 (15 2014).

[59] P. F. Knapp, P. F. Schmit, S. B. Hansen, M. R. Gomez, K. D. Hahn, D. B. Sinars, K. J. Peterson, S. A. Slutz, A. B. Sefkow, T. J. Awe, E. Harding, C. A. Jennings, M. P. Desjarlais, G. A. Chandler, G. W. Cooper, M. E. Cuneo, M. Geissel, A. J. Harvey-Thompson, J. L. Porter, G. A. Rochau, D. C. Rovang, C. L. Ruiz, M. E. Savage, I. C. Smith, W. A. Stygar, and M. C. Herrmann. "Effects of magnetization on fusion product trapping and secondary neutron spectra". *Physics of Plasmas* 22.5, 056312 (2015).

[60] S. B. Hansen, M. R. Gomez, A. B. Sefkow, S. A. Slutz, D. B. Sinars, K. D. Hahn, E. C. Harding, P. F. Knapp, P. F. Schmit, T. J. Awe, R. D. McBride, C. A. Jennings, M. Geissel, A. J. Harvey-Thompson, K. J. Peterson, D. C. Rovang, G. A. Chandler, G. W. Cooper, M. E. Cuneo, M. C. Herrmann, M. H. Hess, O. Johns, D. C. Lamppa, M. R. Martin, J. L. Porter, G. K. Robertson, G. A. Rochau, C. L. Ruiz, M. E. Savage, I. C. Smith, W. A. Stygar, R. A. Vesey, B. E. Blue, D. Ryutov, D. G. Schroen, and K. Tomlinson. "Diagnosing magnetized liner inertial fusion experiments on Z". *Physics of Plasmas* 22.5, 056313 (2015).

[61] D. A. Yager-Elorriaga, A. M. Steiner, S. G. Patel, N. M. Jordan, R. M. Gilgenbach, Y. Y. Lau, M. R. Weis, and P. Zhang. "Sausage, Kink, and Magneto Rayleigh-Taylor Instabilities on Initially-Solid, Imploding and Exploding Cylindrical Liner Plasmas". *Third RHEDP Workshop*. 2015.

[62] D. A. Yager-Elorriaga, N. M. Jordan, S. G. Patel, A. M. Steiner, Y. Y. Lau, and R. M. Gilgenbach. "Z-Pinch Instability Experiments on the UM Linear Transformer Driver". *International Conference on Plasma Science*. 2015.

[63] D. A. Yager-Elorriaga, S. G Patel, A. M. Steiner, N. M. Jordan, R. M. Gilgenbach, and Y. Y. Lau. "Experimental Investigation of the Effects of an Axial Magnetic Field on the Magneto-Rayleigh-Taylor Instability in Ablating Planar Foils". *APS Meeting Abstracts*. 2014.

[64] A. M. Steiner, S. G. Patel, D. A. Yager-Elorriaga, N. M. Jordan, R. M. Gilgenbach, and Y. Y. Lau. "Experimental Investigation of the Electrothermal Instability on Planar Foil Ablation Experiments". *Third RHEDP Workshop*. 2015.

[65] A. M. Steiner, S. G. Patel, D. A. Yager-Elorriaga, N. M. Jordan, R. M. Gilgenbach, and Y. Y. Lau. "Characterization of a MA-Class Linear Transformer Driver for Foil Ablation and Z-Pinch Experiments". *20th IEEE Pulsed Power Conference*. 2015.

[66] Peng Zhang, Y. Y. Lau, I. M. Rittersdorf, M. R. Weis, R. M. Gilgenbach, D. Chalenski, and S. A. Slutz. "Effects of magnetic shear on magneto-Rayleigh-Taylor instability". *Physics of Plasmas* 19.2, 022703 (2012).

[67] M. M. Marinak, R. E. Tipton, O. L. Landen, T. J. Murphy, P. Amendt, S. W. Haan, S. P. Hatchett, C. J. Keane, R. McEachern, and R. Wallace. "Three-dimensional simulations of Nova high growth factor capsule implosion experiments". *Physics of Plasmas* 3.5 (1996), pp. 2070–2076.

[68] Robert D. Richtmyer. "Taylor instability in shock acceleration of compressible fluids". *Communications on Pure and Applied Mathematics* 13.2 (1960), pp. 297–319.

[69] E.E. Meshkov. "Instability of the interface of two gases accelerated by a shock wave". English. *Fluid Dynamics* 4.5 (1969), pp. 101–104.

[70] F. F. Chen. *Introduction to Plasma Physics*. Springer, NY: Cambridge University Press, 1995.

[71] J. R. Melcher. *Continuum Mechanics*. Cambridge, MA: MIT Press, 1986.

[72] V. N. Goncharov, P. McKenty, S. Skupsky, R. Betti, R. L. McCrory, and C. Cherfils-Clérouin. "Modeling hydrodynamic instabilities in inertial confinement fusion targets". *Physics of Plasmas* 7 (Dec. 2000), pp. 5118–5139.

[73] Steven W. Haan. "Onset of nonlinear saturation for Rayleigh-Taylor growth in the presence of a full spectrum of modes". *Phys. Rev. A* 39 (11 1989), pp. 5812–5825.

[74] J.J. MacFarlane, I.E. Golovkin, P. Wang, P.R. Woodruff, and N.A. Pereyra. "SPECT3D A multi-dimensional collisional-radiative code for generating diagnostic signatures based on hydrodynamics and {PIC} simulation output". *High Energy Density Physics* 3.1-2 (2007). Radiative Properties of Hot Dense Matter, pp. 181 –190.

[75] K. S. Holian. *T-4 handbook of material properties data bases*. Report No. LA-10160-MS. Los Alamos National Laboratory. 1984.

[76] M.P. Desjarlais. "Practical Improvements to the Lee-More Conductivity Near the Metal-Insulator Transition". *Contributions to Plasma Physics* 41.2-3 (2001), pp. 267–270.

[77] S. P. D'Yakov. "On the stability of shock waves". *Zh. Eksp. Teor. Fiz* 27 (1952), pp. 288–296.

[78] V. M. Kontorovich. "Concerning the stability of shock waves". *Sov. Phys. JETP* 6 (1957), pp. 1179–1180.

[79] J. W. Bates. "On the theory of a shock wave driven by a corrugated piston in a non-ideal fluid". *Journal of Fluid Mechanics* 691 (Jan. 2012), pp. 146–164.

[80] V. N. Goncharov, O. V. Gotchev, E. Vianello, T. R. Boehly, J. P. Knauer, P. W. McKenty, P. B. Radha, S. P. Regan, T. C. Sangster, S. Skupsky, V. A. Smalyuk, R. Betti, R. L. McCrory, D. D. Meyerhofer, and C. Cherfils-Clrouin. "Early stage of implosion in inertial confinement fusion: Shock timing and perturbation evolution". *Physics of Plasmas* 13.1, 012702 (2006).

[81] R. P. Drake. *High Energy Density Physics*. New York, NY: Springer Press, 2006.

[82] C. R. Weber, D. S. Clark, A. W. Cook, D. C. Eder, S. W. Haan, B. A. Hammel, D. E. Hinkel, O. S. Jones, M. M. Marinak, J. L. Milovich, P. K. Patel, H. F. Robey, J. D. Salmonson, S. M. Sepke, and C. A. Thomas. "Three-dimensional hydrodynamics of the deceleration stage in inertial confinement fusion". *Physics of Plasmas* 22.3, 032702 (2015).